PHOTOELECTROCHEMICAL NUCLEIC ACID SENSORS

Developing signal enhancement strategies for photoelectrochemical nucleic acid sensing

By

Sudip Kumar Saha

M.A.Sc (McMaster University)

B.Sc (Bangladesh University of Engineering and Technology)

A Thesis Submitted to the School of Graduate Studies in

Partial Fulfillment of the Requirements for the Degree

Doctor of Philosophy in Biomedical Engineering

McMaster University, Doctor of Philosophy (2020) Hamilton, Ontario

(Biomedical Engineering)

TITLE: Developing Strategies to Improve the Performance of Photoelectrochemical Nucleic Acid Sensors

AUTHOR: Sudip Saha, M.A.Sc, Engineering Physics (McMaster University)

SUPERVISOR: Leyla Soleymani, Associate Professor, Department of Engineering Physics, McMaster University

NUMBER OF PAGES: XXIV, 276

Lay Abstract

Detection and quantification of biomolecules is of utmost importance in early diagnosis, disease monitoring, prognosis, and disease management. In the past few decades, enormous efforts have been put towards utilizing photoelectrochemical (PEC) processes for biomolecular detection due to their high sensitivity. Gold nanoparticles are frequently being used to amplify the signal in the PEC bio-detection assay due to their plasmonic properties. However, the exact nature of the interaction between gold nanoparticles and the electrode material has not been determined. In this thesis, we investigated the interaction of gold nanoparticles with photoelectrode materials when they are separated by nucleic-acid sequences. Excitation energy and nucleic-acid length were varied to modulate the PEC current. The improved understanding of this interaction was further utilized to achieve a programmable response of nucleotide sensor from the photoelectrodes upon detecting the analyte of interest. We further developed different types of biosensing assay designs and examined their performance in terms of limit-of-detection, sensitivity, and specificity. Finally, we developed a new class of biosensor for detecting nucleic acids in bodily fluid and assessed the assay by using both electrochemical and PEC signal readout.

Abstract

Recently, photoelectrochemical (PEC) signal transduction, with optical excitation and electronic readout, has been identified as a powerful transduction strategy for bioanalysis due to its high sensitivity and low limit-of-detection. Semiconductive materials have been used as the building blocks of PEC transducers, while plasmonic nanoparticles (NPs) are frequently used as signal amplifiers in these biosensors. Though these approaches have been previously used in PEC biosensing, the interaction between plasmonic and semiconductors NPs linked together through biomolecules are not currently well-understood. Herein, we developed new strategies for preparing photoelectrodes using solution-based methods to enhance the photocurrent of PEC transducers. These transducers were then used to investigate the interaction mechanisms between plasmonic NPs and the photoelectrodes with the goal of enhancing the limit-of-detection of PEC biosensors.

In order to create photoelectrodes that were fabricated using facile benchtop methods designed to enhance the photocurrent of PEC transducers, wrinkled scaffolds were used to fabricate photoelectrodes that show an order of magnitude enhancement in photocurrent compared to the planar electrodes. These electrodes were further used in label-free *signal-off* DNA biosensing without any amplification steps. Limit-of-detection of 200 times lower were reported using these wrinkled photoelectrodes, than planar electrodes.

Gold (Au) and TiO_2 NPs were used as model materials to investigate the interaction between plasmonic and semiconductor NPs on a photoelectrode. The modulation of photocurrent was examined by varying the concentration of Au NPs and under different optical excitation wavelengths. UV light excitation provided larger photocurrent enhancement – at low concentration of Au NP – than visible light excitation. Furthermore, anodic photocurrent generation efficiencies by the photoelectrodes, which were prepared by using only Au NPs, were compared between interband and intraband excitation. The Au NP photoelectrodes demonstrated higher anodic photocurrent at interband excitation than intraband excitation and were further optimized by varying the size and deposition time of the Au NPs. Following this, Au NP- labeled DNA was used to study the effect of the distance between Au NPs and TiO_2 NPs on the magnitude of the measured photocurrent. When Au NPs were in proximity with TiO_2, they increased the generated photocurrent; however, they reduced the measured photocurrent when they were positioned further away from TiO_2 NPs. Utilizing this switching behavior of PEC signals, a differential signal generation strategy was adopted to achieve a biosensor with enhanced sensitivity and signal-to-noise ratio.

Ultimately, we designed a PEC signal transduction strategy to detect nucleic acids without target labeling. In this assay, Au NP-labeled DNA was used as a signal-amplification-barcode that was introduced to the assay following target binding. This label-free PEC biosensor showed a low limit-of-detection (3 fM), broad (1 fM – 100 pM) linear range, and capability to detect single and double base-mismatched sequences of DNA. Thus, this work presents materials and signal transduction innovations that enhance the performance metrics of biosensors.

Acknowledgements

First, I would like to offer my sincerest gratitude to my supervisor Dr. Leyla Soleymani for her excellent guidance, advice, and encouragement throughout the work. I greatly appreciate her continuous support, patience, and dedication to this work. During my graduate study she has always inspired me to develop new ideas and let me pursue these ideas, while providing insightful feedback. Her deep understanding of photoelectrochemical processes and semiconductor characteristics was very helpful.

I would also like to thank my supervisory committee members, Dr. Ravi selvaganapathy and Dr. John Preston for always providing me the thoughtful feedback while continued to inspire me in my work. Both of them provided me a lot of helpful suggestions and many new experimental ideas to reach scientifically sound conclusion.

Many thanks to my research partner Amanda Victorious who collaborated closely on several aspects of this work and made significant contributions. Specifically, I acknowledge her for developing electrode materials and optimizing the electrode fabrication process. She had also worked heavily on the DNA recognition works with both clinical and synthetic oligonucleotides. We also had several scientific discussions which helps me to advance my project and keeping me on the right track. Apart from the lab works, she also helped me to improve my writing on the journal articles and dissertation.

I feel lucky to be able to work with several incredible graduate and undergraduate students and post-docs from our lab, including, Richa Pandey, Amin Hosseini, Larona Toteng, Sarah Traynor, Jie Yang, Sadman Sakib, Sara Imani, Elaheh Bakhshandeh, and Marta Skreta. Dr. Richa Pandey also helped me to improve my writing of dissertation. All of my lab mates have supported me in my research work in several times. I always have fruitful discussions with them, which helps me to understand many aspects of my project clearly.

I would also like to express my gratitude to all the members of Dr. Soleymani's lab for making the research work more enjoyable – thanks to the fun time that we shared together.

I would like to thank my brother, Sanjib Kumar Saha for his continuous inspiration to be enrolled in PhD program. My parents, Alpana Rani Saha and Sontosh Kumar Shaha always supported me by encouraging and helping me to go through the difficult times. Not only I was able to receive mental support from them, the scientific discussion with my parents also enable me to think clearly towards my research project. My wife, Anwesha Sikder was always beside me during the whole graduate study. She always believed in me and inspired me every day in my work. As she has a biology background, I received several useful advices regarding my projects and writings from her. Also, thanks to my father-in-law and mother-in-law for believing in me and always encouraging at my work. I feel grateful to my family for their moral support. Without their support this thesis would have been impossible.

Finally, I would like to acknowledge the Natural Sciences and Engineering Research Council of Canada (NSERC), and McMaster University for their financial support.

Table of Contents

List of Figures

List of Tables

List of Abbreviations

ART	Antiretroviral Treatment
CAGR	Compound Annual Growth Rate
CE	Counter Electrode
CV	Cyclic Voltammetry
DNA	Deoxyribonucleic Acid
DPV	Differential Pulse Voltammetry
EIS	Electrochemical Impedance Spectroscopy
HIV	Human Immunodeficiency Virus
IPCE	Incident Photon-to-Current Conversion Efficiency
ITO	Indium-Tin-Oxide
LOD	Limit-of-Detection
MB	Methylene blue
NP	Nanoparticle
NTA	Nanoparticle Tracking Analysis
NHE	Normal Hydrogen Electrode
PCa	Prostate Cancer
PEC	Photoelectrochemical
PIRET	Plasmon-Induced Resonance Energy Transfer
POC	Point-of-Care
PS	Polystyrene
QD	Quantum Dot
RE	Reference Electrode
RNA	Ribonucleic Acid

SAB	Signal Amplification Barcode
SEM	Scanning Electron Microscopy
TAS	Transient Absorption Spectroscopy
TEM	Transmission Electron Microscopy
UV	Ultraviolet
WE	Working Electrode
WHO	World Health Organization

Declaration of Academic Achievement

This dissertation was written to fulfill the requirements of the doctoral degree in the department of Biomedical Engineering at McMaster University. The work described here were performed between the time period of September 2016 to November 2020.

The majority of the work in this written document was conducted, conceived, analyzed, and written by the author of this thesis, in consultation with the supervisor Dr. Leyla Soleymani, with the exception to the following:

Chapter 2: Amanda Victorious and Dr. Richa Pandey contributed writing of the manuscript equally.

Chapter 3: Yuting Chan calculated the CdTe quantum dot density from the TEM images.

Chapter 4: Amanda Victorious aided with photocurrent measurement and sample preparation. She also contributed equally to the manuscript writing.

Chapter 5: Dr. Jie Yang have taken the TEM images for Au NPs. Shayan aided in manuscript writing.

Chapter 6: All photocurrent measurements and sample preparation works were performed equally with Amanda Victorious. She also has equal contribution in the manuscript writing.

Chapter 7: The analytical work was performed at Fraunhofer institute and co supervised with Dr. Dirk Kuhlmeier. Susann Allelein performed EV extraction procedure, NTA measurement and TEM of EVs. She also contributed to the manuscript writing.

Chapter 8: All photocurrent measurements and sample preparation steps were performed in conjugation with Amanda Victorious. She also contributed equally to the manuscript writing. Dr. Richa Pandey assisted in the probe density measurement and calculation.

Chapter 1 Introduction

This chapter discusses the motivation behind developing photoelectrochemical (PEC) biosensors for nucleic acid detection. It will review the projected growing market size of the molecular point-of-care (POC) biosensors and the current technical challenges facing the development of marketable POC devices. It will also review different transduction methods for POC biosensors with the presentation of their advantages and disadvantages. It will justify the use of PEC readout in POC biosensors and will present the basic concepts of Photoelectrochemistry. Finally, this chapter will discuss the organization and objectives of this thesis.

1.1 Point-of-Care Biosensors – Motivation, Technical Challenges and Future Needs

Biosensors are the analytical devices that can detect and/or quantify biological analytes by having an output signal which is proportional to the concentration of the analyte.[1,2] Biosensors are created by integrating biorecognition elements with signal transduction devices.[3] The field of biosensing holds great promise for revolutionizing health care by providing rapid disease diagnostic and frequent disease management possibilities.[4] Disease diagnostics are either performed in a traditional laboratory-based setting where samples are delivered to a centralized location for analysis or in a POC setting where tests are performed at the point of patient care.[5] In the former case, the results are often obtained in days, whereas the turnaround time for POC devices is in the order of minutes to hours.[1] Currently, POC testing dominates the research arena of medical diagnostics.[6] The major advantages of POC tests over conventional tests include: rapid sample-to-result times and the possibility of early intervention, their ability in rapidly controlling the spread of infectious disease outbreaks, lower cost of testing,[7] and the possibility of delivering high quality disease management capabilities to remote and resource-poor communities.[8]

Due to the rapid growth in the development of POC platforms, this area is required to have proper monitoring and guidelines. World Health Organization (WHO) has established a guideline that is required for developing efficient POC devices, known as ASSURED. The acronym ASSURED stands for affordable, sensitive, specific, user-friendly, rapid and robust, equipment-free, and deliverable to end-users.[5,9] It is important to keep in mind that developing an ASSURED test that provides laboratory-quality test results is challenging because as the operation of the biosensor device is required to be simple (minimal training requirement), with the chemical reactions - pertinent to biorecognition and signal generation - occurring in small volumes inside in a self-contained device.[4,10]

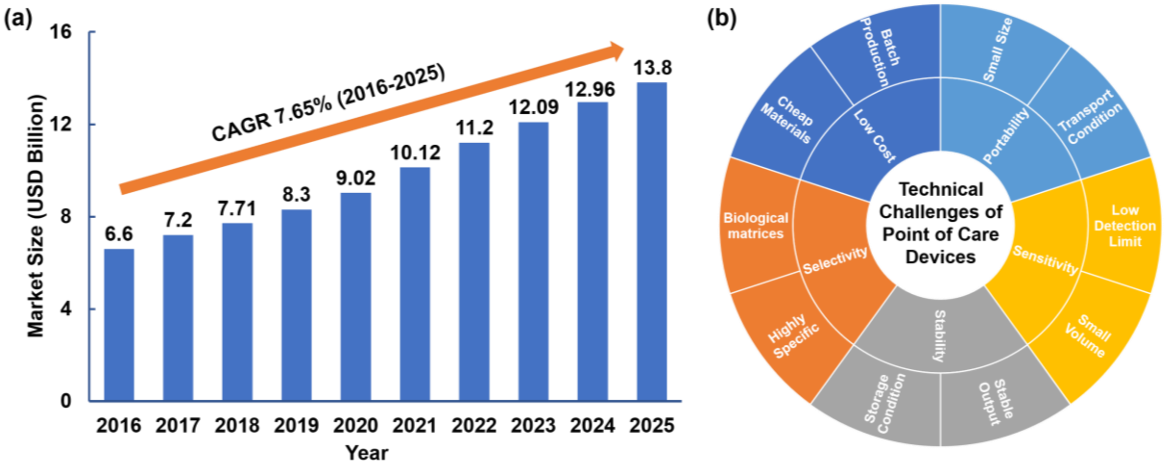

Figure 1-1: (a) Molecular Point-of-Care Diagnostic device market size and forecast for the year from 2016 to 2025. Data are collected from different reports of the market research.[8,11–13] (b) Technical challenges of point-of-care biosensors

Molecular POC testing - integrating molecular diagnostics (detection of biomarkers in genome and proteome)[11] with POC transducers[9] - is becoming increasingly popular as they offer fast decision, making at the time and point they are needed.[14] The market size of molecular POC is anticipated to grow from USD 6.6 billion in 2016 to USD 13.8 billion in 2025 with a compound annual growth rate (CAGR) of 7.65% (Figure 1-1a).[8,11] North America holds the largest share of POC devices in comparison to other geographical regions due to the government initiatives for increased POC-based lipid and blood sugar testing.[12,13]

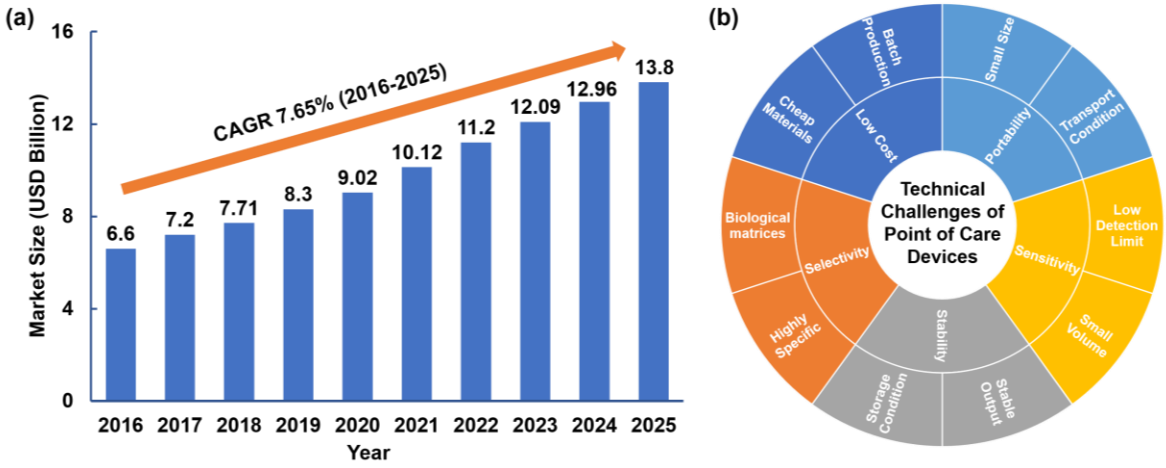

There is a pressing need to develop POC biosensing devices for diagnosis and prognosis of different diseases including infectious diseases (such as Malaria, Ebola, Covid-19, Dengue, COVID-19, Tuberculosis),[15,16] cancers,[17] cardiovascular diseases,[4,18] and sepsis.[19] With increased international travel enabling the spread of infectious diseases and contributing to higher morbidity and mortality rates in the developing nations, the utilization of POC biosensing has become crucial for early detection, containment of infectious spread, securing public health, and expediting treatment.[15] For example, WHO recognizes the urgent demand for developing POC platform for monitoring human immunodeficiency virus (HIV), as the effectivity of the antiretroviral treatment (ART) is dependent on the regular monitoring of CD4+ T-lymphocytes numbers and HIV viral loading.[20] It is critical to develop POC biosensing for Cancer detection and monitoring with high specificity and accuracy, reasonably priced and multiplexing capability.[17,21,22] The survival rate of cancer patients is highly dependent on the stage of cancer at the time of diagnosis. For example, detecting lung cancer (leading cause of cancer related death), at stage I yields a 1-year survival rate of 81-85%. In contrast, this rate sharply drops to only 15-19% if the detection occurs at stage III/IV.[23] A 5-year survival rate for breast cancer is reported as 100%, 85%, 58% and 19% for detecting at stage I, II, III and IV, respectively.[24]

In spite of the growing market size and the clinical need, there are only a few POC biosensors for disease diagnostics available on the market, which include electrochemical-based systems for blood glucose monitoring, and blood gas analysis,[25] PCR-based systems for detecting gene from pathogens,[26] and colorimetric-based systems for pregnancy tests, and cancer diagnosis.[2,17,27]

The key requirements for POC biosensors that have slowed down their translation from the research lab include low-cost, high sensitivity, selectivity, stability, and portability (Figure 1-1b). According to the ASSURED criteria defined by WHO, a POC device needs to be a low-cost device. The technical challenges in developing low-cost diagnostic devices stem from the cost of manufacturing, materials, reagents, and integrating multiple parts to a single portable device.[27–29] The bioreagents that are often required to be used in POC devices are not stable to large temperature fluctuations, and have limited lifetime when they are not refrigerated.[30] Additionally, most POC devices and their reagents are manufactured as single-use only, which in turn raises the cost.[6] The fabrication process of the device and its components are also required to be suitable for batch processing and automation. Paper or plastic-based devices are widely-used substrates for fabricating POC biosensors due to the low-cost batch-manufacturing process.[31,32]

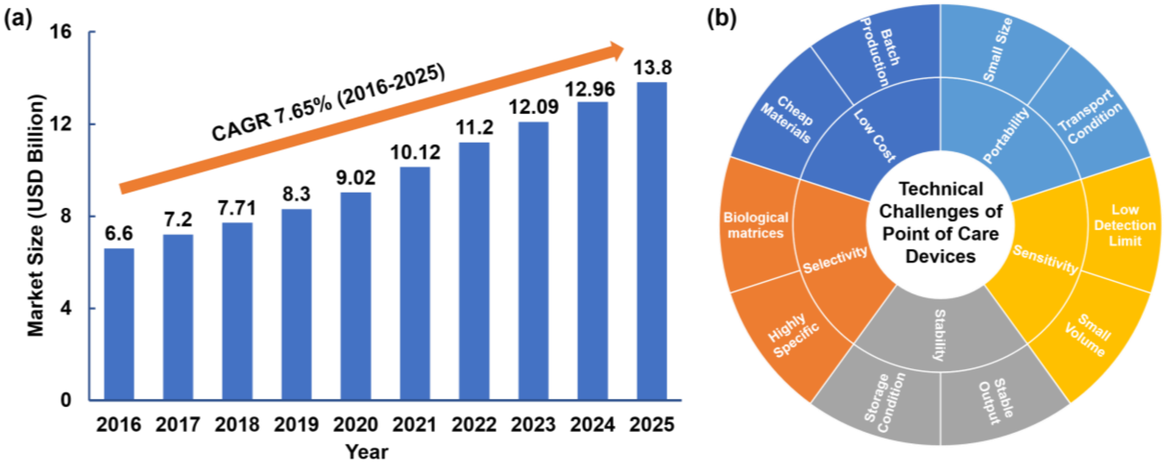

Furthermore, the processes and components encompassing from sample collection to data reporting needs to be seamlessly integrated and automated such that minimal hands-on intervention is required from the end-users.[18,33] A POC biosensing device needs to have a simplified process workflow - from sample collection to processing (i.e., plasma separation, centrifugation, mixing with reagents) – to be accessible to all users, including those with minimal technical expertise.[29,33] For example, the plasma separation process usually requires centrifugation and usage of pipettes, which are not readily available in rural settings.[7] Microfluidics is often used to automate the sample processing steps; however, it introduces additional costs for the final device.[29] Safe disposal of biological waste, is also an important technical challenge.[33]

Obtaining high sensitivity is critical for POC diagnostic devices for detecting the analyte of interest in the clinically relevant concentration range.[34,35] Achieving a low detection limit helps to the early detection of diseases, thereby lowers the mortality rate and healthcare cost.[30] Additionally, new clinical range of interest can also be found when the technology is able to detect lower than the concentration of current clinical range as it would provide the insight on disease progression and/or recurrence.[34] Special attention should also be given to the required sample volume while designing the bioassay. Usually, POC devices require minimal sample volume (0.1 μL – 1 mL)[18] as it lowers the cost of the assay as well as reduces the complexity of the sample collection process.[9,27] However, small sample volumes can introduce larger errors in sample processing as a few microliters variation can yield large discrepancies in the number of analytes present in the sample solution, leading to inaccurate quantitative outputs and issues with reproducibility.[36] Automated sample processing methods such as absorption pads and microfluidics are often used to solve this issue, which, however, introduce a higher chance of sample contamination.[33,36]

It is also crucial to develop POC bioassays that are highly selective or specific as the targets need to be detected from complex biological matrices (i.e., urine, plasma, saliva) containing a number of interferent species.[27,34,37] Selectivity of a biosensor is defined as the degree to which an analyte of interest can be detected without the interference from other biomolecules present in the clinical samples.[37] A POC device needs to achieve high specificity in the complex biological matrix (low non-specific detection) in order to lower false positives and negatives outcome.[17,38]

It is desirable to have a POC device that is small, compact, and portable which will allow transporting the device in rural areas where the expensive or cumbersome medical diagnostic devices are not available.[27] While, there exist many proposed POC biosensor designs that are compact, the reagents and bioreceptors are not stable during transportation.[9,39,40] This was a serious concern in the recent Zika and Ebola outbreaks, where most of the outbreaks occurred in remote areas.[41] Moreover, many POC nucleic acid detection devices require isothermal amplification and/or target recognition at a fixed temperature, which requires an external heater for the successful operation of these devices.[38]

The use of bioreceptors and reagents that are thermally, chemically and environmentally stable at ambient conditions are critical to a diagnostic device's successful translation to POC settings.[15,42,43] Some biomolecular receptors (such as antibodies, DNAs, enzymes) and reagents lack stability at room temperature,[4,28,33] often contributing test inaccuracy and result irreproducibility when applied in the primary health care settings, at the point-of-care.[44] Test strips are repeatedly affected by humidity, light, and temperature.[6] To circumvent these issues, such devices are shipped in sealed foil pouches and in a desiccated chamber, thus contributing to the increased the cost of the POC devices.[33] Moreover, surface binding kinetics are dependent on temperature and other environmental conditions (i.e., pH, humidity),[45,46] making it susceptible to unreliable outputs if the conditions are changed.

1.2 Signal transduction in biosensing

A typical POC biosensor consists of three segments, namely the biorecognition element, transducer, and output of the device (Figure 1-2).[1,2] Biorecognition elements are usually the molecules or chemical compounds that can recognize the analyte of interest (e.g., nucleic acid, enzyme, cell, antibody).[47] It is important to carefully choose bioreceptors with high specificity.[39] Transducers are the sensor elements that are responsible for converting biorecognition events into a signal that can be measured. The signals produced by the transducer are required to be proportional to the analyte concentration for quantitative evaluation.[48,49] Both the choice of biorecognition elements and transducing techniques are important to determine sensitivity, specificity, and limit-of-detection of the biosensor.[2,50,51] The output unit is consisting of a signal processor and display. The signal obtained from the transducer is required to be processed (i.e., amplification, analog-to-digital conversion) for quantitative analysis.[36] This processed signal is then compared with the calibration data previously saved in the device and then converted to a concentration value that is of interest to the end-user.[25]

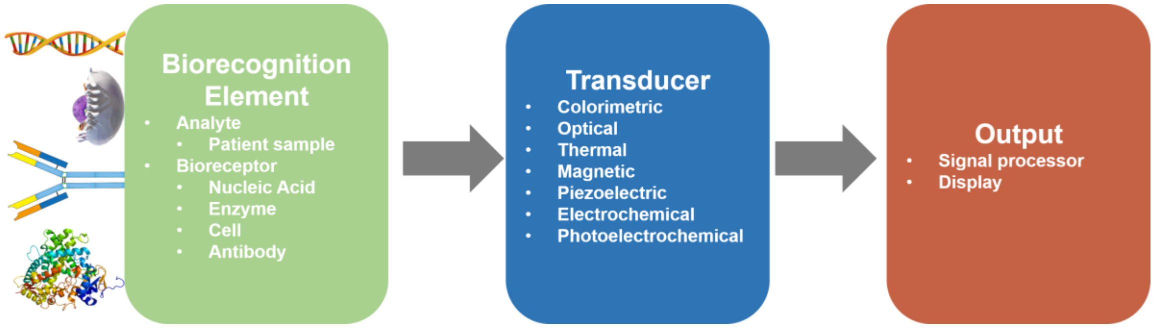

Figure 1-2: Components of a biosensor

The choice of biorecognition element largely depends on the analyte to be detected; In contrast, the choice of the transduction element depends on different requirements such as target users, cost, reliability, and analysis time. Commonly used transduction methods include colorimetric, optical, thermal, piezoelectric, magnetic, electrochemical, and photoelectrochemical techniques. It is imperative to recognize the advantages and limitations of each transduction methods prior to its selection for a specific application. However, these transduction modalities are continuously undergoing optimizations and innovations to overcome their limitations.[52]

Colorimetric biosensors work by generating a colour change upon target detection, often detectable by the naked eye, thus, eliminating the need for an additional readout interface.[52] Colorimetric transduction techniques are very common in paper-based lateral-flow biosensing.[53] In order to have better quantification capability, smartphone cameras are often incorporated in such colorimetric sensing systems.[41,54] These types of POC devices are quite lucrative as they are simple-to-operate, low-cost, and require minimal instrumentation.[55] On the downside, colorimetric assays have relatively low sensitivity and poor detection capabilities as compared to techniques such as electrochemical, optical, and magnetic.[34,52]

In optical signal transduction, photons emitted from dyes or other photoactive molecules are detected and typically correlated to the concentration of the target analyte.[49,56] In these assays, fluorescent probes are designed to become active follow their interaction with target analytes.[52] Besides fluorescence-based methods, absorption, reflection, chemiluminescence, and phosphorescence are also popular techniques in optical detection.[27] However, photobleaching is a major obstacle to achieving a stable and reliable signal using such techniques.[41] Furthermore, it is also challenging to obtain highly sensitive optical transducers that are both inexpensive and miniaturized.[57]

Thermal transducers measure the temperature change induced in response to biorecogntion and convert it into a measurable signal such as electrical current, and resistance.[58] A target analyte can be detected by measuring the heat evolution or absorption during a biochemical reaction.[47,59] A typical thermal biosensing devices utilizes enzymes that reacts with the target analyte and consequently release or absorb heat.[60] Thermal transducers can be operated non-invasively and therefore these sensors are frequently used for continuous monitoring of analytes.[61] However, these transducers demonstrate a lack of specificity due to non-specific heating effects.[47] Interfering reactions can cause enthalpy changes in the system and thereby affect the measurement.

Magnetic transducers often use magnetic nanoparticles (NPs), conjugated with antibodies or other biomolecules, possessing a high binding affinity with target moities.[62] These conjugated NPs are known as magnetic probes and shows long-term stability and good sensitivity.[49] As biological samples usually lack magnetic properties, the background noise for these transducers is very low, making it superior to optical and fluorescence-based transduction techniques.[52] This is an attractive method of POC biosensing as manipulation of magnetic probes can be easily achieved remotely by applying an external magnetic field. Although magnetic nanoparticle-based assays are inexpensive and easy to run, the instruments required to manipulate the magnetic field is not portable and is relatively expensive for a POC device.[63]

Piezoelectric transducers change the oscillation frequency of piezoelectric crystals based on the changes in mass, induced by the target binding at the transducing surface.[64] The piezoelectric properties are typically exhibited by anisotropic crystals that do not have a center of symmetry.[65] Quartz crystal microbalance coated with gold electrodes is the most popular choice of material to develop piezoelectric POC biosensors due to its reliability and availability.[64,65] As this method of transduction depends on mass change, it doesn't require any labels or reagents. Piezoelectric biosensors are generally inexpensive, simple, and able to provides fast response.[66] However, these transducers lack stability with varying temperature, with some crystals being water soluble.

Electrochemical transducers convert the analyte concentration into electrical signals using different types of electrochemical techniques such as potentiometry, amperometry, and impedimetric.[25] The most used electrochemical biosensor is the glucometer,[2,67] which utilizes enzyme-immobilized screen-printed electrodes as a test strip and a pocket-size potentiostat as a transducer.[35] Another popular commercial POC biosensor device utilizing electrochemical transducers is the iSTAT blood analyzer, which can simultaneously analyze multiple biomarkers in blood.[68] The advantages of using electrochemical transducers over other conventional methods (such as cell-culture, immunofluorescence assays, and PCR) include low-cost, high sensitivity and specificity, ease of miniaturization, and small analyte volume.[52,69,70]

Among different electrochemical techniques, amperometric techniques measuring changes in current upon modulations in the external bias voltage remains the most popular.[48,71] However, background signals stemming from the applied voltage reduces the signal-to-noise ratio at low concentrations of the target analyte. A drawback of electrochemical readout is that most biomolecules are not electrochemically active, thereby necessitating the used of signaling beacons in the assay design.[18]

Photoelectrochemical (PEC) transducers are similar to electrochemical transducers in terms of signal readout, with, light illumination used instead of or in addition to the applied voltage and the corresponding current reported as the signal footprint.[72,73] This method inherits the advantages of electrochemical methods while reducing background contributions, generally requiring lower applied voltages as compared to purely electrochemical readout methods.[74,75] By utilizing optical excitation, the reliance of PEC systems on electrical biasing reduces. Due to the separation of excitation and readout signals, the PEC biosensors show a high sensitivity.[76] Although, no PEC biosensor has been commercialized yet, this transduction method holds the potential to meet the requirement of the POC diagnostics device. The basic theory of PEC devices is described in the next section and the principles of PEC transducers with their advantages and disadvantages are described in Chapter 2.

1.3 Basics of the Photoelectrochemical cell

The basic structure of a PEC cell is shown in Figure 1-3a. It consists of a light source with photon frequency, υ, a working electrode (WE) prepared from photoactive material, a reference electrode, (RE) and a counter electrode (CE). A popular choice of the reference electrode is Ag/AgCl which has an electrochemical potential of 0.197 V *vs.* normal hydrogen electrode (NHE).[77] A voltage is applied or measured with reference to the RE and the current is measured with respect to the CE. The measured current flows through the ionic conductor or the electrolyte.[77] It should be noted that the light source often contains photons with a range of frequencies instead of a fixed frequency, υ (i.e., use of white light).[72,78]

In a PEC cell, the conversion of light to electrical or chemical energy originates from the light source which plays the role of an electron pump.[79] The electrodes are prepared from photo-active materials (such as semiconductors) that absorb photons with energy higher than their bandgap (E_g), and create an electron-hole (e^--h^+) pair.[79–81] Considering a semiconductor material, (S) that absorbs a photon of frequency, υ with energy higher than its bandgap (energy of a photon is hυ), an electron-hole pair is generated due to the optical excitation and thereby, S will be at the excited state, S^* (Figure 1-3b).

$$S + h\vartheta = S^*$$

The excited states of a material are rarely stable, with the generated charges quickly subject to recombination processes. To utilize the energy, it is essential to separate the charges before recombination. The electron-hole pairs can be separated by suitable acceptor (A) or donor (D) species in the electrolyte[79] and, hence, the light energy is converted to chemical energy. The electron donor is known as hole scavenger and the electron acceptor is known as electron scavenger.[82]

$$S^* + A \rightarrow S^+ + A^-$$

$$S^* + D \rightarrow S^- + D^+$$

Usually, the reaction between S^+ and A^- or S^- and D^+ is spontaneous.[79] Therefore, to utilize the chemical energy obtained in the PEC cell, these species are needed to be separated before reacting with each other, which can be obtained by applying an electrical bias and/or from the intrinsic electric field arising from the semiconductor/electrolyte interface.[79,83]

In PEC cells, light is absorbed by semiconductors. Hence, it is important to understand the semiconductor-electrolyte interface in order to succinctly explain the energy conversion mechanisms taking place in a PEC cell. In a semiconductor, valence bands are nearly filled, and the conduction bands are almost vacant, and they are separated by a bandgap of energy, E_g. When a semiconductor substrate is immersed in an electrolyte solution it will form a solid/liquid junction. In equilibrium conditions and without any excitation source, the electrochemical potential (μ_e) of the two material must attain equlibrium.[84] It needs to be mentioned that the μ_e of a semiconductor is equal to its Fermi level (E_F). The Fermi level is usually expressed with respect to the vacuum level whereas the electrochemical potential is expressed with respect to the NHE. The μ_e of NHE is equal to -4.5 ± 0.1 eV.[84]

Let us consider the formation of the junction between an n-type semiconductor and a solution containing a redox couple O/R. Charge transfer occurs at the interface due to the difference in the electrochemical potential between the semiconductor and the electrolyte. If the Fermi level of the semiconductor resides above the μ_e of the solution, electrons will flow from the semiconductor to the solution until equilibration of the Fermi level is achieved. This results in upward band bending at the interface, generating a depletion layer as electrons are extracted by the electrolyte (Figure 1-3c). An electric field forms at the interface in the direction from the bulk of the semiconductor toward the interface.

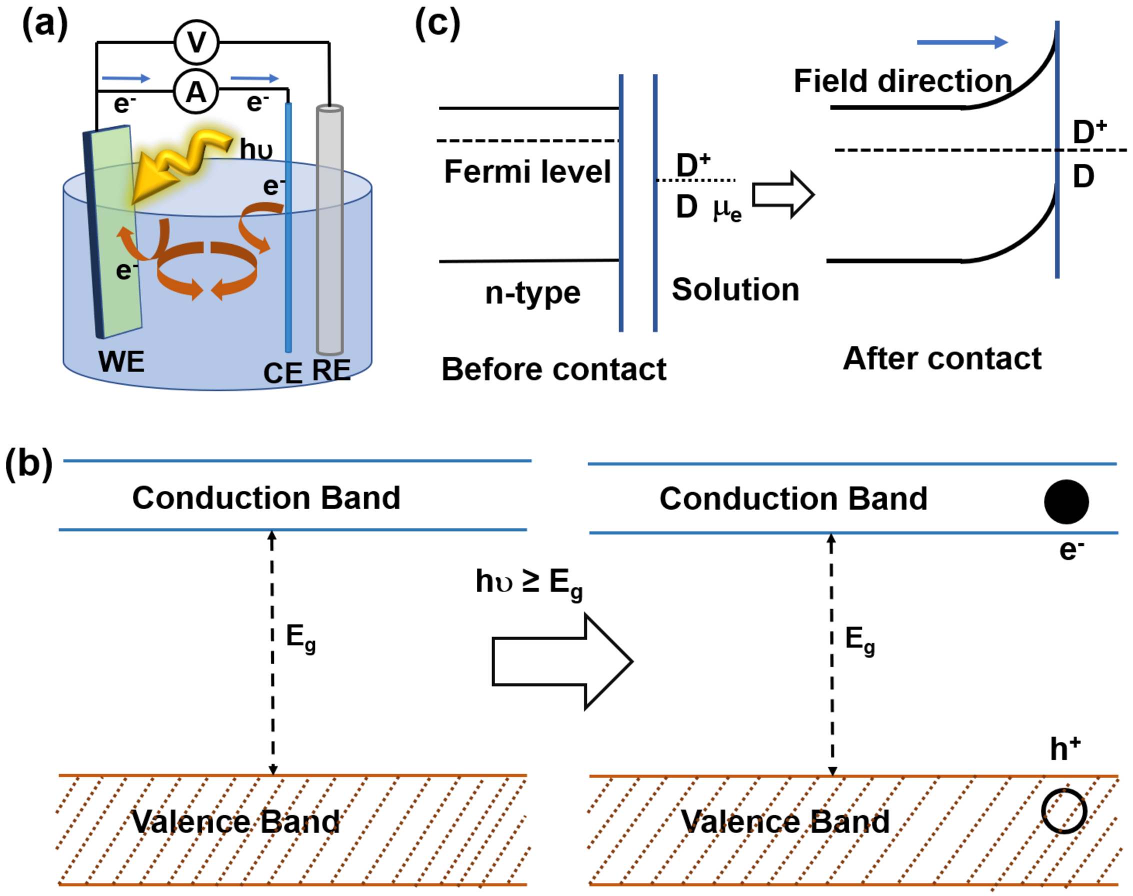

Figure 1-3: (a) Schematics illustrating the basic structure of a photoelectrochemical cell comprising three electrodes, namely, working electrode (WE), reference electrode (RE) and counter electrode (CE); (b)

Electron-hole pair generation by absorbing light of frequency υ; (c) Formation of space charge by immersing the substrate into electrolyte solution with redox couple D/D^+.

When light is absorbed at the semiconductor-electrolyte interface, it creates an electron-hole pair. If the solution contains a donor species with a redox potential above the photo-generated hole at the surface, then the hole moves towards the solution.

$$D + h^+ \rightarrow D^+$$

Electrons are transferred from the semiconductor to the counter electrode, reducing the oxidized form of the redox species, O, in the solution.

$$O + e^- \rightarrow R$$

The electric field that forms at the interface helps to accomplish this separation. It is worth mentioning that electrons move spontaneously in “downhill” and holes in the “uphill” direction.[85]

1.4 Research Objectives

The main goal of this research is to develop a low-cost signal-on ultrasensitive photoelectrochemical nucleic acid sensor by utilizing plasmonic nanoparticle interactions with semiconductors. In order to achieve this objective, the following specific goals were defined:

I. *Exploring solution-based photoelectrode fabrication methods for PEC biosensing*

To achieve a low-cost POC diagnostic device, it is important to develop a fabrication method that is robust, scalable, and is inexpensive. Solution-processed semiconductor quantum dots (QDs) and NPs are well-known due to their tunability of optical properties, ease of biofunctionalization, and excellent light-harvesting properties.[82,86,87] To achieve high photocurrent generation from these electrodes, the electroactive surface area also needs to be enhanced. We explore benchtop all-solution-processing techniques to deposit photoactive material on the substrate of the photoelectrode and optimize the fabrication parameters by analyzing the photocurrent. Furthermore, we investigate the suitability of the developed electrodes by detecting DNA. We answer the question: Can benchtop solution-processed photoelectrodes be used in biosensing and provide stable outputs?

II. Exploring the role of Au NPs in the photoelectrochemical process

Colloidal Au NPs are often used as labels for signal amplification in biosensing applications.[88,89] The optical properties of Au NPs can also be tuned by varying their size and the energy of optical excitation.[90–92] Additionally, optically excited Au NPs generate hot carriers which can take part in the PEC processes.[93,94] Photocurrent response from Au NP electrode may enable designing PEC biosensors without incorporating another photoactive materials. However, the exact role of Au NPs in PEC processes is still unknown. In this work, we investigated the effect of the excitation wavelength, and size and concentration of Au NPs on photocurrent generation efficiency. We answer the question: How will the size, concentration, and the excitation energy of the Au NPs affect PEC processes?

III. Investigating the interaction between photoactive semiconductors and metal NPs (i.e., Au) and understanding their influence on photocurrent

Plasmonic NPs (i.e., Au, Ag, Cu) have been utilized to enhance the limit-of-detection of optical and photoelectrochemical biosensors.[72,95] However, the interaction of these plasmonic NPs at different wavelengths and when attached through biomolecules are still under investigation. We investigated the interaction of plasmonic NPs with semiconductors using Au NPs and TiO_2 NPs. The knowledge obtained from this investigation is then used to design a DNA detection assay. We raised the question: what is the light wavelength regime that should be used to excite the photoelectrode when plasmonic NPs are being used along with semiconductors and what is the role of DNA when it is used to link the plasmonic NP with the semiconductor?

IV. Designing and implementing novel bioassay to detect nucleic acids (i.e., DNA/RNA) utilizing the plasmonic interaction with photoactive semiconductor

The knowledge obtained from the previous two objectives were combined to develop a novel bioassay to detect DNA/RNA from a complex biological matrix. The bioassay has been applied in both electrochemical and PEC systems to verify its design. We sought to achieve femtomolar detection for the developed bioassay. Furthermore, a differential approach was used to enhance sensitivity. We asked the question: Can differential photoelectrochemical readout be used to achieve signal-on biosensing using a non-labeled target in a complex biological matrix?

1.5 Thesis Overview

The remainder of this thesis is organized as follows:

Chapter 2 provides the literature review of PEC biosensors focused on different types of photoactive materials and transduction methods adopted.

Chapter 3 discusses the development of a wrinkled scaffold to load photoactive materials. The wrinkled surface showed a higher nanoparticle density compared to its planar counterpart. Scanning electron microscopy (SEM) and Transmission electron microscopy (TEM) were performed to gain insight into the mechanism of photocurrent enhancement. The electrical quality of the films was determined by measuring sheet resistance. Finally, the wrinkled electrodes were used for DNA detection.

Chapter 4 explores the different mechanisms of plasmonic PEC current enhancement for the Au/TiO_2 system. In this work, we used modified P25 NPs to prepare the photoelectrode. The Au NPs were introduced on the surface of the prepared electrodes. The optimum amount of Au NPs for obtaining the highest PEC current strongly depends on the excitation energy. The knowledge obtained from this mechanistic study was further applied to demonstrate a proof-of-concept DNA sensing assay where both *signal-on* and *signal-off* responses were achieved from a single electrode by simply switching the optical excitation wavelength.

Chapter 5 focuses on comparing the anodic photocurrent generation process by interband and intraband hot carriers in Au NP in order to understand their role when used for PEC signal amplification and when used as only photoactive material for photoelectrode preparation. The photoelectrodes were prepared by depositing Au NPs on a carbon substrate. A higher anodic photocurrent was achieved for interband excitation using different electrolytes containing a hole scavenger. Finally, these electrodes were used for direct oxidization of methanol under both interband and intraband illumination. The knowledge obtained from this study and Chapter 4, was used to select the excitation wavelength and the size of Au NPs used in biosensing assay design.

Chapter 6 exploits the knowledge obtained from the previous two chapters to design a differential PEC biosensing assay using a single robust and stable label. DNA was used as a nano-ruler between Au and TiO_2 NPs. The dynamic motion of the DNA strands was also analyzed to explain the effect of Au NPs on the electrode for varying lengths of probe DNA. Nanoscopic interactions between plasmonic NPs and TiO_2 electrodes were utilized through the PEC readout strategy.

Chapter 7 focuses on a label-free novel biosensing assay design that utilizes redox marker labeled nucleotides for signal generation. The bioassay design involves an extra hybridization step (two-steps) before introducing a redox marker labeled DNA in the second step, that is similar to the process in Chapter 6. This two-step hybridization assay was implemented by using electrochemical transducer and microRNA 200b as a target biomolecule. Methylene blue (MB) – tagged DNA sequence (similar to target sequence) was used as signal amplification barcode. The electrochemical biosensing techniques was further challenged by extracellular vesicles from human prostate cancer cells and human urine samples.

Chapter 8 utilizes the bioassay design used in Chapter 7 and knowledge obtained from Chapter 6 to construct a photoelectrochemical DNA sensor. A differential approach was developed to identify single and double base-pair mismatches from the target sequence. The effectivity of the PEC biosensor was further evaluated by detecting target DNA in human urine samples.

Chapter 9 discusses the conclusions of this research and contributions made in the field. It also provides a summary of the key findings and potential future work.

Chapter 2 Background on photoactive species and transduction mechanism

In the first chapter, we discussed the challenges associated with nucleic acid sensing in POC settings. We discussed different transduction methods and examined how PEC functions as a valuable platform to surmount those challenges. This chapter contains a literature survey on affinity-based PEC sensor development. The photoactive materials used in PEC biosensing are reviewed and divided into three parts, with the pros and cons of each of these photoactive species carefully deconstructed and extensively analyzed. Finally, we tap into the different PEC transduction mechanisms critical to biosensor development and provide feedback on the advantages and disadvantages of each of these mechanisms.

Authors: Amanda Victorious, Sudip Saha, Richa Pandey, Tohid F. Didar and Leyla Soleymani (Equal contribution with Amanda Victorious and Richa Pandey)

Publication: Frontiers in Chemistry, 7, 2019, 617

Publication Date: September 2019

2.1 Abstract

Detection and quantification of biologically-relevant analytes using handheld platforms are important for point-of-care diagnostics, real-time health monitoring, and treatment monitoring. Among the various signal transduction methods used in portable biosensors, photoelectrochemical (PEC) readout has emerged as a promising approach due to its low limit-of-detection and high sensitivity. For this readout method to be applicable to analyzing native samples, performance requirements beyond sensitivity such as specificity, stability, and ease of operation are critical. These performance requirements are governed by the properties of the photoactive materials and signal transduction mechanisms that are used in PEC biosensing. In this review, we categorize PEC biosensors into five areas based on their signal transduction strategy: a) introduction of photoactive species b) generation of electron/hole donors c) use of steric hinderance d) in situ induction of light, and e) resonance energy transfer. We discuss the combination of strengths and weaknesses that these signal transduction systems and their material building blocks offer by reviewing the recent progress in this area. Developing the appropriate PEC biosensor starts with defining the application case followed by choosing the materials and signal transduction strategies that meet the application-based specifications.

2.2 Introduction

Biosensors are devices that are used for analyzing biologically-relevant species using specific biorecognition elements and transducers.[96] Based on the nature of the biorecognition event, biosensors are classified into biocatalytic and affinity-based devices.[82] In biocatalytic biosensors, immobilized enzymes are used to recognize their specific substrate molecule, whereas affinity-based biosensors incorporate a synthetic or biological capture agent such as aptamers,[76] DNAzyme,[78] single stranded DNA,[72] or antibodies[97] to specifically capture the biologically-relevant target. The interaction between the analyte and the capture agent is translated into a readable signal by a transducer. To date, transduction methods relying on acoustic,[98] optical,[99] gravimetric,[100] electrochemical,[39] electronic,[42] and photoelectrochemical mechanisms[82] have been reported for use in biosensing systems. Researchers often choose a transduction method that offers the right level of sensitivity, specificity, speed, and multiplexing for the desired application, and meets requirements with respect to instrumentation cost, size, and ease-of-use.

Due to the growing demand for rapid clinical diagnosis and health monitoring using handheld systems, there has been an increasing push for the development of new bioanalytical techniques that combine high sensitivity, specificity, and speed with portable and inexpensive readout instrumentation. Photoelectrochemistry is an emerging signal transduction method that has the potential to meet the stringent requirements of the field of biosensing. In photoelectrochemical (PEC) bioanalysis, biological interactions between the analyte and the biorecognition element result in a change in the generated PEC current or voltage. In these systems, the photo-electrode or PEC label used in the biosensor is activated upon optical excitation. This optical excitation or biasing reduces the reliance of PEC systems on electrical biasing, which allows them to be operated under low or no applied electric potential. It has been shown that a lower limit-of-detection can be achieved using PEC signal readout compared to a similar assay that is coupled to electrochemical readout.[101,102] Although PEC biosensors rely on *both* optical and electrochemical mechanisms, they can be excited using low powered broad-spectrum light sources and read using inexpensive electrical circuits. As a result, it is possible to miniaturize PEC systems into inexpensive and integrated platforms that are similar in operation to handheld electrochemical readers.[102] Additionally, PEC biosensors can be easily multiplexed by incorporating multiple individually accessible electrodes on the same platform.

Affinity-based PEC biosensors combine the high specificity of biorecognition agents such as ssDNA, antibodies, and aptamers, with the sensitivity of PEC biosensors, and are the focus of this review article. There are previously-published review articles that are focused on a specific type of biorecognition-target interaction such as DNA sensing,[72] immunoassays,[97] enzymatic sensing,[78] and aptasensing.[76] However, our focus is on the elements that are important for building a PEC biosensor, regardless of the target analyte. Towards this goal we will discuss the construction of a photoelectrochemical cell, photoactive materials used in creating these devices, and the signal transduction mechanisms that are employed in PEC signal generation (Figure 2-1).

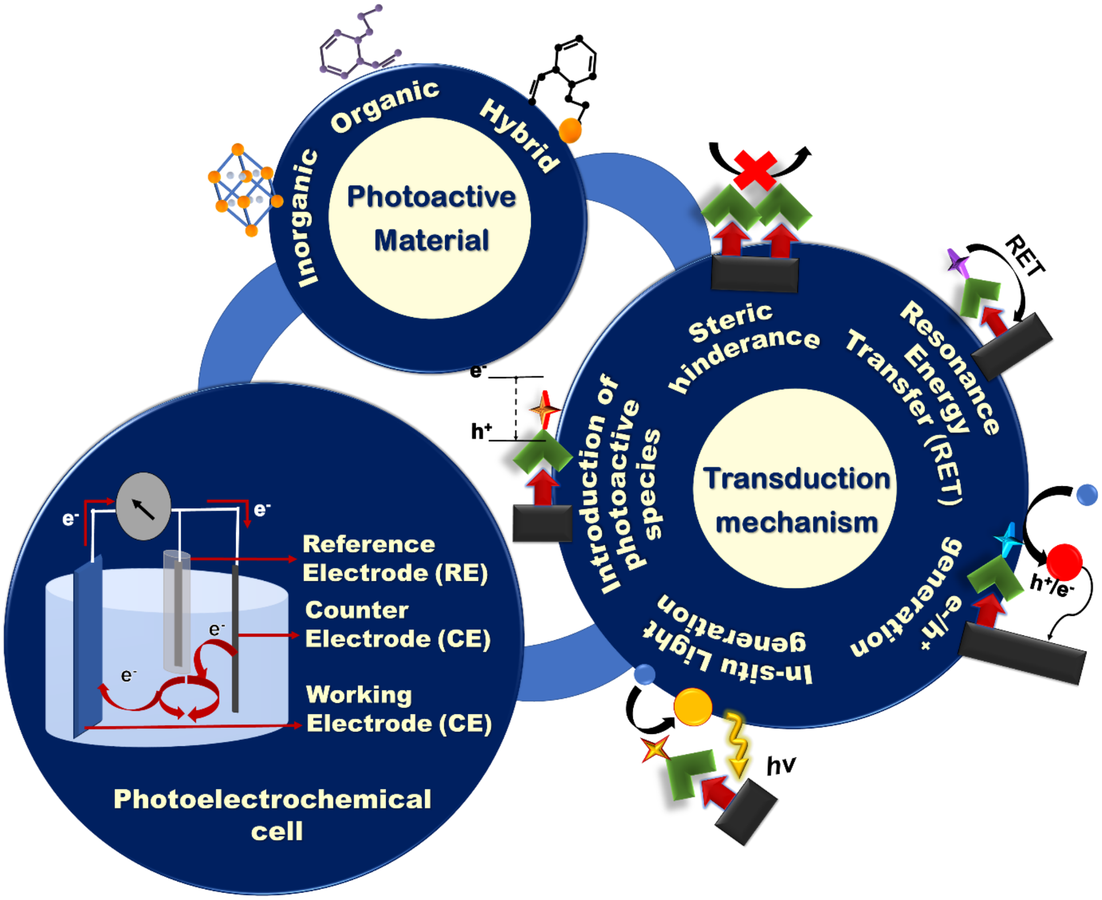

Figure 2-1: Scheme of a PEC cell and Affinity based PEC biosensor; photoactive materials and different transduction mechanism.

2.3 Construction of a photoelectrochemical cell

Generally, a PEC cell consists of an optical excitation source, an electrochemical cell, and an electrochemical reader. The electrochemical cell consists of four main components (Figure 2-1): (i) a working electrode (WE) that is often constructed by immobilizing photoactive materials on a conductive substrate, (ii) a counter electrode (CE), (iii) a reference electrode, and (iv) an electrolyte to generate PEC signals using redox reactions. Upon illumination, the redox reactions driven by the electrochemically active species in the electrolyte generate an electric signal between the WE and the CE that is recorded by the electrochemical reader. To create an application-specific PEC biosensor, much attention has to be paid to the design of: (i) the sensing electrodes using photoactive species having the appropriate electronic and optical properties and/or conductive collectors; (ii) the transduction mechanism based on the target analyte and device application; and iii) the electrolyte that contains the redox species that participate in the generation of the photoelectrochemical signal. The majority of the affinity-based PEC biosensing strategies reported to date rely on measuring photocurrents for signal readout.[97] To design a PEC bioassay, suitable for a specific application, it is important to have a comprehensive knowledge of these components and the strategies that are used in incorporating them in a synergistic fashion.

2.4 Photoactive species for PEC biosensors

Photoactive species are materials that respond to optical excitation by generating excited electronic states and converting optical energy to chemical and electrical energy.[103] These species enable a PEC cell to generate or modify an electrochemical signal in response to light or electromagnetic radiation. In PEC biosensors, photoactive species are used as the building blocks of photoactive electrodes and/or as labels or reporters that associate with the biorecognition element,[104] target analyte,[105] or solution-borne surfaces such as magnetic beads and metallic nanoparticles (NPs).[106] Due to its instrumental role in signal transduction, choosing the right photoactive material is critical to the development of PEC biosensors.

The photoactive materials used in PEC biosensing are chosen based on their electronic and optical parameters (incident photon-to-current conversion efficiency (IPCE), carrier mobility, response time, energy levels, and absorption spectrum), size/structure, stability against photobleaching, and ability to functionalize and integrate into devices. One of the most important parameters for evaluating photoactive materials used in PEC devices is IPCE. IPCE measures the photocurrent collected per incident photon flux as a function of illumination wavelength, which allows researchers to compare the efficiency of the photoactive species at different regions of the electromagnetic spectrum.[107] IPCE *collectively* evaluates the optical and electronic properties of materials such as their ability to absorb electromagnetic radiation and transport and collect charged carriers through the PEC cell. The electronic and optical properties of photoactive materials need to be selected such that the materials can supply charge carriers having sufficient energy (indicated by the band structure of the material) to drive the desired electrochemical reaction. It is also important for these electrochemical reactions to occur at high rates (measured using IPCE). The wavelength dependence of IPCE is important in understanding the type of optical excitation source that is required for designing a PEC biosensor.[108] Fine-tuning the size and shape of photoactive species in the nanoscale is also important for enhancing the PEC performance of the biosensor as structural tunability on the nanoscale changes the band structure of the materials, and can be used to enhance the surface-to-volume ratio of electrodes created from photo-active materials.[109] Resilience to photobleaching is important because photoactive materials that degrade due to multiple cycles of photoinduction do not allow the target-induced changes in the photocurrent to be reliably measured in a PEC biosensor.[108] Furthermore, for a photoactive material with the desired electronic, optical, and stability parameters to be used in a biosensing device, it is critical for it to have a chemical structure that can be easily functionalized with the typical termination chemistries of biorecognition elements (amine, thiol, carboxyl, aldehyde, to name a few). Finally, it is critical for these photoactive materials to have the sufficient level of mechanical robustness and adhesion to be integrated into miniaturized chips or strips used in biosensing platforms.

The three major classes of photoactive materials commonly used in PEC biosensors include (i) inorganic semiconductors, (ii) organic semiconductors and (iii) hybrid semiconductors,[110,111] which will be discussed in detail in this section.

2.4.1 Inorganic Semiconductors

Semiconductors from non-carbonous materials are known as inorganic semiconductors. Generally, in inorganic semiconductor transducers, electrons are excited from the valence band (VB) to the conduction band (CB) upon absorption of photons with energies higher than that of their band gaps. This results in the generation of electron-hole pairs that can engage in redox reactions at the surface of the working electrode. The direction of the photocurrent (anodic or cathodic) depends on the applied electric field and the position of the semiconductor Fermi level with respect to the electrochemical potential of the electrolyte (Figure 2-2). In general, the mobile charge carriers (electrons for n-type and holes for p-type semiconductors) in the semiconductor traverse the bulk of the electrode while minority carriers take part in the redox reactions at its surface.[83] Therefore, usually n-type semiconductors are used to produce anodic photocurrents, whereas p-type semiconductors are chosen for cathodic photocurrent generation.[112]

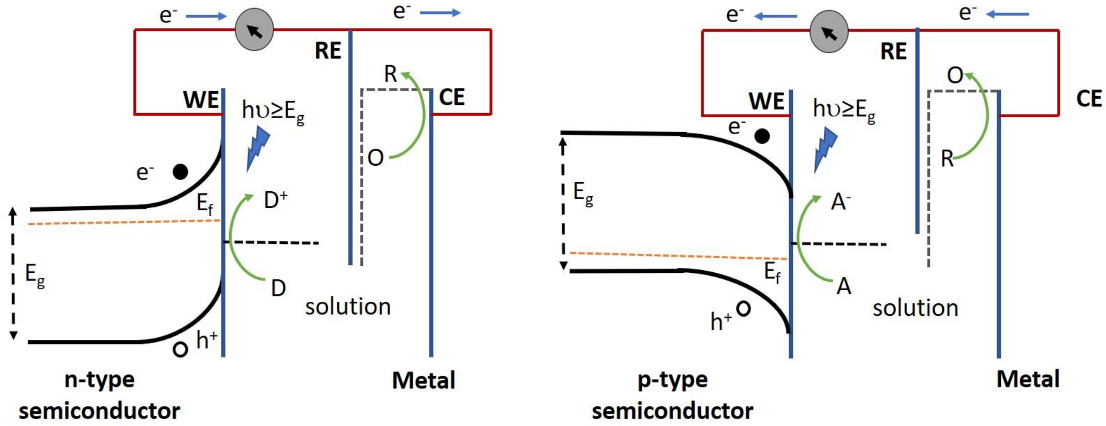

Figure 2-2: Operation of n-type semiconductor (left) and p-type semiconductor (right) in a PEC cell. Electron donors (D) in the redox couple are oxidized by the photoactive species, thereby resulting in the loss of an electron which is then relayed to the collector (underlying conductive substrate), thus yielding an anodic current. Alternatively, electron acceptors (A) in the redox couple gain an electron from the photoactive species following their reduction upon light illumination, subsequently giving rise to a cathodic current. E_g, E_f, WE, RE, CE represent band gap energy, fermi energy, working electrode, reference electrode and counter electrode, respectively.

Inorganic semiconductors such as titanium dioxide (TiO_2),[113] cadmium telluride (CdTe),[114–116] cadmium sulphide (CdS),[117–119] Molybdenum disulphide (MoS_2),[120,121] cadmium selenide (CdSe),[122,123] and zinc oxide (ZnO)[124] are used extensively in affinity based PEC biosensors.[114–116,125] Inorganic semiconductors offer a few advantages over their organic counterparts as discussed in the following section. These materials typically exhibit longer stability under mechanical, electrical, and environmental stress.[126] High-performance inorganic semiconductors can be precisely fabricated into various structures at the nanoscale, matching the size of subcellular and molecular components and allowing better probing of biological targets.[127] Inorganic semiconductors usually require lower bias voltages (due to their higher charge mobility and charge-carrier separation efficiency),[128] exhibit faster response time in the generation of charge carriers upon excitation, and allow for easier device passivation for use in physiological fluids as compared to organic SCs.[127]

Photochemical stability and high catalytic efficiency make TiO_2 a promising material for affinity-based PEC biosensing.[129,130] While promising, pristine TiO_2 suffers from a variety of problems such as poor response in the visible range owing to its wide band gap[131] and relatively fast recombination of photogenerated charge carriers.[132] In order to overcome these limitations, scientists are turning to hybrid TiO_2 architectures that incorporate other materials such as metal cations and anions,[133] semiconductors of M_xS_y[134] and M_xO_y[135] configuration, and carbon based materials.[136] CdTe is also widely used in PEC biosensing owing to its large bulk absorption coefficient ($>10^4$ cm^{-1} in the red, $\sim 10^5$ cm^{-1} in the blue)[137] and near-infrared band gap ($E_g \approx 1.5$ eV)[138] making it suitable for operation in the visible region of the solar spectrum. One of the issues with CdTe is the low abundance of tellurium, which makes it economically inviable for biosensing.[139] Due to the availability of precursors and ease of crystallization,[140] there is a move towards other chalcogenides of CdE (E= S, Se). These alternatives are mostly used as sensitizers due to their narrow band gaps (CdS= 2.4eV, CdSe= 1.7eV).[140] In addition, they offer higher conduction bands edges compared to most metal oxides (ZnO, TiO_2), making them useful for reactions where electrons need to be transferred from the conduction band of these materials.[140] However, their inability to integrate into device fabrication due to their poor adhesion onto the substrate and the inherent toxicity of Cd limit the possibility of using Cd-based materials in commercial biosensing platforms.[141] ZnO is another wide band gap (direct band gap of 3.37 eV in the near UV spectral region) semiconductor used in PEC biosensors, which offers biocompatibility, excellent photoactivity (large exciton binding energy at room temperature,[142] high charge carrier mobility, and thermal and chemical stability.[143] ZnO can be structurally tuned and has been used in flower,[105] rod,[144] wire,[145] and pencil[146] architectures for biosensing applications. Nevertheless, the photocatalytic performance of ZnO diminishes in aqueous solutions due to the fast recombination of photogenerated charge carriers.[147] Apart from these materials, emerging inorganic semiconductors are being investigated for use in PEC biosensing. Specifically, MoS_2 is under investigation for use in PEC cells due to its ability to generate an internal electric field at the contact surface for photoinduced charge separation, which increases the carrier lifetime.[148] Additionally, Bi-X (X= S,V,O) materials are being investigated due to their tunable bandgap and photostability in acidic solutions.[148]

Inorganic semiconductors are widely used in developing PEC biosensors; however, a remaining challenge, as with other types of materials used in biosensors is related to non-specific adsorption causing interference to the signal by producing high noise levels or low reactivity.[149] Hydrophilic coating strategies have been employed for metal oxides and sulphides but most of these strategies have downsides under severe biological conditions or where long-term stability is needed. Furthermore, conditions such as high temperature, high salinity, and non-neutral pH, intensify these effects.[150,151] To overcome these challenges, researchers are focusing on integrating inorganic semiconductors into hybrid antifouling networks, which has been previously reviewed.[76]

2.4.2 Organic Semiconductors

Organic materials such as graphitic carbon nitride (g-C_3N_4), porphyrin, azo dyes, chlorophyll, bacteriorhodopsin, and polymers such as semiconducting polymer dots (Pdot), phthalocyanine, poly(thiophene), phenylenevinylene (PPV) and their derivatives have been used for constructing photoactive electrodes that can be applied to PEC biosensors.[152–154] Some of the main advantages offered by organic semiconductors lies in their improved mechanical compliance,[155] intrinsic stretchability,[155] and their amenability to low-temperature all-solution-based processing.[127,156] This allows inexpensive fabrication of large-area films on flat, irregular, and flexible substrates, which provides opportunities for the development of flexible and printed electronic based biosensors used in wearable technology.[156,157]

Graphitic carbon nitride (g-C_3N_4) is a metal-free two dimensional polymeric semiconductor, which is attractive for PEC biosensing due to its high physicochemical stability and inexpensive and earth abundant nature.[158] It has a smaller band gap (~2.7 eV)[159] compared to commercial TiO_2 NPs (~3.0-3.2 eV) and is able to absorb light in the visible portion of the solar spectrum up to 460 nm.[160] G-C_3N_4 has a desirable electronic band structure due to the presence of π-conjugated sp^2 hybridized carbon and nitrogen. It is also electron-rich and has basic surface functionalities due to the presence of Lewis and Brönstead basic functions.[161] This has enabled g-C_3N_4 to be applied to the degradation of organic pollutants, hydrogen evolution reaction, biosensing, and energy conversion.[162–167] Da *et al.* constructed a novel “signal-off” PEC aptasensor using an aptamer bridged DNA network in conjunction with g-C_3N_4 to detect vascular endothelial growth factor (VEGF165).[153] This photo-electrode exhibited a stable photocurrent response with no severe decay under periodic off-on-off light excitation for nine cycles over a timeframe of 350 seconds. While g-C_3N_4 is a promising material, its low quantum yield in its pristine form (0.1% at 420–460 nm)[168] remains an obstacle to its incorporation as a high-performance photoactive material for biosensing.[169,170] In order to enhance the efficiency of this material, the use of g-C_3N_4 in conjunction with materials like TiO_2 and CdS has been reported for biosensing applications.[171–173] The formation of heterojunction with these materials helps to accelerate the charge transport and reduce the recombination rate by separating the charge carriers generated in g-C_3N_4.[160]

Porphyrins, a group of macrocyclic organic compounds composed of four pyrrole rings joined via methine (=CH-) bonds are being investigated for use as photoactive materials or sensitizers in PEC systems[174] due to their wide availability in nature, high molar absorptivity and thermal stability.[175] One such example is the use of porphyrin derivative, iron(III) meso-tetrakis (N-methylpyridinum-4-yl) porphyrin (FeTMPyP), in a PEC DNA biosensor.[176] In this case, CdS QDs modified with ssDNA formed the photo-active electrode. The porphyrin derivative specifically binds to dsDNA via groove interactions and reports the presence of dsDNA by catalyzing the oxidation of luminol to generate chemiluminescence. The photocurrent intensity of the biosensor did not show a detectable change after storage for 10 days, highlighting the stability of this biosensor. Porphyrin-based materials have been used in conjunction with inorganic semiconductors such as TiO_2,[177] ZnO,[143] and CdTe[178] to enhance the IPCE of these systems. A major difficulty in the wide spread use of porphyrin is that its chemical synthesis usually requires several steps with low overall yield, amounting to a high material cost.[179,180]

Pdots are a class of emerging photoactive nanomaterials that offer incredible photostability (photobleaching quantum yield of 10^{-7} to 10^{-10}), tailorable electrical and optical properties, minimal toxicity, good biocompatibility and ease of processing.[154,181–183] Pdots and PPV derivatives have recently been used in PEC biosensors[154,184] due to their extraordinary light harvesting ability resulting from their large two-photon absorption cross sections.[185] However, their use in biosensing architectures are required to be thoroughly explored because of their pH dependence and tunability of PEC properties according to their molecular weights.[186,187] Moreover, the PEC properties of these materials are highly dependent on the electron transfer processes within the π-conjugated bonds,[188] requiring a fundamental understanding of these processes to be able to design highly efficient photoelectrochemical biosensing devices.

Organic semiconductors are attractive due to their tunability, low cost, metal free nature, and relative abundance; however, their low quantum efficiency often requires them to be coupled with other photoactive materials for creating photoelectrodes. Unlike the ionic or covalent bond in inorganic semiconductors, organic semiconductors are made of molecular units held together by weak van der Waals interactions.[189] As a consequence, the mobility of the charge carriers in organic materials is generally smaller with longer response times upon excitation as compared to their inorganic counterparts[189] leading to smaller conductivity.[190] Consequently, more research is needed towards creating *all organic* photoelectrodes that can be used in biosensing.

2.4.3 Hybrid Semiconductors

Hybrid semiconductors are formed by: (i) coupling two inorganic semiconductors with different band gaps, (ii) complexation of organic and inorganic semiconductors,[112] and (iii) combining metal NPs (usually Au or Ag) with organic/inorganic semiconductors.

Coupling two or more inorganic semiconductors extends the absorption spectrum and increases the charge separation efficiency of the PEC system.[191] As a result, hybrid material systems offer a higher photon-to-current conversion efficiency, which is important for enhancing the performance of biosensors.[72] For example, when TiO_2 NPs are used with CdS QDs in insulin detection,[191] CdTe is excited using visible light, and the photo-induced electrons are transferred from CdTe to the conduction band of TiO_2 NPs. Liu *et al.* demonstrated improved sensitivity of microcystin detection by forming Z-scheme heterojunction of CdTe with Bi_2S_3 nanorods[192] due to enhanced charge separation. Another strategy used to enhance the solar light harvesting efficiency of photoanodes composed of wide bandgap semiconductors (i.e., TiO_2, ZnO) is upconversion[193]. This is a type of anti-stoke process in which emission of higher energy photons is achieved by the absorption of two or more low-energy photons.[194] Qiu *et al.* developed a hybrid upconverting structure where the narrow absorption band of TiO_2 was improved by the use of core−shell $NaYF_4$:Yb,Tm@TiO_2 upconversion microrods.[195] In this system, doped Yb^{3+} ions absorbed near-IR light, whereas the doped Tm^{3+} emitters produced the UV light through energy transfer upconversion (ETU). The upconverted photons were then absorbed by the TiO_2 NPs, thereby, yielding effective IR-UV upconversion.[195] This core-shell $NaYF_4$:Yb,Tm@TiO_2 structure was used to detect carcinoembryonic antigen (CEA), which is a biomarker for colorectal cancer.

Complexation of organic and inorganic semiconductors are used to overcome the low charge conductivity, narrow absorption spectrum, and strongly bound excitons that are encountered in organic semiconductors.[157,196] This class of transducers typically demonstrates improved PEC response and physical and chemical properties compared to their purely organic or inorganic counterparts.[76,197] This type of complexation was demonstrated using TiO_2 mesocrystals (inorganic semiconductor) sensitized with polyethylenimine (organic polymer).[198] Polyethylenimine reduces the electron transport energy barrier of TiO_2 mesocrystals by reducing the work function and thereby increasing the generated photocurrent. This type of performance enhancement was also seen in reduced graphene oxide (RGO)/CdS/ZnS photoelectrode, where a widened light absorption range, spatial separation of photogenerated electron-hole pairs, accelerated electron transfer, and reduction of surface defects resulting from the coupling of ZnS (wide bandgap, ~3.8 eV) and CdS (narrow bandgap, ~2.4 eV) was observed.[145] By using RGO further enhancement of the photocurrent was achieved as it facilitates the excited electron transfer from the conduction band (CB) of CdS to the CB of ZnO. Ultrafast electron transport was also realized by Matylitsky *et al.* and Wang *et al.* by adsorbing an electron acceptor, methyl viologen (MV) on the surface of CdSe QDs. Here, MV acted as an electron relay and facilitated ultrafast electron transport in a timeframe of ~70 fs.[122,123] The ability of MV in enhancing IPCE by working as an electron relay was exploited by Long et al. to demonstrate ultrafast electron transport in cysteine bioanalysis by using a MV coated CdS QD based system.[199] Surface sensitization of a wide band gap semiconductor with an organic material such as a dye is an alternative method of creating efficient hybrid materials. Here, an increase in efficiency of the excitation due to the injection of electrons directly into the CB of the semiconductor from the excited dye and expansion of excitation wavelength range results in higher photocurrent generation.[200–202] Neto *et al.* demonstrated the usefulness of such hybrid materials in sensing L-Dopamine by using iron phthalocyanine (FePc) dye sensitized TiO_2 system to enhance the PEC performance due to the charge transfer property of FePc.[203] Additionally, the antioxidant character of FePc is also hypothesized to enhance stability of the biorecognition units used in this study by inhibiting PEC-induced damage to the attached biomolecules typically seen in the case of wide band gap semiconductors such as TiO_2.

The coupling of inorganic/organic semiconductors with metal nanoparticles is increasingly used in PEC devices due to the ability of metal NPs such as gold, platinum and silver to enhance the photoresponse of the system through surface-plasmon resonance (SPR). Han *et al.* detected α-fetoprotein (AFP), a key clinical indicator used for diagnosing primary liver cancer, using Au-ZnO flower-rods.[105] Here, Au NPs enhanced the anodic photocurrent of ZnO flower-rods by extending the absorption to the visible region and by enhancing charge separation. Besides the SPR effect, Au NPs have been shown to improve the charge transfer properties of the substrate. For example, Lv *et al.* deposited Au NPs on p-$CuBi_2O_4$ electrodes to reduce the charge transfer resistance and hence enhance the cathodic photocurrent of p-$CuBi_2O_4$.[117] Another hybrid photoelectrode used in biosensing is created by Au NP-decorated hematite (α-Fe_2O_3) nanorods.[204] Despite being widely used in other PEC applications (such as PEC water splitting, photovoltaic cells), α-Fe_2O_3 has been rarely used in PEC biosensing due to poor electron mobility and lack of binding with capture biomolecules. Enhancement of electron mobility was achieved by decorating α-Fe_2O_3 with Au NPs. Moreover, Au NPs were also used to covalently attach capture biomolecules to the photoactive electrodes. Au NPs have also been used as anchors to deposit probe DNA and for improving the photocurrent of g-C_3N_4- based photoelectrodes.[205] In this work, Au NPs are used with g-C_3N_4 for detecting zeatin, one of the main cytokines found in plant tissues responsible for promoting plant growth.

Hybrid semiconductors are gaining popularity as transduction elements for PEC biosensors owing to their performance enhancement resulting from the coupling of desirable qualities of its constituent materials and the unique properties generated as a consequence of their complexation. To be able to achieve higher IPCE from these hybrid structures, it is important to carefully choose the materials and control their composition and morphology. Controlling interfacial defects is an important consideration for designing hybrid PEC systems. A summary of the photoactive materials used in PEC biosensing is presented in Table 2-1.

Table 2-1: Properties of various photoactive species used in PEC biosensing. RSD represents relative standard deviation, which signifies the reproducibility of the sensor.

Photo electrode material	**Excitation**	**Stability ('N' cycles, Rsd (%), period)**	**Base photo-current (A)**	**Enhanced absorption**	**Enhanced charge separation**	**Ease of functionalization**	**Reference**
1.1 Inorganic Semiconductors							
TiO_2 NWs	Simulated sunlight	-	1.15 x10^{-3}	No	No	Yes TiO_2 NWs functionalized with HRP via APTES-gluteraldehyde coupling.	130
CdTe QD	Xenon lamp; 420 nm cut-off filter	Fairly stable. N=17, ~Rsd ~9.16%, 360 s	~2.17x10^{-7}	No	Decreased. Trap sites resulting from Ag_2Te formation create new electron−hole recombination centers.	Yes; 3-Mercaptopropionic (MPA) modified CdTe via one pot synthesis; resultant carboxyl terminated surface.	114
CdTe QD	590 nm	Very stable. N=8, Rsd ~0.9%, 275 s	~3.80x10^{-7}	No	No	Yes; MPA modified CdTe via one pot synthesis; resultant carboxyl terminated surface.	115

CdTe QD	590 nm	Very stable. N=15, no decrease in photocurrent, 425 s	~2.10x10^{-7} (anodic) ~1.20x10^{-7} (cathodic)	No	No	Yes; MPA modified CdTe via one pot synthesis; resultant carboxyl terminated surface.	116
1.2 Organic Semiconductors							
g-C_3N_4	Visible	Very stable. N=9, no significant decrease in photocurrent, 350 s	~3.00x10^{-6}	Yes	Yes; MB intercalators following duplex formation at g-C_3N_4 enhance separation efficiency.	No	153
FeTMPyP	Chemiluminescence	Very stable. Rsd ~4.3%. Long term stability over 10 days.	~2.50x10^{-7}	Yes	No	No	Zang *et al.*, 2015)
PFBT Pdots (Polymer dots)	450 nm	Stable. N=20, 400 s	~3.00x10^{-8}	No	Yes; photogenerated electrons transferred to the proton in solution at low pH value.	Yes; Carboxylated surface obtained via synthesis procedure allows for easy immobilization of pDNA via amine-carboxyl interaction.	154
1.3 Hybrid Semiconductors							
1.3.1 Inorganic -Inorganic							
CdTe-Bi_2S_3	Visible	Fairly stable. N=8, Rsd~7.3%, 350 s	~4.00x10^{-7}	Yes	Yes; Z-scheme heterojunction formation between CdTe and Bi_2S_3.	No	192
CdS/ZnS	Visible	Good long-term stability; 95.6% of its original value after 5 months	~3.00x10^{-5}	Yes	Yes; Formation of heterojunction allowed the transfer of photogenerated electrons to ZnS conduction band.	Yes; CdS was modified by carboxyl groups which was used to attach with amine terminated DNA.	166
Core−shell $NaYF_4$:Yb, Tm@TiO_2	Infrared	Fairly stable. N=10, Rsd ~7.9%, 250 s	~1.25x10^{-7}	Yes	Yes; Enhanced separation due to formation of Z-scheme heterojunction	No	195
1.3.2 Organic-Inorganic							

TiO_2 – polyethylenimine mesocrystal	Visible	Very stable. N=10, Rsd ~2.04%, 250 s Excellent long-term stability; 94.8% of initial value after 12 days	~4.00x10^{-6}	Yes	Yes; Improved charge separation via ligand (OAM/PEI) modification	Yes; Organic ligand (OAM/PEI) modification confers the complex with reactive amine terminations capable of further chemical reaction.	198
CdS - MV	Xenon lamp	Poor stability.	~1.00x10^{-7}	No	Yes; MV coating of CdS facilitates fast charge separation and a slow charge recom-bination upon irradiation.	Yes. Thioglycolic acid (TGA) capped CdS QDs formed via precipitation-based synthesis; resultant carboxyl terminated surface.	199
TiO_2-EPM	380-480 nm	Very stable. N=10, Rsd ~2.04%, 400 s	~3.00x10^{-6}	Yes	No	Yes; Amine and hydroxyl terminations on TiO_2 conferred via EPM (ligand) conjugation.	202
1.3.3 Metal NP -Inorganic/Organic							
AuNP-ZnO FRs	Simulated sunlight	Very stable. N=15, no decrease in photocurrent, 300 s	~2.50x10^{-5}	Yes	Yes; Au NPs in the Au-ZnO FRs heterostructure enhances charge separation.	No	105
AuNP on p-$CuBi_2O_4$	>420 nm	Good long-term stability; 99.8% of its original value after 3 weeks	~4.00x10^{-7}	No	Yes; Au NPs, as a front contact of p-$CuBi_2O_4$ enhance the efficiency of charge separation	Yes; Au NPs, as a front contact of *p*-$CuBi_2O_4$ allow conjugation with thiol terminated biomolecules.	117
Au NP/Graphene QD/g-C_3N_4 nanosheet	Xenon lamp	Very stable. N=15, Rsd ~1.5%, 20 s	~4.5x10^{-7}	No	Yes; g-C_3N_4 and GQD reduce the probability of recombination of photogenerated electrons and holes.	Yes; Au NPs allow conjugation with thiol terminated biomolecules	205

2.5 Transduction mechanism

Several signal transduction strategies have been proposed to translate a biorecognition event to a PEC signal. The signal of a PEC biosensor depends on the properties of the photoactive material, applied potential, light intensity, wavelength, and the type and concentration of the electron donor or acceptor.[206] Depending on the mechanism chosen, the PEC biosensor operates in either *signal-on* or *signal-off* mode. In the former case, the PEC signal increases upon target recognition, and in the latter case it decreases.[97] In this review, we have categorized the signal generation strategies used in affinity-based biosensors as: (i) introduction of photoactive species, (ii) generation of electron/hole donors, (iii) use of steric-hindrance, (iv) *in situ* induction of light, and (v) resonance energy transfer (Figure 2-3). In this section, we discuss the recent biosensing reports categorized under these mechanisms.

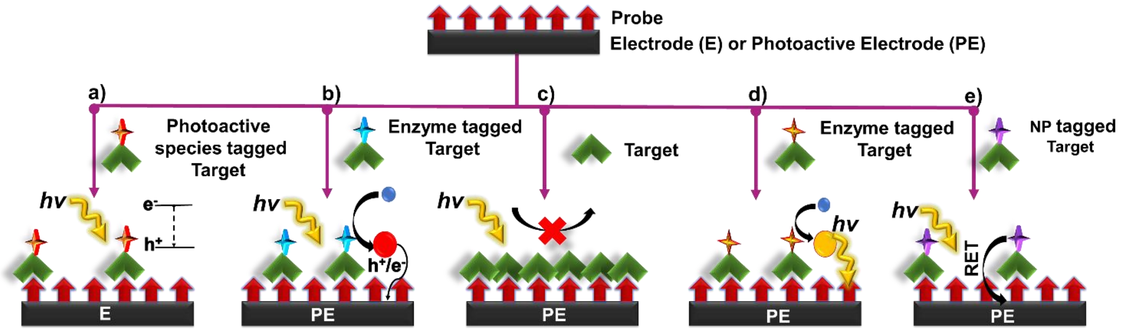

Figure 2-3: Principles of signal transduction in PEC biosensors a) Introduction of photoactive species b) Generation of electron/hole donors c) Use of steric hinderance d) In situ induction of light e) Resonance energy transfer.

2.5.1 Introduction of Photoactive Species

In this signal transduction strategy, the photoactive material is incorporated into the target/probe complex in the form of a label, which enhances or quenches the PEC response.

Signal modulation is initiated by bringing the label into the close proximity of a conductive/ photoactive substrate following a biorecognition event. Once in proximity to the appropriate substrate, electron hole pairs are generated at the surface of the photoactive material upon light excitation. These electron-hole pairs then take part in chemical reaction with the redox species in the electrolyte or interact with the underlying substrate to either generate a measurable signal or enhance an existing one (Figure 2-3a). Different types of photoactive species, such as semiconductor nanocrystals,[141] metallic nanoparticles[121] and organic semiconductors such as g-C_3N_4, PFP (poly(9,9-bis(6′-(N,N,N,-trimethylammonium)hexyl) fluorene-co-alt-1,4-phenylene) bromide,[207,208] have been commonly used as a signal label. In this strategy, it is crucial to (i) minimize the size of bioconjugated labels to reduce steric hindrance, (ii) decrease the effect of the label on the mass transport and complexation of the biomolecule, and (iii) diminish nonspecific protein adsorption to develop labels that do not interfere with assay functionality. Semiconductor nanocrystals possess dimensions in the order of 1-100nm, making them an excellent choice as PEC labels. The PEC signal of QDs in a complex environment stems from a myriad of factors such as the intensity of excitation source, the magnitude of applied bias potential, the absence/presence of electron donors and acceptors, as well as the inherent photophysical properties of QDs.[209] These materials are particularly appealing owing to their tunable excitation spectrum resulting from quantum confinement, narrow and symmetrical emission spectrum, high quantum yield and good optical stability.[210] Noble metal NPs are also commonly exploited for this approach.[102,211] Plasmonic features of these particles such as intensive localized electric field generation in the near field, strong far-field light scattering, large absorption cross section in plasmonic resonance band, and light induced charge separation exhibited by these labels offer photocurrent modulation.[211,212]

In this sensing scheme, in addition to the type of labels used, the electrode material greatly influences the assay design. Here, the electrode is typically constructed from wide bandgap semiconducting materials such as TiO_2, g-C_3N_4, ZnO, p-$CuBi_2O_4$, and hematite (Fe_2O_3), where the photoactive label extends the absorption to the visible wavelength and improves the charge separation efficiency of the electrode. However, given that signal transduction is induced using a photoactive label, non-photoactive electrodes can also be used in these assays.[102,213]

QDs are widely used as signal transduction reporters in PEC biosensors following the pioneering work of Wilner et.al. in the early 2000s.[102,213] In one of these works, ssDNA immobilized on a gold substrate was hybridized with CdS NP-tagged target DNA to a create a crosslinked CdS/DNA network.[101,102] It was observed that the photocurrent emanating from these networks could be switched ‘on’ and ‘off’ using the light source through the photoejection of conduction-band electrons of CdS particles that were in contact with or at tunneling distances from the electrode using $Ru(NH_3)_6$ as an electron mediator. Using a similar strategy, Chai *et al.* reported an approach where they used DNA tetrahedron (TET) to deposit CdTe QDs and a methylene blue intercalator in the presence of the target analyte. Since the electrode was not photoactive, this system was operated at near-zero noise level and with a limit-of-detection of 17 aM and a linear range of 50 aM - 50 pM in the presence of target miRNA-141 under light excitation (590 nm). When the

DNA TET-CdTe QDs-MB complex was used as a signal probe, the PEC response (0.82 μA) was ~2.5 fold higher as compared to the PEC response based on the DNA TET-CdTe QDs complex alone[115] (Figure 2-4a). In contrast to the previously discussed assays, the introduction of photoactive materials can also occur in the *absence* of the target analyte.[214] In an assay of this type, the dsDNA capture probe contains a carboxyl-terminated ssDNA building block that is removed, through strand displacement, from the electrode upon target introduction. In the absence of the target strand, $CuInS_2/ZnS$ (ZCIS) QDs and n-doped carbon dots are captured and increase the PEC signal under xenon lamp excitation (spectral range 200-1200 nm) (Figure 4b). This biosensor exhibited a limit-of-detection of 0.31 pM with a linear range of 1 pM - 100 nM in the presence of target miRNA-21. Furthermore, single base mismatch studies conducted using miRNA-21 (target), SM miRNA-21and miRNA-141 showed ~4x higher response in the case of target as compared to the interfering miRNAs, showcasing the excellent selectivity of this sensor. In addition to nucleic acid sensing, QDs are widely used in PEC biosensors created for protein analysis. In an assay of this type, the presence of insulin instigated the formation of an immunocomplex containing DNA-labelled antibody, insulin, secondary DNA labelled antibody and CdTe-labelled reporter DNA.[191] CdTe induces a sensitization effect on the $CdS/TiO_2/ITO$ electrode, thereby enhancing the photocurrent under white light excitation (spectral range 200-1200 nm) (Figure 2-4c). A limit-of-detection of 3 fM was exhibited by this sensor with a linear range of 10 fM - 10 nM using insulin as the target. The fabricated sensor exhibited desirable long-term stability with no significant change in photocurrent following storage for 10 days and excellent selectivity when incubated with a solution containing interfering agents (IGF-1 and C-peptide). Micro-RNA (miRNA-155) detection has been shown by introducing Au NP functionalized N-doped porous carbon ZnO polyhedra (NPC-ZnO) on CdSe QD based photoelectrode.[215] Following, miRNA hybridization with a hairpin structure probe, Au NP functionalized NPC-ZnO was brought close to the hybridized double-stranded RNA by using second hairpin DNA structure (Figure 2-4d). The NPC-ZnO is also photoactive and thereby generated a signal-on response under visible light excitation. This creative design strategy enabled ultrasensitive miRNA detection with a limit-of-detection of 49 aM (linear range of 0.1 fM – 10 nM), which is much lower than the previously reported photoelectrochemical miRNA detection bioassays.[191,214]

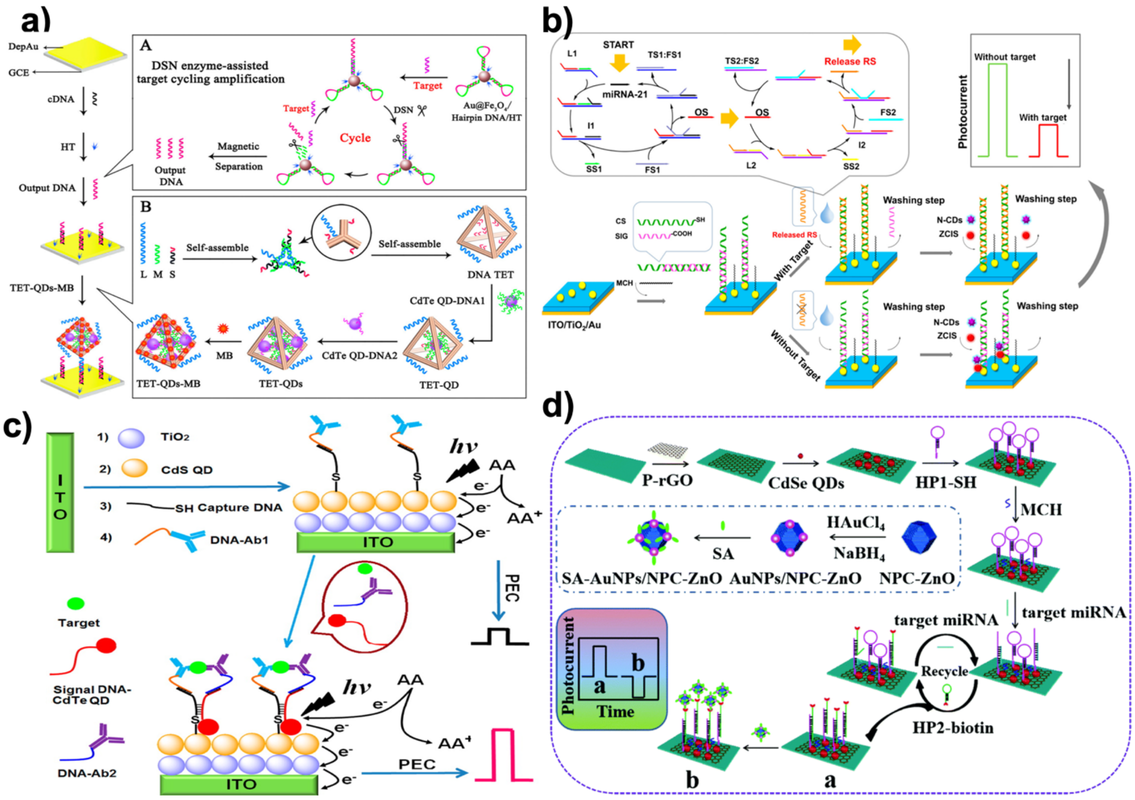

Figure 2-4*:* Introduction of QDs as Photoactive species: a) Schematic Diagrams of PEC Biosensor for miRNA-141 detection using DSN enzyme-assisted target cycling amplification strategy and DNA TET-CdTe QDs-MB complex (Reprinted from ref [115] with permission from American Chemical Society); b) Schematic illustration of the PEC detection of miRNA-21 by bringing photoactive N-doped carbon dots following hybridization of the target RNA (Reprinted from ref [214] with permission from American Chemical Society); c) Schematic representation of ultrasensitive insulin detection based on CdTe QD labels brought into proximity of CdS/TiO_2/ITO electrode upon affinity-based binding of CdTe QD labeled insulin target (Reprinted from ref [191] with permission from American Chemical Society); d) Schematic representation of the detection of miRNA-155 based on NPC-ZnO labelled target. Here, NPC-ZnO performs the role of electron scavenger, thus generating a signal-on response (Reprinted from [215] with permission American Chemical Society).

Dai *et al* demonstrated a multiplexed PEC immunoassay by using two different photoactive materials – graphitic carbon nitride (g-C_3N_4) which exhibited an anodic photocurrent and CS-AgI which exhibited a cathodic photocurrent – on a polyamidoamine dendrimer modified cube anatase TiO_2 mesocrystal (PAAD@CAM) substrate (Figure 2-5a).[208] A competitive immunoassay was designed to analyze PSA and IL-6 biomarkers using anti-PSA and anti-IL-6 antibodies labelled with g-C_3N_4 and CS-AgI respectively. Application of different bias voltages allowed each of the complexes to be individually analyzed with IL-6 having a dynamic range of 10^{-5} - 90 pg mL^{-1} (3.3×10^{-5} pg mL^{-1} limit-of-detection) and PSA having a dynamic range of 10^{-6} - 90 ng mL^{-1} (3.3×10^{-3} pg mL^{-1} limit-of-detection).

Metal nanoparticles are used in combination with photoactive materials as signal reporters in PEC biosensors. In an assay of this kind, liposomes loaded with AgNP were labelled with IgG antibodies to detect IgG on a BiOI/Ni electrode.[216] In a sandwich protein binding assay, the liposome-antibody conjugates were used to label the captured antigen. Upon binding, the Ag NPs were released using Triton X-100 and reacted with the p-type BiOI substrate to form an AgI/Ag/BiOI z-scheme heterojunction, enhancing the cathodic photocurrent of the electrode due to the reduction of dissolved O_2 by AgI and transferring electrons from the conduction band of BiOI to the valence band of AgI through metallic Ag upon illumination (410 nm excitation light source) (Figure 2-5b). This assay demonstrated a limit-of-detection of 100 fg mL^{-1} and was linear in the 100 fg mL^{-1} - 100 ng mL^{-1} range.

As seen in the previous reports, target labeling provides the sensitivity and specificity that is needed for bioanalysis in complex biological samples. However, the introduction of photoactive species via labelling often impairs the rate and efficiency of bio-recognition, makes it difficult to perform quantitative analysis of biomolecular species in real time, and adds to the assay complexity due to the washing steps. An alternative method that can overcome some of the drawbacks of labeling is signal transduction via *in situ* generation of electron/hole donors, which is discussed in the following section.

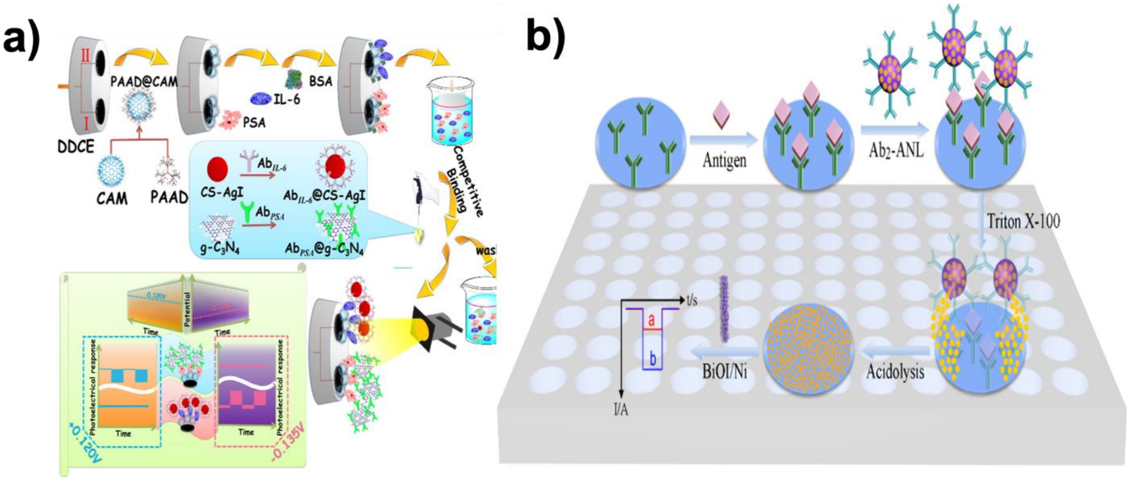

Figure 2-5: Introduction of photoactive species: a) Schematic representation of two potentiometrically resolvable protein detection assays for PSA and human interleukin-6 involving the affinity-based binding of CS-AgI tagged IL-6 and CS-AgI tagged PSA (Reprinted from ref [208] with permission from American Chemical Society); b) Liposomal PEC bioanalysis using photocathode and AgI/Ag; Reproduced with permission from (Reprinted from ref [216] with permission from American Chemical Society).

2.5.2 Generation of Electron/Hole Donors

In this approach, target introduction releases free electron/hole donors (scavenging species) that interact with the photoactive electrode surface, induce charge separation, and modulate the photocurrent. A common method to produce electron/hole donors is by using an enzyme[206] to generate hydrogen peroxide (H_2O_2) or ascorbic acid (AA). Alkaline phosphatase (ALP) is used in DNA and protein sandwich assays[217,218] to catalyze the conversion of ascorbic acid 2-phosphate (AAP) to ascorbic acid (AA) upon target binding. AA acts as a hole scavenger and increases the lifetime of photo-induced carriers, which enhances the PEC current.[217] Using a similar approach, an assay incorporating dual enzyme tags for multiplexed PEC detection was developed to differentiate between two cardiac markers – cardiac troponin I (cTnI) and C-reactive protein (CRP) [218]. ALP-tagged antibody was used for troponin T detection, and acetylcholine esterase (AChE)-tagged antibody was used for detecting C-reactive protein.[218] These tags generate electron donating ascorbic acid (AA) and thiocholine (TC) by specifically catalyzing the hydrolysis of AAP or acetylthiocholine (ATC) (Figure 2-6a). Under visible light irradiation, the generated electron donors scavenge photoinduced holes at the surface of the CdS QDs/TiO_2 electrode, inhibiting the recombination of the holes and electrons, thus enhancing the photocurrent. A linear range of 100 ng mL^{-1} - 0.1 mg mL^{-1} (a limit-of-detection of 50 ng mL^{-1}) was exhibited for CRP, and a linear range of 1 ng mL^{-1} - 0.01 mg mL^{-1} (a limit-of-detection of 0.1 ng mL^{-1}) was exhibited for cTnI.

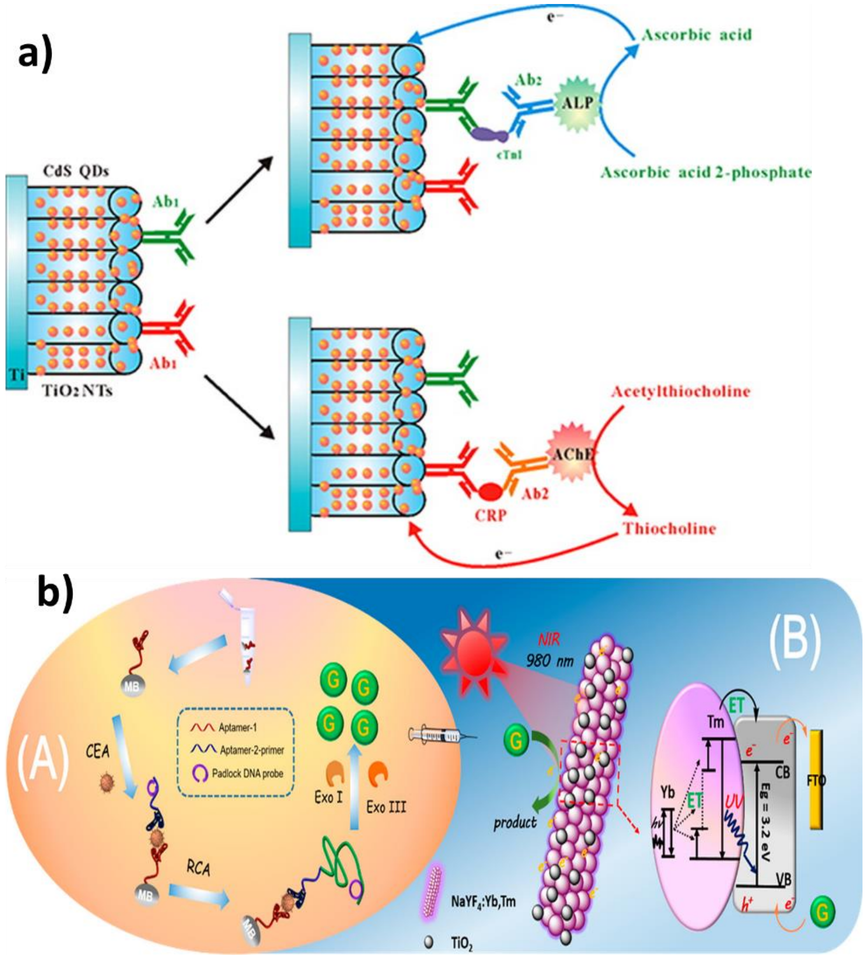

Figure 2-6: In situ generation of electron/hole donors : a) Incorporation of dual enzyme tags for multiplexed cardiac troponin I (cTnI) and C-reactive protein (CRP) detection (Reprinted from ref [218] with permission from American Chemical Society); b) Schematic Illustration of near infrared to ultraviolet light-mediated photoelectrochemical aptasensing for cancer biomarker detection and mechanism of signal generation in $NaYF_4$:Yb,Tm@TiO_2 photoactive electrode (Reprinted from ref [195] with permission from American Chemical Society).

In the previous assays, the biorecognition event, the generation of electron/hole donors, and signal measurement were performed on the electrode surface. However, it is possible to perform biorecognition and generate electron/hole donating species in solution and use the resultant species to modulate the PEC signal at an electrode surface. An assay of this type detects carcinoembryonic antigen (CEA) using a sandwich assay on the surface of magnetic beads.[195] Upon aptamer−CEA−aptamer reaction, the primer DNA on the terminus of the secondary aptamer initiates rolling circle amplification (RCA) reaction, resulting in the generation of long guanine (G) rich oligonucleotide strands (Figure 6b). Subsequent introduction of exonuclease I and III releases guanine (G) bases following digestion of the RCA product. The free guanine bases function as electron donors and enhance the photocurrent of the NaYF4:Yb,Tm@TiO_2 microrod electrodes under near-infrared light excitation. The limit-of-detection of the assay for CEA target was 3 pg mL^{-1} with a linear range of 10 pg mL^{-1} to 40 ng mL^{-1}. Furthermore, high specificity is demonstrated by this assay when tested against a complex mixture containing interferents such as PSA, TB, and human IgG.

In addition to using photoactive species and electron/hole donors separately, it is possible to combine these signal transduction mechanisms. For example, the synergistic effect of electron donor generation and photoactive species introduction was used to detect alpha-fetoprotein (AFP), which is a biomarker for liver cancer.[219] In this assay, AFP-CdS-GOD complex was formed by conjugating AFP with CdS QD and glucose oxidase (GOD). In this work, chitosan which helps to covalently bind anti-AFP antibody was first deposited on the photoelectrode composed of ZnO inverse opal structure. Upon biorecognition with AFP-CdS-GOD, the photocurrent was enhanced. The enhancement of the photocurrent is attributed both to the increased absorption spectrum due to CdS QD and generation of H_2O_2 by GOD as electron donor. This bioassay showed a limit-of-detection of 0.01 ng mL^{-1}

(linear range is 0.1 ng mL^{-1} - 500 ng mL^{-1}). Moreover, this assay showed good specificity against CEA, PSA and H_2O_2.

Although assays using electron/hole generation overcome the limitations encountered in labelled assays, they have some drawbacks that must be considered for using them in analyzing real-life samples. Enzymes that are typically used to induce the formation of local electron/hole donors are known for their instability, relatively low shelf life, and expensive reagent cost. Additionally, to ensure effective detection using this scheme, utmost importance must be paid to minimize interfering scavenging species found in native samples that may consume the locally generated electron/hole donors required to transduce the biorecognition events.

2.5.3 Steric-Hindrance Based Assay

Introduction of a biomolecule at the biosensor surface can sterically hinder the access of electrolyte to the photoactive transducer to modulate the measured PEC current. This transduction approach is one of the simplest mechanisms for developing a biosensor because it usually does not require labeling steps following the target capture. However, most of these sensors operate in a signal-off fashion.[206,220,221]

In signal-off PEC biosensing, it is crucial to have a high photocurrent before target introduction because high concentrations of the target can completely diminish the PEC signal.[222] Different approaches have been used to obtain high baseline PEC currents. Depositing photoactive materials into three-dimensional scaffolds such as wrinkled electrodes has been used to increase the photocurrent of PEC biosensors.[222] The wrinkle electrodes showed 10 times higher photocurrent than a planar electrode composed of CdTe

QDs. This wrinkled photoelectrode was used to detect single stranded DNA by simply hybridizing with the complementary sequence as a proof-of-concept. Moreover, it showed stable photocurrent following storage at 4ºC in dark conditions for seven days and exhibited high specificity against single or multiple pair mismatch. Metal NPs are also deposited in combination with photoactive materials to enhance the photocurrent due to their plasmonic properties.[223,224] Wang *et al.* used Au NPs as a photoelectronic transfer promoter in photoactive molybdenum disulfide (MoS_2) nanosheets to detect micro-RNA.[221] To obtain further reduction of photocurrent, bulky biotin-streptavidin coupling was used in conjunction with probe hairpin DNA and target microRNA to increase the signal changes caused by steric hindrance. This PEC sensor presented a broad linear range of 10 fM – 1 nM (limit-of-detection of 4.21 fM) (Figure 2-7b). Signal transduction using steric hindrance is ideally suited for cellular detection because the large size of cells compared to biomolecules enhances their steric hindrance effect. A signal-off sensor was constructed to rapidly detect early apoptotic cells using phosphatidylserine binding peptide (PSBP) bound to the surface of TiO_2/Graphene/$ZnIn_2S_4$ photoelectrode as the biorecognition element.[225] Here, the access of AA to the electrode surface was sterically hindered by the binding of the apoptotic cell decreasing the photocurrent. This biosensor exhibited an LOD of 3 cells mL^{-1} with a linear range of 1×10^3 - 5×10^7cells mL^{-1} (Figure 2-7a). A paper-based cytosensor was reported for detecting breast cancer cells (MCF-7) constructed from ZnO spheres immobilized on Au nanorod-modified paper and sensitized with CdTe QDs and nanogold-assembled mesoporous silica nanoparticles (GMSNs) at their surface to create the photoactive portion of the biosensor.[226] Multiple horseradish peroxidase (HRP) molecules and branched capture sites were then immobilized onto the GMSNs using double stranded DNA (Figure 2-7c). HRP was used in this assay to generate optical excitation through chemiluminescence. A signal decrease is observed upon capture of graphene quantum dot (GQD) labelled cancer cells as H_2O_2, the oxidant of luminol based chemiluminescence, is sterically hindered. These biosensors demonstrated a linear range of $63 - 1.0\times10^7$ cells mL^{-1} and limit-of-detection of 21 cells mL^{-1}. Lymphoblast (CCRF-CEM) cells were also detected based on steric hindrance in a PEC biosensor.[227] These cells were captured using hairpin DNA targeting overexpressed protein tyrosine kinase-7 on their surface. A decrease in PEC signal was exhibited on $AgInS_2$ NPs photoelectrodes due to steric hindrance of AA. A limit-of-detection of 16 cells mL^{-1} and linear range of $1.5x10^2$ - $3.0x10^5$ cells mL^{-1} were demonstrated.

Another interesting signal transduction method involves the generation of a passivating compound as a result of target capture, which is used to decrease the PEC current generated on the photo-electrode.[195,228] An assay of this type combines biorecognition and isothermal target amplification in solution with signal modulation on the photoelectrode to detect T4 polynucleotide kinase (PNK), an important cellular regulator.[228] In this detection scheme, a hairpin DNA (HP2) strand is phosphorylated upon the introduction of target PNK and is partially digested by λ-exo to yield an endogenous primer which initiates solution-based amplification generating DNA fragments. These DNA fragments activate the peroxidase-mimicking DNAzymes on the hairpin DNA probes immobilized on the photoelectrode (HP1) to catalyze the formation of insoluble precipitates at the electrode surface and attenuate the photocurrent response of the photoactive electrode. This target induced attenuation of current, and enabled PNK to be analyzed in the linear range of 2 to 100 mU mL^{-1}. Zhang *et al.* used this strategy to detect prostate specific antigen (PSA) on a CdS nanorod electrode.[229] The presence of PSA led to the formation of a sandwich complex on Au NPs that contained DNAzyme concatamers that catalyzed the precipitation of 4-chloro-1-naphthol onto the photoactive electrodes in the presence of H_2O_2. The insoluble precipitate resulted in an attenuation of signal by inhibiting electron transfer from the electron donor AA to the photoelectrode. PSA detection was achieved in the 0.005 ng mL^{-1} - 50 ng mL^{-1} range with a limit-of-detection of 1.8 pg mL^{-1}.

Multi-channel PEC biosensors operated based on steric hindrance have been developed for improved reliability.[230–232] In an assay that uses sunlight instead of an external light source, a two-channel design enables the device to calibrate its photoresponse by considering the incoming sun light intensity.[231] In this assay, biorecognition event of aflatoxin B1 by the covalently bound aptamer with the underlying Ag/TiO_2/3D nitrogen-doped graphene hydrogel (3DNGH) resulted in a decrease of photocurrent. The decrement of the photocurrent is attributed to the enhanced steric hindrance of the electrolyte (0.1M PBS) to the electrode surface. Using this ratiometric approach an LOD of 2.5×10^{-4} ng $mL^{-1}$and linear range of 1.0×10^{-3} ng mL^{-1}-1.0×10^{3} ng mL^{-1} were achieved for the detection of aflatoxin B1 (AFB1), a highly toxic carcinogen mainly found in agricultural and sideline products such as cereals and dairy products. Building on this strategy, Hao et. al. developed another two channel device using CdTe-graphene oxide (GO) and CdTe photoelectrodes for detecting AFB1.[116] A signal increase was observed on the CdTe-GO electrode because the aptamer was released from the electrode surface upon target capture, which improved the access of electrolyte (0.1 M PBS) to the photoelectrode (Figure 2-7d). A signal decrease was observed on the CdTe electrode upon target capture by the immobilized aptamer. Using this detection strategy, a limit-of-detection of 0.01 ng mL^{-1} and a linear range of 10 pg mL^{-1} - 100 ng mL^{-1} were observed. Compared to single channel PEC biosensors, this self-referencing design can provide better accuracy and reliability, thus providing a promising route for the future development of PEC biosensors.

Steric-hindrance based assays can also combined with other strategies, for example p53 (cell cycle regulator and tumor suppressor) detection has been shown by combining two detection strategies – (i) *in situ* generation of electron donors and (ii) the subsequent hindering of AA.[233] A protein G molecular membrane was used to immobilize ALP conjugate anti-p53 antibody on ordered TiO_2 nanotubes containing Au NPs. ALP enzymatic reaction in the presence of AAP generates AA for scavenging the holes localized on Au NPs. In this system, immunocomplexation with the target (p53) decreases the photocurrent signal due to (i) increased steric hindrance caused by the immunocomplex and (ii) a change in dielectric permittivity of the Au NPs-TiO_2 NTs interface following target capture, which in turn influences the energy coupling between Au NPs and TiO_2 NTs. This sensor demonstrated a limit-of-detection of 0.05 ng mL^{-1} and a linear range of 20 - 100ng mL^{-1} under 410 nm light illumination. Additionally, excellent selectivity was demonstrated by the immunoassay when faced with interfering agents such as glucose oxidase (GOD), prostate specific antigen (PSA), lysozyme (LZM), and thrombin. Furthermore, given that the average level of p53 in lung cancer patient serum samples is

0.55 ng mL^{-1}, the limit-of-detection of this assay, along with its excellent selectivity point to its applicability for clinical use.

The simplicity of steric hinderance based signal transduction makes it appealing for use in PEC biosensing. However, due to its signal-off nature, this transduction method is associated with a higher incidence of false positives as compared to the other transduction methods discussed in this section. To overcome this, strategies such as multi-channel sensing with built-in calibration[116] have been developed for more accurate and robust biosensing.

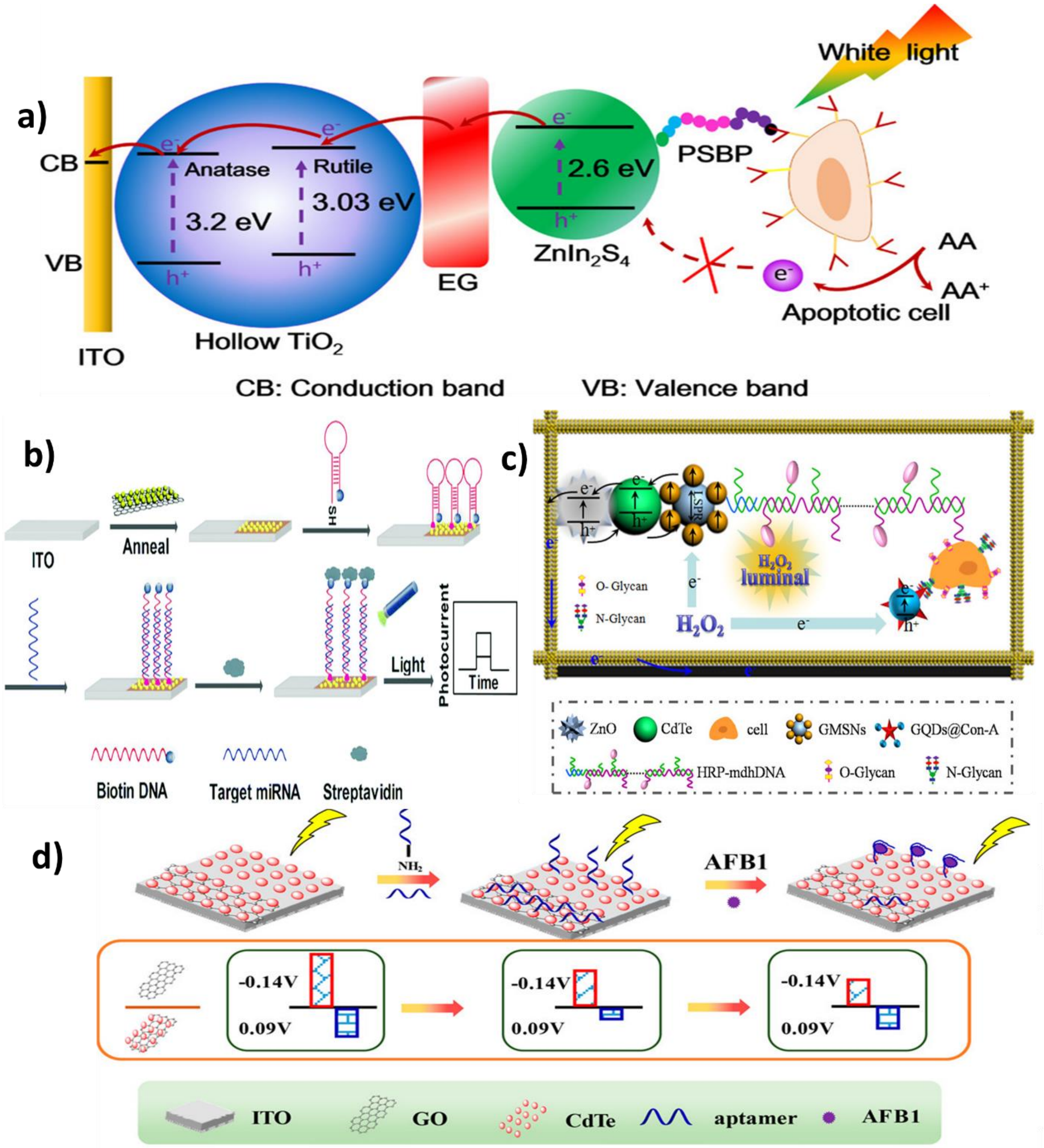

Figure 2-7: Steric-hindrance based biosensing: a) Detection of apoptotic cells by TiO$_2$/EG/ZnIn$_2$S$_4$ electrodes (Reprinted from ref [225] with permission from American Chemical Society); (b) Use of Au NPs in conjunction with a semiconductor (MoS$_2$) to achieve higher photoresponse (Reprinted from ref [221] with permission from The Royal Society of Chemistry); c) Detection of N glycan on ZnO$_2$/CdTe/GMSNs electrode modified with GQD@conA (Reprinted from ref [226] with permission from American Chemical Society); d) Two-channel approach for detecting AFB1 (Reprinted from ref [116] with permission from American Chemical Society).

2.5.4 *In situ* Introduction of Light

In conventional PEC biosensing, an external light-source is used for optical excitation, which imposes additional complexities for miniaturizing the biosensing platform.[106] Elimination of the external light source is often achieved by employing chemiluminescence (CL) in the PEC biosensor for generating *in situ* light of various emission wavelengths.[206,234] In an assay of this type, prostate specific antigen (PSA) was captured and labelled in a sandwich assay with Au NPs modified with glucose oxidase (pAb_2-AuNP-GOx).[235] GOx generates H_2O_2 enhancing the CL of the system, which in turn increases the photovoltage generated on the graphene oxide-doped $BiVO_4$ photoelectrode (Figure 2-8a). This system showed a detection limit of 3 pg/mL and good specificity against CEA and AFP. A similar approach was used in a paper based PEC biosensor with porous Au/ SnO_2/rGO photoelectrodes for detecting ATP.[236] In this assay, the aptamer for ATP detection was split into two oligonucleotides. One of them (SSDNA1) were immobilized initially at the electrode surface and the other (SSDNA2) was conjugated with luminol and GOx into Fe_3O_4@Au NP. This nucleotide conjugate NP was brought to the electrode surface following the ATP introduction and thereby formed the complex shown in Figure Figure 2-8b. Once GOx is bound to the electrode, it catalyzes the CL reaction by generating H_2O_2, which further reacts with the luminol. The sensing platform demonstrated a limit-of-detection of 0.025 pM with specificity against guanosine triphosphate (GTP), cytidine triphosphate (CTP) and uridine triphosphate (UTP). A proof-of-concept PEC DNA assay was also shown using this approach on CdS/MoS_2 photoelectrodes.[120] In this assay, target DNA is captured using an immobilized hairpin probe. Following the target-induced unfolding of the probe, the target DNA is displaced by a hemin-labeled DNA recycling probe. Hemin catalyzes luminol oxidation and generates CL, exciting the photoelectrode. This assay demonstrated a limit-of-detection of 0.39 fM and specificity against other forms of DNA (smDNA, tmDNA). The elimination of external light source makes this form of signal transduction appealing for the development of point-of-care devices. Yet another advantage of this method lies in the tunability of chemiluminescence by changing environmental factors such as the concentration of oxidizing species, environmental pH value, hydrophobicity of the solvent, and solution composition.[237–239]

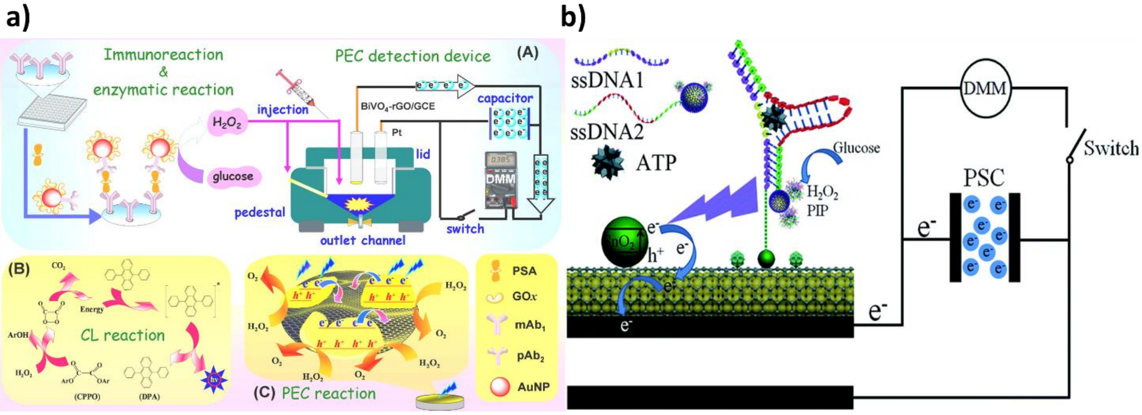

Figure 2-8: In situ generation of light. a) PSA detection by coupling H_2O_2 – triggered peroxyoxalate self-illuminated system with an external capacitor on the photoanode and digital multimeter as readout device (Reprinted from ref [235] with permission from American Chemical Society); b) Schematic of the photocurrent generation mechanism in the modified paper sample zone of the Au-PWE under a CL light source (Reprinted from ref [236] with permission from Royal Society of Chemistry).

The signal transduction strategies elaborated thus far involved the reaction of photoactivated excitons with solution-based electron donors and acceptors to generate a measurable photocurrent, i.e., the signaling strategy established was based on the direct interfacial electron transfer between the photoactive material and ambient environment.

The following section discusses signal transduction based on resonance energy transfer that involves the transfer of acquired *electronic energy* following photo-excitation.

2.5.5 Resonance Energy Transfer

A powerful mechanism for modulating the PEC activity of the photoactive material in response to biorecognition is resonance energy transfer (RET).[240] In this approach, the biorecognition event serves as a mediator to bring a noble-metal NPs (Generally Au or Ag) to the proximity of the photoelectrode.[206] Noble-metal NPs have very high extinction coefficients[241] and can function as either signal quenchers[242] or amplifiers[243] depending on the distance between the metal and the other photoactive materials. If the absorption spectrum of the metal NP overlaps with the emission spectrum of the photoactive material, a significant portion of the exciton energy is transferred to the metal NPs, subsequently decreasing the photocurrent.[244] However, when excited at plasmonic absorption wavelengths, a high electric field can surround the metal NPs and enhance the photocurrent generated by the photoactive material.[245] In these assays, metal NPs are excited by the emission of the semiconductor already present in the electrode which is different from the approach where to enhance the PEC current, metal NPs are introduced during biomolecule recognition followed by external light as described in section 2.5.1.

Semiconductor QDs are commonly used as photoactive materials for electrodes in this approach because it is possible to tune their emission wavelength by varying their size. Mi-RNA detection has been shown by using RET between CdS QDs and Ag NPs under the illumination at a wavelength of 410nm.[246] As shown in Figure 2-9a, target microRNA induces conformational change in the Au NP labelled hairpin probe deposited on CdS QD. ALP causes Ag deposition on the Au NPs, which significantly amplifies the signal decrease that is measured on the photoelectrode.This assay has demonstrated a detection limit of 0.2 fM with a linear range of 1 fM - 100 pM. The same group has also shown DNA detection without the Ag deposition-induced amplification strategy[247] using CdS QDs and Ag NPs and achieved a limit-of-detection of 0.3 pM and a linear range of 1 pM - 10 nM. Ma *et al.* also used energy transfer between CdS QDs and Ag NPs to detect tata binding protein[248] and achieved a limit-of-detection of 1.28 fM (linear range of 2.6 fM - 512.8 pM). The CdS QDs used in this work have an emission peak around 530 nm which overlaps with the absorption peak of Au NPs. DNA hybridization was used to bring Au NP into the proximity of the semiconductor QDs (Figure 2-9b). Tata binding protein can further bend this dsDNA structure and bring Au NPs even closer to the CdS QDs. The TATA binding protein increases the signal attenuation due to the combined effect of RET and steric hindrance. This assay showed excellent selectivity against AFP, CEA, lysozyme, PSA, and thrombin.

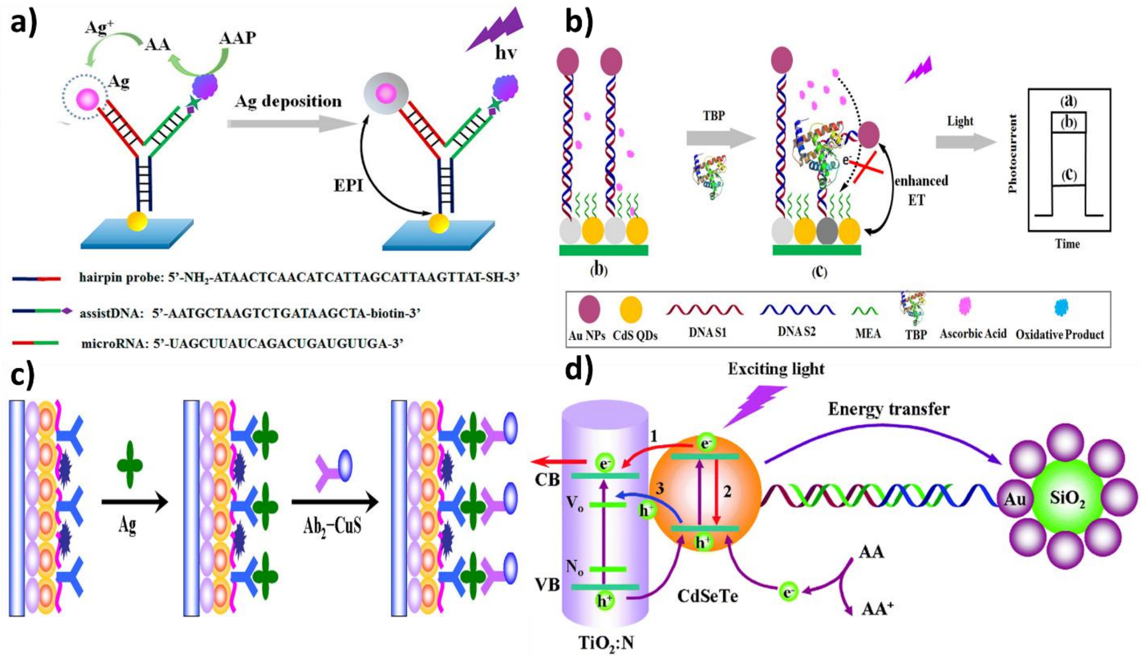

Figure 2-9: Resonance energy transfer based photoelectrochemical biosensors: a) Energy transfer between CdS QDs and Ag NPs upon the ALP induced Ag deposition on Au NPs (Reprinted from ref [246] with permission from American Chemical Society); b)Tata binding protein bends the double-stranded DNA structure and brings CdS QD and Au NPs closer (Reprinted from ref [248] with permission from American Chemical Society); c) Schematic illustration of the signal-off sandwich type immunoassay was developed by using CuS nanocrystals as photocurrent quencher for early detection of CEA (Reprinted from ref [249] with permission from American Chemical Society); d) Thrombin detection using a PEC aptasensing platform based on exciton energy transfer between CdSeTe alloyed quantum dots and SiO_2@Au nanocomposites. In this approach, RET significantly reduces the photocurrent, which is then quickly restored following the target's competitive binding and subsequent release of the metal NP tagged capture probe (Reprinted from ref [104] with permission from The Royal Society of Chemistry).

Although Au and Ag NPs are the most popular materials used for RET-based PEC biosensing, other materials can also be used in these assays. For example, a *signal-off* sandwich-type immunoassay was developed by using CuS nanocrystals as the photocurrent quencher for early detection of CEA on CdSeTe@CdS:Mn-sensitized TiO_2 NPs.[249] In this assay, CEA target antigens were captured using anti-CEA antibodies immobilized on the electrode surface, and a signaling antibody labelled with CuS was introduced to reduce the PEC current (Figure 2-9c). A limit-of-detection of 0.16 pg/mL with a linear range from 0.5

pg mL^{-1} to 100 ng mL^{-1} were achieved using this assay. The specificity of this assay was validated against PSA, AFP, carbohydrate antigen 19-9 and 15-3.

PEC biosensors that operate based on RET are highly sensitive. However, many of the RET biosensing assays reported to date are signal-off.[206] It is possible to design a signal transduction method based on RET where the photocurrent is initially reduced and is *turned on* following target capture and the resultant removal of the metal NP.[250,251] Thrombin detection was demonstrated using this approach where AuNP-decorated SiO_2 nanoparticles were initially immobilized on CdSeTe QD-photoelectrodes through a dsDNA construct containing a thrombin-selective aptamer. Upon target capture, the signal diminishing Au NPs were removed from the electrode vicinity and a limit-of-detection of 2.8 fM with a linear range of 10 fM - 50 pM was achieved(Figure 2-9d).[104] Consequently, it is possible to combine the high sensitivity of RET with reliability of signal-on sensing to create a high-performance biosensor. A summary of these recently published affinity-based PEC biosensor including their sensing mechanism, transduction approach and LOD are depicted in Table 2-2.

Table 2-2: Summary of the recent affinity-based PEC biosensor

Photoactive Material	**Target**	**Sensing Approach**	**Transduction mechanism**	**LOD, linear range**	**Reference**
AgI/Ag/BiOI	IgG	Immunosensor, Signal on	Introduction of photoactive species	100 fg mL^{-1} 100 fg mL^{-1} - 100 ng mL^{-1}	[216]
TiO_2-CdS	Estradiol	Immunosensor, Signal off		2 pg mL^{-1} 5 pg mL^{-1} - 4 ng mL^{-1}	[252]
Donor–Acceptor-type PTB7-Th	Thrombin	Aptasensor, Signal on		34.6 fM 100 fM – 10 nM	[253]
CdS NPs	Oligonucleotides	DNA sensor		-	[213]
(PAAD)@ TiO_2CAM, g-C_3N_4, CS-AgI	PSA, IL-6	Immunosensor, Signal polarity change.		3.3×10^{-5}pg mL^{-1}, 10 - 90 pg mL^{-1} (IL-6) 3.3×10^{-3} pg mL^{-1}, 10^{-6} - 90 ng mL^{-1} (PSA)	[208]
CdS QDs/ NPC-ZnO	miRNA-155	DNAsensor, Signal on		49 aM 0.1 fM - 10 nM	[215]

CdS/TiO_2, CdTe QDs	Insulin	Immunosensor, Signal on		3fM 10 fM to 10 nM	191
Cationic polyfluorene derivative	Breast cancer cells (SKBR-3)	Cytosensor, Signal on		24 cells/mL^{-1} 1.0×10^{2} to 5.0×10^{5} cell mL^{-1}	207
TiO_2/ITO, Au NPs, $[Ru(bpy)^{3}]^{2+}$	DNA	Peptide sensor, Signal on		5.0×10-^{3} U mL^{-1} 10 – 50 U mL^{-1}	254
TiO_2/Au, $CuInS_2$/ZnS (ZCIS) QDS	miRNA-21	Aptasensor, Signal on		0.31 pM 1 pM - 100 nM	214
CdTe, MB	miRNA-141	Aptasensor, signal on		17 aM 50 aM -50 pM	115
MoS_2/g-C_3N_4/black TiO_2, Au NPs	miRNA	Aptasensor, Signal off		0.13 fM. 0.5 fM - 5000 fM	121
GO/g-C_3N_4	Kanamycin	Aptasensor, Signal on		0.2 nM 1 nM - 230 nM	255
TiO_2	miRNA	DNAsensor, Signal Off-On		20 fM	256
MB	miRNA	DNA sensor, Signal on		27 aM 80 aM -10 pM	257
CdS/TiO_2 NT	cTnI, CRP	Immunosensor, Signal on	Generation of electron/hole donor	0.1 ng mL^{-1}, 1 ng mL^{-1} - 0.01 mg mL^{-1} (cTnI). 50 ng mL^{-1},100 ng mL^{-1} - 0.1 mg mL^{-1} (CRP)	218
$NaYF_4$:Yb,Tm@TiO_2	CEA	DNAsensor, Signal on		3.6 pg mL^{-} 10 pg mL^{-1} to 40 ng mL^{-1}	195
Au NPs, MoS_2	mi-RNA	DNAsensor, Signal off		4.21 fM 10 fM–1 nM	120
WS_2, Au NP	MCF-7 cells	Aptasensor, Signal off		21 cells mL^{-1} $1x10^{2}$ to $5x10^{6}$ cells mL^{-1}	258
AuNP/g-C_3N_4	PNK	Aptasensor, Signal off		1 mU mL^{-1} 2 to 100 mU mL^{-1}	228
Au NPs, TiO_2	p53	Immunosensor, Signal off		0.05 ng mL 20 – 100 ng mL^{-1}	233
Ag NPs, TiO_2	AFB1	Aptasensor, Signal off		2.5×10^{-4} ng mL^{-1} 1.0×10^{-3}-1.0×10^{3} ng mL^{-1}	231
Graphene loaded carbon QDs, g-C_3N_4	E. Coli	Aptasensor, Signal off		0.66 cfu/mL 2.9 cfu/mL to $2.9x10^{6}$ cfu/mL	232
CuO nanopyramid-island, AO	ALP	Immunosensor, Signal off		0.33 U L^{-1} 0.5 to 40.0 U L^{-1}	259
TiO_2 sensitized with $ZnIn_2S_4$	Early apoptotic HL-60 cells	Aptasensor, Signal off		3 cells mL^{-1} 1×10^{3}-5×10^{7} cells mL^{-1}	225
ZnO, Au nanorods, CdTe QD	MCF-7	Aptasensor, Signal off	Steric-hindrance	21 cells mL^{-1} 63−1.0×10^{7} cells mL^{-1}	226
TiO_2/CdS:Mn, $CuInS_2$ nanoflower	PSA	Aptasensor, Signal off		0.32 pg mL^{-1} 1 pg mL^{-1} to 100 ng mL^{-1}	260
CdS, Au NP	PSA	Aptasensor, Signal off		1.8 pg mL^{-1} 0.005 ng mL^{-1} - 50 ng mL^{-1}	229
$AgInS_2$ NP	CCRF-CEM cells	Aptasensor, Signal off		16 cells mL^{-1} 1.5×10^{2} to 3.0×10^{5} cells mL^{-1}	227
CdS-MoS_2 QD	DNA	DNA sensor, Signal On		0.39fM 1fM -100pM	120
TiO_2-CdS:Mn	PSA	Immunosensor, Ratiometric		0.32 pg/mL 1 pg/mL - 100 ng/mL	260
p-$CuBi_2O_4$ -Au NP	AFP	Immunosensor, Signal Off		14.7 pg/mL 50 pg mL^{-1} - 20 ng mL^{-1}	117
TiO_2-EG-$ZnIn_2S_4$	Apoptotic cells HL-60	Immunosensor, Signal Off		158 cells/mL 1000 – $50x10^{7}$	225
TiO_2 Nanoneedls @MoO_3	RAW264.7 Macrophage Cells	Immunosensor, Signal Off		50 cells/mL 50 cells/mL-1500 cells/mL	220

ZnO spheres Au nanorod- CdTe QDs	Breast cancer cells (MCF-7)	Immunosensor, Signal Off	In-situ induction of light	21 cells/mL 100 - 10^7 cells per mL.	226
t-mercaptopropionic acid capped $AgInS_2NP$	Tumor cells	Aptamer sensor, Signal Off		16 cells/mL 1.5×10^2 - 3.0×10^5 cells/mL	227
CdS-TiO_2	CEA	Dnazyme sensor, Signal Off		70 ag/ mL, 70 ag/mL – 500 fg/mL	119
CdTe, CdTe-GO	AFB1	Aptasensor, Simultaneous signal on-off		10 pg mL^{-1} 10 pg mL^{-1} to 100 ng mL^{-1}	116
$BiVO_4$-rGO-AuNP	PSA	Immunosensor, Signal On		3 pg/mL 10 pg/mL- 80 ng/mL	235
SnO_2QD-RGO	ATP	Aptamer sensor,		0.025 pM 0.1 pM -100 nM	236
CdS-Ag NP	Micro RNA/ ss DNA	Aptamer sensor, Signal Off	Resonance Energy Transfer	0.2 fM 1fM- 100 pM 0.3 pM 1pM – 10nM	246,247
CdS- AuNP	Thrombin TATA binding protein	Aptamer sensor, Signal Off		0.1 fM 1 fM- 10 pM 50 fg/mL 100 fg/mL – 10 ng/mL	248,261
TiO_{2-x}- AuNP	ss DNA	DNA sensor, Signal On		0.6 pM 1 pM-10 nM	262
CdSeTe-SiO_2@Au	Thrombin	Aptamer sensor, Signal On		2.8 fM 10 fM-50 pM	104

2.6 Challenges and Future Perspectives

Affinity based biosensors using photoelectrochemistry as their transduction mechanism have garnered a lot of interest over the past decade due to their exceptional limit-of-detection. Biosensor development starts with considering the target analyte of interest, required limit-of-detection and specificity, interference caused by the native sample, and constraints of the operating environment (point-of-care, lab-based, resource poor compatible). This review aims at helping the reader choose the building blocks – materials and signal transduction mechanisms – of a PEC biosensor based on the constraints imposed by the application.

Inorganic and organic semiconductors are used as the photoactive building blocks for PEC biosensors. In PEC devices, photoactive materials are primarily chosen based on their efficiency in converting optical energy to electrochemical current or voltage. Using these materials in PEC *biosensing* adds additional requirements in terms of stability, size/structure, integration, cost, and functionalization. Given that photoactive materials used in PEC biosensing directly interact with nanoscale biomolecules, solution-processed photoactive *nanomaterials* that can be readily used as labels, reporters, or building blocks for the photoelectrode are primarily used in these systems. An important challenge with using these materials is their varying performance and stability in biosensing conditions that often require operation in complex biological environments and under stringent washing protocols. Affinity-based PEC biosensors operate by measuring signal changes that occur upon target binding; consequently, the lack of stability can cause non-target related signal changes, leading to false-positive or false-negative results. A key development towards the practical use of PEC biosensors involves incorporating *in situ* calibration measures in the PEC system to account for signal variations that are caused by the instability of photoactive materials. It is also critical to integrate functionalized photoactive materials into biosensing chips, strips, or cartridges using fabrication methods that are amenable to large volume processing.

We have reviewed the five most widely used signal transduction mechanisms used in PEC biosensing: introduction of photoactive species, generation of electron/hole donating species, use of steric hindrance, *in situ* induction of light, and resonance energy transfer. It is evident that it is possible to use any of these mechanisms to detect various classes of targets including nucleic acids, proteins, and cells. Additionally, a low limit-of-detection is possible using all of these assays. However, these assays vary greatly in terms of their fabrication and operation complexity. Ultimately, biosensing devices that are fabricated using scalable materials and methods have a higher chance for commercialization. Additionally, assays that can be operated using robust reagents in a simple and rapid one-pot manner have a higher chance for wide-scale adoption and success compared to those that require a sequence of washing and labeling steps. Consequently, choosing the right transduction method can be achieved by considering the collective requirements of a biosensing platform for use in real-life settings.

Chapter 3 Developing a nucleic acid biosensor using photoelectrochemical signal transduction- a signal-off approach

Chapter Introduction (Objective I):

As Chapter 2 outlined, photoelectrodes are required to have high baseline photocurrent generation efficiency in order to be successfully utilized in biosensing. In addition, the fabrication processes of the photoelectrodes also need to be inexpensive and scalable in order to be deployed as POC diagnostic devices. Solution-based electrode fabrication processes are considered highly scalable and inexpensive.[263,264] In this chapter we focuses on developing benchtop all solution-based photoelectrode fabrication methods, using quantum dots (QDs) as photoactive material, in order to obtain high photocurrent and low detection limit.

Surface wrinkling has been recently considered as a useful approach for various applications including enhancement of light extraction efficiency.[268–270] The process of surface wrinkling has the advantage of being facile and low-cost.[264] Generally, wrinkling occurs when a thin film of different elastic moduli is deposited on a substrate and is exposed to a compressive in-plane strain.[271] Wrinkles can also occur upon the removal of tensile strain.[272] It is possible to control the amplitude and wavelength of the wrinkle by tuning the mechanical properties and the thickness of the deposited film with the amount of induced strain.[271]

In this chapter, we utilized a wrinkled surface to develop photoelectrodes. Wrinkled Au electrodes have previously been used in electrochemical biosensing.[273] However, for PEC application, substrate materials are usually transparent at the wavelengths probed, while simultaneously exhibiting higher charge collection efficiency from the photoactive particles.[270] Therefore, Indium-Tin-Oxide (ITO) rather than Au is usually used in PEC application. Nevertheless, the use of ITO in wrinkled surfaces is severely limited by its high stiffness, making it susceptible to breakage upon shrinking.[270] Herein, we compared between a planar substrate and two types of wrinkled substrates incorporating ITO as the conductive material. Cadmium Telluride (CdTe) quantum dots (QDs) were deposited on all the substrates as the photoactive material. Of the constructs being investigated, one type of wrinkled substrate preparation incorporates the surface wrinkling process following ITO deposition, while the other integrates the surface wrinkling process prior to ITO deposition. The ability to texture shape memory polymers for enhanced current generation further enriches this work, given its applicability in biosensor development, functional textiles, and smart customer products due to its biocompatibility, flexibility, light-weight, and softness.[274,275]

Finally, the wrinkled electrodes developed in this work were used in a *signal-off* DNA detection system. The photoactive quantum dots (QDs) were deposited on both the wrinkle and planar electrodes. The QDs were functionalized with the capture probe, followed by the introduction of the target sequence. Remarkably, the wrinkled photoelectrodes showed a 200 times enhancement in the detection limit in comparison to planar electrodes.

Authors: Sudip Saha, Yuting Chan, and Leyla Soleymani

Publication: ACS Applied Materials & Interfaces, 10, 2018, 31178-31185

Publication Date: September 2018

3.1 Abstract

Photoelectrochemical biosensors, with optical biasing and electrochemical readout, are expected to enhance the limit-of-detection of electrochemical biosensors by lowering their background signals. However, when photoelectrochemical transducers are functionalized with biorecognition layers, their current significantly decreases, which reduces their signal-to-noise ratio and dynamic range. Here, we develop and investigate a wrinkled conductive scaffold for loading photo-active quantum dots into an electrode. The wrinkled photo-electrodes demonstrate an order of magnitude enhancement in the magnitude of the transduced photoelectrochemical current compared to their planar counterparts. We engineer photoelectrochemical biosensors by functionalizing the wrinkled photo-electrodes with nucleic acid capture probes. We challenge the sensitivity of the wrinkled and planar biosensors with various concentrations of DNA target and observe a 200 times enhancement in the limit-of-detection for wrinkled versus planar electrodes. In addition to enhanced sensitivity, the wrinkled photoelectrochemical biosensors are capable of distinguishing between fully complementary and targets with a single base-pair mismatch, demonstrating the suitability of these biosensors for use in clinical diagnostics.

3.2 Introduction

In photoelectrochemistry, light is used to generate electron/hole pairs in a photoactive material, and these electron/hole pairs, when separated, are used to drive redox reactions.[79] Depending on the reactions occurring in the photoelectrochemical cell, light is then converted to electrical or chemical energy. Regardless of the type of the photoelectrochemical cell – photovoltaic, photosynthetic, or photocatalytic[276] – increasing the light harvesting efficiency is crucial for enhancing the overall energy conversion efficiency.

Recently, PEC signal transduction has been demonstrated for biological sensing.[72] In PEC biosensors, light is used to generate charge carriers in photo-active materials, and the transduced electrochemical current is measured for analyzing biologically-relevant targets.[82] Because signal readout is electrochemical, this method inherits the benefits of electrochemical biosensing: the signal is read using inexpensive[277] and easy-to-use instrumentation, and multiplexed detection is achieved using multi-electrode microchips.[278] Due to optical excitation, photoelectrochemical measurements are performed at lower bias potentials compared to their electrochemical counterparts.[279] This lowers the measured electrochemical background currents, and increases the signal-to-background ratio.[280]

PEC readout has been used to detect biomolecules such as DNA,[72] RNA,[74] and proteins.[76,281–283] In biomolecular sensors with PEC readout, the surface of the photoactive material is functionalized with biorecognition layers, such as nucleic acids,[284] antibodies, or, aptamers.[72,285] This bio-functionalization significantly reduces the photoelectrochemical signal magnitude by limiting the access of redox or electron donor/acceptor species to the photo-active material.[80] As a result, similar to the conventional PEC cells, enhanced light absorption and extraction efficiency are of paramount importance in sensing cells.

Implementing micro/nanostructures on the surface of the photoactive electrodes significantly improves the light absorption efficiency[267,286] due to the increased particle density,[287] internal scattering[288] and increased optical path length of the incident light.[289] Lithography,[290] electrochemical processing,[291,292] chemical etching, and energetic beam-based treatment[293–295] are widely used in implementing surface structuring. However, when using these fabrication methods, a tradeoff must be made between the degree of structural tunability, throughput, and cost. Surface wrinkling is a facile and inexpensive method[264] for introducing tunable micro and nanostructuring[291] into thin films,[296] porous networks,[297] and assembly of nanoparticles.[264,271,298] Wrinkling occurs when a compliant substrate modified with a stiff skin is exposed to compressive in-plane strain[271] or when the substrate is subjected to the removal of tensile strain.[272] The mismatch in the elastic moduli of the stiff layer and the compliant substrate results in the formation of wrinkles. The amplitude and wavelength of wrinkles are tuned by varying the layer thickness, layer and substrate mechanical properties, and the amount of induced strain.[271] Recently, surface wrinkling has been explored for enhancing the light extraction efficiency of photovoltaic devices.[268,270] In a photovoltaic device with an organic semiconductor used as the active layer, the amount of light absorption with infrared illumination increases from <4% to 7% for a wrinkled substrate and up to 22% for a wrinkled substrate containing folds.[268] This dramatic enhancement in light absorption is due to wave guiding and light trapping in wrinkled substrates. Another study revealed that wrinkled indium tin oxide (ITO) substrates significantly enhance light scattering over a broad range of wavelengths (400-800 nm).[270] Considering these studies, we sought to answer the following question: is it possible to use wrinkling to enhance the efficiency of photocurrent generation in sensing photoelectrochemical cells?

The challenge involved in answering the abovementioned question is related to the complex material architecture involved in sensing photoelectrochemical cells. The signal in these cells is generated at the interface between a solid photoactive electrode modified with a biorecognition layer and a liquid electrolyte solution. To take advantage of the tunability of nanomaterials and porosity of nanostructured films, the solid electrode is often created by the self-assembly of semiconductive quantum dots (QDs).[299,300] Previous studies have shown that it is possible to wrinkle porous nanoparticle films;[271] however, the films created *solely* from semiconductive QDs are not conductive enough for photoelectrochemical signal measurement. In this work, we created a unique method for loading photoactive QDs into a wrinkled scaffold of a transparent conductive oxide to enhance the generated photocurrent. By functionalizing the photoactive QDs embedded in the wrinkled film, we developed a sensor for detecting DNA targets, paving the way for high sensitivity photoelectrochemical sensors.

3.3 Materials and Methods

Chemicals: Phosphate buffer solution (PBS, 1.0M, pH 7.4), L-Ascorbic acid (99%), 1-Ethyl-3-(3-dimethylaminopropyl) carbodiimide (EDC), *N*-hydroxysuccinimide (NHS) and Poly diallyldimethylammonium chloride (PDDA) solution (20 wt%, molecular weight

400,000 – 500,000) were purchased from Sigma-Aldrich. CdTe quantum dots (510±5 nm emission wavelength) with -COOH functionalization were bought from PlasmaChem. Ethanol was purchased from Commercial alcohols (Brampton, ON). Milli-Q grade ultrapure water (18.2 MΩ.cm) was used for all washing steps and for preparing the solutions.

Device fabrication: Prestrained polystyrene sheets were purchased from Graphix shrink film, Ohio. Polystyrene sheets were cut according to the desired size and shape using the digitally driven robotic cutter. These polystyrene substrates were sonicated using ethanol and deionized (DI) water for 15 min before use. A 100nm ITO film was sputtered onto the substrate. The sputtering was carried out by radio frequency magnetron sputtering system from Angstrom science. The sputtering target was 90% In_2O_3 and 10% Sn_2O_3. Argon was used as the working gas for the sputtering.

CdTe QDs were deposited using an electrostatic layer-by-layer approach demonstrated by Wang et al.[301] The cleaned and dried ITO substrates were plasma cleaned for 1 minute. Plasma cleaning created a negatively charged surface. The layer-by-layer assembly was performed as follow. The substrates were (1) immersed into a solution of PDDA (0.5 wt%, pH=3), (2) rinsed with DI water thoroughly, (3) dipped into a CdTe solution for 20 minutes, and (4) rinsed with DI water thoroughly. In this process, PDDA was positively charged and CdTe QDs were negatively charged. This cycle was repeated multiple times to obtain the optimum number of layers.

Two types of wrinkled substrates were prepared in this work. In the first type, ITO was deposited on the polystyrene substrate and was heat shrunk at 140°C for 5 minutes. In the second type, polystyrene substrates were exposed to Ultraviolet-Ozone (UVO) for 4 min. UVO treatment created a thin oxide layer on the surface of the polystyrene substrate.[302] UVO-treated substrates were thermally shrunk at 140°C for 5 min. ITO was then sputtered onto the shrunk UV-treated substrate. Following ITO deposition, CdTe quantum dots were deposited using the layer-by-layer technique for both types of wrinkled surfaces.

Imaging: To characterize the samples, both topographical and cross-sectional imaging was done. Topographical imaging was performed using scanning electron microscopy (SEM) and cross-sectional imaging was done using transmission electron microscopy (TEM). The SEM images were obtained using JEOL JSM-7000S with an accelerating voltage of 2 kV and a working distance of 6 mm. Low probe current was used to obtain the images. TEM images were obtained using JEOL 2010F using an accelerating voltage of 200 kV.

PEC Measurements: All PEC measurements were performed with a three-electrode setup using a CHI 660D electrochemical workstation (CH Instruments, Austin, Texas). Ag/AgCl (1.0M KCl) was used as the reference electrode and a platinum wire was used as counter electrode. The electrolyte solution contained 0.1 M PBS and 0.1 M ascorbic acid. Ascorbic acid was used as a hole scavenger as previously demonstrated in the literature.[303] All PEC measurements were done with a zero-bias voltage.

DNA Detection: The sequence of oligonucleotides (IDTDNA, Coralville, Iowa) used in this work is as follows.

Probe: 5′-NH_2-AGG GAG ATC GTA AGC-3′

Complementary Target: 5′-GCT TAC GAT CTC CCT-3′

Single-base mismatch Target: 5’-GCT TAC GTT CTC CCT-3’

Double-base mismatch Target: 5’-GCT AAC GTT CTC CCT-3’

Three-base mismatch Target: 5’-GCT AAC GTT CTG CCT-3’

Noncomplementary Target: 5′-TTT TTT TTT TTT TTT-3′

Probe DNA was attached to the -COOH functionalized CdTe quantum dots using EDC/NHS coupling in an acidic buffer. The substrates were immersed into a 20 mM EDC and 10 mM NHS solution for 50 minutes.[303] The substrates were then incubated with 0.5 μM probe DNA (DI water was used as solvent for DNA) for 3 h. For target hybridization, incubation was done with 1 μM target solution for 30 min at room temperature.

The limit-of-detection of the system was calculated by using the data presented in Figure 4(d), and using the equation:

$$\textit{Limit of detection} = 3x3\sigma/s$$

where σ is the residual standard deviation of the regression line, and s is the slope of the line.[304]

3.4 Results and Discussion

To explore the role of wrinkle-induced surface structuring on the efficiency of PEC signal transduction, we developed three classes of photo-electrodes. In the first class, a layer-by-layer assembly of CdTe QDs was formed on a planar ITO layer deposited on an unshrunk polystyrene substrate (Figure 3-1a). In the second class, the QDs were loaded into a wrinkled ITO layer, which was created by shrinking the ITO-modified polystyrene substrate (Figure 3-1b). In the third class, wrinkles were created directly on polystyrene by forming a stiff oxidized surface layer and shrinking the substrate. The ITO and QDs were then sputtered and loaded into the wrinkled polystyrene scaffold respectively (Figure 3-1c).

Figure 3-2 shows the differences in surface topography and continuity between the three classes of photo-electrodes. The baseline photo-electrodes are planar, and their ITO layer was free of breaks (Figure 3-2a). Shrinking the ITO-coated polystyrene substrate resulted in a wrinkled film (wrinkled photo-electrode); however, the wrinkled ITO layer was discontinuous and broken (Figure 3-2b). Creating a wrinkled scaffold *directly* on polystyrene (Figure 3-2c) yielded films (scaffolded-wrinkled photo-electrodes) with smaller feature sizes and wrinkle amplitudes compared to the wrinkled ITO electrode (Figure 3-2) and resulted in improvements in wrinkle quality and continuity. Wrinkling occurs when compressive stress is applied to a complaint substrate modified with a stiff skin. The wavelength of the wrinkles depends on the thickness of the stiff skin and the degree of mismatch between the mechanical properties of the substrate and the skin.[305] In Figure 3-2b, the ITO layer formed a stiff skin on the compliant polystyrene substrate, and heat shrinking the substrate resulted in the creation of wrinkles. Breaks and cracks appeared in the wrinkled layer because ITO is a brittle material, which cracks at strains as low as ~2%.[306] This makes ITO an undesirable stiff skin for use in wrinkled films created on pre-strained polystyrene experiencing a strain of about 40%. In Figure 3-2c, oxidizing polystyrene forms a stiff skin directly on its surface[307] which wrinkles upon applying a compressive stress to the substrate forming a scaffold for ITO deposition. The combination of a thinner skin layer and less significant mismatch in the skin/substrate mechanical properties resulted in wrinkles with smaller wavelengths in Figure 3-2c compared to Figure 3-2b. These factors also enabled the oxidized layer to conform rather than break in response to the applied strain, creating a continuous wrinkled layer.

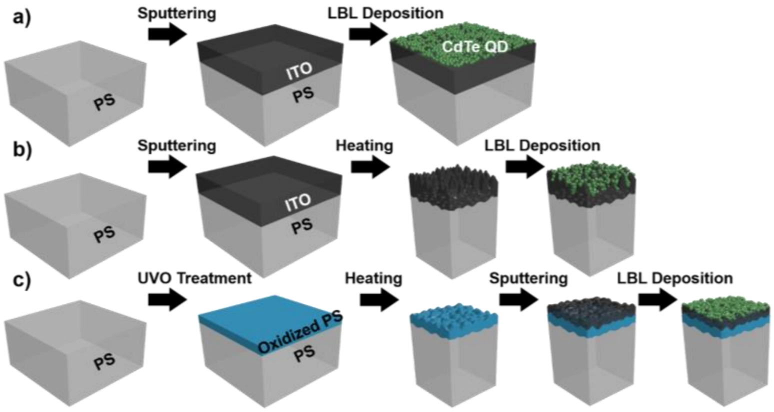

Figure 3-1: Fabrication of quantum dot-based photo-electrodes. (a) Planar photo-electrodes were fabricated by sputtering ITO on polystyrene (PS in the figure) and layer-by-layer assembly of CdTe QDs. (b) Wrinkled photo-electrodes were fabricated by sputtering ITO, heat shrinking polystyrene at 140 ^{O}C, and layer-by-layer assembly of CdTe QDs. (c) Photo-electrodes with a wrinkled scaffold were fabricated by oxidizing the surface of polystyrene using UV/ozone (UVO) treatment, heat shrinking polystyrene at 140^{O}C, sputtering ITO, and layer-by-layer assembly of CdTe QDs.

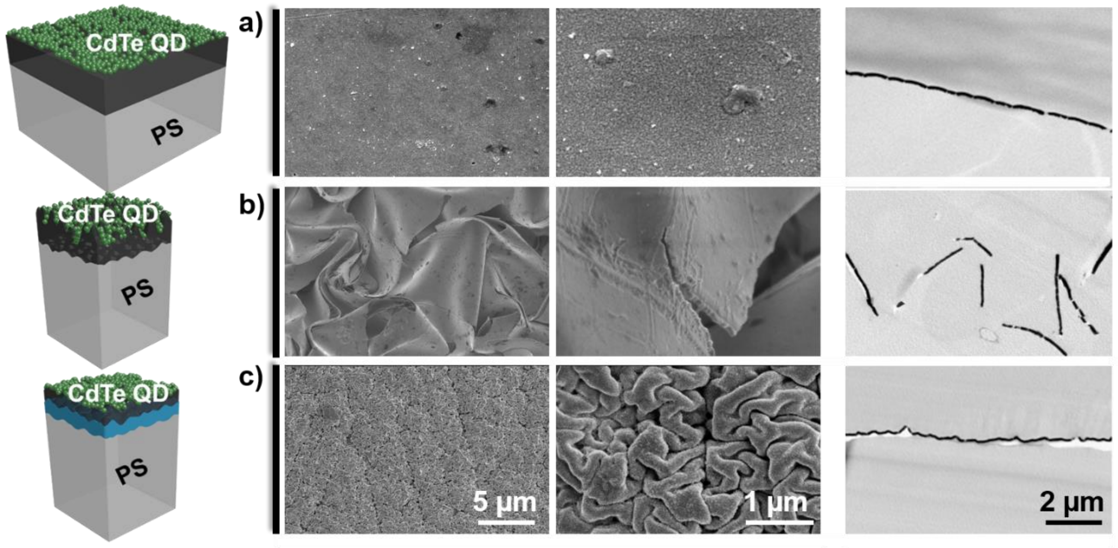

Figure 3-2 : Comparison of photoelectrodes with different structures. From left to right: the schematic illustration, low magnification scanning electron micrograph, high magnification scanning electron micrograph, and cross-sectional scanning transmission electron micrograph of a (a) planar electrode created by depositing CdTe on a planar ITO electrode, (b) wrinkled electrode created by depositing CdTe on a wrinkled ITO electrode, and (c) scaffolded-wrinkled photo-electrodes created by depositing ITO and CdTe on a wrinkled oxidized polystyrene scaffold.

We explored how loading light-absorbing quantum dots into a three-dimensional nanostructured scaffold influenced photoelectrochemical signal transduction. We measured the PEC current density in planar and scaffolded-wrinkled surfaces loaded with 1-10 layers of CdTe QDs using ascorbic acid as the redox reporter. Visible light is absorbed by CdTe QDs generating electron-hole pairs (Figure 3-3a). Under the bias potential used here (0 V versus Ag/AgCl), the holes oxidize ascorbic acid, generating a light-modulated anodic photoelectrochemical current.[308,309] The PEC currents observed with the planar and scaffolded-wrinkled surfaces followed dramatically different trends. For the planar surface, the photoelectrochemical current increased with increasing the number of layers. However, the current reached its maximum value at three layers, decreased, and reached a plateau at five layers for the scaffolded-wrinkled surface. The magnitude of the PEC current was significantly larger for the scaffolded-wrinkled surface compared to the planar surface at every loading level. The highest observed PEC current for the scaffolded -wrinkled surface (at 3 layers) was about 10 times larger than the current achieved in the planar surface (at 10 layers), even though the wrinkled surface contained fewer QD layers.

To understand the different PEC current trends seen with planar and wrinkled photo-electrodes, we studied the materials architecture in each case using scanning transmission electron microscopy (STEM) (Figure 3-3d). In the wrinkled photo-electrode, the distance between CdTe particles was reduced, and the overall particle density and size was increased compared to the planar photo-electrode. We present two hypotheses for explaining the current decrease observed after adding three QD layers to the wrinkled ITO electrode. First, in the wrinkled architecture, where the QDs are already densely packed, going beyond three layers is expected to cause the QD size to increase. This reduces the quantum confinement and absorption cross section of the QDs,[287] reducing the collected photocurrent. Second, adding more QDs to the device through layer-by-layer deposition is expected to place them farther from the ITO surface, and it introduces more surface recombination centre.[309] As the charges travel through the network of quantum dots and the PDDA spacer, resistive losses, diffusion losses and recombination decrease their collection rate by the ITO electrode,[310,311] further reducing the photocurrent.

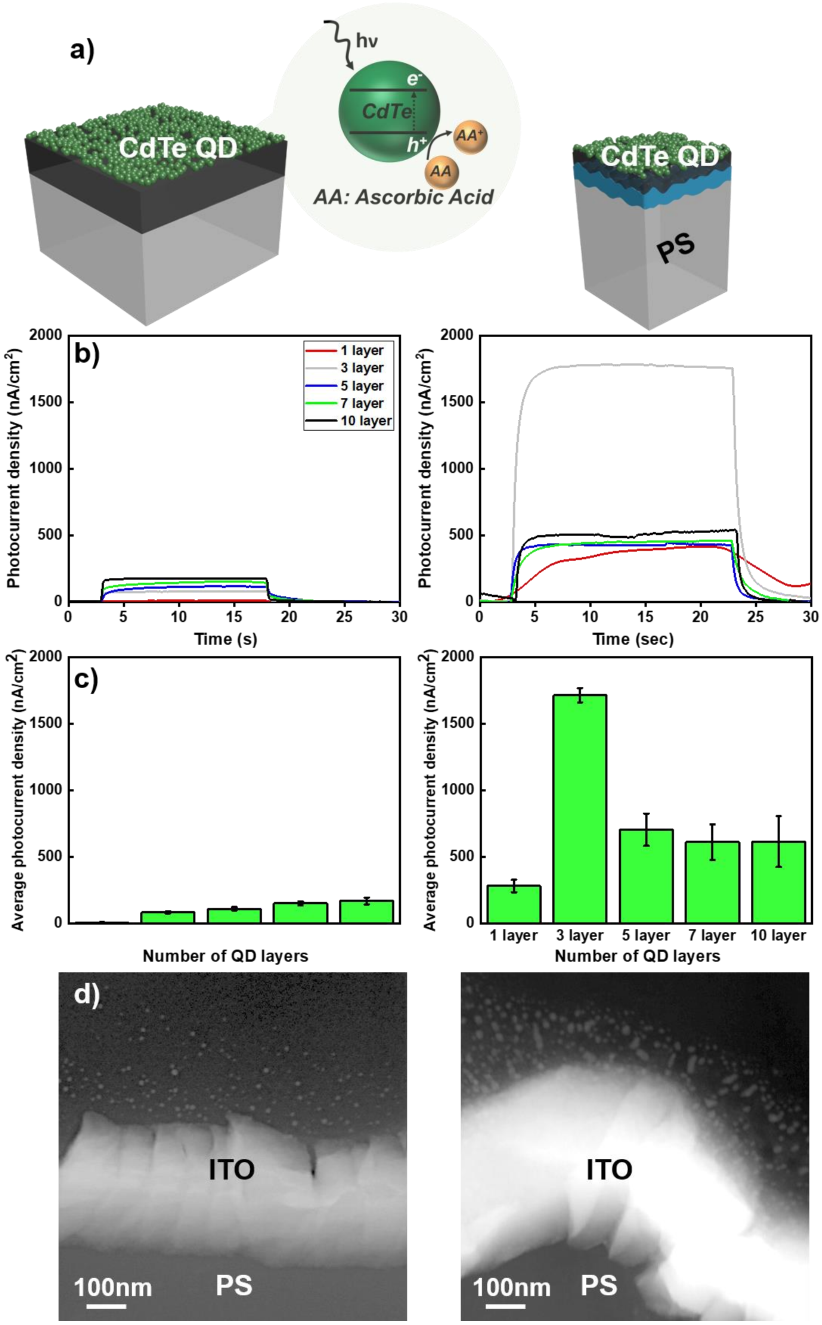

Figure 3-3 : PEC measurements at planar and scaffolded-wrinkled photo-electrodes. (a) Visible light (470 nm) induces electron/hole pairs in CdTe QDs. Holes oxidize ascorbic acid generating an anodic redox current. (b) PEC current densities measured on planar (left) and scaffolded-wrinkled (right) devices using 100 mM ascorbic acid at 0 V with respect to Ag/AgCl. The QD layers are increased by depositing alternate layers of quantum dots and poly(diallydimethylammonium chloride) (PDDA). The 470 nm LED is turned on at 3 s and turned off at 23 s. (c) The average PEC current densities measured on planar (left) and scaffolded-wrinkled (right) devices for different numbers of QD layers. (d) Scanning transmission electron micrographs of cross sections of planar (left) and scaffolded-wrinkled (right) devices. The imaged devices contain three QD layers.

In the planar device, the QD network near the electrode surface is sparse, and it is possible for quantum dots to fill the gap within this network without increasing the size of quantum dots or forming additional layers. This "filling the gap" process is expected to increase the current in the planar photo-electrode. However, the planar device failed to catch up to the wrinkled device even when a 10-layer network was created, making the wrinkled photo-electrode the ideal choice for PEC sensing.

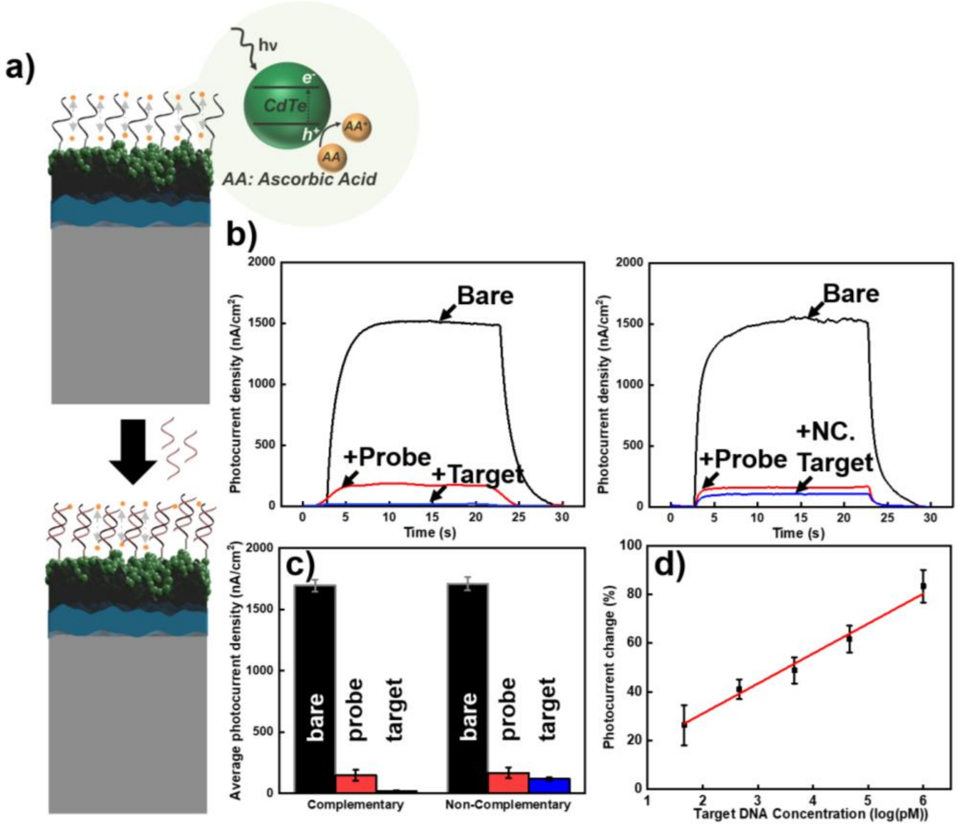

Figure 3-4 : DNA hybridization on scaffolded-wrinkled electrodes. a) Schematic diagram of DNA hybridization on scaffolded-wrinkled electrodes. The photoelectrochemical signal is generated due to the oxidation of ascorbic acid. Functionalizing the surface of CdTe quantum dots with DNA reduces the access of ascorbic acid to the surface and decreases the photocurrent. (b) Photocurrent of the electrode as prepared, following modification with probe DNA, and after incubation with complementary (left) and non-complementary target (right) with a concentration of 1 μM. (c) Quantification of photocurrent for bare, probe-modified, and target-incubated photo-electrodes. (d) The absolute value of change in photocurrent after incubation with target DNA ($|I_{target}-I_{probe}|/I_{probe}$) at varying concentrations. All error bars represent standard deviation obtained from measuring the photocurrents of at least three devices.

DNA biosensors coupled with PEC readout use nucleic acid probes to capture specific DNA sequences.[72,76,285] These biosensors translate DNA capture to an increase or a decrease in PEC currents leading to signal-on or signal-off sensing. In these sensors, transducer surfaces are created using semiconducting nanoparticles,[40,80] which can be combined with metallic nanoparticles.[283,312] DNA biosensing has been demonstrated using structure-switching hairpin DNA probes modified with semiconductive QDs. Target capture unfolds the hairpin probe and increases the separation between the QDs and the substrate, which decreases the PEC current.[309,312] Alternatively, target labeling or the use of labeled reported probes have been used for delivering a semiconductive or plasmonic nanoparticle label to the proximity of the substrate for creating signal-on[283,313,314] or signal-off[315] PEC biosensors.

We investigated the changes in PEC current when the scaffolded-wrinkled photo-electrodes were interfaced with probe and target DNA strands (Figure 3-4). Adding single-stranded DNA probes to the photo-electrode surface as the biorecognition layer significantly decreased the photoelectrochemical current (Figure 3-4b). Adding complementary DNA target caused another significant decrease (83% for 1 μM) in the photoelectrochemical current (Figure 3-4b). However, adding non-complementary DNA target caused a much smaller signal change (16% for 1 μM, (Figure 3-4b). Adding a DNA monolayer to the surface of quantum dots reduces the accessibility of ascorbic acid to the surface, and reduces the photoelectrochemical signal.[280] This highlights the importance of increasing the baseline photoelectrochemical current using the wrinkling strategy. Complementary DNA hybridizes with probe DNA forming DNA duplexes on the photoelectrode surface. This further decreases the accessibility of ascorbic acid to the quantum dot surface, and reduces the induced photoelectrochemical signal[316] (schematically depicted in Figure 3-4a). Although it was not expected for non-complementary DNA to change the measured current, it is hypothesized that the small current decrease is caused by non-specific adsorption of DNA on the photoelectrode.

The response of the system featuring wrinkled photo-electrodes was measured at varying concentrations of target DNA. The change in PEC current increased linearly with increasing the target concentration (Figure 3-4d), leading to a limit-of-detection (LOD) of 5 pM. The LOD of the assay with planar photoelectrodes was 1 nM (Figure S3-1), demonstrating that wrinkled photo-electrodes enhanced the LOD of the PEC biosensor by ~200 times. The experiments reported in Figure 3-4 demonstrate that the wrinkled materials architecture forms a robust platform for creating photoelectrochemical sensors with a high sensitivity. The LOD of this system is higher than systems that use probe or target labeling (with reports of attomole level sensitivity);[313] however it is in line with the studies focused on *direct* and *label-free* PEC DNA sensing.[280] As observed in *electrochemical* DNA biosensing, optimization of the biorecognition layer, tuning the photo-electrode surface structure, and the use of surface passivation elements are expected to further enhance the performance of this system.[278]

To assess the applicability of the wrinkled PEC assay to clinical applications, we evaluated its stability and specificity. The photostability test[188,266,317] was performed by measuring the PEC current of the bare wrinkled photo-electrodes through 15 cycles of optical excitation (Figure S3-2). The bare photoelectrodes showed a stable PEC current for 10 repeated cycles, and by 15 cycles, the photocurrent reduced by 10%. The stability of the *biosensor* (photoelectrode modified with DNA probe) was assessed by comparing its PEC response immediately after fabrication and after seven days in the dark. The PEC current of the biosensor did not significantly change during the testing period (Table S3-1). Specificity of the PEC biosensor was assessed by introducing targets that had one, two, or three base pair mismatches with the probe DNA (Figure S3-3).[72] This experiment demonstrated that the PEC assay is capable of distinguishing between complementary and single-base mismatched targets. It was also possible to detect targets that had a sequence with single and multiple mismatches. These experiments demonstrate the suitability of the wrinkled PEC biosensors for applications beyond the research laboratory.

3.5 Conclusions

In this work, we created a high-quality conductive scaffold for assembling photo-active materials into a micro/nanostructured electrode. The scaffold was created by wrinkling the surface layer of polystyrene, which was stiffened by an oxidizing treatment, followed by depositing a conformal layer of indium tin oxide. Depositing CdTe quantum dots onto the wrinkled scaffold increased the photoelectrochemical signal by an order magnitude compared to quantum dots deposited on planar surfaces. Scanning transmission electron microscopy images demonstrated that CdTe particles form a denser network inside the wrinkled scaffold compared to the planar surface. The larger PEC current obtained using the wrinkled scaffold is essential for building PEC biosensors. Modifying the quantum dot surface with DNA capture probes decreased the PEC signal to less than 10% of its original value. The capture of DNA targets also reduced the photoelectrochemical signal. As a result, a large baseline current is essential in obtaining sufficient signal-to-noise ratio and dynamic range when analyzing low target concentrations. The enhanced PEC current obtained using the wrinkled materials architecture enabled us to develop a sensitive and label-free DNA biosensor with picomolar limit-of-detection.

3.6 Acknowledgements

We acknowledge the financial support provided for this work from NSERC and Ontario Ministry of Research and Innovation. L.S. is the Canada Research Chair in Miniaturized Biomedical Devices and is supported by the Canada Research Chairs Program. L.S is the recipient of the Ontario Early Researcher Award. S.S is the recipient of the NSERC PGS-D scholarship. The microscopy work was carried out at the Canadian Centre for Electron Microscopy, a facility supported by the Canada Foundation for Innovation under the Major Science Initiative program, NSERC, and McMaster University.

3.7 Supplementary Information

Limit of detection of planar photo-electrodes

Figure S3-1 shows the calibration curve for the planar substrates. The calibration line equation is the following:

$$y = -7.64 + 10.95x$$

Here, solid black line showed average photocurrent reduction of 18.95% with the standard deviation of 6.65, when non-complementary target is introduced on the electrode. Therefore, minimum concentration that can be detected using the planar substrate will have the photocurrent reduction of 25.6%. Using the calibration line, the limit of detection is calculated to be 1 nM.

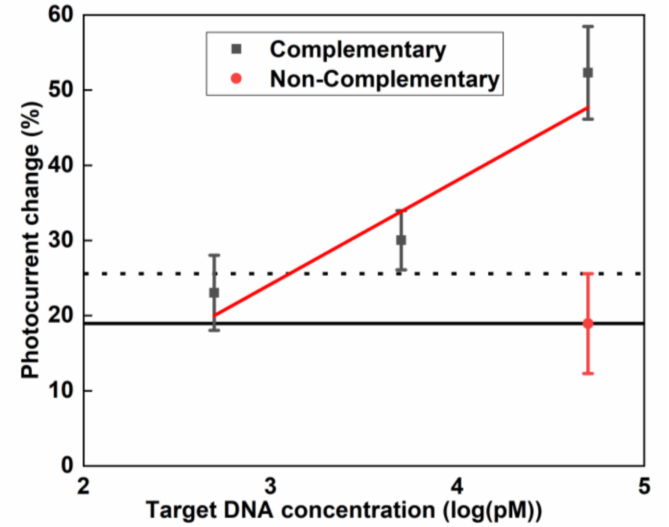

Figure S3-1: Limit-of-detection of planar photo-electrodes

Stability of wrinkled photo-electrodes

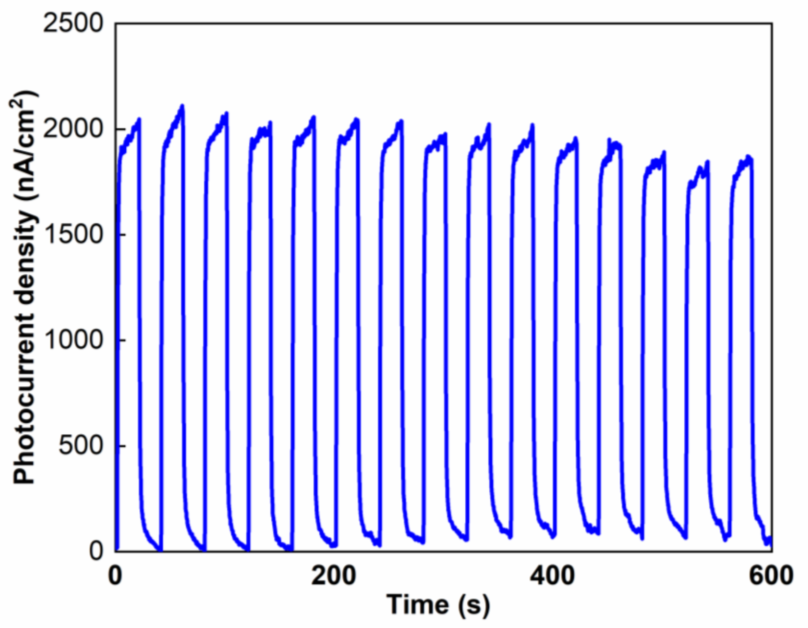

Figure S3-2: Stability of wrinkled photo-electrodes over 15 illumination cycles

The photocurrent density was reduced by 10 % after 15 illumination cycles.

In the other test, the photocurrent density was measured for the probe deposited substrate on 1st and 7th day. The photocurrent density on 1st day was 435nA and on the 7th day was 433nA.

Table S3-1 : Stability test of the probe-deposited wrinkled photo-electrode

	Photocurrent density 1st day	Photocurrent density 7th day
Probe-deposited wrinkled electrode	435 nA	433 nA

Specificity test of the wrinkled substrate

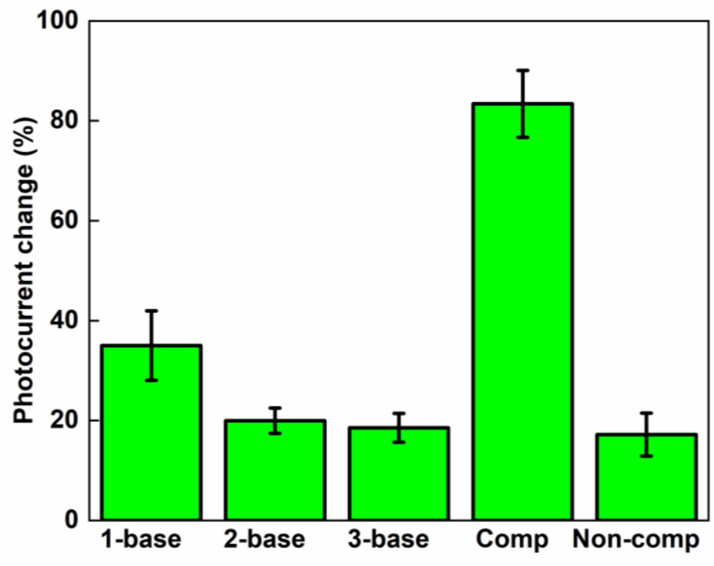

Figure S3-3 : Specificity of the wrinkled photo-electrodes

The change in photoelectrochemical current was measured when probe-modified photo-electrodes were subjected to complementary sequences or targets with one or larger number of base-pair mismatches.

Chapter 4 Understanding the interaction between TiO_2 and Au NPs for building a signal-on photoelectrochemical biosensor

Chapter Introduction (Objective II and III)

Micro structuring of the electrodes was shown in chapter 3 to improve the photocurrent, as well as the LOD obtained from the photoelectrode when operated in signal-off mode. As Chapter 2 describes, there are other methods to improve the PEC signaling for signal-on detection. Introducing noble metal nanoparticles (i.e., Au, Ag) to obtain plasmonic enhancement in photocatalytic driven mechanisms is one of the most studied avenues.[318] Biofunctionalized Au NPs are often used in PEC biosensing applications to achieve enhanced sensitivity and a lower detection limit.[117,248,312,319,320] However, it is important to understand how Au NPs affect the photocurrent generation of the photoelectrodes. The Au NP concentration dependencies on photocurrent generation needs to be realized before utilizing Au NP labeled DNA to correlate with the analyte detection event. Several different explanations have been presented to explain the improvement in photoconversion efficiency. These include (i) increased absorption due to surface plasmon resonance and light-trapping, (ii) improved charge separation due to the localized electromagnetic field, (iii) promoting electron transfer to the adsorbed species, and (iv) storage of electrons that drive the Fermi level to more negative potentials.[321] The precise nature of the interaction depends heavily on the optical properties of the materials used.

Among the different semiconductor NPs, TiO_2, a wide bandgap material, is the most used due to its stable performance and facile preparation.[322–324] Recently, Victorious *et al.*

modified TiO_2 with 3,4-dihydroxybenzaldehyde (DHB) and chitosan (CHIT), providing good surface coverage of the electrodes as well as a mesoporous structure. The surface modification of TiO_2 NPs also paves the way for easy biofunctionalization. Though there are various studies where the interaction of Au NPs with TiO_2 is investigated, wavelength and concentration dependent study of Au NPs on TiO_2 is still lacking. In this study, the interaction of Au NPs has been studied with the above mentioned modified TiO_2 NPs. Interestingly, the Au NP's effect on the photocurrent strongly depends on the excitation wavelength used. Different mechanisms play a role based on the incident electromagnetic field wavelength. The interaction between Au NPs and TiO_2 NPs was studied for various concentrations of Au NPs by performing electrochemical and photoelectrochemical characterization techniques. Finally, the understanding obtained from this study was used to demonstrate a proof-of-concept DNA sensing application where both signal-on and signal-off readout can be achieved for a single target DNA sequence.

Authors: Sudip Saha, Amanda Victorious, and Leyla Soleymani

Publication: Submitted in Electrochimica Acta, Nov 2020

4.1 Abstract

Gold (Au) nanoparticles (NPs) have been widely used to modulate the photoelectrochemical current of TiO_2 photoelectrodes in energy conversion and sensing systems. Understanding the different mechanisms responsible for photocurrent modulation at different frequencies is important for building optimized photoelectrochemical systems.

Herein, we investigated the photocurrent magnitude at different excitation wavelengths by varying Au NP concentration at the photoelectrode surface. Under UV illumination, increasing the surface loading of Au NPs initially increased the photocurrent, and above a threshold loading level, decreased the measured photocurrent. However, under visible light excitation, increasing the Au NP surface density resulted in a steady increase in photocurrent. Mott-Schottky measurements, incident photon to current conversion efficiency measurements, and electrochemical impedance spectroscopy were used to understand the mechanisms responsible for these different observations. It was found that both current loss – due to reduced light absorption by TiO_2 – and gain – due to direct charge transfer between Au and TiO_2 NPs were possible under UV light. Under visible light illumination, strong light absorption and localized surface plasmon resonance of Au NPs and negligible light absorption by TiO_2 NPs led to signal gain at varying Au NP surface concentrations. This bimodal signal modulation was further demonstrated in the context of biosensing using Au NP-labeled DNA barcodes, optically excited at different wavelengths. This study allows photoelectrochemical systems to be engineered for programmable signal-off, signal-on, or ratiometric biosensing combining the former sensing modes.

4.2 Introduction

Titanium dioxide (TiO_2) is among the most widely used semiconductive materials for photocatalysis and photoelectrochemistry.[324–326] TiO_2 nanoparticles (NPs) have recently attracted tremendous attention for use in the abovementioned areas, compared to bulk TiO_2, because of their high surface-to-volume ratio, enhanced light absorption, and increased optically-excited carrier density.[327] In spite of this, TiO_2 NPs present low quantum efficiency and poor visible light absorption.[328] Plasmonic metal NPs such as gold (Au), silver (Ag), and platinum (Pt) have been previously used in conjunction with TiO_2 NPs to improve their quantum efficiency and visible light absorption.[328,329] The interaction between TiO_2 NPs and these plasmonic NPs is guided by their complementary optical properties: well-separated and long-lived excitons in semiconductors and localized electromagnetic modes in plasmonic NPs.[330] The integration of these two classes of NPs allows researchers to tailor and engineer materials systems with specific optical properties based on exciton−plasmon interactions. Au NPs have drawn a lot of interest when used in direct contact or close proximity to TiO_2 surfaces due to their photochemical and chemical stability, ease of preparation, and tailorable electronic and optical properties.[331] The complexes resulting from the incorporation of Au NPs on TiO_2 surfaces have been extensively explored to enhance photoelectrochemical (PEC) activity.[332,333] Various theories have been put forth to explain the enhancement demonstrated in these systems, which include the electron-sink effect, enhanced conductivity due to improved interfacial charge separation,[334] reduced bandgap energy of the resultant complex,[335] plasmon-induced resonance energy transfer,[336] and electric field amplification[333] to name a few.

Systems that use the direct contact of Au NPs with TiO_2 electrodes for PEC signal enhancement require an optimized surface density of Au NPs for maximizing the PEC current. Rayalu et. al varied Au NP loading from 2.5% to 10% weight by weight (w/w) with respect to anatase and P25 TiO_2 and studied the effectivity of the resultant complex for photocatalytic water splitting under mercury light illumination.[337] An enhancement in the hydrogen evolution rate and yield, by a factor of 2 and 4 respectively, was exhibited upon increasing the concentration of Au NPs to 4% while an increase in concentration to 5% and beyond resulted in a significant decline in activity and yield. This was thought to be the result of a delicate tradeoff between loading-based enhancement and scattering caused by the increase in Au loading. At lower loading concentrations (4% w/w), the light path of incident radiation remains uninterrupted by the metal NPs. However, increasing the loading concentration (5% and 10% w/w) causes these metal NPs to act as half mirrors capable of reflecting incident radiations, consequently affecting the overall light absorption capacity and catalytic activity of the metal–semiconductor composite. This is in accordance with the report by Murdoch *et al*. where Au NP loading of only 4 wt% on anatase TiO_2 NPs showed the highest H_2 production rate in a TiO_2/Au NP system, where further loading of Au NPs reduced the photoreaction rate of hydrogen production.[338] Additionally, Kamat et al. investigated the Au NP loading effect on TiO_2 NPs and also found that the photocurrent under UV light excitation increases only for up to 2 wt% of Au NPs, beyond which a photocurrent decrease was observed.[339] Similar trends have also been observed using TiO_2 nanowires.[333]

The abovementioned studies do not precisely investigate the impact of Au NP concentration in photocurrent enhancement for TiO_2/Au NP systems under different excitation wavelengths that are linked to distinct interaction mechanisms. In this study, we used two different light excitation modes to understand the effect of Au NP density on PEC current generation. In the same materials system, one wavelength mode probed the localized surface plasmon resonance (LSPR) of Au NPs; whereas the other probed the interband excitation of Au NPs in conjunction with the bandgap excitation of TiO_2 NPs. The new understanding generated here is utilized to design a DNA detection strategy, where both *signal-off* and *signal-on* response can be achieved from the same electrode simply by changing the excitation wavelength. This bimodal readout system can be exploited for reducing background noise and enhance the sensitivity of the biosensor in the future.[340–342] The knowledge obtained from this study can be further used for effectively programming and predicting the PEC current response of TiO_2/Au NP systems.

4.3 Experimental Section

Materials and Reagents: Phosphate buffer solution (PBS, 1.0M, pH 7.4), L-ascorbic acid (99%), sodium chloride (NaCl), chitosan (CHIT, from shrimp, degree of deacetylation of 85%, Mw=200,000)), glacial acetic acid, 3,4-dihydroxybenzlaldehyde (DHB), Chloroauric acid ($HAuCl_4$), Trisodium citrate, Potassium chloride (KCl), Potassium ferrocyanide ($K_4Fe(CN)_6$), Potassium ferricyanide ($K_3Fe(CN)_6$), poly(diallydimethylammonium chloride) (PDDA) and tris (2-carboxyethyl) phosphine hydrochloride (TCEP, 98%) were purchased from Sigma-Aldrich. 100 nm Indium Tin oxide (ITO) glass substrates were also bought from Sigma-Aldrich. P25-TiO_2 was obtained from Nippon aerosol Co. Ltd. Acetone and Ethanol were purchased from commercial alcohols (Brampton, ON). Milli-Q grade (18.2 MΩ cm) de-ionized (DI) water was used for all solution preparation and washing steps.

Synthesis of TiO_2 and Au nanoparticles (NPs): Modification of TiO_2 NPs were completed by using the procedure reported earlier.[343] In brief, 16gL^{-1} DHB solution was made in de-ionized (DI) water. CHIT solution with a concentration of 3 gL^{-1} was made in acetic acid solution (1%). Then, DHB-modified CHIT solution was prepared with mass ratio 4:1 as DHB:CHIT. Finally, 20mg of P25-TiO_2 was added to the previously prepared DHB-modified CHIT solution. DHB enables superior signal generation by improving the electronic and optical properties of TiO_2 NPs,[344] while CHIT aids in the formation of uniform and stable films. The synergistic effects of these two materials were exploited to create a robust and reliable photoelectrode for our experimental design.[343]

The Au NP solution was synthesized according to the protocol reported by Grabar et al.[345] Briefly, chloroauric acid ($HAuCl_4$) of 1 mM was added onto 38.8 mM trisodium citrate solution with 10:1 ratio (volume). The mixed solution was heated at boiling temperature while stirring vigorously for 10 minutes. After that, stirring was continued at room temperature for 15 min. This procedure resulted in Au NPs with a diameter of 12 nm.[345]

Electrode fabrication: All ITO substrates were cleaned by sonicating in acetone, ethanol and DI water for 10 minutes. Vinyl tapes were used to mask the electrodes in order to preserve electrode contact area. The electrodes were plasma treated for one minute. Mesoporous P25-TiO_2 films were prepared by drop-casting 10 µl of solution onto the exposed electrode area and heated at 100°C for 5 minutes. The procedure was repeated three times to deposit 30 µl of P25-TiO_2 solution in total. The electrodes were washed and air dried prior to use.

Photoelectrochemical characterization: All PEC experiments were performed in a three-electrode cell setup where Ag/AgCl works as the reference electrode and Pt wire works as counter electrode. Zahner potentiostat was used for all the electrochemical and PEC measurements. Optical excitation was obtained using TLS03 LED light source (adjustable wavelength) from Zahner. Zahner CIMPS-QE/IPCE photo-electrochemical workstation was used for PEC measurements. Electrolyte for photocurrent and IPCE measurements consists of 0.1 M ascorbic acid (AA) in 0.1 M PBS solution. Photocurrents were calculated by subtracting the current with light from the dark current without any optical excitation. The measurements were performed under a bias voltage of 0 V vs. Ag/AgCl. Incident-photon-to-current-conversion efficiency (IPCE) was also measured by using the same electrolyte and bias voltage. IPCE can be defined as:

$$\mathrm{IPCE}(\%) = \frac{1240 \times \mathrm{I}(\mathrm{A/cm^2})}{\lambda(\mathrm{nm}) \times \mathrm{P_{inc}}(\mathrm{W/cm^2})} \times 100$$

Where, I is the measured photocurrent, λ is the incident wavelength of light and P_{inc} is the incident optical power.[346]

Electrochemical Impedance Spectroscopy (EIS) and Mott-Schottky: EIS measurements were performed at room temperature by using Zahner potentiostat at open circuit potential by using 2 mM ferri/ferro cyanide in 0.1 M KCl as the electrolyte. The frequency range used for EIS was 100 kHz to 0.1 Hz and excitation amplitude was 5 mV.

Mott-Schottky experiments were performed at a frequency of 1 kHz and using the same electrolyte and excitation amplitude as EIS.

Scanning Electron Microscopy (SEM): The surface structure of the electrodes was visualized using FEI Magellan 400 scanning electron microscope (SEM). A Matlab code was used to calculate the Au NP density. At-least 5 different areas were used to calculate the Au NP density.

Absorption spectroscopy: UV-Visible (UV-VIS) absorption spectroscopy was performed using an ocean view Flame-S-XR1-ES assembly.

AuNP-DNA conjugation: For the DNA detection experiment, single-stranded DNA (ssDNA) target was conjugated with Au NPs according to the literature[347]. Briefly, 1 ml of the AuNP solution was (1 nM) resuspended in 10 mM PBS buffer (pH 7.0). Target DNA (thiolated) of 100 µM was reduced using TCEP and 35 µl of the reduced DNA was added to the AuNP solution. This solution was then incubated for 16 h at room temperature (RT). After that, 2 M NaCl in 10 mM PBS were added slowly to make the final concentration of 0.1 M NaCl. This solution was kept at RT for 40 h while shaking continuously. Finally, the solution was washed with 10 mM PBS and 0.1 M NaCl buffer (pH 7.0).

DNA sensing: The electrodes were biofunctionalized by depositing ssDNA (1µM) probe for 3 h. Following the probe deposition, electrodes were incubated in 100 pM of Au NP labeled target solution. Electrodes were washed thoroughly between each step. The measured percentage change (ΔI_{DNA} (%)) is calculated as:

$$\Delta I_{DNA}\ (\%) = (I_{Target} - I_{Probe}) / I_{Probe}$$

Where I_{Probe} and I_{Target} is the photocurrent after probe deposition and target hybridization, respectively.

The DNA sequences used in this work are as follows:

15-mer probe: 5′-NH_2-AGG GAG ATC GTA AGC-3′

Complementary target: 5′-SH-TTT TTT TTT TGC TTA CGA TCT CCC T-3′

Non-Complementary target: 5′-SH-TTT TTT TTT TTT TTT TTT TTT TTT T-3′

4.4 Results and Discussion

In order to investigate the effect of Au NP surface density on modulating the PEC properties of TiO_2 NPs, we varied the deposition time of Au NPs (~12 nm, Supplementary Figure S4-1) from 5 to 45 minutes (Figure 4-1(a)). This in turn increased the surface density of Au NPs on TiO_2 photoelectrodes (Figure 4-1 (b)). These photoelectrodes were created by drop casting a porous network of TiO_2 NPs, integrated within a catecholic polymeric network of chitosan (CHIT) and 3,4-dihydroxybenzaldehyde (DHB), onto conductive indium tin oxide (ITO) supports.[343] DHB enables superior signal generation by improving the electronic and optical properties of TiO_2 NPs,[344] while CHIT aids in the formation of uniform and stable films. The synergistic effects of these two materials were exploited to create a robust and reliable photoelectrode for our experimental design.[343] From the scanning electron micrographs (SEMs) obtained at different deposition time points (Figure 4-1 (b)), the amount of Au NPs was calculated as 134, 181, 433 and 623 per μm^2 for 5 min, 10 min, 20 min and 45 min deposition times, respectively. The distance between the nearby Au NPs also decreased with the increase in deposition time.

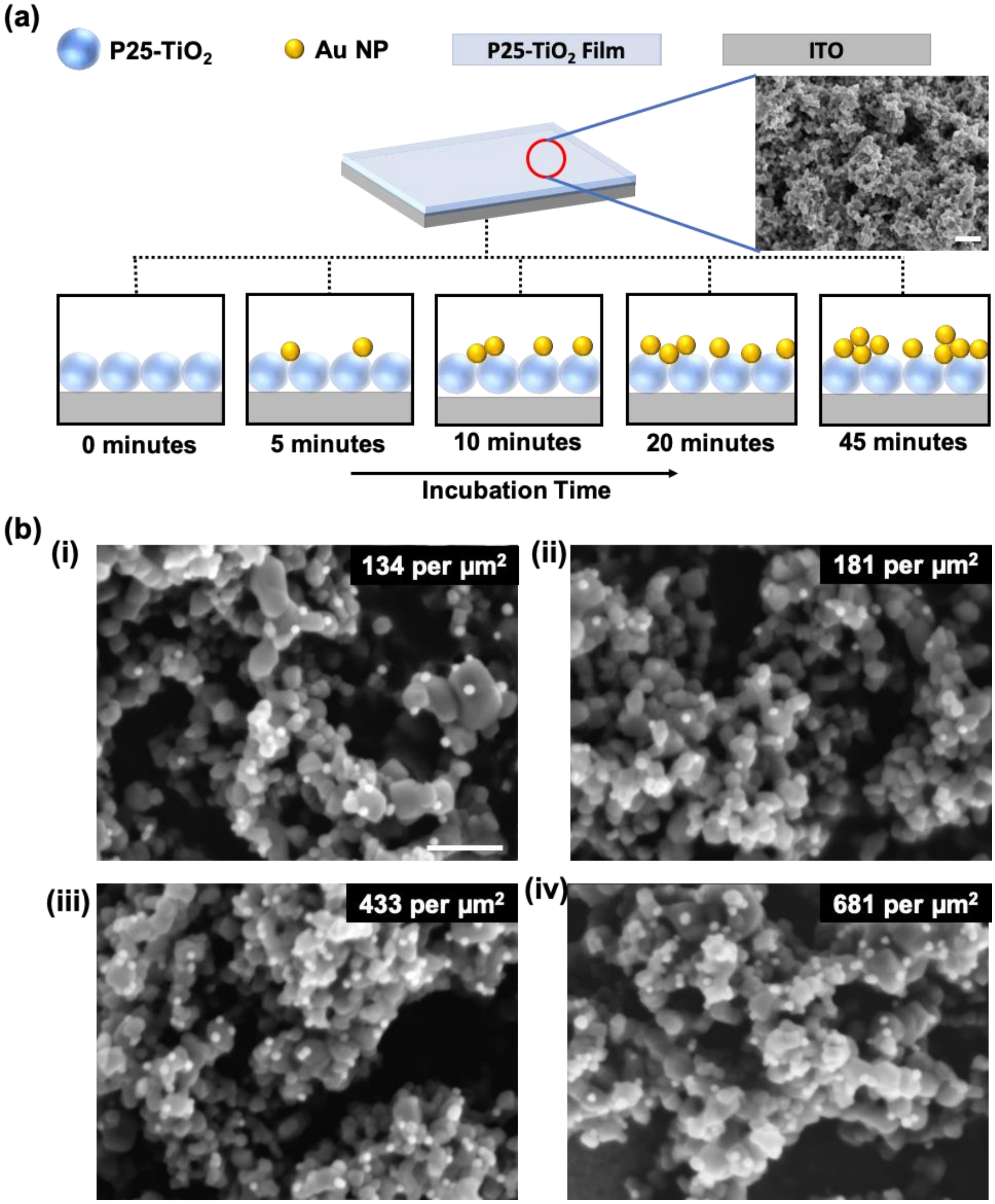

Figure 4-1: Development of the TiO_2-AuNP photoelectrodes. (a) Schematic diagram illustrating the Au NP deposition on P25-TiO_2 films by varying the deposition time from 5 minutes to 45 minutes with SEM image of the TiO_2 electrodes (scale bar represents 200nm); (b) SEM image of the Au NP-deposited P25-TiO_2 electrodes for the deposition times of (i) 5min, (ii) 10min, (iii) 20min, (iv) 45min (scale bar represents 100 nm). The density of Au NPs is shown at the top-right corner of each SEM image.

In this study, we investigated the PEC performance of the TiO_2/Au system under two wavelengths: 540 nm and 397 nm (Figure 4-2). TiO_2 NPs have limited optical response and PEC current generation capability at 540 nm; however, Au NPs have strong absorption at this wavelength due to LSPR (Figure 4-2a)[2], through which *intraband* carriers are generated.[92] The plasmon peak of Au in water occurs at approximately 525 nm (Figure 4-2a). However, as TiO_2 shifts the plasmon peak of gold,[348] a 540 nm excitation source was used in this work. At 397 nm, TiO_2 NPs absorb light and generate electron-hole pairs; while *interband* hot carriers are generated in the Au NPs.[349,350] As a result, the 397 nm illumination is expected to generate charge carriers in both TiO_2 and Au NPs, whereas the 540 nm excitation is expected to only generate plasmonic hot carriers in Au NPs, which would be subsequently injected as hot electrons into the conduction band of the TiO_2 NPs.[351] We hypothesized the optimal surface concentration of Au NPs in TiO_2/Au electrodes for PEC current generation to be wavelength dependent because of the strong wavelength dependence of the optical properties of the two materials.

The photocurrents of the TiO_2/Au electrodes, with various surface concentrations of Au NPs, were measured under UV (397 nm) and visible (540 nm) illumination (Figure 4-2b), and the percentage change in photocurrent (ΔI) from the baseline photoelectrode (TiO_2 without Au NPs) was plotted for every deposition time (Figure 4-2c). Striking differences are observed in ΔI values and trends between UV and visible light excitation. For visible light excitation, ΔI increased steadily due to the increase in the Au NP deposition time; However, under UV illumination, ΔI decreased starting at 5 minutes with negative values starting at 20 minutes. This indicates that, under UV illumination, increasing the Au NP surface concentration initially increases the photocurrent; however, beyond a certain surface concentration (between 10-20 minutes), it decreases the photocurrent below the baseline level.

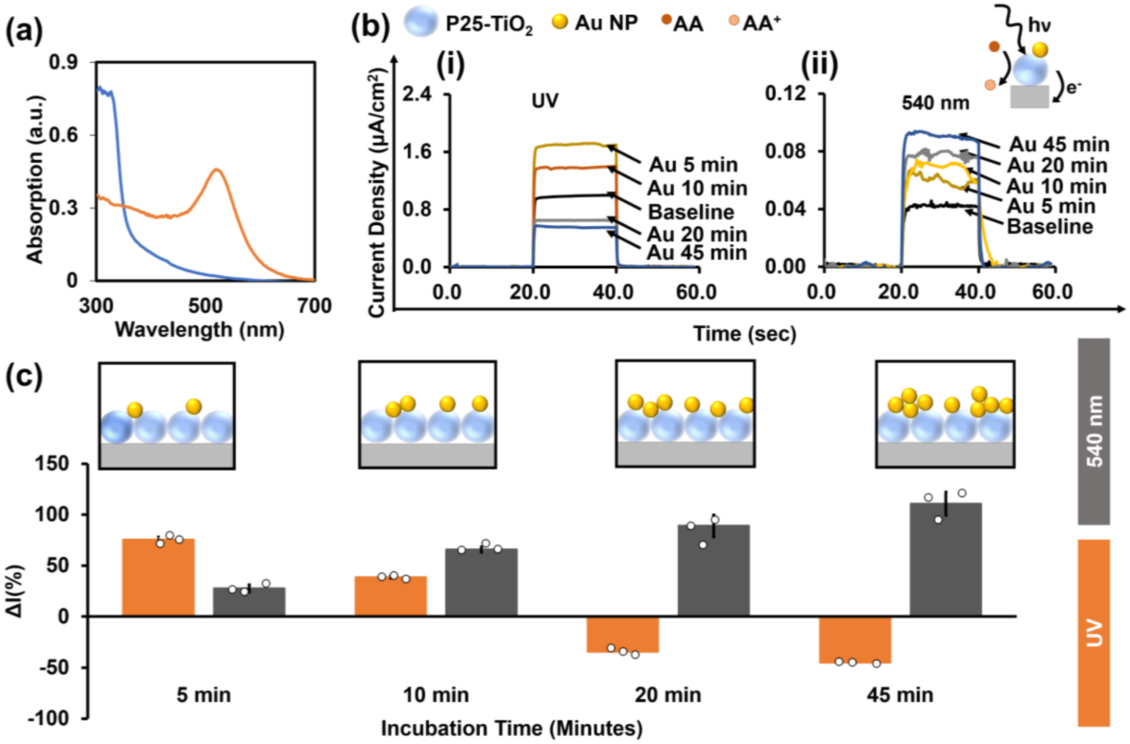

Figure 4-2 : Photoelectrochemical characterization of the TiO_2-AuNP photoelectrodes. (a) Absorption spectrum of TiO_2 NPs and Au NPs (b) Representative PEC curves of the photoelectrode obtained using chopped light chronoamperometry at 0 V bias versus Ag/AgCl at excitation wavelength of (i) 397 nm and (ii) 540 nm. (c) Bar plots summarizing the percentage change in photocurrents of the P25-TiO_2 electrodes following the immersion in Au NP solution. Error bars represent one standard deviation, with experiments performed using at least three separate electrodes.

We also measured the IPCE spectra of the baseline and TiO_2/Au electrodes (Figure 4-3a). As demonstrated in the PEC measurements, for UV excitation (wavelengths below 450 nm), the IPCE increased from the baseline for the 5-minute Au NP deposition; however, it decreased (from 350-480 nm) with further increases in Au NP deposition times. In contrast, a peak appears in the IPCE spectra at 540 nm which increases from the baseline up until the 45-minute Au NP deposition time.

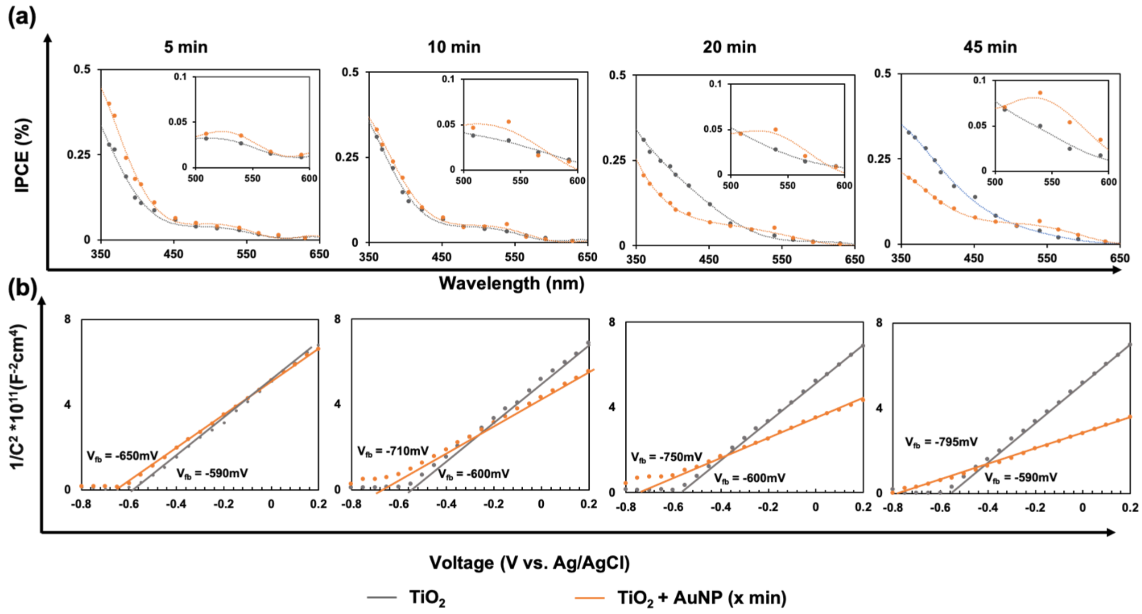

Figure 4-3 : Understanding the mechanisms of photocurrent modulation in the TiO_2-AuNP photoelectrodes. (a) IPCE spectrum of the photoanodes before and after Au NP deposition (inset shows zoomed in spectrum from 500nm to 600nm). (b) Mott-Schottky ($1/C^2$ vs. voltage) diagram for the photoanodes before and after AuNP deposition.

The negative shift in the flat-band potential from the base line value is measured as 60 mV, 110 mV, 150 mV and 205 mV for the 5, 10, 20 and 45-minute Au NP deposition time, respectively (Figure 4-3b). The flat-band potential becomes more negative with the increase in the Au NP density on the electrode. This is expected as the Fermi level of Au lies below the conduction band of TiO_2[352] and the shift of the flat-band potential is the direct consequence of Fermi-level equilibration.[353,354] The negative shift in the flat band potential after the addition of Au NPs to TiO_2 is associated with improved charge separation[339] and reduced charge recombination in the electrode.[346,355] Improved charge separation upon light illumination, through photocharging, enhances AA oxidation, augmenting photocurrent generation.[348,356] Furthermore, the positive slope of the M-S curve indicates that the photoelectrode is n-type.[93] The slope decreases with the addition of Au NPs, which also indicates a higher charge carrier density in the photoanode as the slope of the linear region of the M-S plot is inversely proportional to the electron density of the electrode (Table S4-1).[357] This was further confirmed by measuring the charge transfer resistance of the electrodes using EIS (Table S4-1), which showed a lower charge transfer resistance at a higher Au NP surface density (Figure S4-2).

We hypothesize the differences in the trends observed here under UV and visible light to be related to the different mechanisms for current generation under these light excitations. At 397 nm, both TiO_2 and Au NPs are excited. Electron-hole pairs are generated in the TiO_2, whereas hot electrons and hot holes are induced in Au NPs (d-sp transition). Electrons from the conduction band of TiO_2 move to the Au NPs, which improves charge separation efficiency (Figure 4-4a). However, interband transition in AuNPs is also known to generate highly energetic hot holes and hot electrons that are also capable of taking part in redox reactions.[283,322,358] These hot holes, generated at the surface of Au NPs, can directly oxidize AA in conjunction with the holes generated in the underlying TiO_2 matrix upon UV excitation (Figure 4-4a).[339,350] Interband hot electrons may also possess sufficient energy to overcome the Schottky barrier at the TiO_2/Au interface, causing electrons to move from the Au NPs to TiO_2.[359] This phenomenon can also be responsible for increasing the anodic current generated and collected at the working electrode.

Both abovementioned charge transfer mechanisms would increase the PEC current in the UV regime with an increase in the surface density of Au NPs. In the light of this, what are the mechanisms responsible for the signal decrease observed here? To answer this question, we consider that the loading of Au NPs at the TiO_2 surface also influences the absorption and scattering of the incident light.[360,361] Au NPs can hinder the photoexcitation of the underlying TiO_2 in areas of high Au NP loading.[339] Additionally, the presence of Au NPs on the TiO_2 surface limits the direct access of TiO_2 to the electrolyte, potentially attenuating photocurrent generation.[360] While the direct charge transfer mechanisms discussed above, photocharging and hot electron transfer, both increase the generated photocurrent, the reduced access to light and electrolyte decreases the photocurrent generated by TiO_2. As a result, these enhancement and loss effects become competitive with a delicate optimum occurring at low Au NP concentrations. At lower Au NP loadings (incubation times < 20 minutes), the influence of charge transfer is dominant, yielding enhanced photocurrents while at higher loadings a higher prevalence of loss mechanisms yields to decreasing photocurrents. This is in accordance with prior studies that demonstrate for TiO_2/Au interfaces under UV excitation, enhancement of photocurrent is obtained at only very small amounts of AuNPs.[359,362,363] It should be noted that Increased light absorption and scattering can also enhance the local electric field surrounding Au NPs, which can in turn increase the photocurrent generated by TiO_2.[333,364] However, this becomes negligible for small Au NPs (diameter < 30nm) at UV excitation.[365] For TiO_2/Au systems, Au NPs can also transfer their absorbed energy to TiO_2 via plasmon-induced resonance energy transfer (PIRET)), which is only evident when the Au NPs are excited at their LSPR wavelengths.[365]

Interestingly, under the 540 nm illumination, the photocurrent increases with the increase of Au NP surface density on the electrode. Au NPs exhibit strong absorption under 540 nm excitation due to their LSPR properties and generate hot electron-hole pairs through *Landau damping*.[366] These hot carriers lose their energy through electron-electron scattering on time scales of less than 100 fs.[366] It is important to have high density of electron-accepting states in the semiconductor in order to transfer these hot electrons into the conduction band of semiconducting nanoparticles. TiO_2 has a large density of states in the conduction band, and exhibits efficient coupling with Au NPs.[367] Due to this efficient coupling, the plasmonic excitation of Au NPs (540nm) exhibits steadily increasing photocurrent with increasing Au NP concentration (Figure 4-2b,c). Moreover, exciting AuNPs at the plasmonic wavelength significantly increases the electric field in their surrounding region (Figure 4-4b),[364] which can enhance the photocurrent by energy transfer to TiO_2 via PIRET.[368]

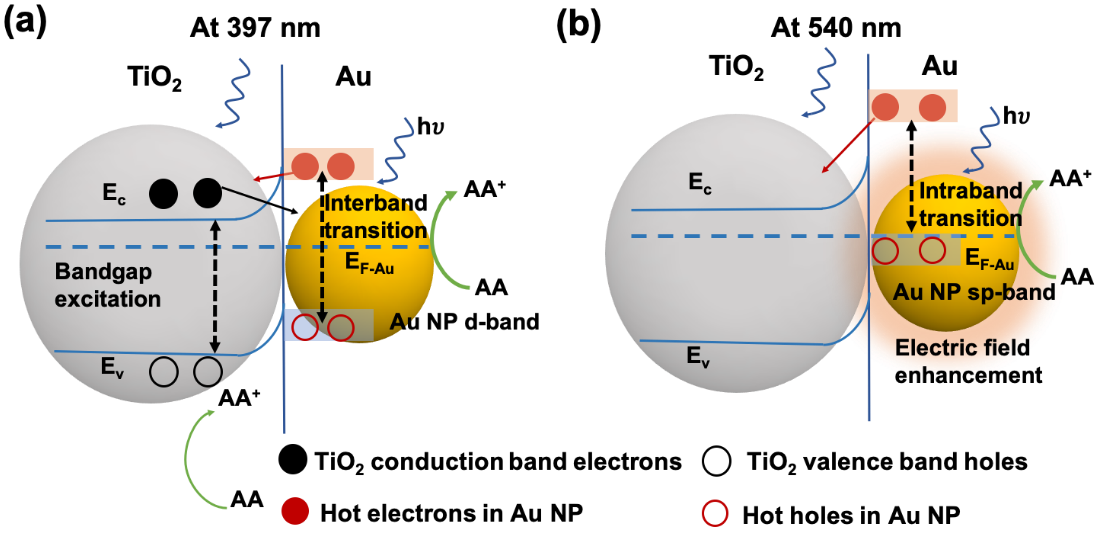

Figure 4-4 : Schematic drawing showing the mechanisms of Au-TiO_2 interaction at UV (a) and visible (b) light excitation.

As the photocurrent generation mechanism differs for the two excitation energies used here, we probed whether this effect could be utilized to design a DNA detection assay where an analyte will be able to provide both *signal-off* and *signal-on* response on the same electrode. Although TiO_2/Au electrodes have been used in biomolecular detection,[214,369] there is no report of obtaining both signal-on and signal-off response on a single electrode for these systems. Both baseline TiO_2 and TiO_2/Au (20 min) electrodes were used to examine the wavelength-dependent photocurrent modulation. Au NP-labeled DNA was used as a target that hybridizes capture probes immobilized at the electrode surface (Figure 4-5). Due to the differences in the length of probe (15-mer) and target (25-mer) DNA strands, target hybridization is anticipated to bring the Au NP label present at the single stranded end of the target to the vicinity of the electrode surface (Figure 4-5a(i)), effectively increasing the concentration of Au NPs on the electrode.[340] We expect a *signal-on* response for the baseline electrodes for both excitation wavelengths (Figure 4-5a(i)) and a combination of *signal-off* (at 397 nm) and *signal-on* (at 540 nm) responses for the TiO_2/Au electrodes (Figure 4-5b(i)) as DNA binding is hypothesized to increase the AuNP concentration beyond the threshold loading level after which a signal loss would be expected for UV excitation.

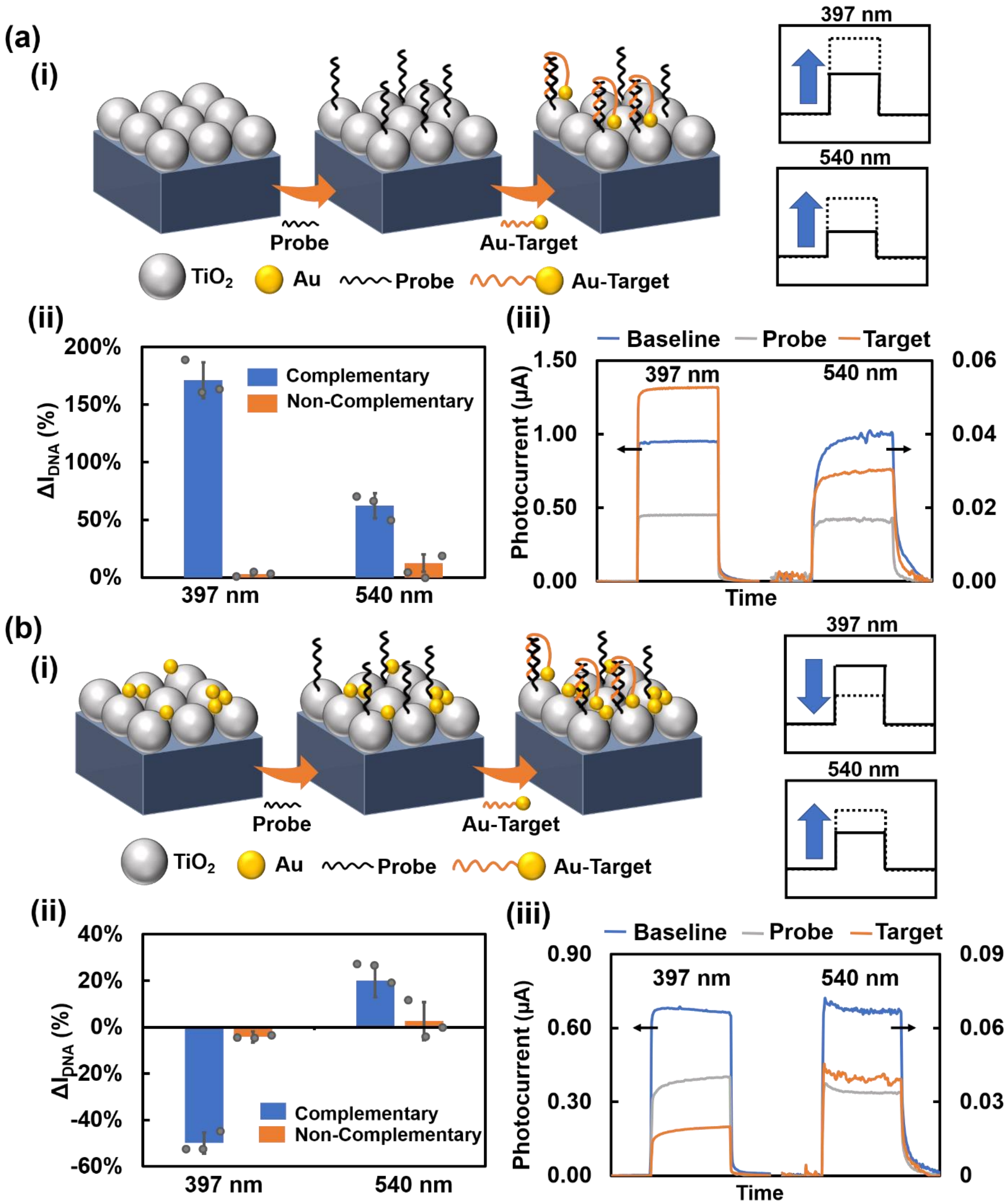

Figure 4-5: DNA detection assay built on the interactions between Au and TiO_2 NPs (a) DNA detection assay on baseline TiO_2 electrode. (i) Schematic illustration of the assay design. (ii) Percentage change in PEC current showing *signal-on* response for UV and visible light excitation. (iii) Representative PEC graphs obtained on the baseline TiO_2 electrode. (b) DNA detection assay on TiO_2/Au electrode. (i) Schematic demonstration of the assay design. (ii) Percentage change of PEC current for showing *signal-off* response for UV and *signal-on* response for visible light excitation. (iii) Representative PEC graphs obtained on the

TiO_2/Au electrodes. Photocurrent measurements were performed at a bias voltage of 0 V vs. Ag/AgCl and 0.1 M PBS with 0.1 M ascorbic acid was used as the supporting electrolyte. Error bars represent one standard deviation from the mean for the PEC measurements performed with at least three separate devices.

As excepted, target binding on the baseline electrode increased the PEC current for both UV (171%) and visible (61%) light excitations (Figure 4-5a(ii)). In contrast, a 50% decrease and a 20% increase in PEC currents were exhibited by the TiO_2/Au electrode following target binding (Figure 4-5b(ii)) for the UV and visible excitations, respectively. The concentration of Au NP labeled target DNA bound by surface immobilized probe DNA dictates the amount of Au NPs anchored at each electrode. The low concentration (1 pM) of target DNA utilized here is anticipated to increase Au loading by a small amount following hybridization. As the TiO_2/Au electrode contains Au NPs prior to the introduction of DNA target, it exhibits a markedly different behavior as that of the baseline electrode. A *signal-off* response is yielded under the UV regime while a signal-on response is yielded under visible light excitation. The introduction of additional Au NPs via target hybridization disrupts the delicate optimum of Au loading on the TiO_2/Au electrode, triggering loss effects (reduced access to light and electrolyte) to dominate enhancement mechanisms (photocharging and hot electron transfer) at the UV regime. Conversely, under visible light illumination, increased electric field effects (PIRET) stemming from enhanced Au loading augments the resultant PEC current. It should be noted that the absolute value of the percentage changes of photocurrent, following target hybridization, at both UV and visible light illumination is significantly lower in case of TiO_2/Au electrodes as compared to baseline TiO_2. Increased concentration of Au NPs at the TiO_2/Au electrodes beyond a certain threshold have been shown to introduce recombination centers, thereby reducing carrier lifetime.[370] Nevertheless, the TiO_2/Au electrodes provide different responses for the same DNA target (1 pM) on a single electrode, dynamically controlled by illumination wavelength (397nm and visible) alone. Obtaining both signal-on and signal-off responses for a single target has been shown to improve specificity, sensitivity and signal-to-noise ratio in biosensing.[340,371,372]

4.5 Conclusion

In this study, the distinct interaction mechanisms between Au NPs and TiO_2 NPs were probed under varied excitation regimes (397 nm and 540 nm) to understand the effect of Au NP density on PEC current generation. SEM micrographs demonstrated a rise in Au NP loading (134, 181, 433 and 623 per μm^2) on P25-TiO_2 photoelectrodes with increasing deposition time (5, 10, 20 and 45 min). Negative shifts in flat-band potential, as calculated from Mott Schottky measurements, indicated enhanced charge separation at greater Au NP surface concentrations, which has been linked to enhanced photocurrent generation [338]. Under UV illumination, increasing the surface loading of Au NPs initially increased the photocurrent; however, beyond a certain surface loading (between 10-20 minutes), it attenuated the photocurrent. In contrast, under visible light excitation, a steady increase in photocurrent was depicted upon increasing the surface loading of Au NPs. It was hypothesized that under UV illumination, Au NPs contribute to both current enhancement and current loss mechanisms. Current loss is possible due to the absorption and scattering of light by Au NPs, and the reduction of bandgap light absorption by TiO_2, which in turn reduces the photo-excited charge carriers participating in PEC oxidation reactions. Current enhancement was possible due to the direct charge transfer from TiO_2 to AuNPs through

Fermi level equilibration, and possibly due the transfer of hot interband carriers, generated under UV excitation, from AuNPs to TiO_2. Both of these mechanisms increase the photocurrent by increasing the concentration of photo-excited holes for participating in PEC oxidation of ascorbic acid. The loss and enhancement mechanisms can compete, and their extent can be controlled by the density of Au NPs on the electrode surface. Under visible light excitation, the light absorption of TiO_2 becomes negligible; however, intraband hot carriers are generated in Au NPs through *Landau damping. Hot* electrons are transferred to the conduction band of TiO_2, enabling hot holes to participate in oxidation reactions. These intraband carriers are the main driving force in generating the photocurrent in this wavelength regime.

The knowledge obtained from this study was used to design a DNA detection assay using TiO_2/Au electrodes where both signal-on and signal-off responses were achieved depending on the excitation light wavelength employed. Hybridization of an Au NP-labelled DNA strand on a TiO_2 photoelectrode caused a signal increase under visible illumination and a signal decrease under UV illumination. The ability to achieve both signal-on and signal-off behavior on a single photoelectrode can be exploited to enhance the limit-of-detection of biosensors by achieving differential or ratiometric signal processing possible through combining the two signal transduction modalities.

4.6 Acknowledgement

The authors acknowledge support from Natural Science and Engineering Council of Canada (NSERC) and the Ontario Early Researcher Award granted to L.S., as well as a salary award to L.S. from the Canada Chairs Program. Scanning electron microscopy was performed at the Canadian Centre for Electron Microscopy (CCEM), which is a national facility supported by NSERC and McMaster University. S.S. and A.V also receive NSERC doctoral scholarships.

4.7 Supplementary Information

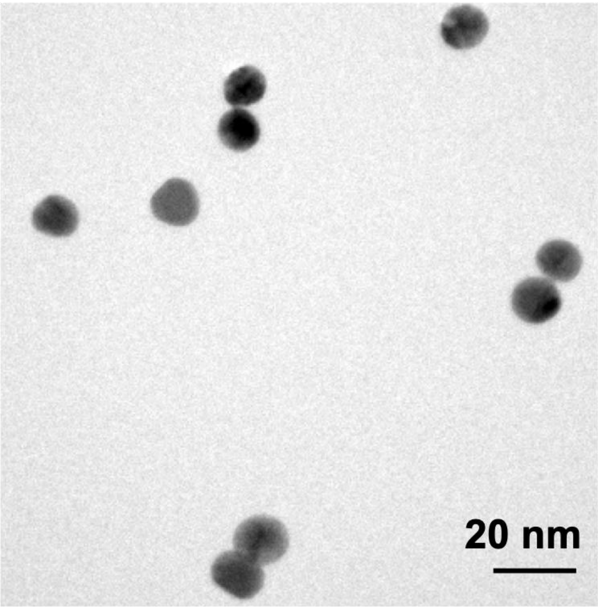

Figure S4-1: TEM image of Au nanoparticles

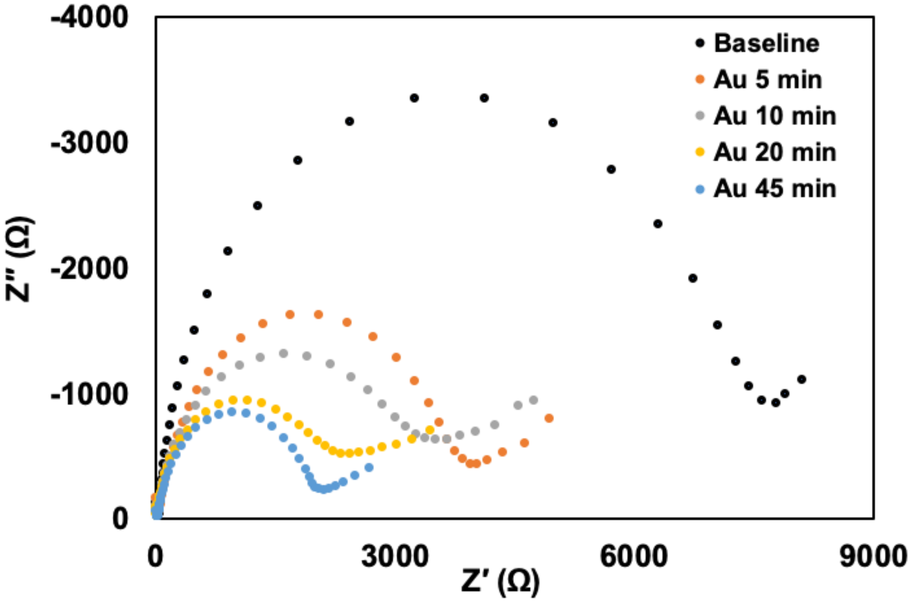

Figure S4-2: Nyquist plots for the photoelectrodes at open circuit voltage. The charge transfer resistance (R_{ct}) decreases as the amount of Au NP increases in the electrode.

Table S4-1: Charge-transfer resistance (R_{ct}), charge carrier density (N_d) and flat-band potential (V_{FB}) of the electrodes used in this work

Sample	**R_{ct} (kΩ)**	**N_d (cm^{-3})**	**V_{FB} (mV)**
TiO_2	8.5	0.99-1.062x10^{17}	-590 to -600
TiO_2-Au (5 min)	4.0	1.15 x10^{17}	-650
TiO_2-Au (10 min)	3.5	1.41 x10^{17}	-710
TiO_2-Au (20 min)	2.8	1.94 x10^{17}	-750
TiO_2-Au (45 min)	2.2	2.27 x10^{17}	-795

Chapter 5 Understanding the PEC response of Au NPs for potential use of biosensing

Chapter Introduction (Objective II)

In previous chapter (Chapter 4) we showed biosensor construction using Au NP modified TiO_2 electrodes. However, Au NPs are frequently functionalized with biomolecules for signal amplification in PEC biosensors.[89] In order to design PEC biosensors with biofunctionalized Au NPs, we need to study the role of Au NPs on the photocurrent generation efficiency without any semiconductor. In addition, achieving a PEC biosensing system using Au NPs as only photoactive material, will remove the dependency on semiconductive materials. Smaller Au NPs (< 25 nm) can generate both intraband (sp band) and interband (d to sp transition) hot carriers due to its quantum size effect.[93,351,373] In Chapter 4, we have demonstrated that these hot charge carriers can influence the PEC properties of the surrounding semiconducting NPs, which was further utilized to design bioassay. It was hypothesized that for TiO_2/Au system, hot holes from Au NPs take part directly in the oxidation reaction under visible light excitation, whereas at the UV excitation, both photocharging effect and hot charge carrier transfer can contribute to enhancing the photocurrent. Additionally, Wang et al. reported direct plasmon accelerated oxidation of glucose under visible light excitation at 532 nm.[374] However, Govorov *et al.* predicted that interband hot holes might be more efficient in oxidation reactions than intraband hot holes.[375–377] Therefore, we sought to investigate the following, “If interband hot carriers can be used directly in the oxidation reaction, what would be the comparative power conversion efficiency between interband and intraband excitation?”

In this section, we have optimized the photoelectrode fabrication by varying the size and Au NP deposition time. The photocurrent generation efficiency was compared between interband and intraband excitation using chopped light voltammetry and IPCE. The optimized electrodes were further used in direct methanol fuel cell applications. Interestingly interband excitation showed higher methanol oxidation efficiency as compared to when excited at the LSPR wavelength. This new knowledge can be used to effectively determine the optimal excitation wavelength and Au NP size while designing PEC devices that use Au NPs.

Authors: Sudip Saha, Jie Yang, S. Shayan Mousavi Masouleh, G. A. Botton and Leyla Soleymani

Publication: To be submitted in 2021.

5.1 Abstract

Optically excited gold (Au) nanoparticles generate plasmon oscillation which is able to generate hot charge carriers by non-radiative decay. These hot charge carriers are often used by researchers to improve the energy conversion efficiency of different photochemical and photoelectrochemical reactions. Depending on the mode of excitation wavelength (i.e., interband and intraband), the energy of hot electrons and hot holes might vary significantly. Although, both interband and intraband hot carriers were used separately for photoelectrochemical reactions, a direct comparison between these two types of hot carriers is still lacking. Herein, we compared the hot hole mediated photocurrent generation efficiencies by Au nanoparticles deposited on screen printed carbon electrodes when excited at 405 nm and 532 nm wavelengths that correspond to interband and intraband

excitation, respectively. Oxidation of ascorbic acid was used as a model reaction system due to its strong hole scavenging properties. Interband excitations showed higher anodic photocurrent than the photocurrent achieved from intraband excitation. The efficiency of photocurrent generation was found to be dependent on the surface distribution of Au nanoparticles. The size and amount of Au NPs were optimized by measuring the anodic photocurrent and comparing among them. Reducing Au nanoparticle's size from 25 nm to 12 nm enhanced the photocurrent whereas further reducing the size decreases the photocurrent. Aggregation of Au nanoparticles also decreased photocurrent as the generation rate of high energy carriers decreased with the size. The optimized electrodes were further used to evaluate methanol electrooxidation performance under illumination with both interband and intraband excitations. An anodic peak current density of 56 µA/µg was achieved when interband carriers are excited which is ~30% higher than the current achieved with intraband excitation (43 µA/µg).

5.2 Introduction

Plasmonic metal nanoparticles (NPs) (e.g., Au, Ag, Al, Cu) have received significant interest in the field of photocatalysis and photoelectrocatalysis[378] due to their strong light absorbance[92,375] and heterogeneous catalytic properties.[374,379] One important advantage of using plasmonic NPS over semiconducting NPs is that their optical and electronic properties can be precisely tuned over a wide range of values (i.e., Absorption peak from UV to infrared, single/multiple absorption peaks, electrical conductivity) by controlling their size, shape, and surrounding environment.[380–382] The interaction of light with the conduction band electrons of these materials can generate coherent oscillations of plasmons, which is known as localized surface plasmon resonance (LSPR).[383] Decay of plasmons can follow either radiative pathway through photon emission[384] or non-radiative pathways via electron-phonon scattering,[377,383] which leads to dissipate heat or *Landau damping* and thereby, generates hot electrons and holes.[92,93,375,380,383,385] These hot carriers are named as such since they have higher energy than the thermal energy at ambient temperatures.[386]

The generation of hot charge carriers is considered as the quantum effect of electron scattering near the nanoparticle surface.[375] These carriers have been used to improve the performance of photovoltaic,[387] photocatalytic,[388] photoelectrochemical,[340] and optoelectronic[389] devices. However, utilizing hot carriers remains challenging due to their short relaxation lifetimes (~100 fs - 1 ps)[93,390] as it is difficult for these carriers to participate in the charge-transfer reactions before recombination.

Despite the short lifetime, charge transfer can occur from the surface of metal NPs to the chemicals adsorbed on the surface or in the solution, if electron or hole accepting levels are present in the surrounding media of metal NPs. Additionally, longer hot carrier lifetime can be obtained at the electrochemical interface[358] if the electrolyte contains strong electron or hole scavengers that are appropriate, in terms of the energy states alignment in Au NPs and the redox moieties, for the specific plasmonic NPs in use. This strategy could be used to directly drive redox reactions, such as glucose oxidiation,[374] by optical excitation of plasmonic NPs.[391] Direct utilization of the hot carriers in redox reactions also allows avoiding the use of semiconductor and thereby the Schottky interface, which has lower efficiency of change injection due to the momentum mismatch between hot carriers and empty energy states in the semiconductor.[93]

Among the different types of plasmonic NPs, Au NPs are of particular interest due to their facile fabrication, ease of surface modification, biocompatibility, and stability.[95,363,374] Additionally, Au NPs exhibit strong plasmonic response at visible light wavelengths and interband excitation from near UV to UV light excitations, thereby covering a wide wavelength range.[392] Hot carriers from Au NP have shown to directly take part or improve the rate of photocatalysis[389,393] and redox reactions.[93] Mukherjee *et al*. showed that hot electrons generated by LSPR excitation can transfer into surface adsorbed hydrogen molecules and thereby dissociate hydrogen at room temperature.[393] Hot holes were also shown to assist glucose oxidation under a suitable bias voltage.[374] The presence of hydroxyl ions (OH^-) in the solution can also scavenge hot holes at the Au NP surface, allowing the formation of hydroxyl radicals (•OH) which can diffuse easily in the and thereby oxidize other redox molecules present in the solution at a faster rate.[374]

It should be noted that in the majority of the abovementioned studies, where direct hot carrier transfer from AuNPs to the solution was used to drive redox reactions, Au NPs were excited at the LSPR frequency inducing intraband carriers. Although Govorov *et al.* have emphasized the potential of using interband hot carriers for generating photocurrent in theory,[394] there are a handful of studies in which interband hot carriers (d band to sp band of Au) have been used experimentally to drive redox reactions. Barman *et al.* demonstrated photocurrent generation by interband hot holes using polyaniline-gold (PAni-Au) nanostructures.[395] PAni-Au nanostructures acted as a transport layer between an Indium-tin-oxide (ITO) anode and an Aluminium cathode. Recently, Guo *et al.* demonstrated the use of interband hot holes to fabricate Au nanostars by enabling site-selective oxidative etching of Au^0 in the presence of iodide.[94] If the plasmon energies are above the interband transition energy, the majority of the hot carriers will be hot holes whose energies lie in the metal d-band and the hot electrons are located just above the Fermi level.[390] Interband hot holes have higher energy than the hot holes generated by the LSPR excitation (intraband hot holes)[375,395], making them act as strong oxidants as they facilitate electron transfer from HOMO levels of the electrolyte to the Au NP.[358]

The computational study of plasmon decay indicates that interband hot holes are more effective than intraband hot holes at participating in redox reactions when Au NPs are used.[394,396] In another theoretical study, it has been found that the interband hot carriers have a longer lifetime than intraband hot carriers.[356] Schlather *et al.* used the interband hot holes to drive the oxidation reaction of citrate ions under optical illumination using $Au@SiO_2@Au$ nanostructure.[358] The experimental results lead to the conclusion that the d-band holes are more effective in carrying out an oxidation reaction than intraband hot holes. However, to date, there are no studies where interband carriers are used to directly drive electrochemical using Au NPs on the photoelectrode. Therefore, we sought to answer the following question: Can interband hot holes directly and without the incorporation of any semiconductor, participate in oxidation reactions, and if so, is the efficiency of the reaction higher than oxidation by intraband hot holes?

Herein, we use interband or intraband hot carriers to drive a single redox reaction using Au NP photoelectrodes, comparing the photocurrent generation efficiency of each excitation mode. We report and compare the anodic photocurrent generated directly from Au NPs - without using another photoactive material (i.e., semiconductors) - of various sizes (5-25 nm) through interband and intraband hot carriers, indicating that it is indeed possible to harness the hot carriers obtained from plasmon decay to drive redox reactions. Furthermore, the concentration and distribution of Au NPs on the electrode was varied to assess the effect on the photocurrent generation. Incident-photon-to-current conversion efficiency (IPCE) measurement was used to investigate the excitation energy dependent photocurrent generation efficiency. Additionally, oxidation activity of Au NPs was compared by using the optimized electrode in direct methanol fuel cells at different excitation modes (i.e., interband and intraband) demonstrating the potential of Au NPs to be used this application. A comparison of anodic photocurrent was also performed for the oxidation of methanol, ethanol, glucose, and ethylene glycol to probe if the higher interband photocurrent is a characteristic phenomenon of small Au NPs.

5.3 Materials and Methods

Materials and Reagents: Screen-printed carbon electrodes (3 mm diameter) were purchased from CH instruments. Phosphate buffer solution (PBS, 1.0M, pH 7.4), L-ascorbic acid (99%), sodium chloride (NaCl), 3-aminopropyl triethoxysilane (APTES), Potassium chloride (KCl), Hydrogen tetrachloroaurate (III) trihydrate ($HAuCl_4.3H_2O$, > 99%), Potassium ferrocyanide ($K_4Fe(CN)_6$), Potassium ferricyanide ($K_3Fe(CN)_6$), Hydrogen chloride (HCl), poly(diallydimethylammonium chloride) (PDDA) and were purchased from Sigma-Aldrich. Au nanoparticle with diameters of 5, 20, and 25 nm were also bought from Sigma-Aldrich. All the gold nanoparticles used in this work were citrate stabilized. Methanol and Ethanol were purchased from commercial alcohols (Brampton, ON). Milli-Q grade (18.2 MΩ cm) de-ionized (DI) water was used for all solution preparation and washing steps. Citrate stabilized 12 nm gold nanoparticles were prepared using the protocol described by Grabar et al.[345]

Au NP Electrode preparation: Carbon electrodes were washed with ethanol and DI water by sonicating for 10 minutes. Cleaned electrodes were put under air plasma for 1 minute to introduce negatively charged hydroxyl group on the surface. After this step, they were immersed in APTES for 2 hours under constant stirring of the APTES solution. After that, the electrodes were cleaned thoroughly with DI water. The electrodes were immersed in 10 nM concentration of Au NP solution of different sizes for varying time.

Photoelectrochemical characterization: Photocurrent and Incident-light-to-photon-conversion efficiency (IPCE) measurements were performed in a three-electrode cell setup where Pt wire works as counter electrode and Ag/AgCl works as the reference electrode. Zahner CIMPS-QE/IPCE photo-electrochemical workstation was used for these measurements. For photocurrent comparison, 405 nm and 532 nm excitations were used. 405 nm Optical excitation was obtained by using a mounted LED from Thorlabs Inc. and 532 nm excitation was obtained by using an LED laser source. The intensity of each source was kept at 550 W/m^2 for comparing the photocurrent. 0.1 M ascorbic acid (AA) in 0.1 M PBS solution was used as electrolytes. Photocurrent and IPCE data were obtained under a bias voltage of 0 V vs. Ag/AgCl. IPCE measurement was obtained by using TLS03 LED light source (adjustable wavelength) from Zahner. IPCE is calculated from the following formula:

$$\mathrm{IPCE}(\%) = \frac{1240 \times \mathrm{I}(\mathrm{A/cm^2})}{\lambda(\mathrm{nm}) \times \mathrm{P_{inc}}(\mathrm{W/cm^2})} \times 100$$

Where, I is the measured photocurrent at each wavelength, λ is the incident wavelength of light source and P_{inc} is the incident light power.[346]

Electrochemical Characterization: Room temperature (RT) electrochemical impedance spectroscopy (EIS) measurements were performed at open-circuit potential by using Zahner potentiostat. The electrolyte used for the EIS measurements contained 2 mM ferri/ferrocyanide in 10 mM PBS. The excitation amplitude was 5mV and the frequency range used was 100 kHz to 0.1 Hz. The electrochemically active surface area was determined by performing a CV scan in 0.1M H_2SO_4 at a scan rate of 0.05V/s and a voltage range between 0V and 1.5V.

Scanning Electron Microscopy (SEM) and Transmission Electron Microscopy (TEM): Distribution of Au NPs on the electrode surface was visualized by using FEI Magellan 400 scanning electron microscope (SEM). TEM images were captured by using JEOL 2010F, which is in the Canadian Center of Electron Microscopy (CCEM).

Determination of Au NP size distribution: The size of the particles was measured by using the TEM micrographs. The sizes were measured by using ImageJ. At least 10 different areas and 100 particles were measured for each sample. The size-distribution graph was plotted by using OriginPro software.

Absorption spectroscopy: Infinite M200 pro (Tecan) plate reader was used to collect UV-Visible (UV-VIS) absorption spectroscopy from the Au NP solution.

Determination of the Au mass in the electrode: The total mass of Au on the electrode was measured by Inductively coupled plasma mass spectroscopy (ICP-MS) using Varian Vista Pro, which is located in the McMaster Steel Research Centre.

5.4 Results and Discussion

In order to prepare Au electrodes with structural tunability, all-solution-processing was used to assemble. Au NPs on screen-printed carbon electrodes. Carbon, instead of the commonly-used indium tin oxide electrodes, was used to avoid Schottky contact and achieve a higher collection efficiency for hot carriers.[374] Carbon electrodes were first plasma treated to remove organic contaminants and introduce negative surface charge (OH^-) on their surface. The electrodes were then immersed in an aminosilane solution (APTES) designed to interact with the carbon surface through the plasma induced OH^- groups (chemical reaction) and citrate-capped Au NPs via the amine ($-NH_2$) group (electrostatic reaction) (Figure 5-1a). Scanning electron microscope (SEM) image confirms the successful deposition of Au NPs on the electrodes (Figure 5-1a). The size distribution of the Au NPs were further measured using transmission electron microscopy (TEM) (Figure 5-1b and supplementary Figure S5-1).

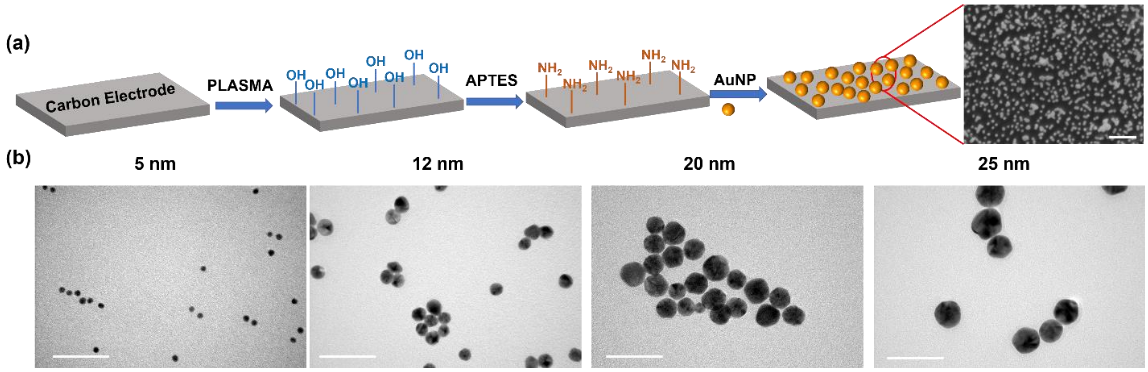

Figure 5-1: Construction of the Au NP-carbon electrode (a) Schematic illustration showing the electrode fabrication steps. SEM image of the prepared electrodes shows the successful deposition of Au NPs (Scale bar represents 100 nm). (b) TEM micrographs of Au NPs used in this work shows their size tunability (Scale bar represents 50 nm).

The absorption spectra for Au NPs with different sizes were measured using UV-VIS spectroscopy and normalized using the LSPR peak magnitude (Figure 5-2a). The LSPR peaks were positioned at 519, 521, 522 and 530 nm for Au NPs having sizes of 5, 12, 20 and 25 nm, respectively. As the Au NP size increased, the peak position was red-shifted and the full-width-at-half-maximum (FWHM) was decreased (Figure 5-2a). Both the redshift and peak narrowing have been associated to the quantum size effect for plasmonic NPs.[383,397] The imaginary part of the dielectric constant changes as particle size varies, which in turn causes the redshift for the larger nanoparticles.[398,399] The plasmon bandwidth for small Au NPs (diameter < 25 nm)[91] were calculated theoretically to be inversely proportional with the particle diameter.[400] In should also be noted that the absorption spectrum of the AuNPs was measured in water; therefore, it is expected that the plasmonic peak position would redshift on the carbon electrode due to its different dielectric constant compared to water[349]. Wang *et al.* reported an 8 nm redshift when Au NPs were deposited on glassy carbon electrodes in comparison to being suspended in DI water.[374] The relative contribution of interband absorption (below 480 nm)[401] in comparison to LSPR peak also increased with decreasing Au NP size (Figure 5-2a). This is in line with the previous studies on the optical properties of the Au NPs.[356,382] The anodic photocurrent generated by the photoelectrode was measured using ascorbic acid (AA) as a hole scavenger in the electrolyte. Interband excitation was achieved using a 405 nm light source and LSPR excitation was induced using a 532 nm light source. The photocurrent magnitude measured for interband excitation was higher than that measured for intraband excitation for all Au NPs (Figure 5-2b and Figure 5-2c).

An EIS analysis was performed to assess the light-induced effect on the charge transfer resistance (R_{ct}). Figure 5-2b showed the Nyquist plot of the electrodes using 12 nm Au NPs both in dark and under illumination (405 nm and 532 nm). Deposition of Au NP to the carbon electrode reduced R_{ct} from 4050 Ω to 390 Ω (Supplementary Figure S5-2), which confirms the superior conductivity attained over the SPCE. Based on the experimental data, an equivalent circuit composed of solution resistance (R_s), R_{ct}, constant phase element (CPE), and Warburg diffusion element (Z_w) is proposed (Figure 5-2b – inset). The magnitude of R_{ct} was determined from the diameter of the semicircle[402,403] and compared between dark and illuminated conditions. Illuminated electrodes – regardless of the excitation wavelength - showed significantly lower R_{ct} (100 Ω) than the electrode in dark (390 Ω). However, EIS curves for both interband and intraband excitation are very similar (Supplementary Table S5-1). It should be noted that the EIS was performed under open circuit potential with small perturbation (2 mV). Therefore, the reduction of R_{ct} indicates charge carrier accumulation at the electrode/electrolyte interface as hot carriers were not extracted at the electrode contact by external electric field, which is the case for photocurrent measurement.[403,404] This result demonstrated that the differences in anodic photocurrent generation in different excitation wavelengths are not related to the number of charge accumulated at Au NP surface.

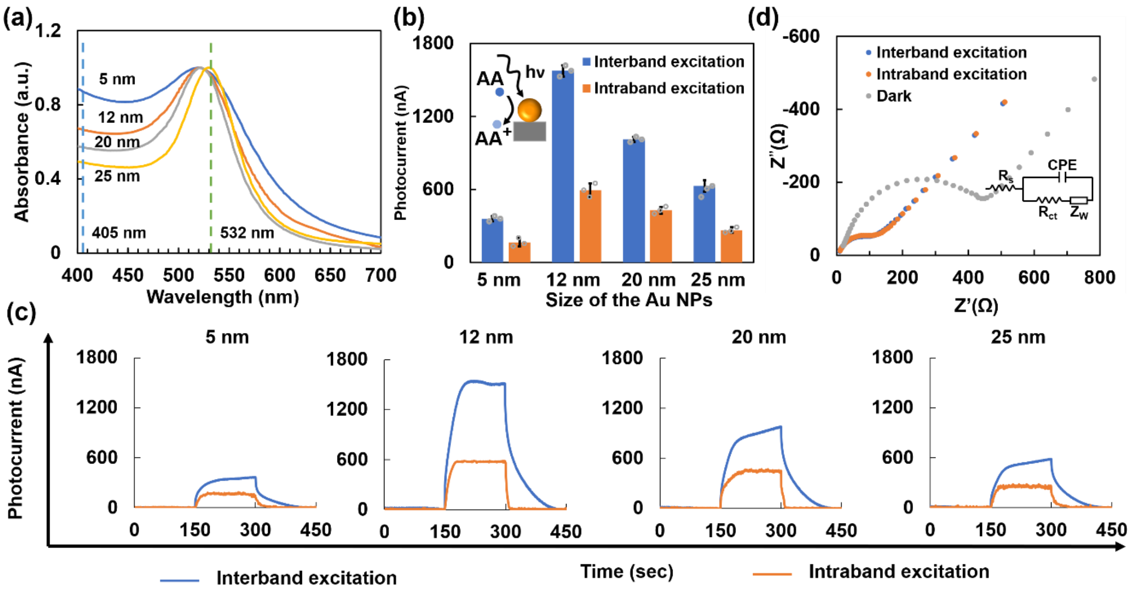

Figure 5-2: Characterization of the Au NP electrodes prepared by using different Au NP sizes (a) Absorption Spectroscopy of different size of Au NPs used in this work (dotted line indicated the excitation wavelengths used in this work); (b) Average PEC current (baseline corrected) for different size of Au NPs. Error bars represent 1 standard deviation. Inset shows the schematics representing ascorbic acid oxidation by Au NP upon light illumination. (c) Respective photocurrent spectra for different size of Au NPs. Optical illumination was turned on at 150s and turned off at 300s. All PEC measurements were performed by using 0.1 M ascorbic acid in 0.1 M PBS at a bias voltage of 0 V vs. Ag/AgCl. Electrodes were prepared using 2 hour Au NP deposition for this figure; (d) Electrochemical impedance spectroscopy measurement (EIS) showing reduction of charge transfer resistance when the electrode is illuminated. EIS was performed at open circuit potential using 2 mM $[Fe(CN)_6]^{3-/4-}$ in 0.01 M phosphate buffer (PBS) solution. Inset shows the equivalent circuit diagram used to obtain the parameters.

Additionally, the magnitude of the photocurrent increases as the Au NP size decreases from 25 nm to 12 nm for both interband and intraband excitations, while reducing the Au NP size from 12 nm to 5 nm results in photocurrent reduction. The higher photocurrent at interband excitation can be explained by examining the hot carrier distribution separately at two different excitation wavelengths. Under interband excitation, hot carriers are generated from the transition of electrons from the d-band to sp-band of Au NPs.[356,373] On the contrary, intraband excitation generates hot carriers by exciting electrons at the sp band.[405] Due to the different plasmon decay processes, interband excitation creates hot hole distribution at the d-band (maximum attainable energy is $E_f - hv$) and the hot electrons are closer to the Fermi level (E_f) of the electrode (Figure 5-3),[405] whereas, interband excitation generates hot holes that lie at the sp band and hot electrons can obtain the energy as high as $E_F + h\nu$ (Figure 5-3). Therefore, interband hot holes have higher than intraband hot holes and intraband hot electrons have higher energy than interband hot electrons.

The initial increase of the photocurrent with decreasing Au NP size (from 25 nm to 12 nm) until reached to optimum value, and subsequent decrease of the photocurrent with further decreasing Au NP size (from 12 nm to 5 nm) can be attributed to the competition between two factors: (i) lifetime of the hot carriers increases with decreasing Au NP size,[358] and (ii) the number of initial hot carrier population increases with increasing Au NP size.[406,407] Representative photocurrent spectra showed that the photocurrent rise and decay are slower for the interband compared to the intraband excitation (Figure 5-2d), which is in line with previous studies.[358,393]

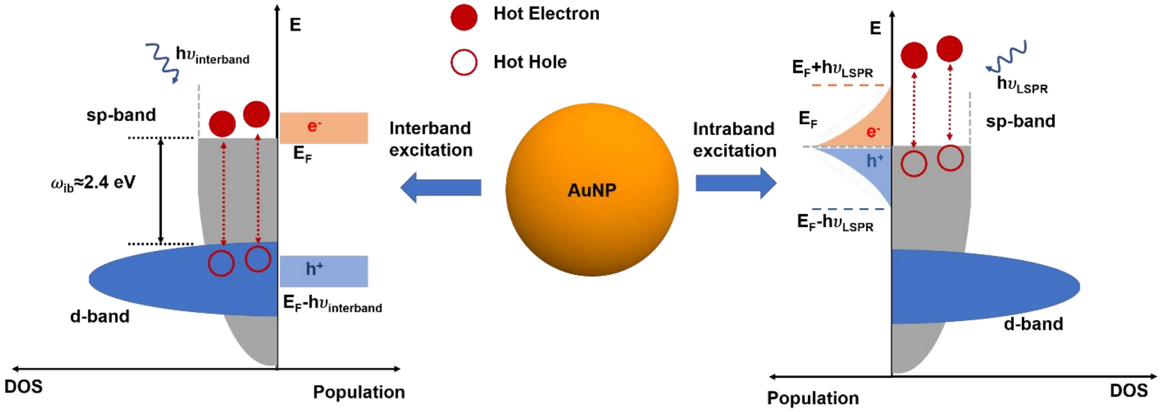

Figure 5-3: Schematic diagram showing the interband and intraband hot carrier generation and their energy distribution.

To confirm that the photocurrent obtained here is due to the participation of hot carriers from Au NPs, we measured photocurrent spectra using carbon electrodes without any Au NP. Carbon electrodes showed no photocurrent at 532 nm excitation (intraband for Au NP) and minimal photocurrent (~1.6 nA) at 405 nm (interband for Au NP) (Supplementary Figure S5-3). Thus, we expect the photocurrent to be generated through the oxidation of AA using Au NP hot holes (Figure 5-2c – inset). To further demonstrate that the anodic photocurrent measured in this work is generated due to the oxidation of AA, we measured photocurrent in the absence of AA in the electrolyte. The photocurrent obtained using only phosphate buffer (PBS) as the electrolyte is negligible (~15 nA for interband and ~0 for intraband excitation) in comparison to the photocurrent obtained when AA is in the solution (Supplementary Figure S5-4). Due to the higher energy of interband hot holes, they can transfer holes to AA with higher efficiency than intraband hot holes. This also explains why intraband excitation is usually used for photoelectrochemical applications reported earlier, as in those cases, hot electrons, instead of holes, were transferred from Au NPs to the electrolyte.[93,385,393]

We further varied the Au NP deposition time on the surface of carbon electrodes to investigate the effect of Au NP concentration on the hot hole-mediated photocurrent. We used 12 nm Au NPs because they produced the highest photocurrent amongst the NP sizes used in this work (Figure 5-2c). As the Au NP deposition time increased from 1 hr to 2 hr, the photocurrent increased for both interband and intraband excitations (Figure 5-4a and Figure 5-4b). however, the photocurrent decreased for both excitations when the deposition time increased from 2hr to 4hr. In order to investigate the relation between Au NP deposition time and photoelectrochemical activity, we measured the electrochemically-active surface area of each electrode, that increased from the 1 hr to the 4 hr deposition time (Supplementary Figure S5-5) and thereby explains the initial increase of photocurrent with deposition time (from 1 hr to 2 hr). However, the photocurrent decreased with further increasing the deposition time from 2 hr to 4 hr despite the increase in the electrochemically-active surface area. Increased active surface area confirms larger number of Au NPs deposited on the electrode with increasing deposition time. Incident photon to current conversion efficiency (IPCE) measurement further confirms the initial increase in photocurrent with deposition time (from 1 hr to 2 hr), followed by the decrease in photocurrent upon increasing the deposition time further (from 2 hr to 4 hr) (Figure 5-4c), for the wavelength range from 350 nm to 650 nm. IPCE data for both 1 hr and 2 hr sample showed a peak near 530 – 540 nm, which is related to the LSPR peak observed in the optical absorption spectrum. However, the peak disappears when the deposition time increased to 4 hr. In order to investigate the reasoning for peak disappearance, we examined the distribution of Au NPs on the electrode surface (Figure 5-4d). It should be noted that most of the Au NPs form clusters (or aggregate) for the sample with 4 hr deposition and thereby the effective size of the Au NPs increases. Additionally, as the Au NP size becomes larger, hot charge carrier’s energy will be lower and thereby, less photocurrent will be obtained.[394]

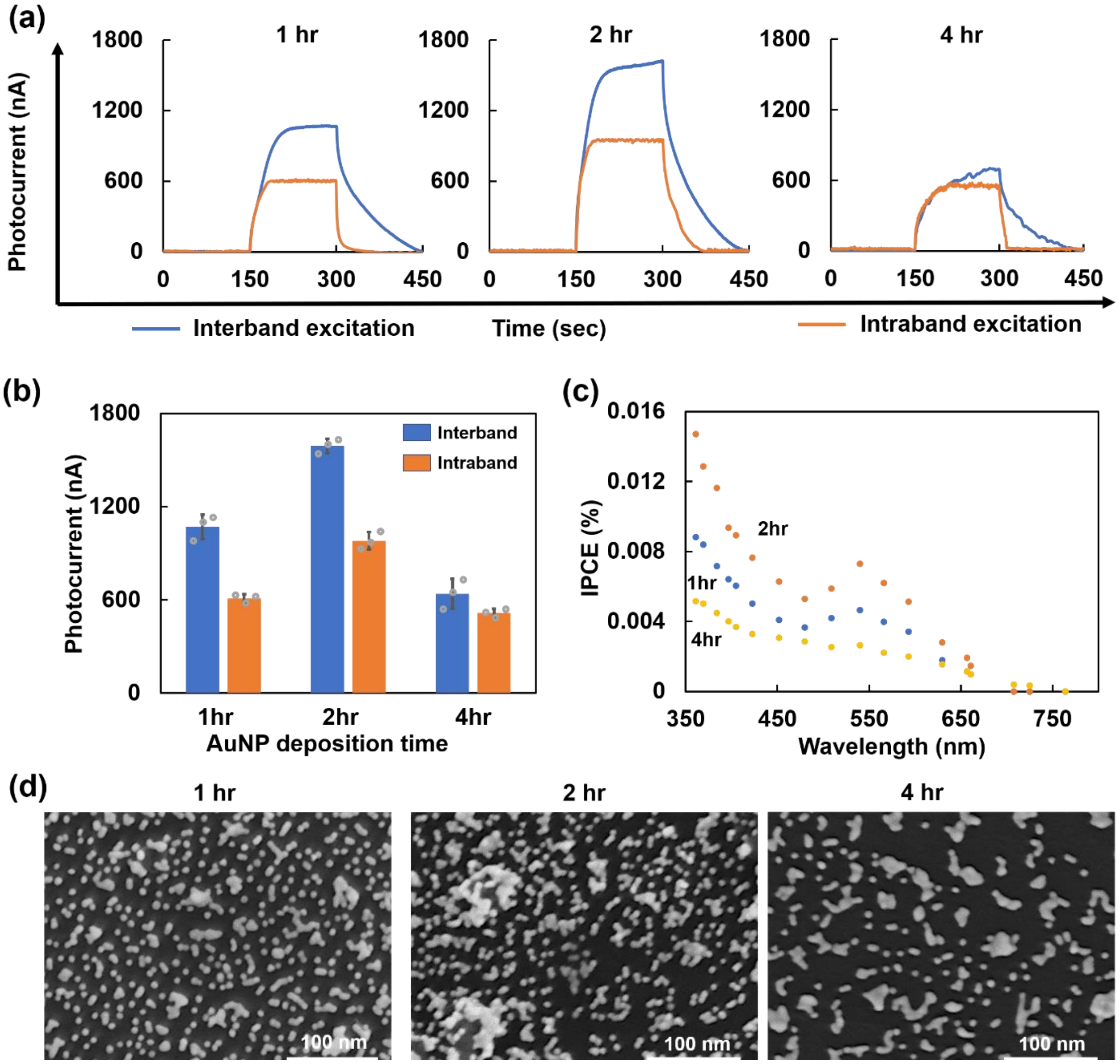

Figure 5-4: Optimization of Au NP deposition time on carbon electrode. (a) Respective photocurrent diagram for the different electrodes used for optimization; (b) Average photocurrent obtained for both interband and intraband excitation; (c) IPCE spectrum for the Au NP electrodes; (d) Scanning electron microscope image of the Au NP electrodes where the electrode was immersed for 1, 2 and 4 hr. All photocurrent measurements were obtained by applying 0 V bias vs. Ag/AgCl using 0.1 M AA in 0.1 M PBS as electrolyte.

The above study showed that the interband hot holes can behave as a stronger oxidant when a suitable electrolyte is used. Hence, it is expected that utilizing optical illumination enhances electrooxidation on AuNP-based photoelectrodes. As a result, we challenged the optimized Au NP electrode (12 nm Au NP, 2 hr deposition time) for the direct oxidation of methanol for potential use in direct methanol fuel cells (DMFC). Although platinum is the most commonly used catalyst used in DMFC, Au nanostructures are also considered as potential catalysts of the methanol oxidation reaction because they oxidize CO at room temperature.[408,409] The catalytic activity of the electrodes was examined with and without illumination (405 nm and 532 nm) using cyclic voltammetry (Figure 5-5a). A well-defined anodic peak (~220 – 240 mV) related to the oxidation of methanol appeared in both dark and illuminated conditions.[410,411] In the dark, the methanol oxidation peak current was 41 µA/µg, which increased only slightly (43 µA/µg) when excited by 532 nm wavelength. On the contrary, the oxidation current enhancement is much higher at 405 nm excitation (56 µA/µg). This corresponds to 33.3% enhancement in the oxidate rate of methanol. The position of the oxidation peak also moved slightly toward lower potentials (212 mV for interband excitation, whereas 223 mV in dark). Therefore, the enhancement of Au NP's electroactivity in DMFC under illumination mainly arises from the contribution of the interband hot carriers.

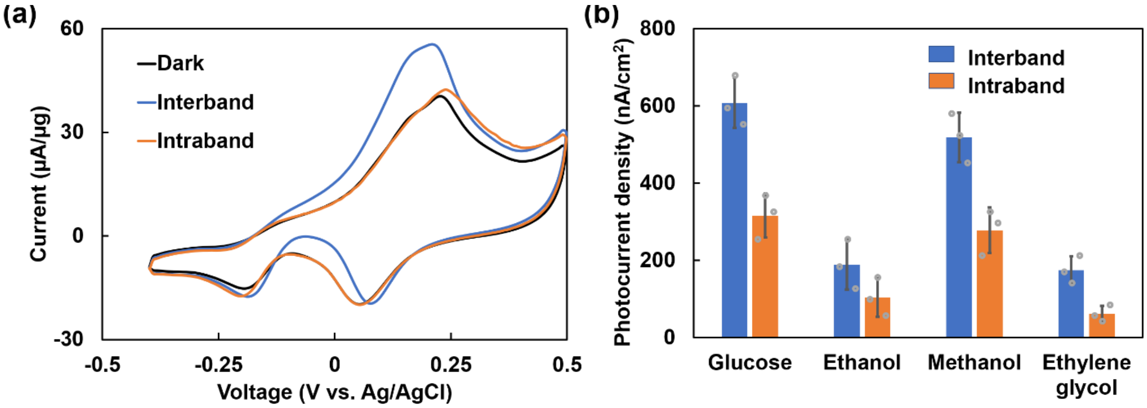

Figure 5-5: Application of hot hole mediated oxidation when using electrodes prepared by (a) Cyclic voltametric (CV) measurement for direct methanol oxidation by the optimized Au NP electrodes when illuminated at 405 nm (interband excitation) and 532 nm (intraband excitation). CV was performed by using 1.5 M methanol in 1M KOH solution. (b) Comparison of interband and intraband photocurrent density for oxidation of glucose, ethanol, methanol, and ethylene glycol. Photocurrent was obtained by applying bias

voltage of 0 V vs. Ag/AgCl and using 10 mM of each chemical in 0.1 M PBS as electrolyte. Errors bars represent one standard deviation calculated from three measurements using different electrodes.

We also measured the photocurrent at different excitation regimes, using ethanol, methanol, glucose, and ethylene glycol. All of these chemicals were shown to produce anodic photocurrents when intraband excitation for Au NPs were used (LSPR excitation).[374] However, higher anodic photocurrents were measured under interband excitation compared to LSPR excitation (Figure 5-5b). This further proves that the direct hot hole mediated photocurrent generation is a characteristic property of the Au nanostructures.

5.5 Conclusion

In summary, we demonstrated that a higher oxidation current can be generated when interband hot carriers are used in comparison to intraband hot carriers, which is related to the higher energy of the hot holes at the interband excitation regime. The solution-based Au NP electrode preparation was optimized for Au NP size and loading amount to maximize the photocurrent. Upon optical illumination, energetic charge carriers (hot electrons and hot holes) are generated via plasmon decay. Interband hot holes can transfer from Au NP to a suitable reducing agent in the electrolyte,[348,396,412] and therefore are able to generate anodic photocurrent. The photocurrent generation were optimized for different size Au NPs, ranging from 5 nm to 25 nm in diameter. Additionally, the deposition time of Au NPs on the electrodes were optimized to achieve optimum concentration and surface distribution of the Au NPs. Maximum photocurrent was obtained using 12 nm Au NPs and 2 hr of deposition time, which generates 1.6 µA and 1 µA upon interband and intraband excitation, respectively. Higher anodic photocurrent at interband excitation than intraband excitation were further confirmed by using five different reducing agents (Ascorbic acid, Glucose, Ethanol, Methanol, and Ethylene glycol). The optimized electrodes were further used in the DMFC application. Interband excitation showed 33.3% enhancement in the methanol oxidation rate, whereas intraband excitation gives only 4.8% enhancement. Using interband hot holes can have many potential applications that involves the oxidation of different chemicals (such as alcohols, CO, sugars, hydrocarbons).

5.6 Acknowledgement

This work was supported by NSERC and Ontario Early Researcher Award grants to L.S., and a salary award to L.S. from the Canada Research Chairs Program. The mass spectrometry was performed at McMaster Steel Research Institute. SEM and TEM images were obtained at the Canadian center for electron microscopy (CCEM), which is a national facility. S.S. is the recipients of NSERC doctoral scholarships.

5.7 Supplementary Information

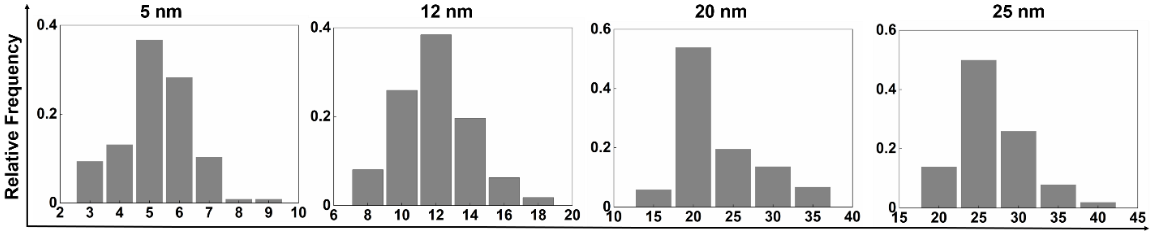

Figure S5-1: Size histograms for the Au NPs used in this work. At least 10 different sample areas and 100 particles were counted to plot the histogram.

Figure S5-1 confirms relatively uniform size distribution of the Au NPs used in this work.

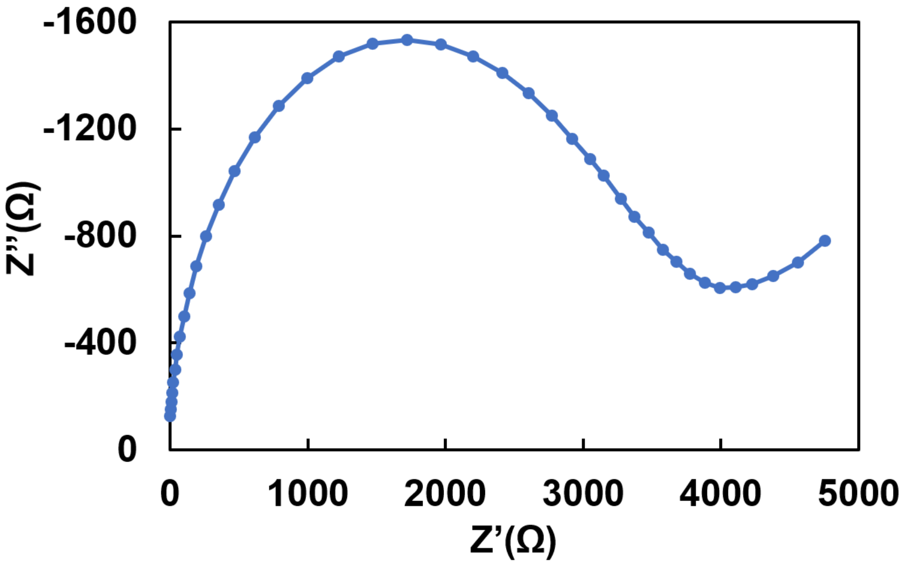

Figure S5-2: Nyquist diagram of Electrochemical Impedance Spectroscopy (EIS) using screen printed carbon electrode without any Au NPs. EIS was performed at open circuit potential using 2 mM $[Fe(CN)_6]^{3-/4-}$ in 0.01 M phosphate buffer (PBS) solution.

Table S5-1 lists the value of charge transfer resistance (R_{ct}), constant phase element (CPE), and n, indicating the constant phase (-90*n) of the CPE for the equivalent circuit model obtained from electrochemical impedance spectroscopy.

Table S5-1: Parameters obtained from the equivalent circuit modeling at dark and illumination:

	R_{ct} (Ω)	CPE (µF)	n
Dark	390	7	0.95
Interband (405 nm)	100	10	0.88
Intraband (540 nm)	100	9	0.88

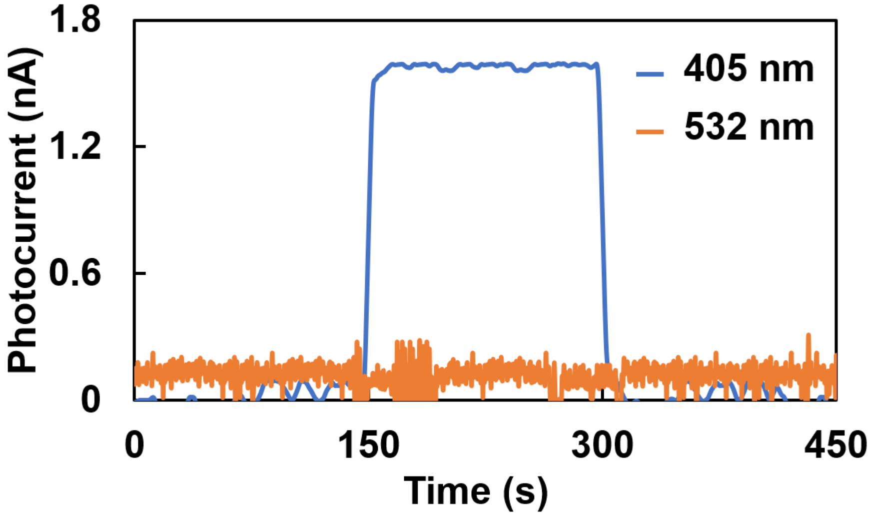

Figure S5-3: Photocurrent measurement for carbon electrode without any Au NP at 405 nm and 532 nm excitation. Photocurrent measurement was performed is 0 V bias vs. Ag/AgCl using 0.1 M AA in 0.1 M PBS. Optical illumination was turned on at 150s and turned off at 300s.

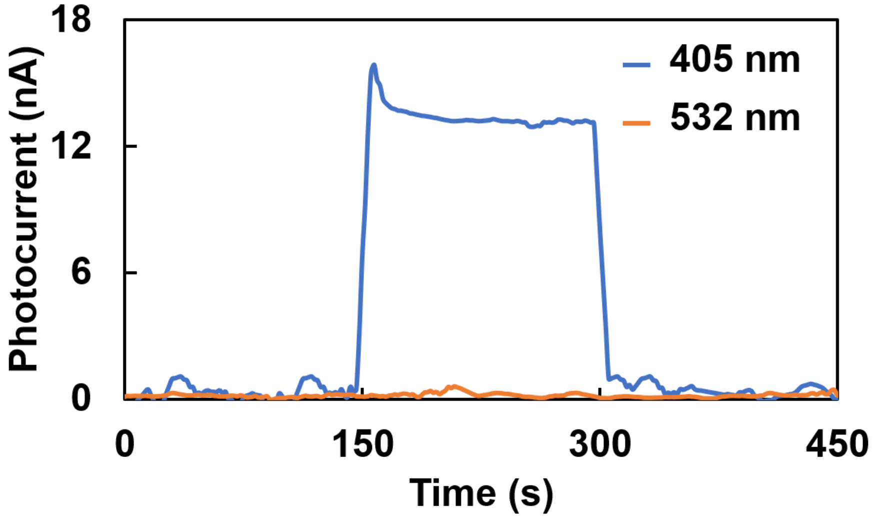

Figure S5-4: Photocurrent measurement by using Au NP deposited (2 hr) carbon electrode at 405 nm and 532 nm excitation. Photocurrent measurement was performed is 0 V bias vs. Ag/AgCl using 0.1 M PBS. Optical illumination was turned on at 150s and turned off at 300s.

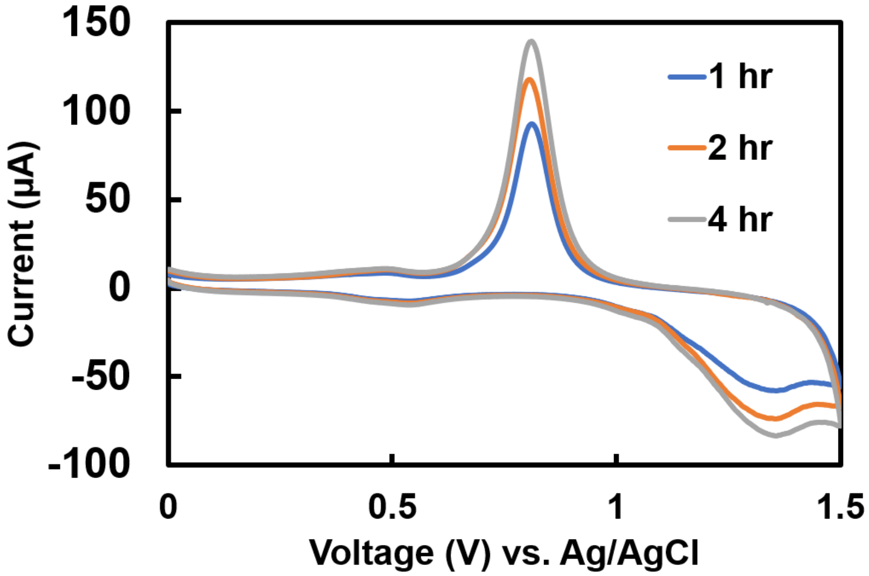

Figure S5-5: Cyclic voltammetry (CV) of the Au NPs deposited carbon electrodes, which is used to determine the electrochemically-active surface area. Cathodic current is plotted as positive. CV was performed at a scan rate of 10 mV/s. Electrochemically-active surface area for 1 hr, 2 hr, and 4 hr electrodes are 0.1195, 0.163, and 0.1932 cm^2, respectively.

Chapter 6 Au-TiO_2 differential biosensing

Chapter Introduction (Objective III)

In Chapter 4, we discussed the role of Au NPs in the PEC process when TiO_2 is used in conjunction. Moreover, in both Chapter 4 and Chapter 5, we investigated the contribution of Au NPs in the PEC process at near-UV (< 420 nm) and visible light excitations. A higher anodic photocurrent was obtained under near-UV excitation as compared to the visible light illumination. Additionally, incorporation of a very small amount of Au NPs in TiO_2 electrodes has been demonstrated to enhance the PEC current of TiO_2 significantly under the near-UV regime. Modification of TiO_2 electrodes with Au NPs was also reported to improve the photovoltaic, photocatalytic, and PEC performance by other researchers.[346,387,413] Despite having a significant amount of progress in this field, the distance dependence effect on the photo-current between TiO_2 NPs and Au NPs, using a biomolecular linker, has yet to be investigated under different wavelengths and target concentrations. DNA functionalized Au NPs are often connected with the semiconductive material in photoelectrode via the DNA, which works as nanospacer.[414,415] However, the distance between Au NPs and the photoelectrodes is highly dependent on DNA structure and conformation. Therefore, in this chapter we try to predict the role of Au NPs on the PEC current when they are connected using oligonucleotides.

In this work, Au NPs were combined with modified P25-TiO_2 via DNA hybridization. We investigated the energy transfer mechanism from Au NPs to P25-TiO_2. Photocurrent enhancement was achieved when Au NPs were in close proximity to the P25-TiO_2 NPs, whereas reduction of photocurrent was obtained for Au NPs further away from the P25-TiO_2 electrode. Based on the experimental results obtained from electrochemical impedance spectroscopy (EIS), Mott-Schottky, incident photon to current conversion efficiency (IPCE), and mathematical modeling of the conjugated structure immobilized on the electrode, we hypothesize that both photocharging and hot electron transfer jointly contribute to the enhancement of photocurrent. Finally, a differential sensor is designed by combining the *signal-off* and *signal-on* sensors, capable of significantly reducing the background signal. Furthermore, this design utilizes a single light source (395nm) and bias voltage (0 V vs. Ag/AgCl) for DNA detection.

Authors: Sudip Saha, Amanda Victorious, Richa Pandey, Amanda Clifford, Igor Zhitomirsky, and Leyla Soleymani

Publication: August 2020.

6.1 Abstract

As dynamic biorecognition agents such as functional nucleic acids become widely used in biosensing, there is a need for ultrasensitive signal transduction strategies, beyond fluorescence, that are robust and stable for operation in heterogeneous biological samples. Photoelectrochemical readout offers a pathway towards this goal as it offers the simplicity and scalability of electrochemical readout, in addition to compatibility with a broad range of nanomaterials used as labels for signal transduction. Here, a differential photoelectrochemical biosensing approach is reported, in which DNA nano-spacers are used to program the response of two sensing channels. The differences in the motional dynamics of DNA probes immobilized on different channels are used to control the interaction between Au and TiO_2 nanoparticles positioned at the two ends of the DNA nano-spacer to achieve differential signal generation. Depending on the composition of the DNA constructs (fraction of the DNA sequence that is double stranded), the channels can be programmed to produce a signal-on or a signal-off response. Incident photon-to-current conversion efficiency, UV/VIS spectroscopy, and flat band potential measurement indicate that direct transfer of electrons between metallic and semiconductive nanoparticles is responsible for the signal-on response and incident light absorption and steric hindrance are responsible for the signal-off response. The differential photoelectrochemical signal readout developed here increases the device sensitivity by up to three times compared to a single channel design and demonstrates a limit-of-detection of 800 aM.

6.2 Introduction

Biosensors combine biorecognition with signal transduction to analyze biologically-relevant targets.[1] Dynamic biorecognition agents such as structure switching aptamers and DNAzymes[1,277,416] are increasingly used in biosensing due to their compatibility with real-time monitoring,[37] ability to target difficult-to-capture analytes such as small molecules,[417] and facile conjugation with reporting probes.[343,418] Optical readout, based on fluorophore/quencher interactions, is currently the most widely used method for transducing these biorecognition events into detectable signals.[418] There is a growing interest in combining these biorecognition systems with electrochemical readout due to the enhanced signal-to-noise ratio (SNR) offered by these transducers, ease of multiplexing, and their applicability to continuous and *in situ* monitoring.[72,419] Inspired by the electronic amplifier circuits, differential (also referred to as ratiometric) signal readout has been used in electrochemical biosensors to enhance their SNR and suppress the effect of background currents generated in unprocessed biological samples resulting from non-specific adsorption.[420,421] The current differential signaling designs typically rely on multiple redox labels for generating correlated or combinatorial signals. This presents a challenge in applying these systems to a wide range of sample environments since the number of redox labels compatible with bio-conjugation that can be used effectively in complex reductive or oxidative sample environments is extremely limited.

Our vision was to create a differential electrochemical readout strategy that used non-redox labels for operation in complex environments. For this purpose, we explored photoelectrochemical (PEC) signal generation that combines optical biasing with electrochemical current measurement. PEC signal readout is possible with a wide range of robust and stable nanomaterial labels (i.e., metal NPs,[422] semiconductive quantum dots,[284] organic semiconductors[423]).

Differential PEC readout is currently possible using two different bias voltages and applied wavelengths,[371,419,424] which result in assays with increased instrumentation complexity. We sought to overcome this complexity by developing a differential PEC biosensor that used a single label, voltage, and light source by controlling the nanoscale interactions of the system using DNA nano-spacers, rather than tuning the parameters of external stimuli. To achieve differential PEC signaling that generates signal increase (signal-on) on one channel and signal decrease (signal-off) on another, we employed the nanoscopic interactions between metallic and semiconducting nanoparticles (NPs). The main reason for using these two types of NPs lies in their complementary optical properties: well-separated and long-lived excitons in semiconductors and localized electromagnetic modes in plasmonic nanoparticles. These properties enable the two classes of nanoparticles to interact when they are positioned in close proximity,[330,425] and allow researchers to engineer new materials and devices that operate based on exciton-plasmon interactions.[333,368,426–428]

PEC assays that use metallic NPs in conjunction with semiconducting photoactive materials build on the foundation that when metallic NPs are in direct contact or close proximity (~10 nm) with semiconducting materials having the desired energetics, the carrier lifetime increases or decreases,[365,425] which modulates the PEC current.[428,429] Au and Ag NPs have been widely used in these assays in conjunction with metal oxide electrodes (such as TiO_2,[283] SnO_2,[422] Fe_2O_3[320]) to design biosensors for detecting various biomolecules (e.g. oligonucleotides,[283] protein,[430] enzyme[320]). We explored whether it would be possible to use DNA capture probes as nano-spacers to tap into the different nanoscale physical processes that occur between metallic NPs and semiconductors on different sensing channels of a single biosensor to predictively increase or decrease the PEC signal based on the separation between the metallic NP label and the semiconducting electrode.

6.3 Experimental Section

Chemicals

Phosphate buffer solution (PBS, 1.0M, pH 7.4), L-ascorbic acid (99%), sodium chloride (NaCl), chitosan (CHIT, from shrimp, degree of deacetylation of 85%, Mw=200,000),), glacial acetic acid, 3,4-dihydroxybenzlaldehyde (DHB), poly(diallydimethylammonium chloride) (PDDA) and tris (2-carboxyethyl) phosphine hydrochloride (TCEP, 98%) were purchased from Sigma-Aldrich. P25-TiO_2 was obtained from Nippon aerosol Co. Ltd. Acetone and Ethanol were purchased from commercial alcohols (Brampton, ON). Milli-Q grade (18.2 MΩ cm) de-ionized (DI) water was used for all solution preparation and washing steps.

Surface modified TiO_2 and Au NP preparation

A 3 gL^{-1} CHIT solution was prepared in DI water using 1% acetic acid. The concentration of DHB aqueous solution was 16 gL^{-1}. DHB-modified CHIT solution was obtained by modifying CHIT in the liquid phase. DHB modified CHIT solution (mass ratio 4:1 as DHB: CHIT) was prepared by adding DHB solution to the CHIT solution. P25-TiO_2 was added to the DHB-modified CHIT solution.

TiO_2 substrate preparation

Fisherband premium plain glass microscope slides were used for substrate preparation. The glass slides were cut into desired dimensions and sonicated using acetone, ethanol and DI water for 15 minutes before using. A 100 nm film of indium tin oxide (ITO) was sputtered onto glass slides using a radio-frequency magnetron sputtering from angstrom science. A 90% In_2O_3 and 10% Sn_2O_3 target was used for the sputtering under the argon gas. All glass/ITO substrates were masked using vinyl tape to preserve electrode contact area and oxygen plasma treated for one minute. All films were fabricated by dropping 10 microliters of solution onto exposed glass/ITO substrate surface and baked at 100°C for 5 minutes. This procedure was repeated for a total of three deposition steps. The resulting electrodes were then air dried and washed prior to use.

Gold (Au) nanoparticle synthesis

Au NPs were synthesized using the protocol reported in literature.[345] Briefly, a 1 mM gold chloride ($HAuCl_4$) solution was added into 38.8 mM trisodium citrate solution with a volume ratio of 10:1. This solution was boiled with vigorous stirring for 10 min, and then the stirring was continued for an additional 15 min without applying heat. This synthesis protocol produced the Au NPs with size approximately 12 nm. The size of the Au NPs were further confirmed by imaging in TEM (Supplementary Figure S6-9).

Au NP-DNA conjugation

DNA conjugated Au NPs were prepared according to the literature.[347] Briefly, 1 ml of Au NPs were suspended in 10 mM PBS buffer (pH 7.0). A 100 µM solution of thiolated DNA was reduced using TCEP and 35 µl of the reduced DNA was added to the Au NP solution. The solution was incubated for 16 h at room temperature (RT). After that, 10 mM PBS and 2 M NaCl solutions were added slowly to make the final salt concentration of 0.1 M NaCl.

This solution was incubated for 40 hours at room temperature. Finally, the solution was washed three times and re-suspended in 10 mM PBS with 0.1 M NaCl buffer (pH 7.0).

Photoelectrochemical Characterization

PEC measurements were carried out in a three-electrode cell setup with an ultraviolet flashlight to facilitate illumination of the photoelectrode surface. The intensity of the flashlight was measured as 470 W/m^2. A Pt wire was used as the counter electrode, Ag/AgCl as the reference electrode, and the glass/ITO/TiO_2NP substrates acting as the working electrode. A 0.1 M PBS solution with 0.1 M ascorbic acid (AA) was used as the supporting electrolyte. Amperometric i-t curve were measured by a CHI 660D electrochemical station, under UV illumination at every 20 s for a period of 100 s. Photocurrents were reported as the difference in current with and without incident light on the face of the TiO_2 electrode.

The IPCE measurements were carried out in a three-electrode cell setup with Pt as the counter electrode, Ag/AgCl as the reference electrode, and a solution of 0.1 M AA in 0.1 M PBS as the electrolyte. All IPCE measurements were performed under a bias voltage of 0 V vs. Ag/AgCl and light illumination in the range of 350–650 nm using a Zahner CIMPS-QE/IPCE Photo-Electrochemical workstation.

IPCE is defined as:

$$IPCE(\%) = \frac{1240 \times I(A/cm^2)}{\lambda(nm) \times P_{inc}(W/cm^2)} \times 100$$

Where, I is the photocurrent, λ is the incident wavelength and P_{inc} is the incident optical power of the excitation light.[346]

Electron Microscopy

The surface structure of the prepared substrate was analyzed using FEI Magellan 400 scanning electron microscope (SEM). UV-Visible (UV-VIS) absorption spectroscopy was measured using Infinite M200 pro (Tecan) plate reader.

X-ray photoelectron spectroscopy (XPS)

XPS measurements were performed using Kratos AXIS supra X-ray photoelectron spectrometer. The survey scan analysis was carried out over an area of 300 X 700 µm using a pass energy of 160 eV.

Mott-Schottky measurements

Mott-Schottky experiments were performed in a three-electrode setup using Ag/AgCl as a reference electrode and Pt as counter electrode. The electrolyte contained 2 mM potassium ferro/ferricyanide in 0.1 M KCl and 10 mM PBS. The experiments were performed with an AC excitation of 5 mV. From the Mott-Schottky plot, flat-band potential and charge carrier density were calculated by using the following formula:[357]

$$\frac{1}{C^2} = \frac{2}{\varepsilon\varepsilon_0 A^2 e N_D}(V - V_{fb})$$

Where, ε and ε_0 are the dielectric constant of the semiconductor and vacuum permittivity, respectively. N_D is the charge carrier density, V_{fb} is the flat band potential, C is capacitance and A is the area of the electrode.

Electrochemical impedance spectroscopy

EIS measurements were carried out using the Zahner potentiostat at RT by using the same electrolyte as mott-schottky measurements. All measurements were conducted at the open circuit potential and within the frequency range of 100 kHz to 0.1 Hz.

DNA hybridization experiments

Electrodes were fabricated using a layer-by-layer drop casting method, followed by ssDNA (1µM) probe deposition for 3 hours and incubation with a blank solution containing 1.2 nM of non-complementary target or complementary targets (100 aM-1 nM) spiked in the blank solution. Electrodes were washed thoroughly between each deposition step. The measured percentage change in signal for each concentration is calculated as:

$$\Delta I = I_{Target} - I_{Probe}$$

$$\%\Delta I_{15\text{-mer}} = (\Delta I_{15\text{-mer}} \text{ X } 100)/I_{Probe\ 15\text{-mer}}$$

$$\%\Delta I_{20\text{-mer}} = (\Delta I_{20\text{-mer}} \text{ X } 100)/I_{Probe\ 20\text{-mer}}$$

$$\%\Delta I_{15\text{-mer}} = (\Delta I_{15\text{-mer}} \text{ X } 100)/I_{Probe\ 15\text{-mer}}$$

$$\%\Delta I = |\%\Delta I_{15\text{-mer}}| + |\%\Delta I_{20\text{-mer}}|$$

$I_{15\text{-mer}}$ indicates the percentage change in photocurrent following hybridization of Au NP-labelled target with the 15-mer probe while $I_{20\text{-mer}}$ indicates the percentage change in photocurrent following hybridization of Au NP-labelled target with the 20-mer probe.

The DNA sequences used in this work are as follows:

15-mer probe: 5′-NH_2-AGG GAG ATC GTA AGC-3′

20-mer probe: 5′-NH_2-AGG GAG ATC GTA AGC AAA AA-3′

Complementary target: 5′-SH-TTT TTT TTT TGC TTA CGA TCT CCC T-3′

Non-Complementary target: 5′-SH-TTT TTT TTT TTT TTT TTT TTT TTT T-3′

Target sequence for the experiment where Au NP is hybridized to be in proximity of TiO_2 is: 5′-TGC TTA CGA TCT CCC TTT TTT TTT T-SH-3′

Limit-of-Detection

To calculate the limit-of-detection of the differential assay, we plotted the photocurrent change versus the log of target concentration in the linear range (10 aM – 100 fM). The linear equation for the regression line is $\Delta I\ (\%) = 22.35 logC + 5.55$ with a correlation coefficient of 97.5% (Figure 4(b)-inset). The limit-of-detection is determined by calculating the concentration where the y-value of the regression line becomes equal to the limit-of-blank (LOB). LOB is defined as:

$$LOB = \Delta I_{blank} + 1.96 \times \sigma_{blank}$$

Where, σ_{blank} is the standard deviation of the blank signal and the factor 1.96 is used to calculate the limit-of-detection within a 95% confidence interval.

Direct deposition of AuNPs on TiO_2 electrodes

In order to directly deposit Au NPs on TiO_2 electrodes, 10 µl of 2% PDDA solution was drop deposited on the electrodes at room temperature. After 10 minutes, the electrodes were washed thoroughly using DI water to remove the PDDA that was not covalently attached. PDDA provides positive surface charge on the electrodes. After washing the electrodes, 30 µl of citrate-capped Au NPs were deposited and kept for 10 minutes. As the Au NPs have negative surface charge, it will be attached to the TiO_2 particles using electrostatic attraction.

6.4 Results and Discussions

To assess the role of DNA probes as nano-spacers for tuning the sensing response of different channels, we created two classes of biofunctionalized photoactive electrodes (Figure 6-1(a)). Both of these photoactive electrodes were created from a porous network of TiO_2 NPs deposited on indium tin oxide (ITO) substrates (Figure 6-1(b,i)). However, one was biofunctionalized with single stranded DNA (ss-DNA) probes having 15 nucleotides (15-mer), and the other harbored a 20 nucleotide (20-mer) long ssDNA probe (Supplementary Figure S6-1). Upon hybridization with Au NP-labelled complementary DNA targets (25-mer), we expected these two classes of photoactive electrodes to experience different Au-TiO_2 NP collision probabilities caused by the differences in the DNA motional dynamics.[431,432] High magnification backscattered electron microscopy demonstrates that Au NPs are indeed introduced to the TiO_2 NP matrix by complementary DNA target strands following hybridization (Figure 6-1(b)). As a result, we expect a fraction of the TiO_2 NPs to experience nanoscale interactions with Au NPs.

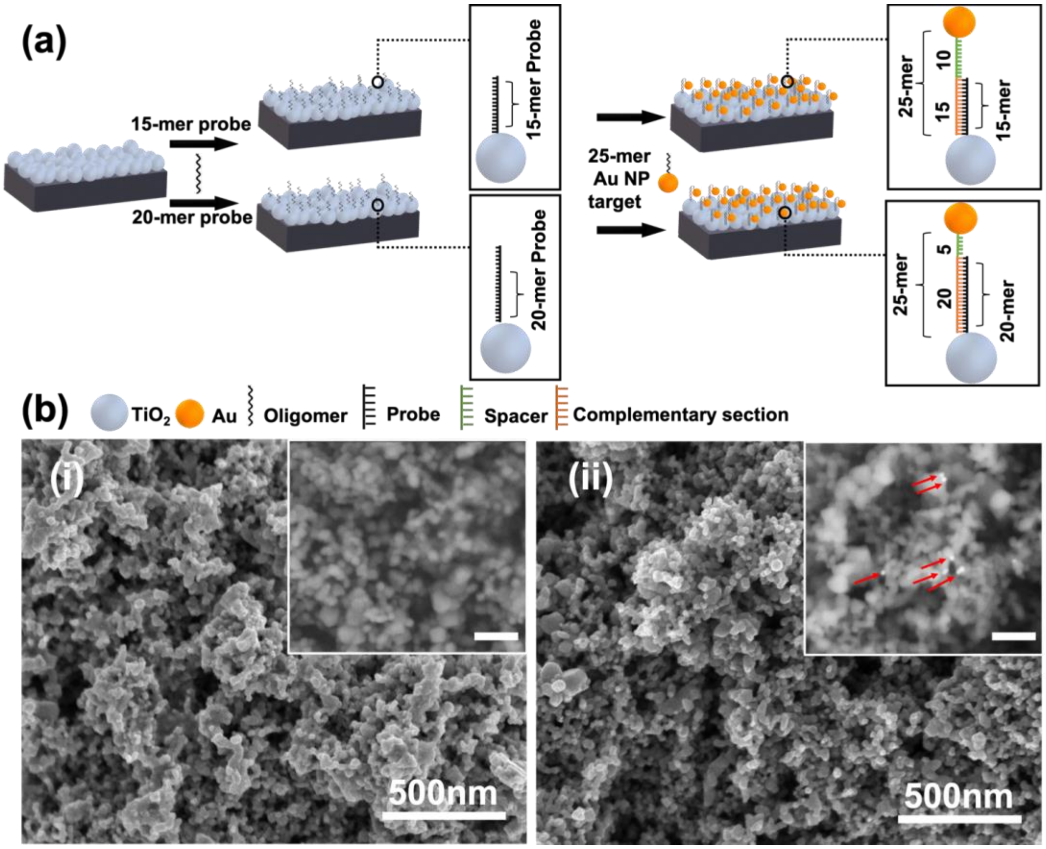

Figure 6-1: Differential photoelectrochemical biosensor. (a) Channels are created by depositing 15-mer or 20-mer probe DNA nano-spacers on photoactive TiO_2 substrates. Au NP-labelled 25-mer targets are hybridized onto the two channels. (b) SEM image of the electrode before (i) and after (ii) DNA hybridization with Au NP-labelled DNA target. The insets show the magnified image of the substrate acquired using the backscatter detector, with the red arrow pointing to Au NPs (scale bar in the inset represents 100 nm).

The incident photon to current conversion efficiency (IPCE) spectrum, which is defined as the number of electrons collected by the electrode per incident photons,[333] was measured to evaluate the wavelength dependence of the PEC response for the 15-mer and 20-mer channels (Figure 6-2(a)). Remarkably, on the 15-mer channel, the IPCE increases after hybridization with the complementary target, whereas for the 20-mer channel, the IPCE decreases. The increase or decrease in the IPCE after target hybridization is observed over the entire absorption spectrum of our photoelectrodes (from 350 nm to 550 nm). It should be noted that absorption of photons with energy lower than the bandgap of TiO_2 NPs (3.09 eV/400 nm as determined from supplementary Figure S6-2) is achieved using our photoelectrodes because of the use of chitosan and 3,4-Dihydroxybenzaldehyde (DHB) in preparing nanoporous photoactive films (Figure 6-2(a)-inset).[343,433]

In addition to the IPCE measurements, we evaluated the sensing capability of the system using PEC readout (Figure 6-2(b)). We optically excited the system using a single light source that operated at a wavelength range at which we observed a large signal change in the IPCE spectrum (Supplementary Figure S6-3 and Figure S6-4). We used ascorbic acid (AA) as the hole scavenger to generate a photocurrent upon optically exciting the TiO_2 photoelectrode. In both channels, an anodic current is generated, which was decreased upon functionalization with probe DNA. The anodic current is generated due to the annihilation of the photo-generated holes in TiO_2 by AA, and the movement of electrons from the conduction band of TiO_2 to the ITO electrode.[422] Modifying the electrode surface with biorecognition elements decreases the PEC signal by hindering the access of AA to the electrode surface.[434]

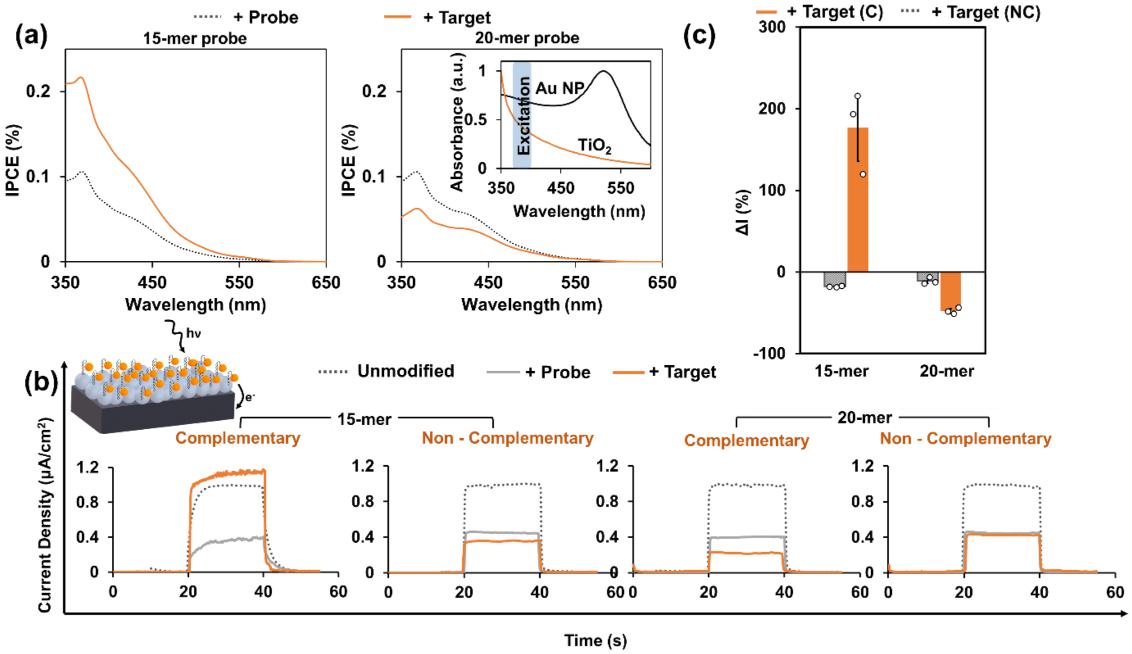

Figure 6-2: Photoelectrochemical characterization of the two sensing channels (a) IPCE spectrum of the photoactive electrode after probe attachment and after hybridization with Au NP-labelled complementary DNA targets (inset shows the absorption spectrum of Au NPs and TiO_2 NPs and the spectral range of the light source). (b) Representative PEC curves of the photoelectrode obtained using chopped light chronoamperometry at 0 V bias versus Ag/AgCl, before modification, following modification with 15-mer or 20-mer probe, and after hybridization with a 25-mer complementary or non-complementary Au NP-labelled target. The photoelectrodes were illuminated at 395 nm for 20 seconds starting at 20s (light on) and ending at 40 s (light off) with 0.1 M ascorbic acid in 0.1 M phosphate buffered solution used as the supporting electrolyte. The inset schematically demonstrates photoelectrochemical readout process. (c) Bar plots summarizing the percentage change in photocurrents following hybridization of 15-mer and 20-mer channels with Au NP-labelled complementary (C) and non-complementary (NC) targets. Error bars represent one standard deviation with experiments performed using at least three separate devices.

As hinted by the IPCE results, striking differences were observed in the signal change when the 15-mer and 20-mer channels were hybridized with complementary 25-mer DNA targets. The 15-mer channel demonstrated a signal increase (~177%), whereas the 20-mer channel yielded a signal decrease (~48%). It should be noted that incubating the probe-modified electrodes with non-complementary target produced a small signal decrease (~2%) in both channels (Figure 6-2(b), (c)), demonstrating the specificity of this readout strategy and its applicability to biosensing. The incubation of the probe-modified electrodes with non-complementary DNA strands served as a control experiment to examine the effect of non-targeted Au NP-labelled DNA sequences on the generated PEC signal.

X-ray photoelectron spectroscopy (XPS) analysis of both channels showed gold to be present at the electrode surface at 0.2 at% (Supplementary Figure S6-5). Although this does not directly measure the amount of the Au NPs present at each channel, it provides a representative snapshot of the amount of gold at the electrode surface, suggesting that the Au NP amounts are similar in both channels. This indicates that the observed differences in signal change on the 15-mer and 20-mer channels are not due to the difference in the surface concentration of Au NPs on these two channels.

The signal-on versus the signal-off response observed on the 15-mer and 20-mer channels, respectively is hypothesized to be related to the different separations and collision probabilities experienced between the Au NPs and the TiO_2 matrix on the two channels. In our designed architecture, following hybridization, the 15-mer channel holds a 15 nucleotide double stranded segment with an estimated length of 5 nm and a 10 nucleotide single stranded segment with a length of 3.33 nm (Figure 6-1a). On the 20-mer channel, the 20 nucleotide double stranded segment is estimated to be 6.67 nm in length, and the 5 nucleotide segment is estimated to be 1.66 nm in length (Figure 6-1a). Double stranded DNA is considered to be significantly more rigid than single stranded DNA having the same number of nucleotides.[435] It is hypothesized that because a larger portion of the DNA nano-spacer is single stranded for the 15-mer channel compared to the 20-mer channel, there is a smaller average separation between the Au NP and TiO_2 surface.

Previous voltammetric studies performed using redox labelled-DNA constructs anchored on the electrode surface using a six-carbon (C_6) linker indicate that the rotational motion of double stranded DNA (dsDNA) around the surface anchoring point allows the redox label to sufficiently approach the electrode for successful electron transfer.[432] Additionally, the probability of electron transfer is influenced by the length of the linker that connects the redox label to the DNA strand, with longer linkers resulting in increased electron transfer.[431] This system can be envisioned as a double hinged system with a spring-like anchor (C_6 linker, Hinge 1), rigid rod-like structure (dsDNA), and a flexible signaling linker connecting the DNA to the label (Hinge 2). Given that our system uses a C_6 linker, includes a double stranded segment, and is terminated by a ssDNA segment conjugated with a Au NP, it can be modelled using the abovementioned double-hinged system (Figure 6-3(a)). For the 15-mer channel, the single stranded portion of the target DNA is 40% of the total nominal DNA length; whereas for the 20-mer channel, the single stranded portion constitutes only 20% of the total nominal construct length. This indicates that the 20-mer channel includes a longer rod-like segment and a shorter flexible portion, which will have a dual effect on the probability of charge transfer between the Au NP and the TiO_2 matrix. The longer rod-like segment increases the bending radius of the DNA construct, and the shorter flexible segment decreases the probability of Au NP/electrode collisions. We expect this dual effect to result in a smaller probability of charge transfer between the Au NP and the TiO_2 matrix for the 20-mer channel in comparison with the 15-mer channel.

In order to calculate the relative collision rate of Au NPs with TiO_2, we performed conformational analysis of the DNA nano-spacers on the 15-mer and 20-mer channels considering the worm-like chain model.[435] We modeled the DNA nano-spacers on each channel by considering each nano-spacer as two separate DNA segments (ssDNA and dsDNA) with different persistence lengths (Supplementary Figure S6-6). Although this model considers probe DNA to be anchored on a planar substrate, it is expected to provide an estimate of the relative collision rate for the rough surface used in this work due to the stochastic motions of the DNA strands. This model indicates that a 5.77-5.83 times higher collision rate is expected on the 15-mer channel compared to the 20-mer channel.

Our experimental results demonstrate that signal enhancement occurs on the 15-mer channel, while signal decrease is seen on the 20-mer channel. We hypothesize that, on average, a larger number of Au NPs directly contact the TiO_2 surface more often on the 15-mer channel than on the 20-mer channel. This difference in signal generation on the two channels is evident despite the uneven surface of the TiO_2 electrodes because the measured current is a collection of the aggregated response of all the nanoparticles present at the electrode surface.

We further explored whether direct contact between Au NPs and TiO_2 electrodes would result in an enhancement in photocurrent, similar to what was observed on the 15-mer channel. we designed an experiment in which Au NPs were deposited directly on the TiO_2 electrodes. Au NPs directly deposited on TiO_2 electrodes showed a higher photocurrent compared to bare TiO_2 electrodes (Supplementary Figure S6-7). Additionally, the IPCE spectrum (Supplementary Figure S6-7) obtained on bare and Au NP-modified TiO_2 electrodes showed a similar behavior to that observed on the 15-mer channel, further corroborating that direct Au NP/ TiO_2 contact could be responsible for the photocurrent enhancement seen on this channel.

Previous studies have demonstrated that Au NPs in direct contact with TiO_2 substrates alter the carrier lifetime measured on the TiO_2 surfaces due to the increased recombination probability.[370] We measured the changes in carrier lifetime by performing electrochemical impedance spectroscopy (EIS) on the two channels before and after hybridization. The phase diagram of EIS shows a positive phase shift after hybridization which delineates a decrease in carrier lifetime on the 15-mer channel, whereas no significant shift is observed for the 20-mer channel (Supplementary Figure S6-8). Reduction of carrier lifetime between probe-modified and hybridized electrodes is calculated as 46.8% and 2.1 % for the 15-mer and 20-mer channels, respectively. The change in carrier lifetime suggests that Au NPs are directly contacting the TiO_2 NPs on the 15-mer channel, which is not observed on the 20-mer channel. This is in line with our hypothesis that the Au NPs on the 15-mer channel have a higher chance of collision with the TiO_2 NPs compared to the 20-mer channel.

To understand the link between the changes in the DNA motional dynamics and the PEC response of the two channels, we consider the possible mechanisms for signal generation. Upon optical excitation of this Au-TiO_2 NP complex, electron/hole pairs are generated at the surface of TiO_2 NPs and interband carriers are generated in Au NPs[350] as the d-band energy lies only 2.4 eV below the Fermi levels of Au[436] (Figure 6-3(b)). When Au NPs are in proximity or contact to the surface of a semiconductor, it is possible to induce multiple effects on the photocurrent of the semiconductor,[352,367] including catalysis, surface passivation, Fermi-level equilibration/photocharging, incident energy absorption,[437] plasmonic-enhancement (light scattering, hot electron injection[318], enhanced semiconductor absorption due to local electric field enhancement,[389] plasmon-induced resonance energy transfer (PIRET)), and Förster resonance energy transfer (FRET).[367,438]

Regarding the signal increase observed on the 15-mer channel and noting that catalysis is insignificant in our electrolyte system, we consider Fermi-level equilibration/photocharging, light scattering, plasmonic hot electron injection, enhanced semiconductor absorption due to local electric field enhancement, and PIRET. Since the gold nanoparticles are 12 nm in size (Supplementary Figure S6-9), plasmonic light scattering is negligible.[367,438] Enhancement of the local electric field at the surface of AuNPs through localized surface plasmon resonance can enhance the photocurrent induced in TiO_2 nanoparticles through radiative and non-radiative (PIRET)[365,438] mechanisms.[367] Radiative energy transfer from metal NPs to the semiconductor enhances absorption cross-section by enhancing electron-hole pair generation in the semiconductor.[389] However, for smaller Au NPs (diameter <30 nm) such as those used here, the efficiency of radiative energy transfer drops significantly, making it an unlikely enhancement mechanism.[367] PIRET is the non-radiative energy transfer process that can increase the electron-hole pair in TiO_2 NPs.[365,438] PIRET occurs as a result of dipole-dipole coupling between the plasmon of the metal NP and the electron-hole pairs in the semiconductor due to the spectral overlap of the plasmonic resonance band of the metal NP and the semiconductor's absorption band.[336] Cushing et al. performed an experiment using transient absorption spectroscopy to investigate whether charge transfer or PIRET is the dominant mechanism for photoconversion efficiency enhancement in the metal NP-semiconductor hetojunctions.[365] It was shown that there is no detectable PIRET effect for the wavelength range of 350-750 nm when Au NP is in contact or proximity with TiO_2. PIRET requires strong dipole generation in a metal, which occurs by exciting plasmons. From the absorption spectra of Au NPs (Figure 6-2(a)-inset), it can be seen that the significant plasmon excitation occurs in the range of 515-525 nm. Due to the fact that the UV excitation used in this work (395 nm) does not include the plasmonic band of Au NPs (in the range of 515-525 nm), we can exclude PIRET mechanism for the photocurrent enhancement seen in 15-mer channel.[365,367] It is important to note that although our materials architecture is not identical to that used in Cushing's work, in both cases, the TiO_2 shows an absorption tail at 395 nm (the excitation wavelength used in this work) and the plasmonic excitation of the gold falls within the 515-530 nm range.

Hot electron transfer and Fermi-level equilibration/photocharging are both potential mechanisms for signal enhancement, suggesting that the 15-mer/25-mer DNA construct enables direct charge transfer to occur between the Au NPs and TiO_2 matrix.[365,439] A large shift in the flat band potential (~140 mV) observed in the 15-mer channel after target hybridization (Figure 6-3(c)) compared to the much smaller shift in the 20-mer channel confirms that there is a larger probability for direct charge transfer in the 15-mer compared to the 20-mer case. This potential shift was not evident when unlabelled target DNA was used (Supplementary Figure S6-10), indicating the importance of the interaction between Au and TiO_2 NPs. The shift in flat band potential has been previously observed in Au NP modified semiconductors and is attributed to Fermi level equilibration,[320,354] which occurs due to the metal deposition at the semiconductor electrode (Figure 6-3(b)) and the direct charge transfer from the semiconductor to the metal.

Photocharging occurs when light-induced electrons move from the semiconductor conduction band to the surface of Au NPs, and is a special case of Fermi level equilibration under light excitation.[321,352] This directional electron movement occurs if the Fermi energy of Au NPs lies below the conduction band energy of TiO_2,[427] which is the case in our experiments (Figure 6-3(b)). Au NPs have been reported to exhibit this electron-sink (photocharging) effect and can minimize charge recombination owing to enhanced charge separation (Supplementary Figure S6-11).[360,426] This enhanced charge separation is supported by the increased carrier density observed from the slope of the Mott-Schottky curve measured after hybridization on the 15-mer channel (Figure 6-3(c) and supplementary Table S6-1).

Hot electron injection or the direct transfer of excited charge carriers also explains the signal enhancement seen on the 15-mer channel, in which there is a large probability for direct electron transfer.[331] Hot holes/electrons are generated by plasmon dephasing[367,438] with the energetics of the hot carriers depending on the excitation energy (Intraband/interband excitation).[375,394] The energy of the hot electrons is higher for intraband excitation; whereas hot holes are more energetic for interband excitation[90,356,375] that is used in our experiments.[349,350] It is hypothesized that interband d-sp transitions in the Au NPs following UV excitation generate highly energetic hot holes and hot-electrons that are capable of taking part in redox reactions.[359,363,440] For interband transitions, the energy of the hot holes can be as high as ($E_{F\text{-}Au}$ - h$\nu_{excitation}$), whereas the energy of hot electrons lies near the Fermi level of Au,[363] where $E_{F\text{-}Au}$ denotes the Fermi level of Au NPs and $\nu_{excitation}$ is the excitation wavelength. These hot holes, generated at the surface of the Au NPs can directly oxidize AA in conjunction with the holes generated upon UV excitation of the underlying TiO_2 matix.[389,441] Interband hot electrons can also have sufficient energy to overcome the Schottky barrier at the Au-TiO_2 interface and therefore the electrons can move from Au NPs to the TiO_2 matrix.[442] This phenomenon can also increase the anodic current generated and collected at the 15-mer channel.

Regarding the signal decrease observed on the 20-mer channel, we expect the DNA motional dynamics to lower the probability of direct charge transfer between the Au NPs and the TiO_2 matrix. Consequently, photocharging and plasmonic hot electron injection can be considered negligible. The 12 nm Au NPs can strongly absorb the incident light;[443] however, the energy uptake by the Au nanoparticles cannot transfer to TiO_2 due to the low probability of charge transfer. Therefore, these gold nanoparticles partially block the incident light received by TiO_2, leading to the reduction of photocurrent in TiO_2. Moreover, DNA labelled Au-NPs are negatively charged[444] and sterically and electrostatically hinder the access of AA to the electrode system, which reduces the system's electrochemical activity.

To confirm that the change in photocurrent is driven by the probability of charge transfer between the Au NPs and TiO_2 matrix and is not sequence-specific, we designed an experiment where the longer probe sequence (20-mer) was hybridized with a longer Au

NP-labelled target sequence (34-mer). In this case, the target/probe length ratio was kept the same as the 15-mer/25-mer channel. Similar to the 15-mer/25-mer complex, the 20-mer/34-mer DNA construct demonstrated a signal increase upon hybridization (Supplementary Figure S6-12), indicating the importance of the length ratio between the single stranded and double stranded segments of DNA complexes in controlling their interaction with the electrode surface. In order to further verify that the signal-on and signal-off responses were related to the different collision probabilities experienced between the Au NPs and the TiO_2 matrix on the two channels, hybridization experiments with Au NPs attached to the proximal end of the target DNA were conducted. It was hypothesized that a similar enhancement in photocurrent would be exhibited in both the 15-mer and 20-mer channels as the Au NPs, when positioned at the proximal end of the DNA target, would have very similar interactions with the TiO_2 NPs. As expected, PEC measurements (Supplementary Figure S6-13) revealed similar enhancements in photocurrent (~174.33% and ~172.38% on the 15-mer and 20-mer respectively) on both channels, thereby confirming that the signal-on and signal-off responses were related to the different collision probabilities experienced between the Au NPs and the TiO_2 matrix on the two channels.

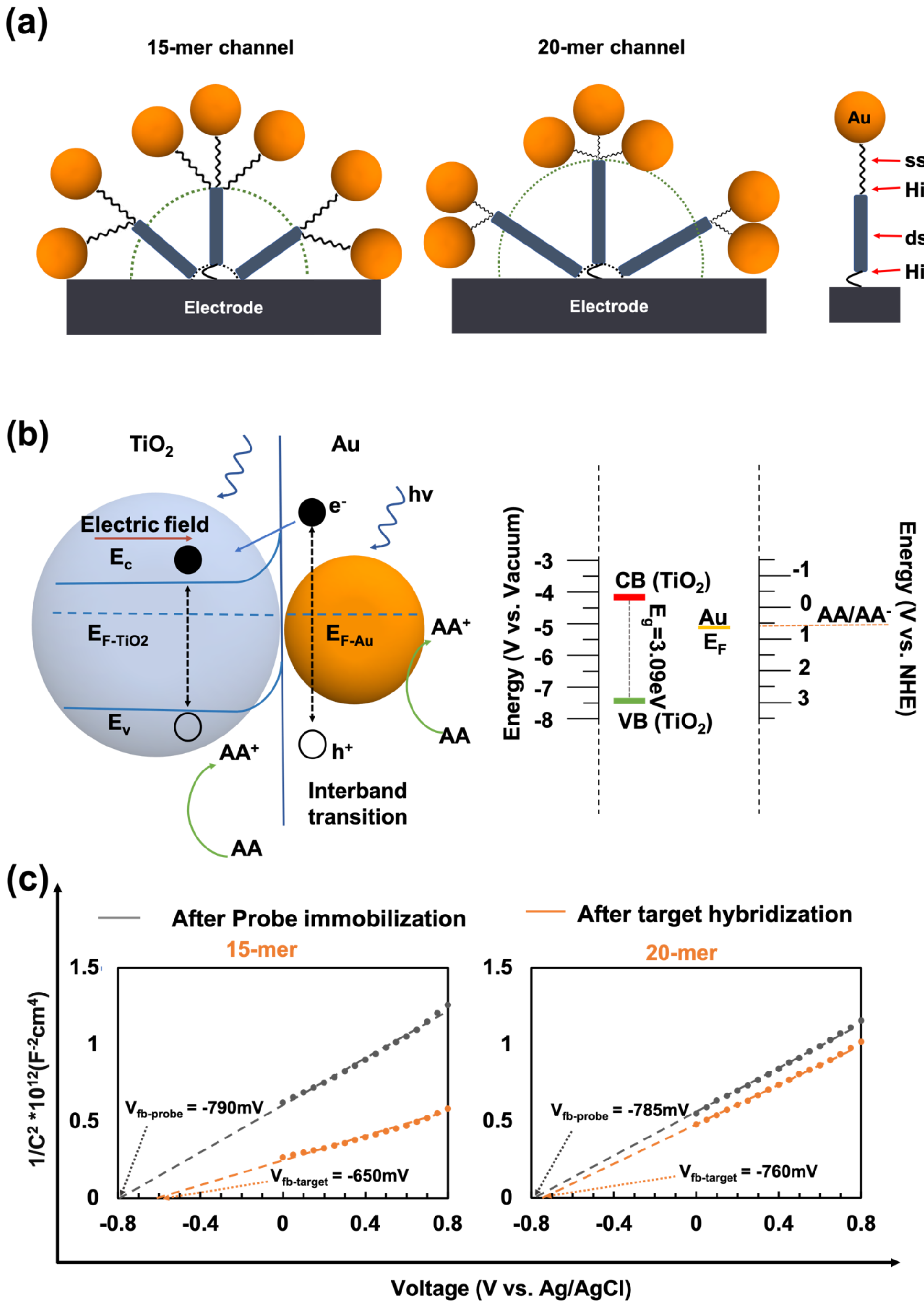

Figure 6-3: The physics of differential signaling in the 15-mer and 20-mer channels. (a) Schematic diagram of the molecular building blocks of the 15-mer and 20-mer channels by considering the dsDNA as a rod-like structure and ssDNA as a flexible string-like structure on a model planar surface. (b) Band diagram and Schottky contact formation at the TiO_2-Au interface (left). Valence and conduction band energy level for TiO_2 and Fermi energy level for Au NP are drawn with respect to vacuum and the normal hydrogen electrode (NHE) (right). Ascorbic acid oxidation potential is depicted here using a dotted red line. (c) Mott-Schottky ($1/C^2$ vs. voltage) plots for 15-mer and 20-mer channels, before and after hybridization with the Au NP-labelled 25-mer target.

We used the knowledge obtained from this DNA nano-spacer study to create an ultra-sensitive differential DNA biosensor. For this purpose, we integrated the 15-mer and 20-mer channels onto a single spatially-multiplexed substrate (Figure 6-4(a)), allowing both channels to be interfaced with a *single* solution. As expected, when a heterogeneous solution containing both complementary and non-complementary DNA sequences was introduced to the device (target drop), the electrodes on the 15-mer channel showed a PEC current that monotonically increased with increasing the concentration of complementary DNA, whereas the 20-mer channel demonstrated a monotonically decreasing current (Figure 4(a)). We then plotted the percentage change that was measured on each channel before and after the introduction of blank and target drops containing 100 aM-1 nM of complementary DNA suspended in the blank solution (Figure 6-4(b)). Additionally, we plotted the differential response of the device by adding the magnitude of changes obtained using the 20-mer and 15-mer channels. This differential processing increased the signal magnitude at every target concentration point. For example, a signal change of 186% for the 15-mer channel at 1 nM was increased to 227% upon differential processing. Moreover, this signaling strategy increased the sensitivity of the measurement from 14% per log for the 15-mer channel and 7% per log for the 20-mer channel to 23% per log for the differential approach (Supplementary Figure S6-14) resulting in a limit-of-detection of 800 aM, with a log linear dynamic range of three decades, which is significantly enhanced compared to previous semiconductive/plasmonic DNA biosensors using a single channel (Supplementary Table S6-2).

The Stability of both channels was evaluated by illuminating the electrodes after target recognition repeatedly for 15 cycles for a period of 600 s (Supplementary Figure S6-15). Through this repeated cycling, both of the15-mer and 20-mer channels showed stable photocurrents with relative standard deviations of 1.35 % and 1.29 %, respectively.

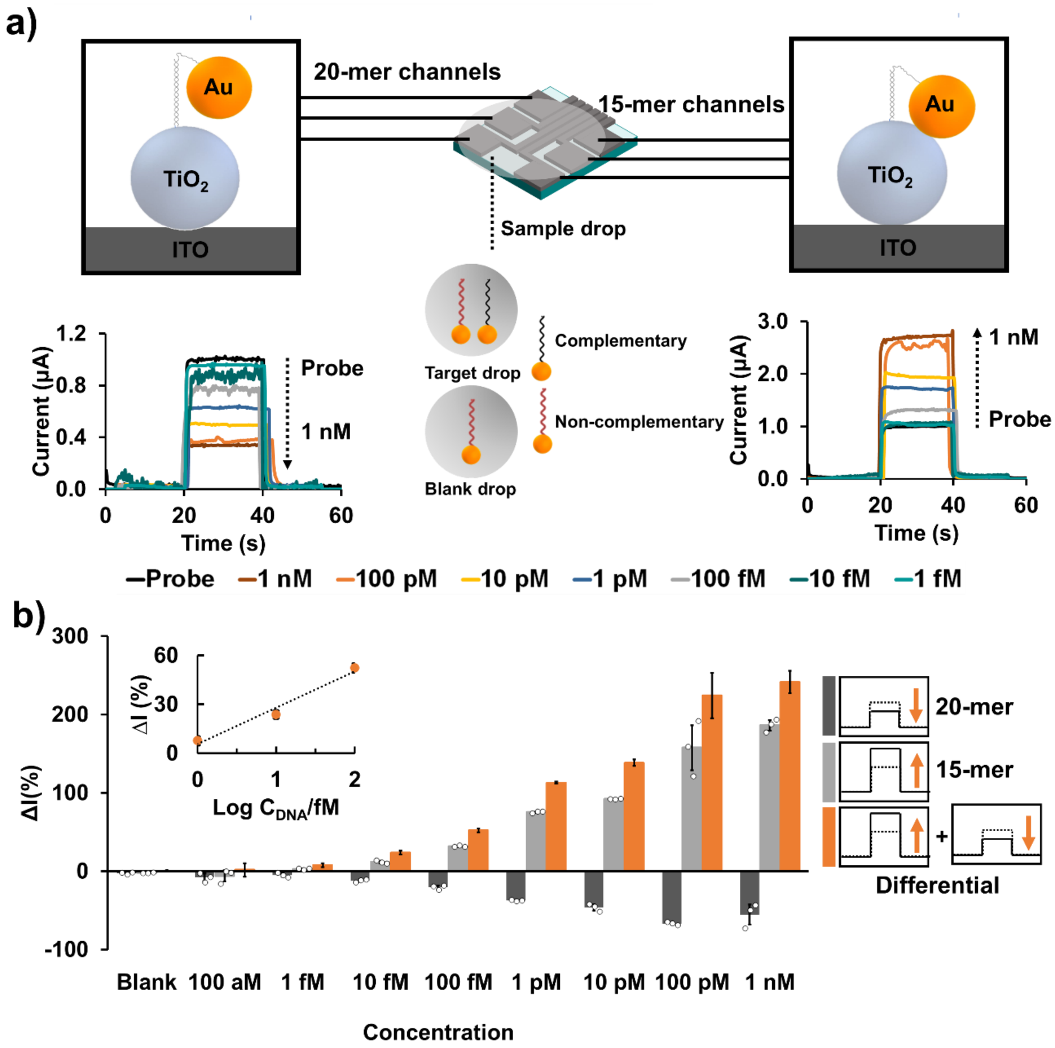

Figure 6-4: Differential biosensing enabled by DNA nano-spacers. (a) Illustration of the spatially-multiplexed differential biosensor design (top) and the corresponding PEC data for various concentrations of target 25-mer Au NP-labeled DNA on the 20-mer and 15-mer channels (b) Signal change obtained upon incubation with blank and target drops on the 15-mer and 20-mer-channels. The differential signal changes are calculated by adding the magnitude of signal changes obtained from the 15-mer and 20-mer channels. The inset shows the calibration curve for determining the limit-of-detection. Error bars represent one standard deviation, with experiments performed using at least three separate devices.

6.5 Conclusions

In this work, we sought to create a differential photoelectrochemical biosensor that uses a single label for obtaining signal-on and signal-off responses on a single multiplexed chip. Single stranded DNA probes of different lengths were used as nano-spacers that modulate direct electron transfer between Au NP-labelled DNA targets and TiO_2 NPs on the electrode surface. DNA sensing channels with 15-mer probes demonstrated a signal increase upon hybridization with a 25-mer Au NP-labelled target DNA; whereas channels with 20-mer probes demonstrated a signal decrease. Measuring the changes in charge carrier density and lifetime, as well as theoretical DNA conformation calculations indicated that increasing the probe length from 15 to 20 nucleotides significantly reduced the probability of direct electron transfer between Au and TiO_2 NPs, and is responsible for changing the sensor response from signal-on (15-mer) to signal off (20-mer).

We combined these signal-on and signal-off PEC channels on a single device to create a differential DNA biosensor, which increased the device sensitivity by a factor of 1.5 or 3.2 compared to using only the 15-mer or 20-mer channels, respectively and resulted in the remarkable limit-of-detection of 800 aM. Given its performance and reliance on robust materials, we expect this differential PEC readout strategy to be applicable to a wide range of electrochemical biosensors where enzymes and redox species are currently used as labels. Although this study demonstrates a proof-of-concept differential signal transduction assay, in the future, it can be extended for analyzing clinically-relevant samples by its integration with DNA machines[55,445–448] where target capture is translated to the release of Au NP-labelled DNA barcodes.[449]

6.6 Acknowledgement

This work was supported by NSERC and Ontario Early Researcher Award grants to L.S., and a salary award to L.S. from the Canada Research Chairs Program, The electron microscopy was carried out at the Canadian Centre for Electron Microscopy (CCEM), a national facility supported by the NSERC and McMaster University. S.S and A. V are the recipients of NSERC doctoral scholarships.

6.7 Supplementary Information

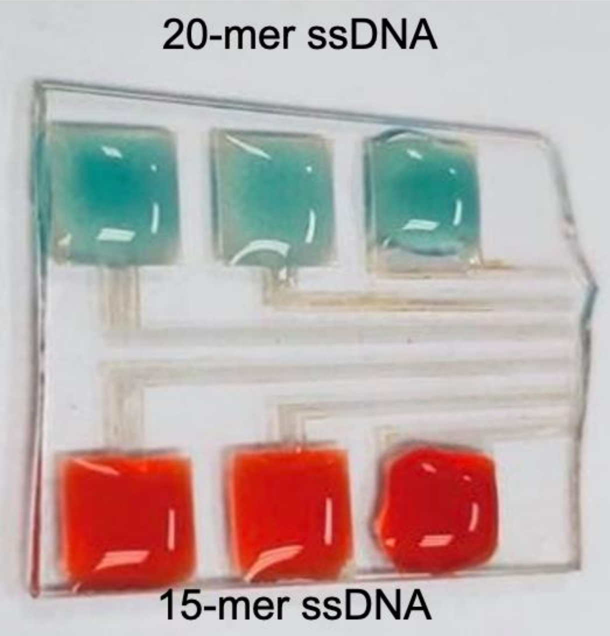

Figure S6-1: Biofunctionalization of photoelectrodes with 15-mer and 20-mer ssDNA probes by drop-depositing the target on the electrodes. Green and Red colors are used to emphasize the spatial difference among the target solutions.

Figure S6-1 shows the photograph of the spatially-multiplexed electrodes. It shows the manual modification of separate areas of the photoactive TiO_2 electrodes with probe.

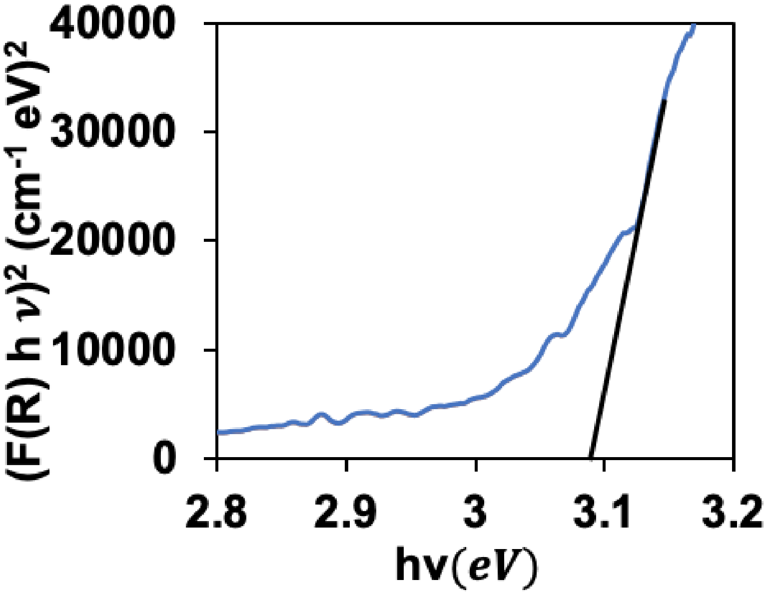

Figure S6-2: Determining the bandgap of the TiO_2 NP films. The intersection of the slope and x-axis determines the bandgap.

It has been shown that the bandgap of TiO_2 nanoparticles (NPs) can be determined from diffuse reflectance spectroscopy.[1] In this work, the Kubelka-Munk (K-M or F(R)) method was applied for the bandgap estimation.[2] By plotting $(F(R)h\nu)^n$ as a function of $h\nu$, one can determine the bandgap. For indirect bandgap, n=0.5, whereas for direct bandgap, n=2. From the above plot in Figure S6-2, we determine the bandgap of the P25-TiO_2 NPs used in this work to be 3.09 eV.

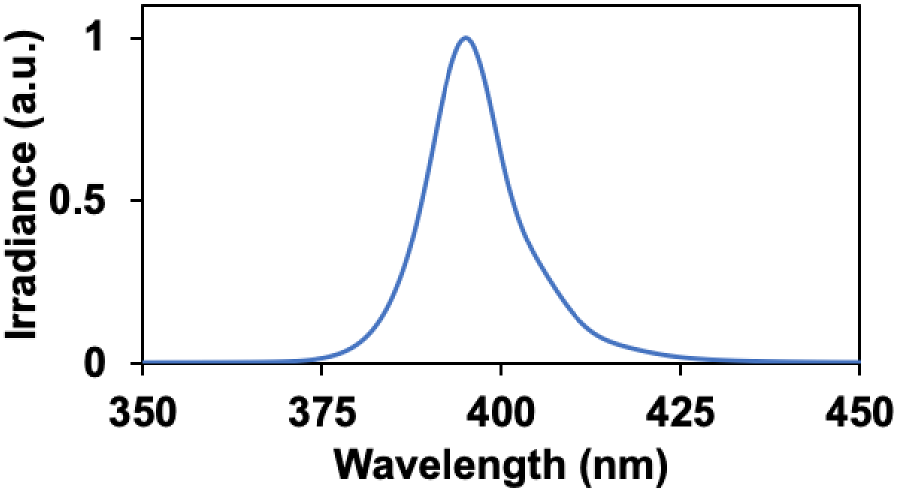

Figure S6-3: Irradiance spectrum of the excitation source used in obtaining the PEC measurements

Figure S6-3 shows the irradiance spectrum of the LED flashlight used in this work for exciting the photoelectrodes. Peak wavelength of the excitation is determined as 395 nm.

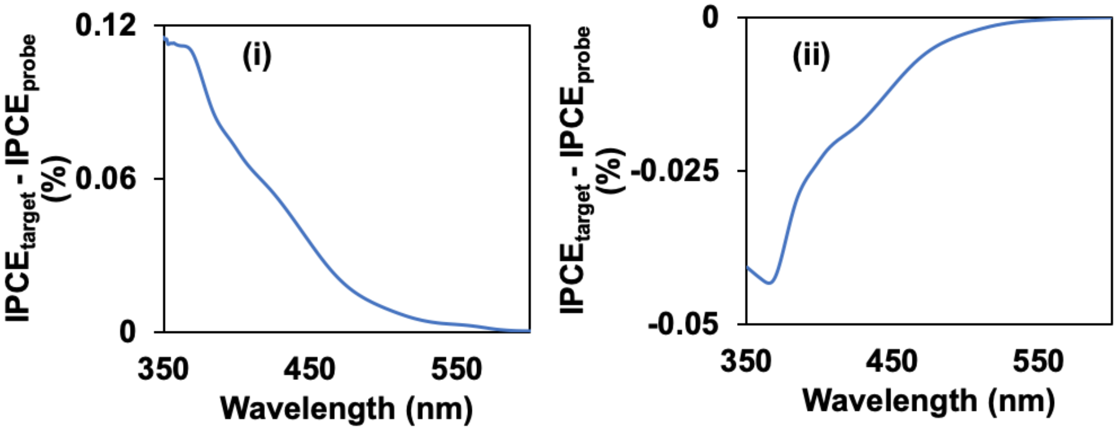

Figure S6-4: Difference of the IPCE values obtained before and after target hybridization for the (i) 15-mer and (ii) 20-mer probes.

The differential IPCE value is calculated to illustrate the wavelength (Figure S6-4) variation of hybridization-induced signal change.

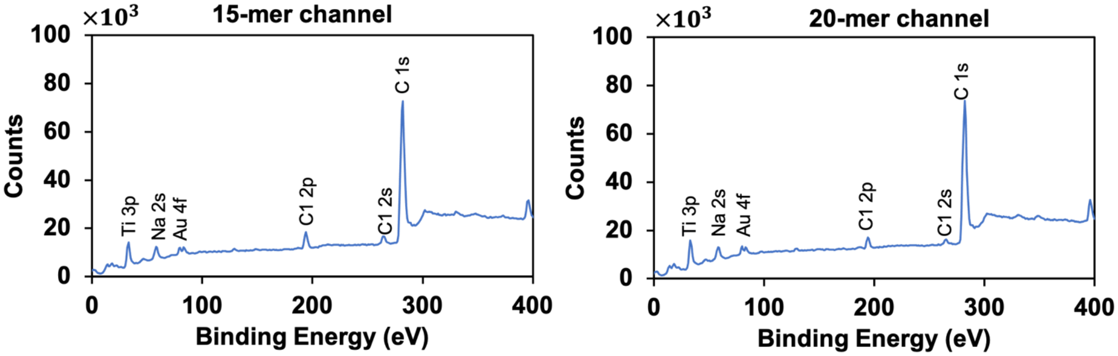

Figure S6-5: XPS analysis of the 15-mer and 20-mer channels. Both channels showed similar amount of Au.

Figure S6-5 shows the spectra obtained by X-ray photoelectron spectroscopy (XPS) technique for the 15-mer and 20-mer channels. Presence of Au NPs on the channels can be confirmed from the characteristic Au 4f spectral line at 83.8 eV. XPS intensity for both channels are similar, which indicates relatively similar amount of surface Au atom on both the 15-mer and 20-mer channels.

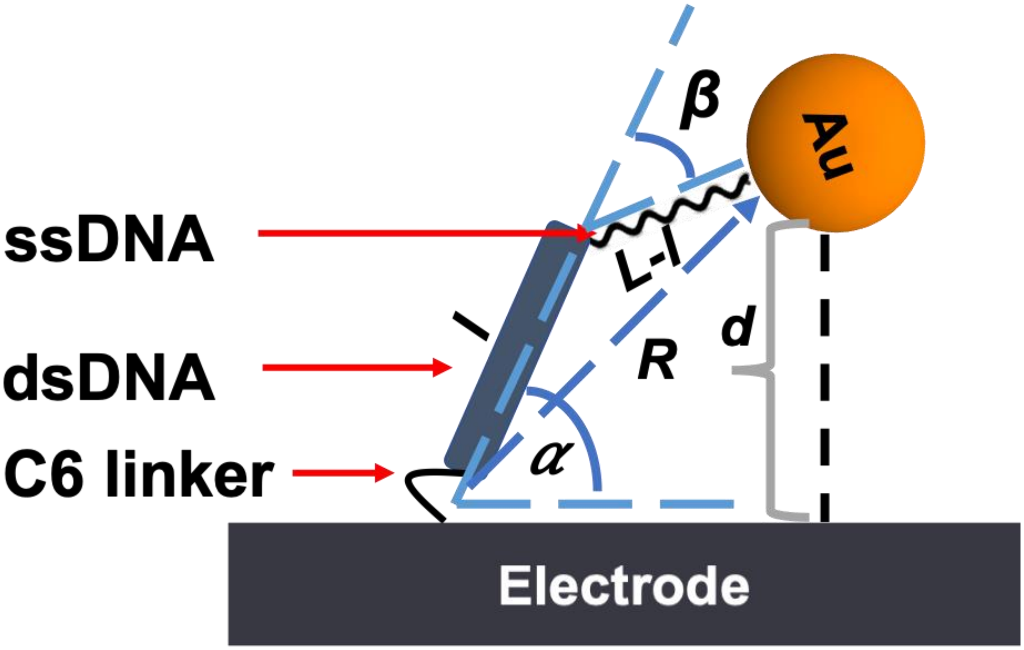

Figure S6-6: Schematic model depicting the DNA structure used in this work having two separate sections (ssDNA and dsDNA) with different persistence length.

Figure S6-6 shows the schematic model of the DNA structure after hybridization. The contour length, L of the DNA is 8.34 nm (25-mer) as each base-pair is shown to be 0.34 nm in length.[3] The overall structure has four sections: C6 linker, dsDNA, ssDNA, Au NP. Length of the C6 linker is considered to be 1 nm.[4] The diameter of the Au NP used in this study is 12 nm. The length of the dsDNA is denoted by l, which is 5 nm for 15-mer channel and 6.67 nm for 20-mer channel. The motion of the structure is governed by the stochastic motion of the dsDNA and ssDNA sections. Therefore, the angle between electrode and dsDNA (α), and the angle between dsDNA and ssDNA (β) will vary with the movement of these two sections. Rivetti et al. showed that the end-to-end distance, R, of the two DNA polymer sections with different flexibility can be calculated as:[5]

$$< R^2 >= 2P_1 l\left(1-\frac{P_1}{l}\left(1-e^{-\frac{l}{P_1}}\right)\right)+2P_2(L-l)\times\left(1-\frac{P_2}{(L-l)}\left(1-e^{-\frac{(L-l)}{P_2}}\right)\right) + 2P_1P_2\left(1-e^{-\frac{l}{P_1}}\right)\left(1-e^{-\frac{(L-l)}{P_2}}\right)$$

Here, P_1 is the persistence length of the dsDNA (45-55nm)[3] and P_2 is the persistence length of ssDNA (2 nm)[6]. In order to calculate the collision rate, we calculate the distance, d from electrode to Au NP. Au NP will be in contact with TiO_2 if d is equal zero. The combination of angle α and β for which the distance (d) becomes negative is considered not real and therefore neglected.

From the above model, distance can be calculated as:

$$d = (1+l) * sin\, sin\,(90-\alpha)\; - (L-l+R_{Au}) * sin\,(\alpha+\beta-90)$$

Where, R_{Au} is the radius of Au NPs, which equals 6 nm for this calculation.

By following the above procedure relative collision rate for 15-mer channel to 20-mer channel was calculated. The collision rate for 15-mer channel is 5.77-5.83 times higher than the 20-mer channel.

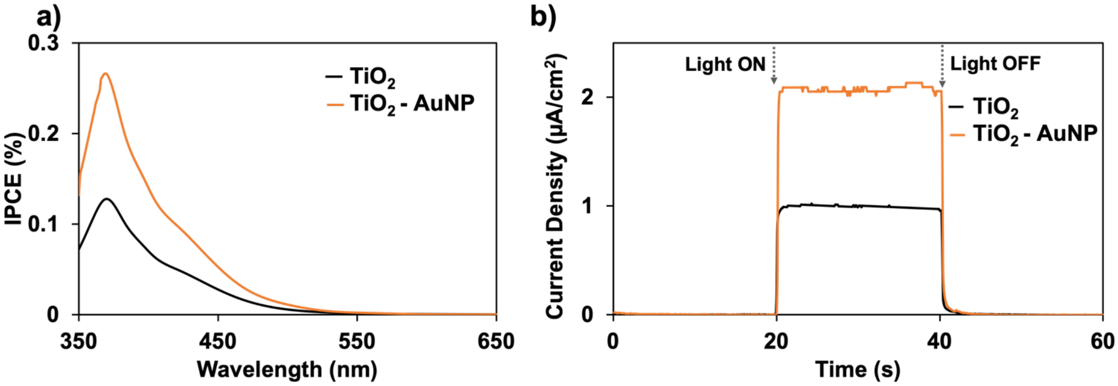

Figure S6-7: Photoelectrochemical comparison between TiO_2 and TiO_2 – Au NP samples. (a) IPCE spectrum of the photoactive electrodes (b) PEC curves of the photoelectrodes obtained using chopped light chronoamperometry. Both measurements were performed at 0 V bias versus Ag/AgCl and the electrolyte used was 0.1 M ascorbic acid in 0.1 M phosphate buffer solution.

TiO_2 matrix was modified with Au NPs by using electrostatic attraction. TiO_2 substrates were immersed into Polydiallyldimethylammonium chloride (PDDA) solution which will have positive surface charge and then the substrates were immersed into Au NP solution. Figure S6-7a shows the IPCE spectrum of the samples before and after modification with Au NPs. In this case, Au NPs are directly in contact with TiO_2 and therefore we expect the behaviour to be similar of 15-mer channel. Chopped light voltammetry at UV showed more than 2 times photocurrent enhancement (Figure S6-7b).

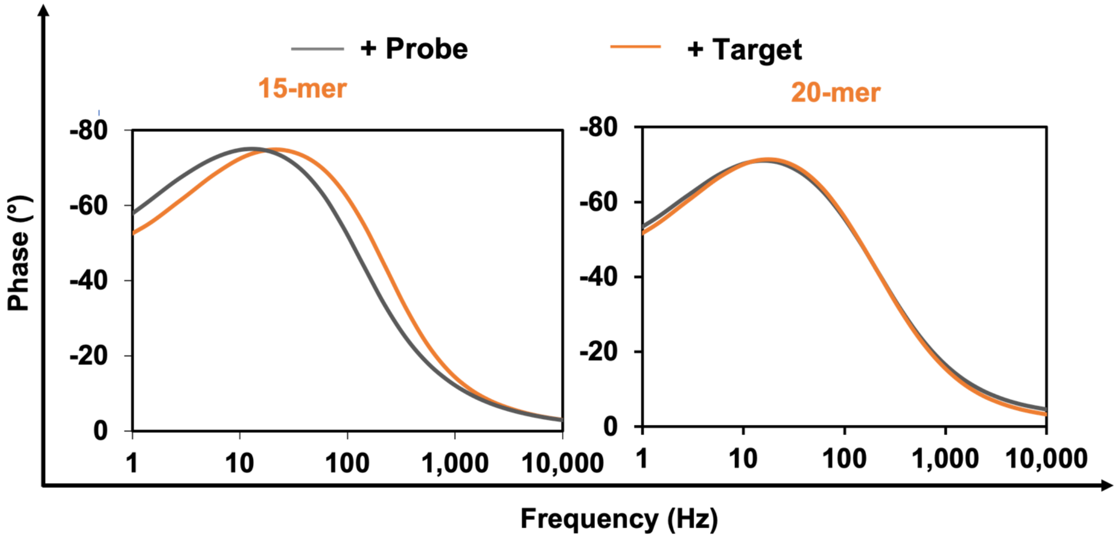

Figure S6-8: Phase diagram of 15-mer and 20-mer channel before and after hybridization obtained from electrochemical impedance spectroscopy (EIS).

Figure S6-8 shows the phase diagram on both 15-mer and 20-mer channel before and after hybridization with a 25-mer Au NP-labelled complementary target using electrochemical impedance spectroscopy (EIS). From the phase response measured using EIS, we can deduce the carrier lifetime as:

$$\tau = \frac{1}{2\pi f_{peak}}$$

where f_{peak} is the peak frequency for the capacitor element in the phase vs. log frequency curve of the Bode plot (Figure S6-8). We observed that after target hybridization on the 15-mer channel, f_{peak} shifted towards higher frequency, indicating a decrease in carrier lifetime. Whereas, for the 20-mer channel, no significant shift in the peak frequency was observed. For probe-modified substrate, carrier lifetime is 13.9 ms, whereas after target introduction carrier lifetime becomes 7.4 ms for the 15-mer channel and 13.6 ms for the 20-mer channel. The carrier lifetime significantly decreased for the 15-mer channel and experienced a much smaller change for the 20-mer channel.

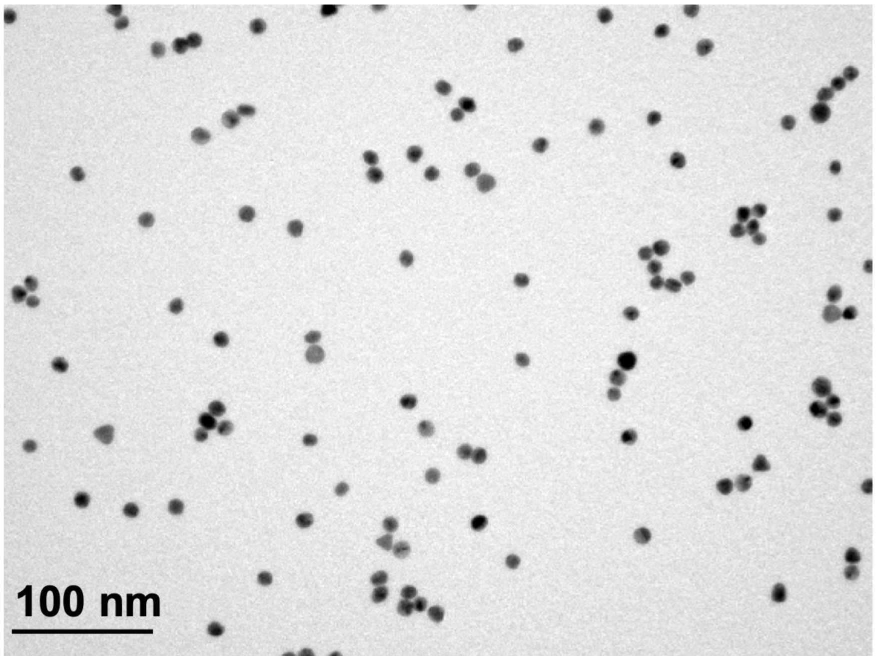

Figure S6-9: Au NPs used in this work imaged using transmission electron microscopy (TEM) showing an average size of 12 nm.

Figure S6-9 shows TEM image of Au NPs. The diameter of the Au NPs were determined as 12 nm.

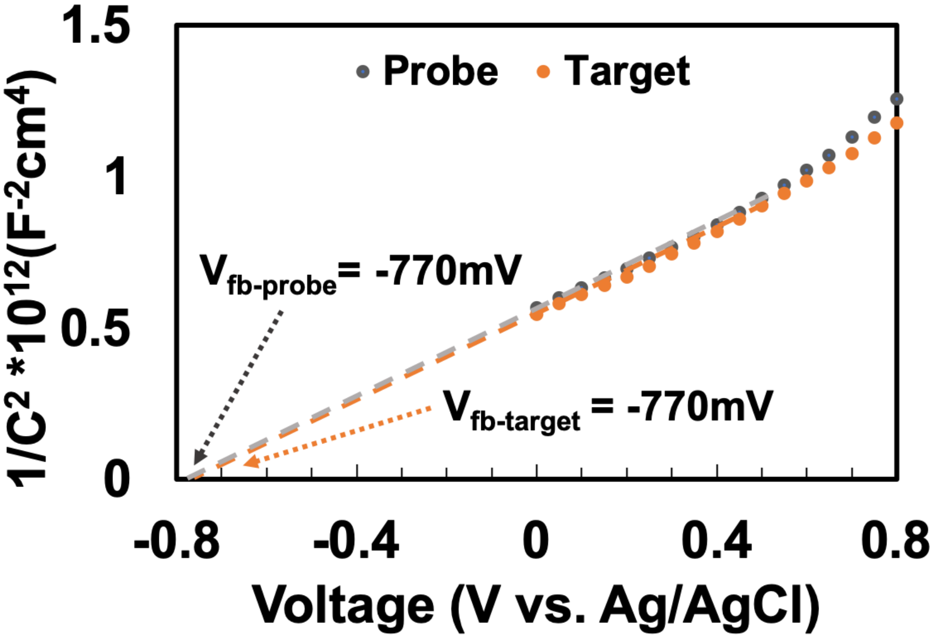

Figure S6-10: Mott-Schottky plot for the hybridization of un-labelled 25-mer DNA targets on the 15-mer channel.

Figure S6-10 shows the Mott-Schottky plot with an un-labelled 25-mer target DNA hybridized on the 15-mer channel. Both the slope and flat-band potential remain unchanged after target hybridization. From the Mott-Schottky plot, flat-band potential and charge carrier density were calculated using the following formula:[7]

$$\frac{1}{C^2} = \frac{2}{\varepsilon \varepsilon_0 A^2 e N_D}(V - V_{fb})$$

Where, ε and ε_0 are the dielectric constant of the semiconductor and vacuum permittivity, respectively. N_D is the charge carrier density, V_{fb} is the flat band potential, C is capacitance and A is the area of the electrode. The values of the carrier density and the flat-band potentials for different experimental conditions are given in Table S6-1:

Table S6-1: Flat-band potential (V_{fb}) and charge carrier density (N_D) for the 15-mer and 20-mer channels

Material-architecture	$V_{fb\text{-probe}}$ (mV)	$V_{fb\text{-target}}$ (mV)	$N_{D\text{-probe}}$ (cm^{-3})	$N_{D\text{-target}}$ (cm^{-3})
15-mer channel with AuNP labelled complementary target	-790	-650	1.29×10^{17}	2.69×10^{17}
20-mer channel with AuNP-labelled complementary target	-785	-760	1.28×10^{17}	1.43×10^{17}
15-mer channel with AuNP labelled non-complementary target	-770	-770	1.30×10^{17}	1.31×10^{17}

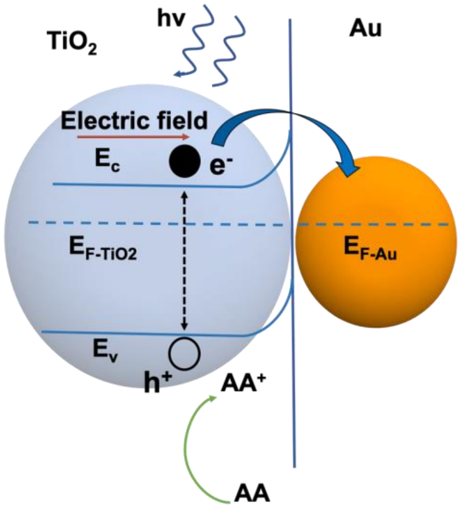

Figure S6-11: Schematics illustrating Photocharging process. Under light excitation, conduction band electrons move to Au NPs and improve electron-hole separation. E_c and E_v denotes the conduction band and valence band position, respectively. E_F denotes the fermi-level position. Holes (h^+) from TiO_2 oxidize ascorbic acid (AA) to produce photocurrent

Figure S6-11 shows the photocharging process. UV excitation generates electron-hole (e^- - h^+) pairs in the TiO_2. The Au NPs act as an electron sink thereby allowing the conduction band electrons (e^-) to move from the TiO_2 to the Au NP, thus enhancing electron-hole separation. This in turn, increases the charge carrier lifetime and consequently the photocurrent.

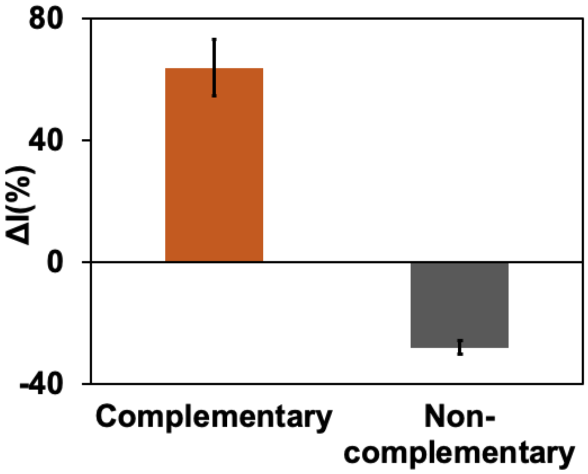

Figure S6-12: Bar plot illustrating the percentage change in photocurrents following hybridization of the 20-mer probes with 34-mer Au NP-labelled complementary targets. The error bars represent standard deviation from at least three separate trials.

Figure S6-12 shows the photocurrent change when 34-mer AuNP-labelled complementary targets were hybridized with electrodes having 20-mer probe. The same trend as the 15-mer channels hybridized with 25-mer AuNP-labelled target was also seen for the 34-mer case. An enhancement in signal of 64 % was seen for the complementary case while a decrease of 28 % observed for the non-complementary case.

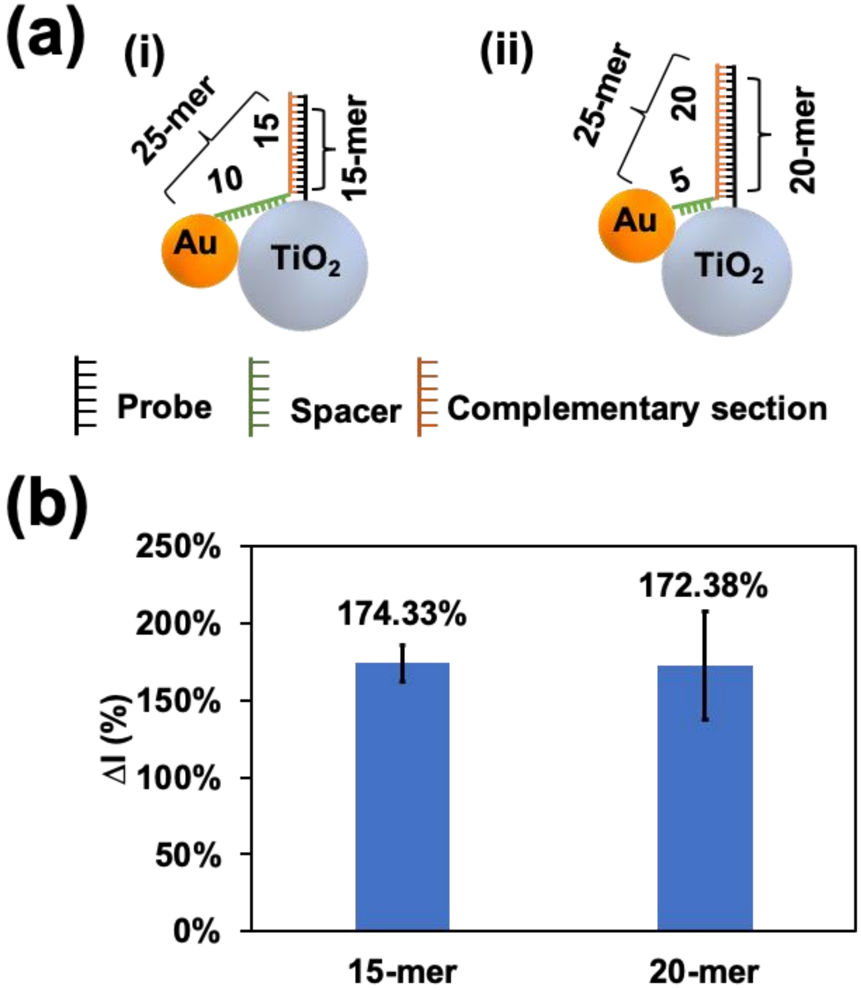

Figure S6-13: Hybridization experiments with Au NP attached to the proximal end of 25-mer DNA and hybridized with 15-mer and 20-mer probes. (a) Schematic illustration of (i) 15-mer and (ii) 20-mer channels after hybridization with AuNP-labelled target. (b) Photocurrent enhancement for 15-mer and 20-mer channels.

Figure S6-13a shows the schematics of both 15-mer and 20-mer channels when hybridized with AuNP-labelled target where Au NP is attached to the proximal end of the target. As it can be seen from the schematics, in both channels, Au NP is expected to directly contact the TiO_2 nanoparticles surface. Figure S6-13b shows the bar plot of the photocurrent enhancement after target introduction for the systems used in a). As the Au NP is expected to contact TiO_2 in both 15-mer and 20-mer channels, we observe similar signal enhancements in both channels.

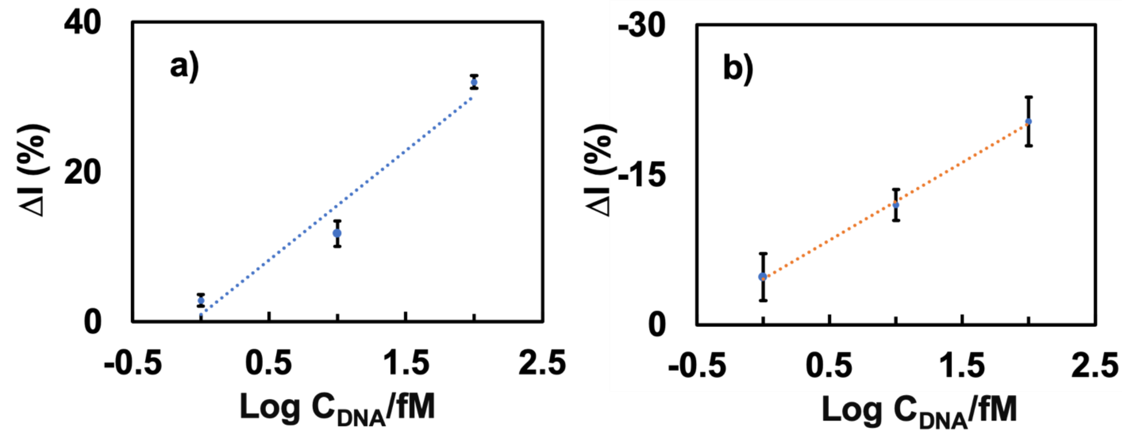

Figure S6-14: Calibration curves for the (a) 15-mer and (b) 20-mer channels for various concentration of target DNA as tested in Figure 6-4.

The linear regions of the calibration curve as shown in Figure S6-14 were fitted using the following equations: (a) $\Delta I\ (\%) = 14.56 logC + 0.98$; correlation coefficient 95.2%, (b) $\Delta I\ (\%) = 7.78 logC + 4.57$; correlation coefficient = 99.8%.

A summary of the recent works for developing PEC DNA sensor using plasmonic properties is provided in Table S6-2. As can be seen from the table, implementing dual channel strategy helps to achieve sub femtomolar sensitivity.

Table S6-2: Summary of the recent PEC DNA sensor utilizing plasmonic properties of metal NPs

Semiconductor-Plasmonic material	**Target**	**Sensing Approach**	**Channels**	**LOD, linear range**	**References**
CdS Quantum dots -Ag Nanocluster	DNA	Signal Off	1	0.3 pM, 1pM – 10nM	[8]
TiO_{2-x} – Au NP	DNA	Signal On	1	0.6 pM, 1pM – 10nM	[9]
Polymer dots – Au NP	DNA	Signal off	1	0.97 fM, 1 fM – 10pM	[10]
TiO_2 NP – Au Nanorod	Micro-RNA	Signal On	1	20 fM, N/A	[11]
TiO_2 NP – Au NP	DNA	Signal On	2	0.8 fM, 1fM – 100fM	This work

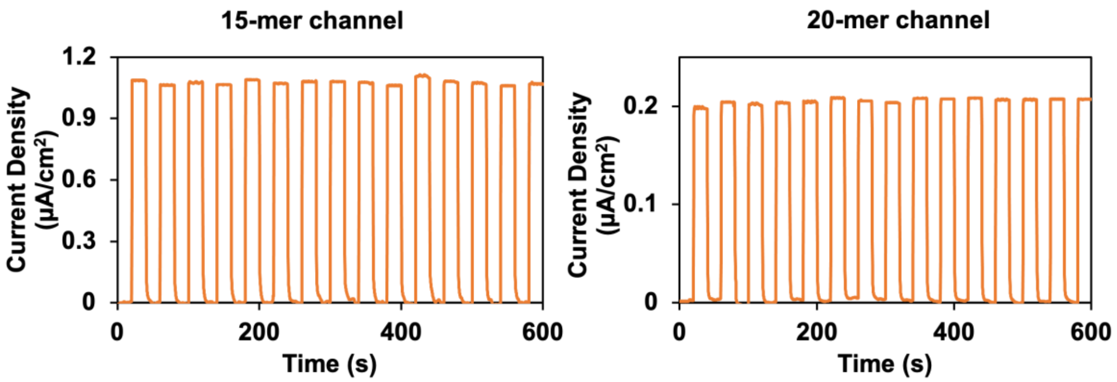

Figure S6-15: Stability test of both 15-mer and 20-mer channels over 15 illumination cycles

Figure S6-15 showed the photocurrent density measurement over 15 illumination cycles. The period of each cycle was 40s with 50% times of illumination. Both 15-mer and 20-mer channel showed stable photocurrents.

Chapter 7 Developing strategies for biosensing without target labeling

Chapter Introduction (Objective IV)

In Chapter 6, we demonstrated the development of a PEC biosensor for ssDNA detection, where the target ssDNA strand was labelled with Au NPs. Techniques for labeling targets are time consuming, expensive and requires complicated sample handling procedure and hence not suitable for POC application.[450,451] In this chapter, we developed a label-free bioassay for nucleic acid detection and verified the assay with electrochemical transduction technique. Electrochemical biosensors are one of the most popular and well-studied diagnostic device platforms.[25,452–454] A *signal-on* electrochemical transducer's limit-of-detection is often compromised due to the high signal to noise ratio because of environmental interference. We sought to overcome this limitation by designing a bioassay which provides a signal output that is inversely proportional to the analyte concentration. This allows us to attain a higher signal-to-noise ratio for low concentration of targets as compared to its *signal-on* analogue whose readout signal magnitude is proportional to the target concentration.[455,456] Methylene blue (MB) labeled ssDNA was used as a signal generation barcode, which is introduced after the target hybridization- and occupies the available capture sites, after target recognition, in the electrode. In this assay design, the background signal before the final readout is negligible as there is no MB in the system before the introduction of signal generation barcode. MicroRNA 200b – a well-studied potential biomarker for prostate cancer detection and prognosis – was used as model analyte.[457–459] We also challenged the sensing platform with exosomes collected from human prostate cancer cell lines and urine samples. In addition, we showed that this assay is able to detect microRNA directly from urine by using commercial lysis buffer, eschewing the intricate and technically challenging exosome extraction procedures.

Authors: Sudip Saha, Susann Allelein, Richa Pandey, Paula Medina-Perez, Dirk Kuhlmeier and Leyla Soleymani

Publication: To be submitted in 2021.

7.1 Abstract

Numerous microRNAs (miRNAs) may act as tumor suppressors or oncogenes in human cancer. Recent biomarker discovery studies have demonstrated that tumor-associated miRNAs can be tracked in a minimally invasive manner, making this cluster of small non-coding RNAs an ideal candidate for diagnosis, prognosis, and personalized treatment of cancers. The electrochemical transduction approach offers potential to fabricate low-cost, reliable, and point-of-care devices for micro-RNA detection in comparison to the conventional PCR-based assays. In this work, we report the novel design of a bioassay to detect human miRNA 200b from extracellular vesicles collected from different human prostate cancer cell lines and urine samples. Enhanced electrochemically active surface area is achieved by electro-depositing gold (Au) nanostructures on star-shaped Au electrodes. At the first step, miRNA 200b is hybridized with the capture probe on the electrode. After that, methylene blue (MB) tagged single stranded DNA, with a sequence similar to the miRNA 200b is introduced on the electrode. The amount of MB-tagged DNA that can bind with a capture probe is inversely proportional to the concentration of miRNA 200b. Here we demonstrated that this bioassay could detect the miRNA 200b as low as 122

aM in clinical samples. This method offers great potential in the low-cost sensitive detection of miRNAs.

7.2 Introduction

Improved cancer management including early-stage diagnosis, accurate prognosis, patient-centered treatment selection, and recurrence monitoring remain challenging for several types of cancer.[460–462] *Liquid biopsy* has demonstrated great promise for improved cancer management as it enables frequent and long-term patient assessment owing to its minimally-invasive nature.[462,463] Among biomarkers analyzed in liquid biopsy, circulating tumour cells, cell-free nucleic acids, metabolites, and extracellular vesicles (EVs),[464,465] EVs are particularly important due to richness and diversity of the biological cargo they carry: proteins, lipids, nucleic acids such as microRNAs (miRNAs).[466–468] Among these cargos, miRNAs are considered as potential biomarkers for both diagnosis and prognosis of several diseases including cancers,[459,469] endometriosis,[470] infectious diseases[471] etc. They have been shown to regulate gene expression at the post-transcriptional level of the messenger RNAs and thereby impact various cellular functions such as cell growth and death, cell differentiation, and cell-to-cell communication.[472,473] Because of the capability of modulating gene expression in tumorigenesis, miRNA expression profile of the patients showed significant difference compared to healthy individual at the early stage of disease progression.[474] Moreover, miRNA expression levels have shown to be correlated with the different stages of the disease and therefore act as suitable biomarker for prognosis application..[467,475] It should also be noted that the miRNAs encapsulated in EVs are protected from degradation due to the lipid layer.[468] Therefore, miRNAs from EVs are considered potential biomarker for both diagnosis and prognosis of several cancers.[476,477]

The current gold standard for quantifying miRNA is reverse-transcription quantitative polymerase chain reaction (RT-qPCR), [458,478,479] a technique that is difficult to implement for frequent and continuous disease monitoring at the point-of-care (POC) due to its reliant on laboratory technicians, as well as laboratory-scale and expensive instrumentation. Electrochemical tests, similar to those used in glucose monitoring, are operated using simple and handheld instrumentation, presenting great potential for rapid analysis at the POC.[52] A major challenge in the direct detection of microRNA – without amplification and target labeling – using electrochemical methods is the low abundance of free and EV-encapsulated microRNAs that are enhanced or suppressed by only a small fraction in cancer patients, resulting in signal changes that are difficult to precisely analyze using inexpensive and handheld current readers (potentiostats).[480]

Multiple electrochemical platforms have been previously developed for microRNA analysis;[451,453,472,481] however, most of these assays are designed to generate an electrochemical current that decreases with decreasing microRNA concentration. Consequently, these assays result in low signal-to-background ratio currents at concentrations regimes that are important for microRNA analysis. Herein, we sought to develop an assay with an inverse relationship between the target microRNA concentration and the current magnitude. This inverse concentration-to-signal assay was developed by integrating two separate but correlated hybridization events. First, unlabelled miRNA targets were captured on single stranded DNA (ssDNA) capture probes immobilized on the transducer, and second, the unreacted capture probes were hybridized with signalling DNA barcodes that were also complementary to the immobilized capture probes. This design would allow miRNA binding at low levels to generate a larger current compared to binding at high concentrations.

Using the newly-developed inverse-concentration-to-signal assay, we analyzed miRNA 200b, in the synthetic form, in crude EV samples extracted from prostate cancer cells, and directly from prostate cancer patient urine samples. With a limit-of-detection (LOD) of 122 aM, our assay indicated low expression levels of miRNA 200b in the exosomes from prostate cells culture and in the prostate cancer patient's urine samples.

7.3 Experimental Section

Materials: Sodium phosphate dibasic (Na_2HPO_4), Monosodium phosphate (NaH_2PO_4), Phosphate buffer saline (PBS), Chloroauric acid ($HAuCl_4$), Sodium chloride (NaCl), Magnesium chloride ($MgCl_2$) 6-Mercapto-1-hexanol (99%) (MCH), Tris (2-carboxyethyl) phosphine hydrochloride (TCEP, 98%), Potassium chloride (KCl), Potassium ferrocyanide ($K_4Fe(CN)_6$), Potassium ferricyanide ($K_3Fe(CN)_6$), Triton X-100, and Hydrogen chloride (HCl) were purchased from Sigma-Aldrich. P25-TiO_2 was obtained from Nippon aerosol Co. Ltd. Acetone and Ethanol were purchased from commercial alcohols (Brampton, ON). Milli-Q grade (18.2 MΩ cm) double distilled de-ionized (DI) water was used for all solution preparation and washing steps. In immunoblotting the following antibodies were used: monoclonal mouse anti-human PSMA (Santa Cruz, F-2, 1:1000), CD9 (Biolegend, HI9a, 1:1000), calnexin (BD, 37, 1:1000), TSG101 (BD Biosciences, 51, 1:1000), beta actin (ThermoFisher Scientific, 15G5A11/E2, 1:10000), Tamm-Horsfall Protein (THP) (Santa Cruz, B-2, 1:1000), CD63 (Biolegend, H5C6, 1:1000) and secondary goat anti-mouse HRP conjugated antibody (Dianova, 1:10000).

Electrode Fabrication: Star-shaped nanostructured gold (Au) electrodes were fabricated to develop the mIRNA sensing platform. Electrode patterns were designed by CAD software and then transferred to vinyl tape (FDC 4301, FDC graphic films, South Bend, Indiana) which is put on top of polystyrene sheet (Graphix Shrink Film, Graphix, Maple Heights, Ohio) using Robo Pro CE5000-40-CRP cutter (Graphtec America Inc., Irvine, CA). A 100 nm thin Au layer was deposited on top of polystyrene by using DC sputtering (MagSput^{TM}, Torr International). This conductive layer functioned as a seed layer for nanostructure deposition. Potentiostatic technique is used for nanostructuring. 10 mM $HAuCl_4$ solution was added into 5 mM HCl. This solution was degassed using a vacuum pump before using. Sputtered electrodes were electroplated using the three-electrode setup (Pt as counter and Ag/AgCl as the reference electrode) by applying -0.7V for 15 min.

Detection of miRNA in buffer: Probe DNA was covalently attached onto nanostructured Au electrodes modified by drop depositing 3µL of 5 µM probe ssDNA. The electrodes were incubated overnight at 4°C. 10 mM of MCH was deposited as surface blocker with incubation time of 30 min. 3 µL target miRNA of different concentrations were drop deposited and incubated for 45 min at 37°C under constant shaking. Finally, 100 nM of methylene blue (MB) conjugated DNAs were deposited and incubated for another 45 min at 37°C under constant shaking. Electrodes were washed by wash solution (25mM PBS, 25mM NaCl) after each step. For both steps of the hybridization, the hybridization buffer contains 20 mM $MgCl_2$ in 1X PBS.

The DNA and RNA sequences used are as follows:

To-detect miRNA 200b

Probe DNA: 5'- SH TCA TCA TTA CCA GGC AGT ATT A -3'

miRNA 200b: 5’-UAA UAC UGC CUG GUA AUG AUG A-3’

Signaling barcode for miRNA 200b: 5’-UAA UAC UGC CUG GUA AUG AUG A-(methylene blue)-3’

To detect miRNA 21

Probe DNA: 5'-SH TCA ACA TCA GTC TGA TAA GCT A -3’
miRNA 21: 5’-UAG CUU AUC AGA CUG AUG UUG A - 3’
Signaling barcode for miRNA-21: 5’-UAG CUU AUC AGA CUG AUG UUG A –(methylene blue)-3’

Non-complementary target: 5’-TTT TTT TTT TTT TTT TTT TTT T-3’

Limit of Detection Calculation: The highest concentration of signaling barcode (methylene blue-tagged DNA) will hybridize when there is no miRNA 200b. Therefore, the highest redox peak current will be obtained when hybridizing with the buffer ($I_{no-target}$). As the miRNA 200b concentration becomes higher, less signaling barcode will be able to hybridize with the electrode and therefore the redox peak current of methylene blue will reduce with the concentration of miRNA 200b. To be able to quantitatively determine the target, the signal is defined by the percentage change of methylene blue redox peak current when the concentration of miRNA 200b is “x” vs. when there is no miRNA 200b.

$$\Delta I = \frac{I_{target\ with\ x\ conc} - I_{no-target}}{I_{target\ with\ x\ conc}}$$

Calculation of limit-of-detection (LOD) was performed by plotting the differential signal versus the log of miRNA 200b concentration in the log-linear range from 100 aM to 100 pM. The log-linear equation of the fitted line is ΔI (%) = 25.4 $\log_{10}C$ + 38.3 with a correlation coefficient of 98.85%. LOD is calculated by calculating the concentration of miRNA 200b, where ΔI becomes equal to the limit-of-blank (LOB). Non-complementary target was used to calculate LOB, which is defined as:

$$\mathrm{LOB} = \Delta I_{\mathrm{blank}} + 2.575 \times \sigma_{\mathrm{blank}}$$

Where, the factor 2.575 is used to calculate LOD within 99% confidence interval and σ_{blank} is the standard deviation of the blank signal.

EV and Urine Sample Analysis: EVs were obtained from the human prostate cell lines PNT1A, 22Rv1, LNCaP and PC3. After harvesting, the EVs were diluted in a solution containing 1X PBS and 20 mM $MgCl_2$ to ensure that each EV sample has a concentration of 10^{10} particles/mL. Before putting the EVs onto electrodes, EVs were lysed by adding 1% Triton X100 (lysis buffer) in a 1:4 ratio. The mixture was incubated for 30 min at room temperature, while vortexing in every 10 min.

For the assay in urine samples, the urine was first diluted in a buffer containing 1X PBS and 20 mM $MgCl_2$ in order to have creatinine level 0.1 µM. After that 5 µL of lysis buffer was mixed into 195 µL of diluted urine. The mixture was kept for 30 min under intermittent vortex. This mixture was used as a target solution for the microRNA detection assay.

Electrochemical Measurements: Electrochemical measurements were performed with PalmSens4 (PalmSens, BV) potentiostat. All electrochemical experiments were performed in a three-electrode cell setup, where Ag/AgCl works as reference electrode, Pt as counter electrode and nanostructured Au as working electrode. Square wave voltammetry (SWV) scan was performed for a potential range of -0.1V to -0.5V to measure the reduction peak of MB. The electrochemically active surface area was determined by performing CV scan in 0.1 M H_2SO_4 at a scan rate of 0.05V/s and a voltage range between 0V and 1.5V. Electrochemical impedance spectroscopy was performed under open circuit potential in 2 mM $[Fe(CN)_6]^{4-/3-}$ solution containing 10mM PBS.

Cell culture and EV concentration: In a humidified atmosphere of 37°C and 5% CO_2, cells were grown in complete media. 22Rv1, PNT1A and LNCaP cell lines were cultivated in RPMI supplemented with 10% fetal calf serum (FCS) and 1% penicillin/streptomycin and PC3 cell line in Ham´s F-12 with 10% FCS and 1% penicillin/streptomycin. Cell viability and mycoplasma PCR test were routinely performed.

For EV isolation, cells were washed twice with 10 mL PBS at an 80% cell confluence. Subsequently, cells were cultivated for 24 h (22Rv1, PNT1A cells) and 30 h (LNCaP, PC3 cells) respectively, in 30 mL media without FCS per 175 cm^2 flask. To remove cells, the supernatant was centrifuged for 10 min at 300xg. The cell-free supernatant was stored at -80°C or directly filtered using a 0.22 µm PES bottle top filter (Millipore) to remove large particles followed by ultrafiltration using Centricon-70 centrifugal filters of 100 kDa MWCO (Millipore). After pre-washing of the filters with 30 mL PBST (0.1%) twice each by 5 min centrifugation at 3500 x g at 4°C, the filtered supernatant was concentrated at 1500 x g at 4°C. The centrifugation time depended on the concentration factor and the loaded volume (approximately 10 min for 100-fold concentration of initially 60 mL supernatant). The ultrafiltrated supernatant was recovered by an up-side-down spin of 2 min at 1000xg and 4°C. Samples were aliquoted and stored at -80°C.

Clinical samples: Urine samples from a cohort of 5 prostate cancer patients with a Gleason Score (characterizing morphological properties of the tumor) of 8-9, an age in the range of 62 to 71 years and a Prostate Specific Antigen (PSA) level between 5.4 and 34.5 ng/mL were used as clinical samples. Samples from 5 patients, aged 66 to 78, with a PSA level below 4 ng/ mL were used as basal controls. Collecting biological plasma samples was performed with the approval of the Ethical Committee of the university medical center in Mannheim (2015-549N-MA) and the participants provided written informed consent.

EV concentration from Urine: Sediment-free urine samples, stored at -80°C, were thawed overnight at 4°C. The urine samples were centrifuged for 30 min at 3000xg at 4°C, the pellet was subsequently resuspended in 1 mL NaCl with 100 mg/mL (w/v) DTT and incubated at 37°C for 10 min with vortexing every 2 min. After a second centrifugation step for 30 min at 3000xg at 4°C, the resulting supernatant was pooled with the one from the first centrifugation step and filtered by a 0.22 µm PES bottle top filter (Millipore). Subsequently, ultrafiltration was performed using Amicon 20 centrifugation filter (Sartorius) of 10 kDa MWCO. The filters were washed twice with 20 mL PBST by centrifugation for 5 min at 3500xg. Urine supernatants were centrifuged for 15 min at

3500xg at 4°C and washed with PBS. The ultrafiltrated supernatants were aliquoted and stored at -80°C.

Protein and creatinine quantification assay: Protein concentration of the ultrafiltrated urine samples was determined by the Qubit® Protein Assay Kit (Thermo Fisher Scientific) according to the manufacturer's recommendations. 10 µL of the three standards and 1 µL of the urine samples were incubated in a final volume of 200 µL by adding 1:200 diluted working solution. After 15 min at room temperature the protein concentration of the sample was analyzed using the Qubit® 4 Fluorometer device (Thermo Fisher Scientific).

Urine creatinine levels were determined after ultrafiltration using the CREJ2 Creatinine Jaffé Gen.2 kit by the automated Roche/ Hitachi comas c311 analyzer (Roche Diagnostics) as described in the manufacturer´s manual.

Nanoparticle Tracking Analysis (NTA): Nanoparticle tracking analysis (NTA) of ultrafiltrated samples was carried out by the NanoSight LM-10 (Malvern) using the NanoSight NTA 3.0 software. The sample chamber was flushed with 10 mL MilliQ H20 and 10 mL PBS (gibco) in between the samples. Samples were diluted with PBS in an appropriate volume and measured at 25 °C on a stable table ST-140. Three measurements of 60 sec were recorded in the capture mode with a gain of 3.9 and a camera level of 13. For analysis, the gain and the detection threshold were set to 5. In subsequent experiments the particle number was used for normalization.

Western Blotting : Samples were heated for 5 min at 70°C in 6x Laemmli buffer (0.375 M Tris-HCl, 0.6 M DTT, 60% glycerol, 12% SDS, 0.06% Bromphenol blue) prior loading on

4 - 20% stain-free SDS-PAGE gels (Bio-Rad). Protein separation according to their size was performed by electrophoresis in a mini-chamber (Bio-Rad, Germany) at 80 V for 20 min followed by 140 V for 100 min in Towbin buffer (0.025 M Tris-base, 0.192 M glycince, pH 8.6). After fluorescent activation using the ChemiDoc device (Bio-Rad, Germany) total protein staining was observed directly. Next, the gel was prepared for transfer to a 0.2 µm nitrocellulose membrane (GE Healthcare) by rinsing twice in ddH_2O followed by equilibration in cathode buffer (48 mM Tris-base, 39 mM glycine, 20% methanol, 0.05% SDS). A sandwich of extra thick Whatman paper and membrane both soaked in anode buffer (48 mM Tris-base, 39 mM glycine, 30% methanol) were placed on a semi-dry western blot chamber (Bio-Rad, Germany) followed by the equilibrated gel and another extra thick Whatman paper soaked in cathode buffer. Protein-transfer to the membrane was achieved at 25 V for 45 min. Immediately blocking of the membrane in 5% BSA in PBST (0.1%) for 1h at room temperature (RT) was performed prior 1:1000 in blocking buffer diluted primary antibody incubation overnight at 4 °C under agitation. After three washing steps of 5 min in PBST at RT, the incubation with the secondary HRP-conjugated anti-mouse antibody (Dianova, Hamburg, Germany) in a final dilution of 1:10000 in blocking buffer for 1h at RT followed. Before analysis, two washing steps for 5 min each with PBST and PBS were carried out. ECL substrate (Bio-Rad, Germany) was applied and signals were detected by the ChemiDoc device with a suitable exposure time.

Transmission electron microscopy (TEM): For TEM imaging, 3 µL of ultrafiltration-enriched EVs were incubated for 1 min at RT on formvar coated electron microscopy cooper grids (200 mesh, Plano GmbH). Three H_2O washes followed before negative staining using 2% uranyl acetate in H_2O for 1 min at RT. Drying was completed after removal of excessive liquid and overnight resting of the grids at RT prior to imaging on a Libra 120 (Zeiss Microscopy GmbH).

Scanning electron microscopy (SEM): Nanostructured electrode surface was visualized by using FEI Magellan 400 scanning electron microscope (SEM) at Canadian Centre of Electron Microscopy (CCEM).

7.4 Results and Discussion

To build the inverse signal-to-concentration assay with high sensitivity and specificity for miRNA analysis, we developed a high surface area hierarchical transducer made from nanostructured gold building blocks assembled into a star-shaped millimeter-sized electrode (supplementary Figure S7-1a).[296] This hierarchical transducer was modified with ssDNA capture probes specific to miRNA200b using gold-thiol chemistry. The detection and quantification of miRNA200b was performed by first capturing the unlabelled target miRNA using the capture probe followed by incubating the same electrode with the signaling barcode, a ssDNA strand modified with a redox species (methylene blue) and having the same sequence as the unlabelled target (Figure 7-1a). The signaling barcode is designed to hybridize with the unreacted capture probes to generate a signal that is inversely proportional to the concentration of the unlabelled target: as the target concentration becomes lower, a larger fraction of unreacted probes become available for binding the signaling barcode, thus, increasing the measured redox signal. The structure of the nanostructured electrodes was examined by scanning electron microscopy (SEM), which confirms the nanostructure formation and hence enhanced surface area (Figure 7-1b). Electrochemical impedance spectroscopy (EIS) was performed to characterize the different steps that were involved in assay engineering (Figure 7-1c). The charge transfer resistance (R_{ct}) - obtained from the diameter of the semicircle[480] - of the hierarchical transducer increases after the deposition of the capture probe and mercapto hexanol used as a surface blocker (Supplementary Figure S7-2), because these molecules hinder the access of the negatively charged redox species ($[Fe(CN)_6]^{3-/4-}$) to the transducer surface via electrostatic repulsion and/or steric hindrance.[482] The R_{ct} further increases after hybridization of the capture probe with the unlabeled miRNA target; however, it decreases after binding of the signaling barcode at the transducer surface (Supplementary Table S7-1). The redox label, methylene blue, available at the redox barcode improves electron transport between the electrode and the electrolyte,[483] thus reducing the R_{ct}.

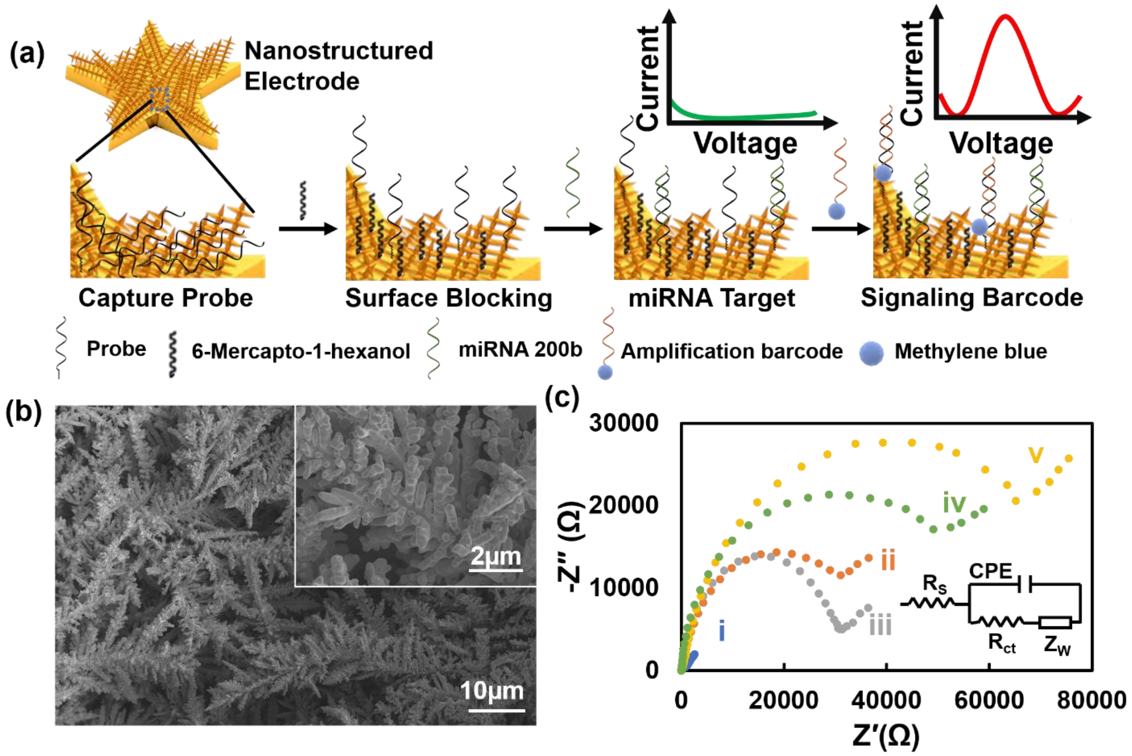

Figure 7-1: (a) Schematics illustrating the microRNA detection architecture. (b) SEM image of the nanostructured electrodes (inset showed magnified image of the structure). (c) Nyquist diagram showing effect of surface change in each step of the microRNA sensor fabrication. (i) Nanostructured Au electrode, (ii) After capture probe deposition (iii) After MCH deposition (iv) Hybridization with miRNA 200b (v) After incubating with MB-DNA. Inset showing the equivalent circuit models obtained from the EIS data. R_s, R_{ct}, Z_w and CPE indicate the solution resistance, charge transfer resistance, Warburg impedance and constant phase element, respectively.

The reverse concentration-to-signal assay was interrogated with synthetic miRNA 200b within a wide concentration range (100 aM to 100 pM). As hypothesized, the redox peak current (observed approximately at -0.3 V vs. Ag/AgCl) monotonically increased with decreasing the miRNA concentration (Figure 7-2a). The current change, quantified against the blank signal ($I_{no-target}$), demonstrated a linear relationship with the log concentration of miR-200b in the 100 aM-100 pM range, leading to the remarkable limit-of-detection of 122 aM (with 99% confidence interval) (Figure 7-2b). A sensitivity of 25.4% /$\log_{10}$ M was obtained from the linear fit of the calibration curve. The specificity of the assay was further verified by using 1 pM miRNA 21 as target, which showed large difference in the differential signal in comparison with 1 pM miR-200b (supplementary Figure S7-3).

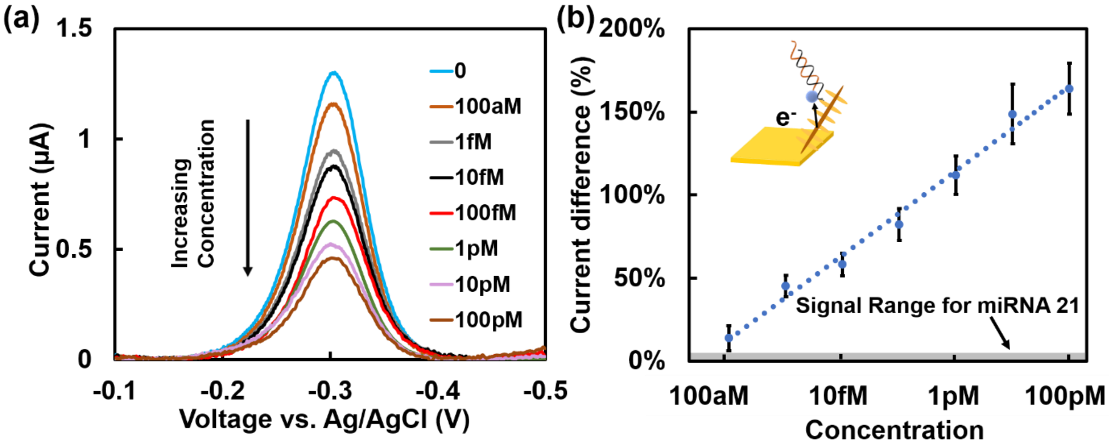

Figure 7-2: Dependence of target concentration in square wave current after introducing signaling barcode. All measurements were performed by using 25 mM NaCl in 25 mM PBS solution as electrolyte. (a) Representative square wave voltammograms for different concentrations of miRNA 200b. The reduction peak at (b) Calibration curve obtained using the percentage difference of redox peak current $((I_{target}-I_{no-target})/I_{target})$ at varying miRNA 200b concentration. The log-linear region of the calibration curve was fitted using the equation $\Delta I(\%) = 25.4 \log_{10}C + 38.3$ with correlation coefficient of 98.85%. Error bars are calculated by measuring at least 3 samples.

To validate the effectiveness of the reverse concentration-to-signal assay in miRNA analysis, we sought to analyze cell lines that were expected to contain free circulating and vesicular microRNA.[484] Four different cell lines, PNT1A, 22Rv1, LNCaP and PC3, were selected as they are commonly used for biomarker analysis in human prostate cancer. Among these cell lines, PNT1A is normal prostate epithelial cell line,[485] whereas 22Rv1, LNCaP and PC3 are the human prostate cancer cell lines of separate origins (22Rv1 is localized to prostate, LNCaP and PC3 is derived from metastatic tumors).[486] The cell lines were first processed using ultracentrifugation and ultrafiltration to concentrate the EV and remove the cellular background (Figure 7-3a).[457,487,488] These processed cell lines were subsequently analysed using nanoparticle tracking analysis (NTA), transmission electron microscopy (TEM), and western blotting to characterize the size, morphology, and protein markers associated with the EVs. This analysis demonstrated the presence of EVs in the 50-200 nm size range (Supplementary Figure S7-4). NTA data further provides the concentration of EVs in each cell line, which is crucial for normalization before comparing the miRNA 200b concentration from the EVs. TEM image shows the presence of EVs in the supernatant and further confirms that particle diameters are less than 200 nm (Figure 7-3b). Additionally, all the extracted EVs were shown positive for CD9 and negative for calnexin (Figure 3c), which confirms the successful separation of small EVs from the cell lysates.[489] It should also be noted that the three cancer cell lines showed higher expression of CD9 protein in the EV than the normal cell line (PNT1A) (Figure 7-3c), which is expected as CD9 positive EVs were shown to contribute to the progression of prostate cancer because of its role in paracrine signaling.[490] Moreover, TSG101 – a luminal EV marker[491] - is positive for the three cancer cell lines (22Rv1, LNCaP, and PC3) and negative for normal cell line (PNT1A).

In order to release the vesicular miRNA, the processed cell lines were further lysed using commercially available lysis buffer (Triton X-100). The processed cell line lysates were introduced on the transducer surface and the electrochemical measurements indicated the highest miRNA 200b level in the PNT1A cell line (Figure 7-3d and Figure 7-3e). This is expected as miRNA 200b is commonly downregulated from normal levels for prostate cancer patients.[492,493] As expected, the cancer cell lines demonstrated a lower concentration of miR-200b as evidenced by the lower ΔI measured by the reverse concentration-to-signal assay. In order to validate our result from EVs, we modified nanostructured Au electrodes with capture probe that is complementary with miRNA21. which has been reported to be upregulated in prostate cancer.[494,495] As expected, ΔI showed higher value in the prostate cancer cell lines 22Rv1, LNCaP, and PC3 than normal cell line PNT1A, when modified by capture probe complementary to miRNA 21. (Figure 7-3f and Figure 7-3g).

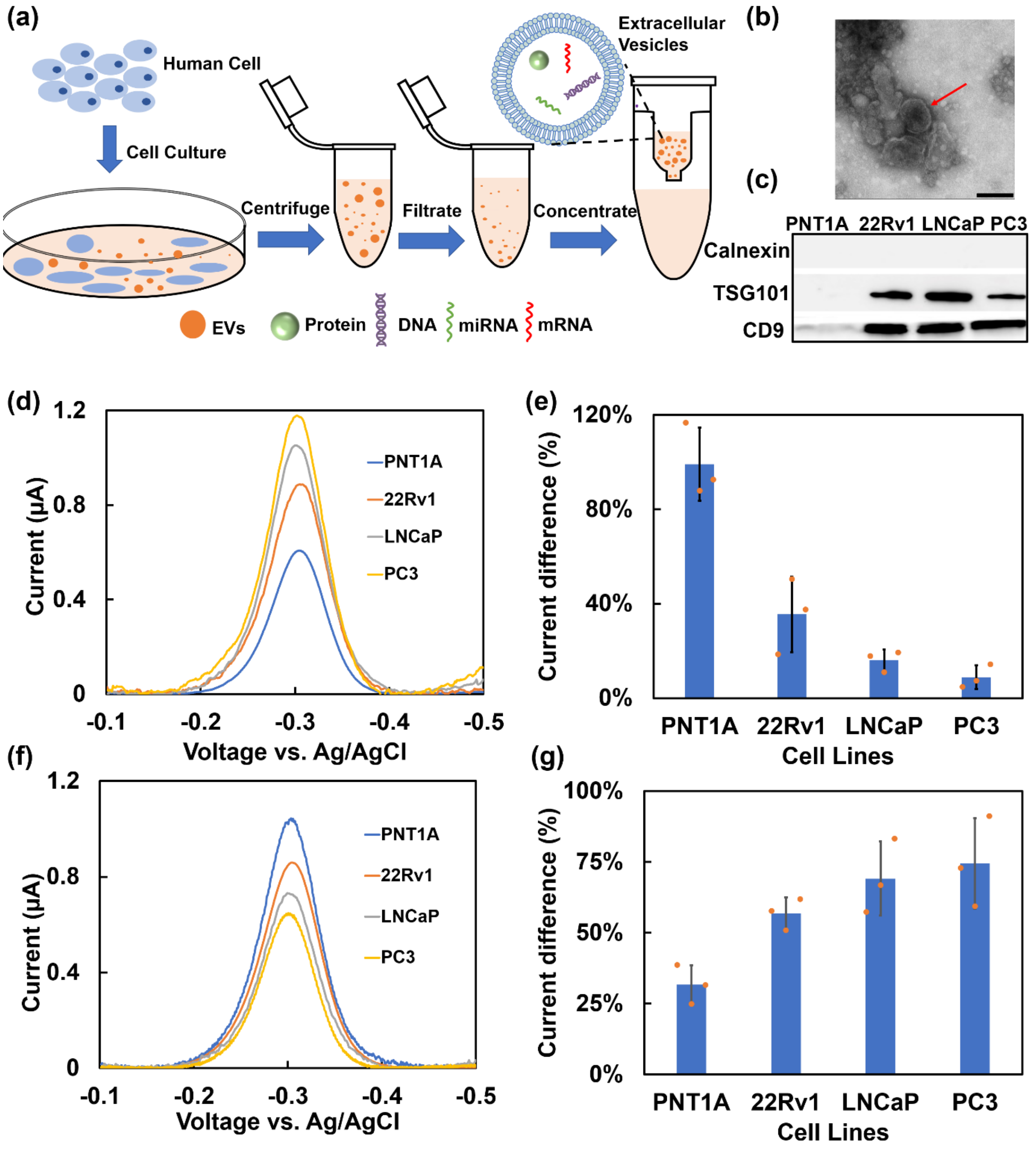

Figure 7-3: EV extraction from cell lines and their characterization and electrochemical measurements. All measurements were performed by using 25 mM NaCl in 25 mM PBS solution as electrolyte. (a) Schematics showing the steps of the EV extraction procedure from cell lines. (b) Transmission electron micrograph obtained from cell line 22Rv1 proving the existence of EVs (indicated by arrow) in the supernatant. Scale bar represents 100 nm. (c) Western blot analysis of protein markers (Calnexin, TSG101, and CD9) in small EVs. (d) and (e) showed representative square wave voltammograms for different EV-enriched supernatants obtained from prostate cell lines and the percentage difference of redox peak current when the electrochemical measurements were performed to detect miRNA 200b, respectively. (f) and (g) showed representative square wave voltammograms for different cell lines and the percentage difference of redox peak current when the electrochemical measurements were performed to detect miRNA 21, respectively. Error bars are determined by measuring at least 3 samples.

In addition to miRNA analysis in processed cell lines, we performed a blinded diagnostic study using the reverse concentration-to-signal assay with clinical urine samples from a cohort of ten patients (Figure 7-4 and Figure 7-5). Each patient was recognized by an ID of 3-digit number (7xx) (Supplementary Table S7-2). Based on diagnosis performed using the PSA levels and the Gleason scores, five of these patients were positive and five were negative for prostate cancer. Gleason score is determined by performing biopsy of the cancer tissue and used as prognostic indicator.[488]

The clinical urine samples were processed and characterized using similar methods as used with the cell lines (Figure 7-4a), indicating the presence of small EVs in the processed samples. The distribution of particle size with 80% of the particles found to be between 110 and 290 nm in diameter, where the mean diameter size was 194.3 ± 1.3 nm obtained from the NTA measurement (Figure 7-4b). TEM image further confirms the existence and size of the EVs (Figure 7-4c). Total protein was measured using stain-free gels, indicating no significant difference for both benign and cancer patients (Figure 7-4d). In order to further characterize the EV content and finding the effectivity of protein marker for patient diagnosis, we performed western blot analysis for the EV biomarkers CD9, TSG101, CD63, Beta-actin, PSMA, Calnexin and Tamm-Horsfall Protein (THP) (Figure 7-4d). Tetraspanin protein CD9 and CD63, and luminal EV protein TSG101 have been shown as highly expressed in cancer cell lines in comparison to normal cell lines and thereby considered as biomarker for prostate cancer.[490,496] The prostate specific membrane antigen (PSMA), located in the cytosol, is over-expressed and shifted to a membrane-bound protein.[497,498] The expression level of CD9 did not show any difference between the normal and patient urine samples. Although, EV extracted from cancer cell lines were CD9 positive in compare to normal cell line (Figure 7-2c), urinal EV analysis did not show such correlation. Both luminal EV protein, TSG101 and tetraspanin protein, CD63 was found in all samples except for the healthy donors 743 and 728. It should be noted that the total protein for these two patients were also lower than other samples, and therefore, these two proteins also do not serve the purpose of urinal biomarker of prostate cancer. Although, beta-actin have not been considered as diagnostic protein, some studies found higher expression of beta-actin in tumor cells compared to normal one.[499,500] All five cancer patients are found to be beta-actin positive, whereas the healthy patients are beta-actin negative, except patient TW773. Protein bands corresponding to PSMA were detected in only 2 tumor samples (777, 767), while the healthy controls showed PSMA bands in 4 of the 5 individuals. Therefore, using PSMA for diagnosing prostate cancer from urine is also not sufficient to provide specificity. As expected, calnexin (negative control), a protein localized in the endoplasmic reticulum and absent in EVs, was not found in any of the samples, whereas the urinary protein THP was observed in every sample. Expected behavior obtained from the control proteins further confirms successful EV extraction from urine. This characterization demonstrated that none of the protein biomarkers can be considered as specific biomarker for prostate cancer when analysis was performed from urine EVs.

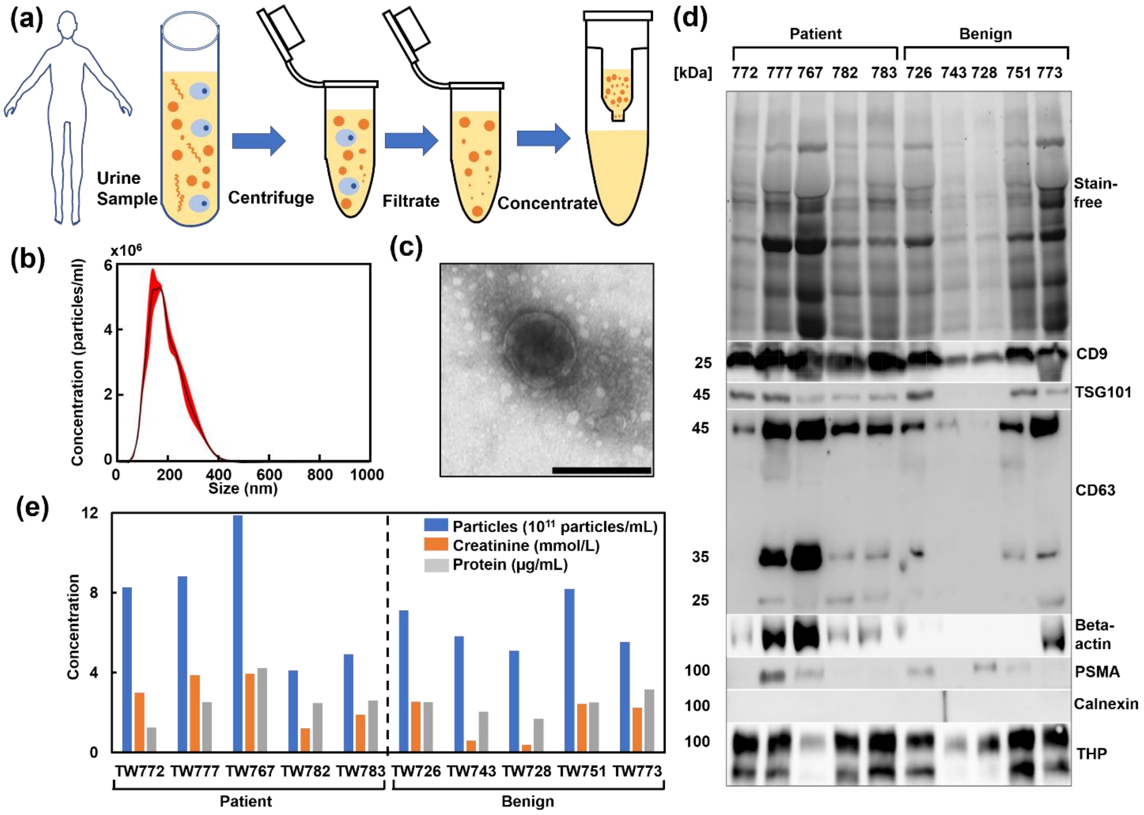

Figure 7-4: EV extraction from human urine samples and their characterization (a) Depiction of the EV extraction steps after collecting urine samples from patients (b) Nanoparticle tracking analysis to determine the mean size and concentration of particles. (c)TEM micrograph proving the existence of EV in the processed urine samples (Scale bar represents 200 nm). (d) Characterization of the ultrafiltrated samples by SDS-PAGE of total protein and by western blot for CD9, TSG101, CD63, beta-actin, PSMA, calnexin and THP. Enrichment of EVs from human male urine of healthy donors and prostate cancer patients by ultrafiltration (MWCO 10 kDa) shown as scheme. The number at the left indicates the size of the protein ladder used. (e) Total concentration of particles, creatinine, and protein for each urine samples.

However, urine samples range from a very diluted to a very concentrated solution depending on the patients drinking behavior and diet.[491,501] Therefore, It is important to normalize the individuals in order to compare miRNA200b concentration among different urine samples using the developed electrochemical sensor. Concentration of EV might not be suitable for normalization due to reported increase in EV release in cancer patients.[502] Although, creatinine concentration is frequently used for urine biomarker normalization, effectivity of this method for miRNA concentration from urine EV is yet to be proved.[501,503] Some studies also reported protein expression level for urinal EV normalization.[491] In order to determine the proper normalization parameter for urine samples, we compared both creatinine and protein concentration with total particle concentration (indicates a measure of EV concentration) (Figure 7-4e). The particle concentration is usually used to indicate EV concentration as there is no standard method for only detecting EV from the complex biological matrix. The correlation coefficient between creatinine and EV concentration is much higher (83%) than the correlation coefficient between protein and EV concentration (46%). Therefore, creatinine concentration was used to normalize urine samples for electrochemical analysis.

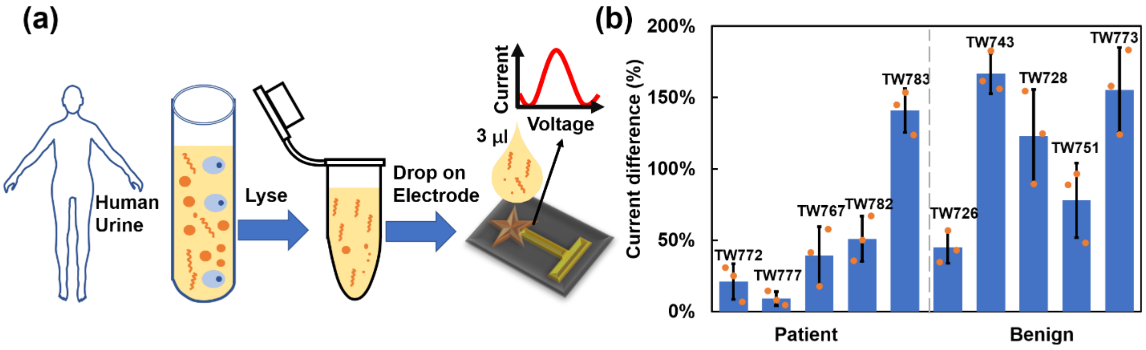

Figure 7-5: Electrochemical detection of miRNA200b to diagnose prostate cancer patients (a) Schematics showing the steps from urine sample collection to electrochemical analysis which only involves lysing the sample after normalizing. (B) Percentage of current difference between blank and patient sample. The error bars represent one standard deviation of the redox peak current obtained from three electrodes.

The analysis of patient urine samples using the reverse concentration-to-signal assay was performed by only using the commercially available lysis buffer directly on the collected urine (Figure 7-5a). After normalizing the lysed urine samples to creatinine value, it was dropped onto the nanostructured Au electrode to determine the current difference from the patient samples to the blank solution (Figure 7-5b). Eight out of the ten samples were diagnosed correctly, except TW783 and TW 726. From this two, TW726 was detected in our sensor as prostate cancer patient whereas the patient is considered at benign stage according to the conventional PSA level, which is 3.9 ng/mL. It should be noted that the PSA level is very close to the clinical threshold value of 4.0 ng/mL, which indicates the individual may be at the risk of onsetting the cancer progression.

Receiver operating characteristic (ROC) curve was obtained by plotting the sensitivity of the diagnostic tests using the electrochemical approach as a measure of false positive (1-specificity) to evaluate the sensor performance based on the patient sample data (supplementary Figure S7-5). According to this plot sensitivity/specificity combination of 80/80% was achieved using the revers concentration-to-signal assay. We acknowledge that, more reliable clinical performance metrics has to be obtained using a larger number of patient samples.

7.5 Conclusion

This work introduced a novel bioassay design for electrochemical detection of miRNA. Although microRNA 200b is used as the model target in this work, the proposed biosensor work can be applied to any single stranded nucleic acid detection (DNA or RNA of length 15-25 mer). Electrodeposited Au Nanostructure electrodes provide more than an order of magnitude higher electrochemically active surface area. These nanostructured electrodes help to achieve a limit-of-detection of 122 aM for synthetic micro-RNA in hybridization buffer. SEM were used to image the electrodes while EIS was used to verify the stepwise modification of the electrodes. These electrodes were then challenged with exosomes extracted from PCa cells and healthy cells. Downregulation of miRNA 200b was observed in the PCa cells, which correlated with previous reports in the literature.[492,504] However, depending on the developmental stage of PCa development, the miR-200b expression may vary. This aspect has not been fully understood and requires further investigation. The biosensor developed here can also provide low-cost platform for research. Furthermore, these electrodes were tested by using urine samples from 10 patients without knowing their PSA level before testing (blind-test). The biosensors showed sensitivity of 80% while maintaining a specificity of 80%. Therefore, in order to detect more reliably, multiple micro-RNA should be used. It should be noted that the quantitative detection of micro-RNA not only helps us to diagnose the patient, it can also be very useful in the prognosis process.

7.6 Acknowledgement

This work was supported by MITACS globalink award grants to S.S. The SEM imaging was obtained at the Canadian center for electron microscopy (CCEM). S.S. is also the recipients of NSERC doctoral scholarships. We also thank Dr. Alexander Ewe of the Rudolf-Boehm-Institute of Pharmacology and Toxicology at the University of Leipzig for support and supply of the NanoSight device for NTA. In addition, we would like to thank Dr. Gerd Hause of the Microscopy Unit at the Biocenter of the University of Halle-Wittenberg in Halle for TEM imaging and Dr. Gábor Köller at the Faculty of Veterinary Medicine of the University of Leipzig for creatinine determination. We would also like to thank Dr. Thomas Worst from the university medical centre in Mannheim for providing

the clinical samples. SEM images were obtained from Canadian Centre for Electron Microscopy (CCEM), which is a national facility.

7.7 Acknowledgement

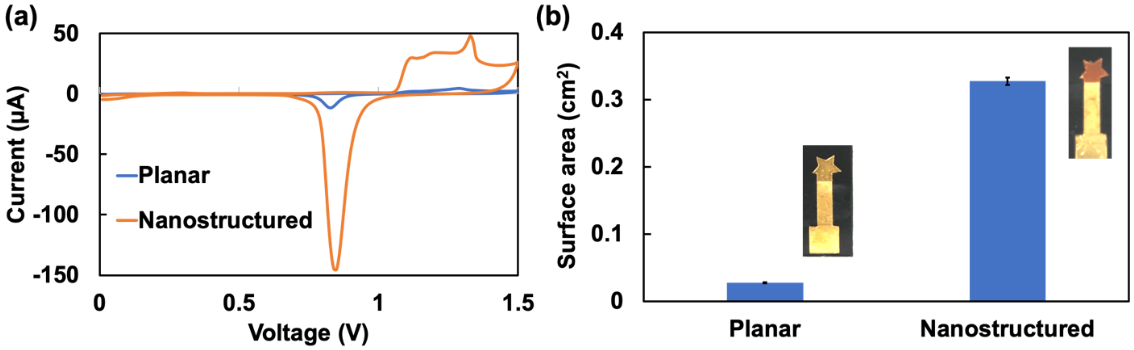

Figure S7-1: (a) Sulfuric Acid (H_2SO_4) scan to determine the surface area of planar and nanostructured electrodes. (b) Average surface area and photographs of planar and nanostructured Au electrodes.

Electroactive surface area was calculated from the CV scan in 0.05M H_2SO_4.[505] The cathodic peak current and area enhanced significantly after hierarchical growth of Au nanostructures. Almost 12 times enhanced surface area is obtained (Figure S7-1b). The color of the electrodes also changed after the nanostructure formation.

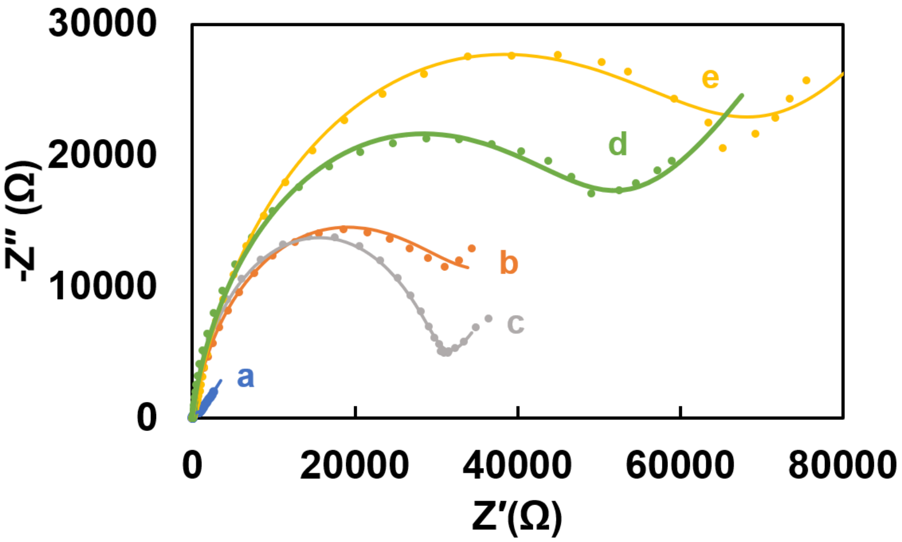

Figure S7-2: Experimental data (dots) and fitted with the equivalent circuit model (line) in each step of the microRNA sensor fabrication. (a) Nanostructured Au electrode, (b) After capture probe deposition (c) After MCH deposition (d) Hybridization with miRNA 200b (e) After incubating with MB-DNA.

Figure S7-2 **s**hows the EIS data overlapped with the data obtained from equivalent circuit model. The equivalent circuit model is in good accordance with the experimental data.

Table S7-1 : Data obtained from equivalent circuit model in each step of bioassay formation:

Steps in Bioassay formation	**R_{ct} (kΩ)**	**CPE (μF)**	**n**
Nanostructured Au	0.72	1.6	0.9
After Capture probe	34.6	4	0.9
After MCH deposition	29.8	3	0.93
After target hybridization	64.5	1.1	0.83
Hybridization with MB-DNA	48.5	1.3	0.87

Table S7-1 lists the parameter that was obtained from the circuit model.

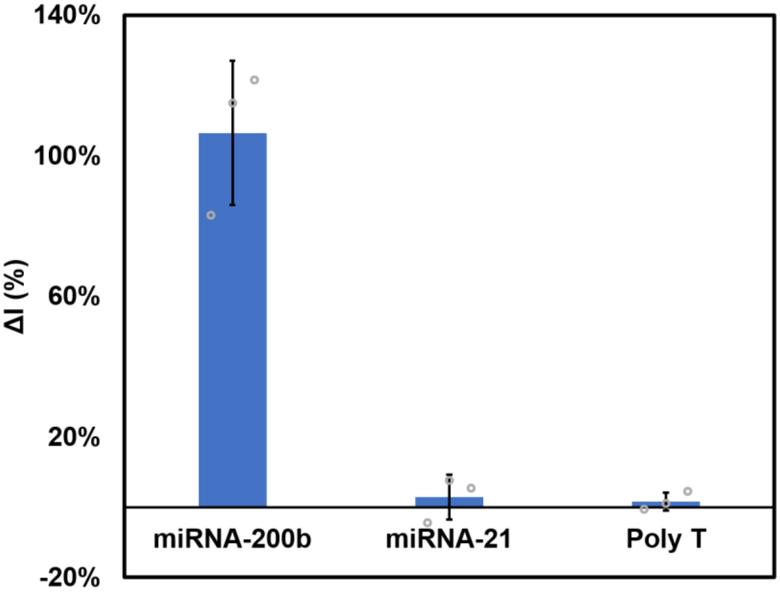

Figure S7-3 : Differential signal obtained when hybridized with miRNA-200b, miRNA-21 and poly T

Figure S7-3 showed the differential signal obtained by running the bioassay where miRNA 21 and poly T is used as non-complementary target. The concentration of the nucleic acids was kept at 1 pM. miRNA 21 is used to test the specificity as it is found to be upregulated for prostate cancer cells.[494,506]

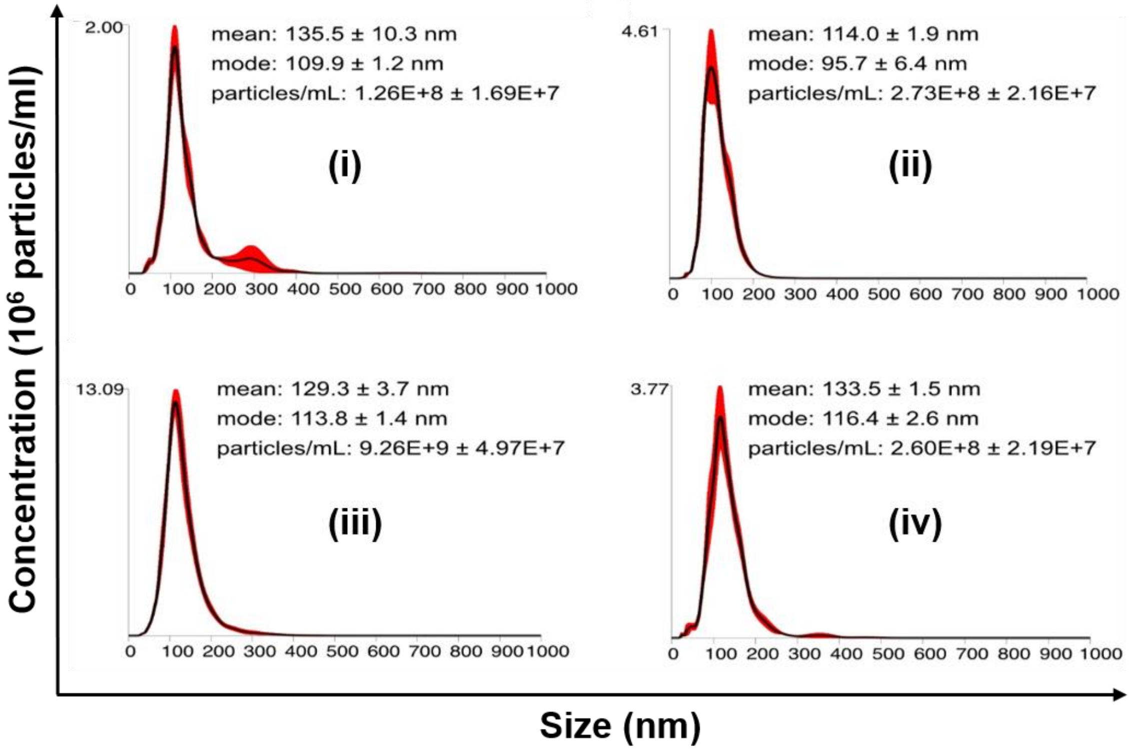

Figure S7-4: Nanoparticle tracking analysis of the extracellular vesicles obtained from human cell lines. (i), (ii), (iii) and (iv) show the mean size and concentration of particles for cell lines PNT1A, 22Rv1, LNCaP and PC3, respectively.

Figure S7-4 shows the nanoparticle tracking analysis (NTA) characterization data for the supernatant collected from human cell lines PNT1A, 22Rv1, LNCaP and PC3. NTA analysis found similar concentration of EVs in all four cell lines.

Table S7-2: Table showing information about PSA level and medication is being used by the patients and the decision from the electrochemical sensor developed in this work

Patient Identification Number	Condition (Gleason Score)	Decision From Nanostructure Au Electrode	PSA Level (ng/mL)	Current Medication
726	Benign	Patient	3.9	Urorec
728	Benign	Benign	2.99	Duodart
743	Benign	Benign	0.95	No medication
751	Benign	Benign	3.5	Urorec

773	Benign	Benign	0.93	No medication
767	Patient (9)	Patient	6.8	Finasterid
772	Patient (9)	Patient	6.71	No medication
777	Patient (9)	Patient	34.50	Urorec
782	Patient (9)	Patient	5.4	No medication
783	Patient (8)	Benign	28	Tamsulosin

Table S7-2 lists the PSA level, Gleason Score and the current medication received by the patients. The electrochemical test was performed without being informed these parameters. After the electrochemical tests, the data was obtained to verify the test result. The Red line showed where the electrochemical device has wrong detection. It is noted that 8 of the 10-sample showed correct detection of miRNA 200b.

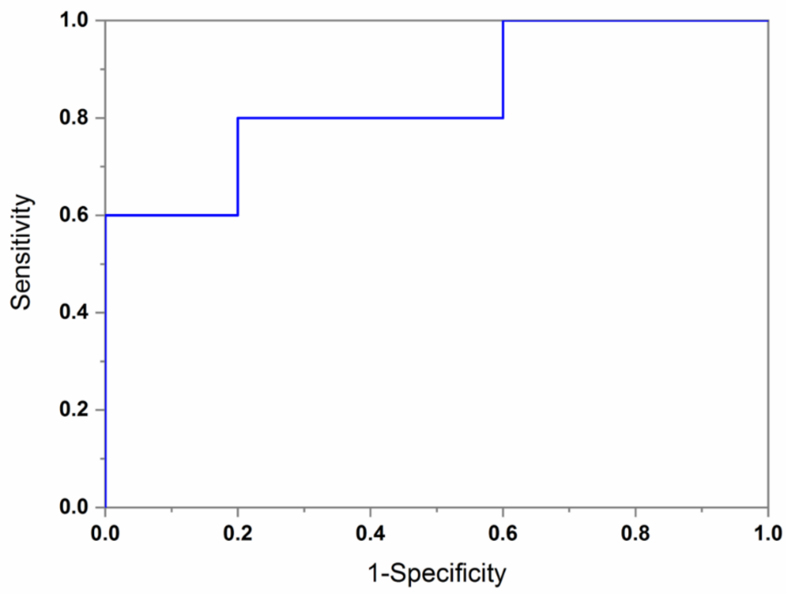

Figure S7-5: Receiver Operating characteristic (ROC) curve for the electrochemical test performed on 10 urine samples.

Chapter 8 Photoelectrochemical detection of nucleic acid from urine samples

Chapter Introduction (Objective IV)

In Chapter 7, we demonstrated electrochemical nucleic acid sensing by introducing a redox-labeled DNA strand to the electrode surface. The current readout obtained in this approach was inversely proportional to the analyte concentration. In this chapter, we have utilized a similar bioassay design for PEC transduction. In this instance, the nanostructured Au electrodes were replaced by mesoporous TiO_2 electrodes, used in the previous chapters, with Au NP labeled DNA strands acting as signal-amplification-barcodes (SABs). The PEC readout strategy used in this chapter enabled us to combine the photocurrent change following target hybridization and SAB introduction. These two signals were combined to develop a differential sensing strategy. The differential strategy used in Chapter 6, has been shown to improve the sensitivity and LOD of the assay. By utilizing differential signaling here, we were able to detect single and double base-mismatches in the target sequence. Unlike the differential device used in Chapter 6, a single electrode is utilized to facilitate this process. Finally, this strategy worked effectively in human urine samples, with an LOD of 3 fM and 5 fM achieved for the target DNA spiked both in buffer and human urine samples, respectively.

Authors: Amanda Victorious, Sudip Saha, Richa Pandey and Leyla Soleymani (Equal contribution with Amanda Victorious)

Publication: Published in Angewandte Chemie in Jan 2021

8.1 Abstract

PEC biosensors hold great promise for sensitive bioanalysis; however, similar to their electrochemical analogues, they are highly affected by the variable backgrounds caused by biological matrices. We developed a new PEC biosensing strategy that uses differential signal generation, combining signals from two separate but correlated binding events on the biosensor, for improving the limit-of-detection, sensitivity, and specificity of PEC DNA biosensors in biological samples. In this assay, the binding of unlabeled target DNA is followed by the capture of a signal amplification barcode featuring a plasmonic nanoparticle. The interaction of the plasmonic barcode with the semiconductive building blocks of the biosensor results in significant signal amplification, and together with differential signal processing enhances the limit-of-detection and sensitivity of the assay by up to 15 and three times, respectively, compared to the previously-used PEC assays with a single binding event, demonstrating a limit-of-detection of 3 fM.

8.2 Introduction

Photoelectrochemical (PEC) biosensors have been heavily explored over the past decade due to their promise for improved signal-to-noise ratio and enhanced limit-of-detection.[285,419,507] These biosensors translate specific biorecognition events into a change in the output PEC signal.[419,508] As with their electrochemical analogues, the limit-of-detection of PEC transducers is often compromised due to signal fluctuations caused by environmental interferents and minute variations in experimental conditions.[78,82,509] In response, ratiometric or differential assays, combining two or more PEC signals, have been implemented to reduce the effect of interference and experimental variations, enhance detection accuracy at trace analyte concentrations, and improve analysis reliability.[371,421,424]

The existing ratiometric PEC biosensors typically use multiple photoactive species – signal reporters[230,232,424] or labels[421] – that need to be activated at various voltages[230,232] or wavelengths[421] in order to obtain multiple signal readings for each biorecognition event. Although this multi-species approach is effective in increasing the signal-to-noise ratio of PEC biosensors, it increases the complexity of the measurement instrumentation and the calibration algorithms needed to deal with the varying baseline signals and chemical and optical stability observed when multiple photoactive materials are used in a single system. For PEC biosensors to be translated from the laboratory to the market, it is highly desirable for high sensitivity and specificity to be paralleled with facile operation and instrumentation. As a result, new approaches for ratiometric/differential PEC signal transduction using a single photoactive species, operated at a single voltage using a single light source are needed.

Several PEC biosensors have recently been developed that use the interaction between plasmonic nanoparticles (NPs) such as Au and Ag with semiconductive photoelectrodes to translate biomolecular recognition to a change in the PEC signal.[224,251] Among these, systems that use robust and stable materials are highly desired for use in biosensing devices that undergo multiple washing, incubation, and potential scan steps. Au/TiO_2 systems offer excellent chemical and photostability and have been used in protein,[510] heavy metal,[511] glucose[512] and nucleic acid detection.[340] The major role of Au NPs in these sensing systems is to improve the photoconversion efficiency of the functionalized TiO_2 electrodes upon biorecognition, thereby enhancing the photocurrent. Depending on the assay design, different roles – injection of hot charge carriers, extending the light absorption range, and excitation of charge carriers in TiO_2 via plasmon energy transfer – can be played by the Au NPs upon target binding to modulate the photocurrent.[312,513,514] More specifically, biorecognition causes the Au NPs to either come into proximity[515] of (*signal-on*) or move away[312] from (*signal-off*) the TiO_2 electrodes. However, these bioassays only focus on harnessing the modulation of photocurrent influenced by Au NPs.

In this work, we sought to answer the question: Is it possible to effectively utilize and combine photocurrent modulation – both upon the capture of the unlabeled target and the binding of a plasmonic barcode (Au NP-modified DNA strand) – to achieve improved analytical sensitivity?

We aimed at developing a differential biosensor using the TiO_2/Au system, using Au NPs as the sole PEC species. To achieve this, we investigated the use of two subsequent and correlated PEC measurements. First, we measured the change in PEC current induced by the binding of an unlabeled target to a probe DNA. Second, we measured the additional PEC current change obtained when the unreacted probes were bound to a signal amplifying barcode (SAB) generated from AuNP-labeled DNA strands, for signal amplification. The signal changes measured during the two binding events were differentially combined to enhance the limit of detection (LOD) of the system. The use of SAB as an amplification sequence builds on the premise that plasmonic NPs in direct contact or close proximity to semiconducting materials possessing favorable energetics, modulate carrier lifetime,[365,516] thus, altering the PEC current. Using this differential strategy, the influence of background contributions is effectively suppressed, which in turn enhanced sensitivity by more than three times and LOD by 14 times compared to an analogues assay that measured a single binding event.

8.3 Experimental Procedure

Materials and Reagents: Phosphate buffer solution (PBS, 0.1 M, pH 7.4), Potassium ferricyanide(III) ($K_3Fe(CN)_6$), potassium hexacyanoferrate(II) trihydrate ($K_4Fe(CN)_6.3H_2O$) , L-ascorbic acid (99%), sodium chloride (NaCl), Magnesium chloride ($MgCl_2$), ethanolamine (MEA), chitosan (CHIT, from shrimp, degree of deacetylation of 85%, Mw=200,000), glacial acetic acid, 3,4-dihydroxybenzlaldehyde (DHB), Hexaammineruthenium (III) chloride ($Ru(NH_3)Cl_3$), Tris buffer, 4-arm polyethylene glycol (PEG) with molecular weight 5000 (PEG-5K), and tris (2-carboxyethyl) phosphine hydrochloride (TCEP, 98%) were purchased from Sigma-Aldrich. P25-titanium dioxide (TiO_2) was obtained from Nippon aerosol Co. Ltd. Acetone and Ethanol were purchased from commercial alcohols (Brampton, ON). Milli-Q grade (18.2 MΩ-cm) de-ionized (DI) water was used for all solution preparation and washing steps. 100 nm indium tin oxide (ITO) glass slides were purchased from Sigma-Aldrich.

Preparation of surface-modified TiO_2 Nanoparticles (NPs): TiO_2 NPs were prepared using the protocol reported by Victorious *et al.*[1] Briefly, 3gL^{-1} CHIT solution was prepared in 1% acetic acid. A 16gL^{-1} DHB solution was prepared in DI water. A DHB-modified CHIT solution was prepared by maintaining the mass ratio of 4:1 for DHB:CHIT. This solution was obtained by adding DHB solution to the CHIT solution. Finally, 60 mg of P25-TiO_2 was added to 15 ml of the DHB-modified CHIT solution.

TiO_2 substrate preparation: ITO glass substrates were treated with air plasma for 1 minute. Prior to the plasma treatment, substrates were masked using vinyl tape for separating contact area and electrode area. This was also used to ensure the uniformity of the geometric surface area of the electrode. TiO_2 films were prepared by placing 10 µL of the surface modified TiO_2 solution onto the ITO substrate surface and subsequently baking at 95°C for 5 minutes. This last step was repeated 3 times. Finally, the electrodes were washed and then air dried before using.

Gold (Au) nanoparticle synthesis: Citrate capped Au NPs were synthesized according to the protocol reported by Grabar *et al*.[345] Briefly, aqueous gold chloride ($HAuCl_4$) solution (1 mM) was mixed with 38.8 mM trisodium citrate solution with a volume ratio of 10:1. This solution was heated under vigorous stirring for 10 min, and then the stirring was continued for additional 15 minutes without applying heat. The diameter of prepared Au NPs was approximately 12 nm.

AuNP-DNA conjugation: DNA conjugation with Au NPs was accomplished by using the protocol provided by Zhang et al.[3] Briefly, 1 ml of 1.2 nM AuNPs was resuspended in 10 mM PBS (pH 7.0). A 100 µM solution of thiolated DNA was reduced by mixing 1 µl of 10 mM TCEP with 35 µl of the DNA. DNA was incubated in this solution for 30 minutes. Reduced thiolated DNA was added to the AuNP solution and this was incubated for 16 hours at room temperature. After the incubation step, 10 mM PBS and 2 M NaCl solutions were added to the DNA mixture as slowly as possible to make the final salt concentration as 0.1 M NaCl. This solution was incubated for 40 hours at room temperature. This solution was occasionally shaken in order to avoid aggregation. Finally, the solution was washed three times and resuspended in 10 mM PBS with 0.1 M NaCl (pH 7.0) and stored at 4°C.

Photoelectrochemical (PEC) Characterization: PEC measurements were conducted in a three-electrode electrochemical cell using a Zahner CIMPS system. Optical excitation was achieved using a 405 nm LED from the tunable optical light source (TLS03). A Pt wire was used as the counter electrode, Ag/AgCl as the reference electrode, and the deposited TiO_2 photoelectrode as the working electrode. All PEC measurements were performed at an applied potential of 0 V (vs. Ag/AgCl). The electrolyte used for all PEC measurements was 0.1 M PBS with 0.1 M ascorbic acid (AA), where AA served as hole scavenger. Period of light excitation was 40s with a 50% duty cycle (illumination time 20s). Baseline correction was performed on the measured photocurrents prior to plotting to the data for the manuscript figures.

Electrochemical Characterization: Electrochemical impedance spectroscopy (EIS) measurements were performed on the Zahner potentiostat under the open circuit potential. The measurements were performed within the frequency range of 100 kHz to 0.1 Hz in a solution containing 2 mM $[Fe(CN)_6]^{3-/4-}$, 0.1 M PBS, and 0.1 M KCl. Cyclic voltammetry was performed by using 10 mM PBS as electrolyte and 50 mV/s scan rate.

Probe Density measurement: The Probe density of the DNA modified TiO_2 electrodes was measured by following the protocol described by *Steel et al.*[517] In short, chronocoulometry was performed sequentially in 10 mM Tris-buffer and in 100 µM Hexaammineruthenium (III) chloride in 10 mM Tris-buffer, on the DNA modified photoelectrodes. From the two graphs, the difference between y-axis intercepts were measured to determine the charge (Q) of the redox marker (Ruthenium ion in this case). From the charge, surface density of the redox marker is calculated using the following formula:

$$Q = nFA\,\Gamma_0$$

Where, n indicates the number of electrons per molecule for a redox reaction, F is the faraday constant, A is the area of the surface, and Γ_0 is the density of adsorbed ruthenium ion. Redox marker density can be converted to DNA probe coverage using the following formula:

$$\Gamma_{DNA} = \Gamma_0 \left(\frac{z}{m}\right) N_A$$

Where, Γ_{DNA} is the density of probe, m is the number of bases in probe DNA, z is the charge of the redox molecule, and N_A is the Avogadro's number.

DNA hybridization experiment: Electrodes were modified with probe DNA by drop depositing 35 µl of 1 µM single stranded probe DNA and incubated for 3 hours at room temperature. Afterwards, a 1 mM MEA solution was deposited as a surface blocker with an incubation time of 50 minutes. A 20 µl solution of unlabeled target DNA with different concentrations was drop deposited on the electrode and incubated for one hour at room temperature. Finally, a 100 pM solution of the AuNP-conjugated DNA (signal amplification barcode (SAB)) was deposited on the electrode and incubated for another 40 minutes at room temperature. After each step, electrodes were rinsed in a wash solution (25 mM PBS, 25 mM NaCl). Percentage change of the photocurrent was calculated in two steps. After target deposition, the measured percentage decrease in signal is:

$$\Delta I_{target} = I_{target} - I_{block}$$

$$\%\Delta I_{target} = (\Delta I_{target}\ X\ 100)/I_{block}$$

‘$\%\Delta I_{target}$’ indicates the percentage change in photocurrent following hybridization of the unlabeled target with immobilized probe, while ‘I_{block}’ and ‘I_{target}’ represent the signals obtained following MEA incubation and target hybridization, respectively. Similarly, percentage increase after SAB hybridization is calculated as follows:

$$\Delta I_{SAB} = I_{SAB} - I_{target}$$

$$\%\Delta I_{SAB} = (\Delta I_{SAB}\ X\ 100)/I_{target}$$

Here, ‘$\%\Delta I_{SAB}$’ indicates the percentage change in photocurrent upon SAB binding by available probe sites following target hybridization. ‘I_{SAB}’ represents the signal obtained following the anchoring of SABs at the photoelectrode surface.

The signal for the developed bioassay ($\%\ \Delta I_{diff}$) is the algebraic sum of both percentage changes calculated above and is computed according to the following equation:

$$\%\ \Delta I_{diff} = \%\Delta I_{target} + \%\Delta I_{SAB}$$

The DNA sequences used in this work are as follows:

Probe DNA: 5‘-NH_2-AGG GAG ATC GTA AGC-3‘

Complementary target: 5‘-TTT TTT TTT TGC TTA CGA TCT CCC T-3‘

Non-complementary (NC) target: 5’-TTT TTT TTT TTT TTT TTT TTT TTT T-3’

DNA for Au NP conjugation: 5‘-SH-TTT TTT TTT TGC TTA CGA TCT CCC T-3‘

1-base mismatch: 5’-TTT TTT TTT TGC ATA CGA TCT CCC T-3’

2-base mismatch: 5'-TTT TTT TTT TGC ATA CGA TGT CCC T-3'

Sensitivity and Limit-of-Detection (LOD) Calculations: In order to determine the LOD of the assay, we plotted the photocurrent change ($\% \Delta I_{diff}$) versus the log of target concentration in the linear range (1 fM – 100 pM) for both steps of hybridization. These changes are algebraically added to obtain the differential signal. The linear equation for the regression line is $\% \Delta I_{diff} = -49 \log_{10}C + 173$ with a correlation coefficient of 97.97% when the target is in the buffer and $\% \Delta I_{diff} = -25 \log_{10}C + 106$ with a correlation coefficient of 99.84% when the target is in diluted urine. The correlation coefficient for both cases is written in Figure 3(b). The limit-of-blank (LOB) was calculated as [4]:

$$\text{LOB} = \mu_B - 1.645 * \sigma_B$$

Here, 'μ_B' is the mean and 'σ_B' is the standard deviation of the background signal, *i.e.*, the signal obtained upon incubation of the photoelectrodes with non-complementary target DNA. The LOD was calculated by determining the concentration where the '$\% \Delta I_{diff}$' value of the regression line becomes equal to the LOB. This was done using the following equation:

$$LOD = 10^{\frac{LOB-x}{m}}$$

Here, 'x' is the x-intercept of the regression line while 'm' denotes the sensitivity of detection and was obtained from the slope of the regression line of the LOD curve.

Similarly, for the signal-off assay, the photocurrent change ($\% \Delta I_{target}$) versus the log of target concentration in the linear range (1 fM – 100 pM) was plotted following target hybridization alone. The linear equation for the regression line obtained for this data set is $\%\Delta I_{target} = -14 \log_{10}C - 3$ with a correlation coefficient of 98.83% when the target is in the buffer and $\%\Delta I_{target} = -8 \log_{10}C - 4$ with a correlation coefficient of 99.13% when the target is in diluted urine. The LOD was calculated by determining the concentration where the '$\% \Delta I_{targef}$' value of the regression line becomes equal to the LOB. The LOB and LOD of the signal-off assay were then calculated as per the aforementioned protocol.

Urine Sample Analysis: Urine samples were collected from a healthy patient cohort. The urine was diluted 10 times and the target DNA was spiked into the diluted urine. All experiments were performed using the methods in the previous section, except for the shortened, 40-minute, hybridization time.

Plasma Sample Analysis: Human plasma was donated by the Canadian Plasma Resources (Saskatoon, Canada). Target DNA (1 pM) was spiked into the 5 times diluted plasma samples. All experiments were performed similarly to the Urine sample analysis, except 1mM PEG-5K was used as the surface blocker instead of 1 mM MEA.

8.4 Results and Discussion

We created the differential PEC biosensor by combining two sequential but correlated binding events on a single photoelectrode. A porous network of TiO_2 NPs was deposited on ITO substrates to create the photoelectrode, yielding the initial photocurrent profile (Figure 8-1a(i)). These photoelectrodes were then bio-functionalized with 15-nucleotide long single stranded DNA (ss-DNA) probes and subsequently blocked with monoethanolamine (MEA) to prevent nonspecific adsorption. The immobilization of probe

DNA on the photoelectrode surface was verified using chronocoulometry and the probe coverage was measured as 5 x 10^{11} molecules/cm^2 (Supporting Figure S8-1).

A resulting decrease in photocurrent was anticipated following bio-functionalization due to the induction of steric hindrance between the photoelectrode and the species in the electrolyte (Figure 8-1a(ii)). Upon incubation with 25-mer complementary DNA targets (unlabeled), hybridization occurs between a fraction of the total probe population and the targets, leaving behind a population of available unhybridized probe strands. A further decrease in photocurrent is expected due to steric hindrance (Figure 8-1a(iii)). The SAB strand is then hybridized with the available probe strands. The length of the ssDNA probe (15-mer) is shorter than the length of the SAB strand (25-mer), with the resulting DNA complex containing both double and single stranded regions.[431,435] It has been previously demonstrated that the Au NPs on the SAB have a high probability of coming into direct contact with TiO_2 NPs owing to the dynamic motion of the DNA complex used in this work.[340] Direct contact between Au and TiO_2 NPs facilitates charge transfer between the two particles, thereby enhancing the anodic photocurrent (Figure 8-1a(iv)).[331,351] The presented DNA sensing approach, involving two hybridization steps, presents two benefits: 1) the target DNA strand does not need to be labeled prior to introduction on the chip, and 2) the combination of the signal changes induced from the two hybridization steps is expected to increase the assay sensitivity (Figure 8-1(b)). It should be noted that this two-hybridization approach makes it possible for the SAB binding to result in the displacement (completely or partially) of the target strands.[518,519] Partial hybridization of the SAB with the existing target-hybridized probes becomes more probable at longer nucleic acid strands.[518,520] Under the conditions used here, the use of a 15-mer DNA probe, a 25-mer DNA target, a 25-mer SAB strand with the same sequence as the target strand, and a room temperature hybridization step, we expect less than 10% of target strands to be removed by the SAB strand,[518,519] thus not making competitive strand replacement a significant contributor to the assay performance. As a result of the assay design, we expect it to be ideally-suited for detecting short nucleic acid targets such as microRNA (18-25 mer) or short DNA barcodes released from DNA machines.[449] MicroRNAs have been identified as clinically important diagnostic biomarkers for various diseases including cancer[521,522], cardiovascular conditions,[523] and infectious diseases.[471]

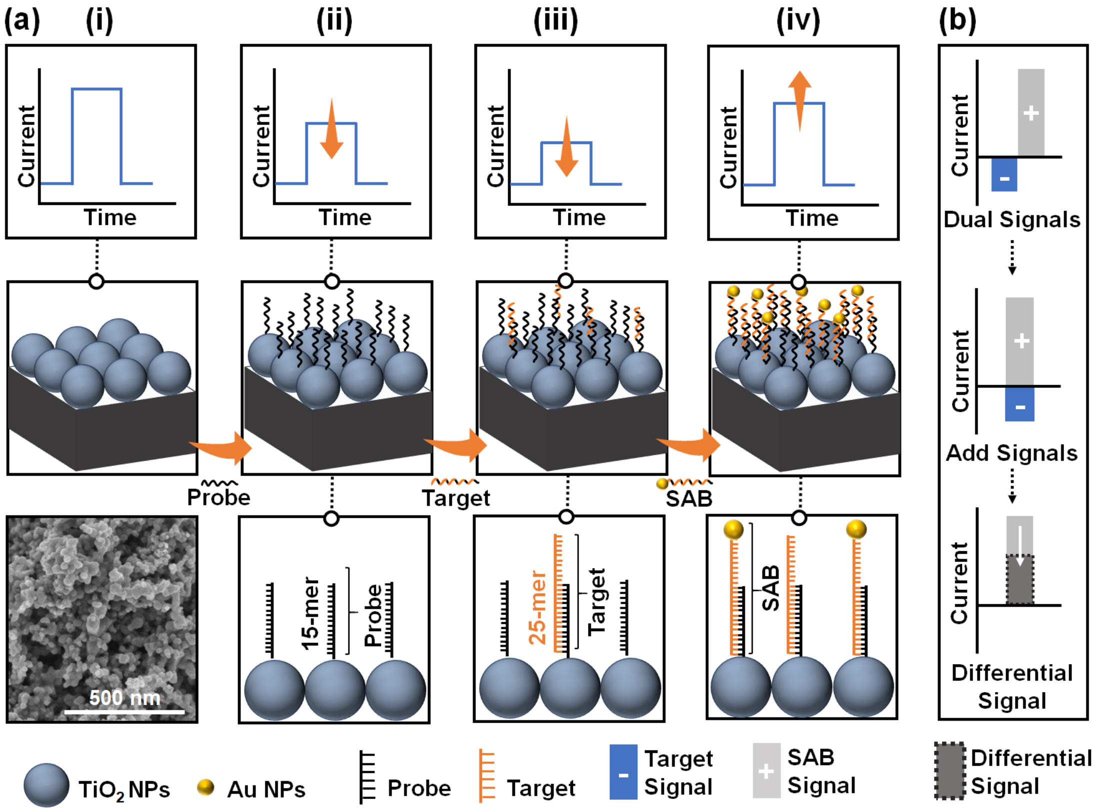

Figure 8-1: The operation of the differential PEC biosensor (a) Schematic illustration depicting the development of the PEC biosensor with the expected change in photocurrent profile depicted at each stage of sensing. A scanning electron micrograph (SEM) demonstrates the photoelectrode surface structure (bottom

left). (i) Baseline photoelectrodes are created via solution deposition of TiO_2 NPs onto ITO substrates, yielding an anodic photocurrent upon 405 nm illumination (ii) Bio-functionalized photoelectrodes are created by depositing 15-mer DNA probes on photoactive TiO_2 substrates, yielding a decrease in photocurrent. (iii) 25-mer nucleotide targets are hybridized onto the transducer, resulting in a further decrease in photocurrent. (iv) Introducing SABs gives rise to an amplified photocurrent following hybridization. (b) A depiction of the combination of signals following target and SAB hybridization to yield the differential signal processing scheme used in this study.

The differential sensor design was verified by measuring the photocurrent and charge transfer resistance in each step of the sensor development process (Figure 8-2). For the photocurrent measurements, we used an LED light source with an excitation wavelength of 405 nm and an intensity of 160 W/m^2. Ascorbic acid (AA) was used as the hole scavenger to generate anodic current upon optically exciting the electrode (Figure 8-2a). A 45% photocurrent decrease was observed after probe deposition due to the steric hindrance of AA caused by the single stranded capture probe (Figure 8-2b).[434] Subsequently, MEA was used to block the unbound sites of the working electrode which further decreased the photocurrent by 35% as MEA impedes the access of AA to the surface of TiO_2 nanoparticles. Following this, target DNA was introduced on the surface and a 45 % photocurrent reduction was observed. As target DNA hybridizes with the capture probe on the photoelectrode, it further hinders the access of AA (Figure 8-2a). Finally, a 105 % enhancement in photocurrent was observed upon the introduction of the SAB to the substrate (Figure 8-2b). Enhancement of photocurrent under UV excitation has been reported in similar systems due to Fermi level equilibration as optically-excited electrons from the conduction band of the semiconductor move to the Au NPs, thereby reducing the carrier recombination rate.[321,352] Optical excitation at 405 nm can also generate hot electron and hot holes via d-sp transition in Au NPs.[92,390,395] It is possible that these hot holes directly oxidize AA, while the hot electrons are transferred to TiO_2 NPs, thereby increasing the photocurrent (Figure 8-2a).

Electrochemical impedance spectroscopy (EIS) at open circuit potential was also used to characterize the stepwise fabrication process of the proposed assay design (Figure 8-2c). The charge transfer resistance (R_{ct}) of the photoelectrode decreased by 78% after DNA probe attachment (Supporting Table S 8-1 and Supporting Figure S8-2). This is contrary to the usual observation found in the literature where probe immobilization increases R_{ct}.[217,524,525] A study reported by Imani *et al.* showed that the addition of ssDNA on dopamine modified TiO_2 NPs results in a higher electron transfer rate due to the quantum mechanical tunneling effect by bridging the molecular medium between the donor and the acceptor sites of ssDNA and TiO_2 NPs, respectively.[402] Therefore, the observed reduction in R_{ct} in this work can also occur due to the amine-modified ssDNA covalently bonding with the aldehyde groups on the 3,4-dihydroxybenzlaldehyde (DHBA) linker on the TiO_2 NP surface having the same linker chemistry as dopamine, thereby enhancing the probability of quantum tunneling. It has also been hypothesized that DNA functionalization reduces carrier trapping sites by passivating the semiconductor (TiO_2) surface, thereby reducing charge recombination.[526] In order to further validate this finding, we performed a study by performing cyclic voltammetry (CV) in 0.1 M phosphate buffer (PBS) to show changes in charge transfer kinetics (Supporting Figure S8-3). This study showed that the amount of stored charges in the photoelectrodes were increased from 0.59 mC to 0.72 mC after DNA functionalization, indicating longer lived excitons. Similarly, the addition of MEA as a surface blocker further decreased the charge transfer resistance by 43%. Upon the hybridization of target DNA, the R_{ct} increased by 110%, which is attributed to increased steric hindrance between the redox species in the solution and the surface of the photoelectrode.[214] Introduction of the SAB resulted in a 33% decrease in R_{ct}, which is attributed to improved charge transfer kinetics due to the addition of Au NPs into the electrode film.[427,527]

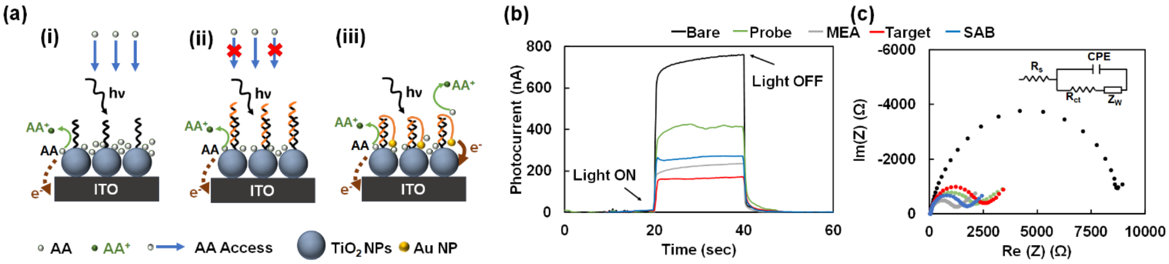

Figure 8-2: Photoelectrochemical signal generation on the differential DNA biosensor. (a) Schematics showing the mechanism for photocurrent generation (i) bare TiO_2 electrode (ii) after hybridization with complementary target (iii) after hybridization with SAB (b) Photocurrent measurement after each step of the biosensor operation with 1 pM target in buffer using a 405 nm LED as excitation source at 160 W/m^2. All photocurrent measurements were performed at 0 V bias vs. Ag/AgCl. using 0.1 M ascorbic acid (AA) in 0.1 M PBS as electrolyte at each step of the biosensor construction. (c) Electrochemical impedance spectroscopy measurements were performed in dark at open circuit potential vs. Ag/AgCl reference electrode using 2 mM $[Fe(CN)_6]^{3-/4-}$ in 0.1 M PBS and 0.1 M KCl as electrolyte. The equivalent circuit based on the shape of the Nyquist diagram is shown in the inset. Charge transfer resistance between the redox couple and the electrode is denoted by R_{ct}, which can be determined from the diameter of the semicircle. R_s, Z_w and CPE denote the solution resistance, Warburg impedance and constant phase element, respectively.

To assess the ability of the differential PEC biosensor in analyzing DNA targets, we analyzed unlabeled DNA targets within a concentration range of 1 fM to 100 pM. As expected, when a solution containing target DNA was introduced to the device, the electrodes showed a PEC current that monotonically decreased with increasing target concentration (Figure 8-3a). As the concentration of target DNA in the first hybridization step decreases, there is a larger population of residual unhybridized probes, allowing more

SAB strands to bind to the photoelectrode yielding a signal increase. As expected, this signal increase is larger at lower target DNA concentrations (Figure 8-3a, b(i)).

The differential PEC sensing strategy is then developed by combining the photocurrent change after target and SAB binding steps. More specifically, the absolute value of photocurrent decrease after target hybridization was subtracted from the absolute value of photocurrent enhancement after SAB binding. The differential signal for each concentration was plotted to generate a calibration curve (Figure 8-3b). A linear fit to the calibration curve yields a sensitivity of 49 % / $\log_{10}$ M and LOD of 3 fM in buffer. The reverse signal-to-concentration effect observed here, where the largest signals are obtained at the lowest concentrations, allows high signal-to-noise ratios to be obtained at low concentrations that are often needed for clinical analysis, a feature that is not possible with traditional sandwich assays. This increase in signal at lower concentrations comes with the inherent drawback of differential signal processing: the experimental errors obtained from each measurement accumulate in the differential signal, leading to a loss of precision at all concentrations. Additionally, the use of two hybridization steps increases the overall assay time; however, preliminary experiments demonstrate that it may be possible to reduce the duration of each hybridization step (Supporting Figure S8-4).

In order to assess the applicability of the differential biosensor in analyzing DNA targets in complex biological matrices, we spiked target DNA at various concentrations into healthy patient urine (Figure 8-3c-d). The differential assay yielded a sensitivity of 25 %/ $\log_{10}$ M and LOD of 5 fM in urine. Both LOD and sensitivity deteriorate moderately in urine compared to buffer (less than a factor of two). This can be attributed to the biofouling of the photo electrode caused by the biological components present in urine.[528]

Adding the signal amplification step using the SAB significantly enhances the LOD of the system in both buffer (from 11 fM to 3 fM) and urine (from 73 fM to 5 fM) compared to using a single target binding step (Supporting Figure S8-5). The large enhancement in LOD (~15 times) observed in urine indicates that the differential signaling strategy is particularly important for compensating for the performance loss that is observed in complex biological samples. In addition to LOD, the differential strategy enhanced the assay sensitivity by about three times compared to the single binding assay for both buffer and urine samples. We further challenged the bioassay by spiking 1 pM target DNA into human blood plasma (Supporting Figure S8-6). It should be noted that the bioassay utilized polyethylene glycol (PEG), in place of MEA, to reduce non-specific adsorption at the biosensor surface. The photocurrent changes observed after incubating the sensor with the target and SAB strands were similar to when human urine was used, indicating the potential use of this assay for biomarker detection in blood plasma.

To assess the specificity of the nucleic acid biosensor and its ability in distinguishing between fully-matched and mismatched targets presenting point mutations, detection was carried out for targets with sequences having 1-base, and 2-base mismatches with the original sequences. The photocurrent changes obtained following each hybridization stage (after target and SAB binding) were then evaluated against those obtained for a perfectly complementary and a fully mismatched sequence tested in the same manner (Figure 8-4).

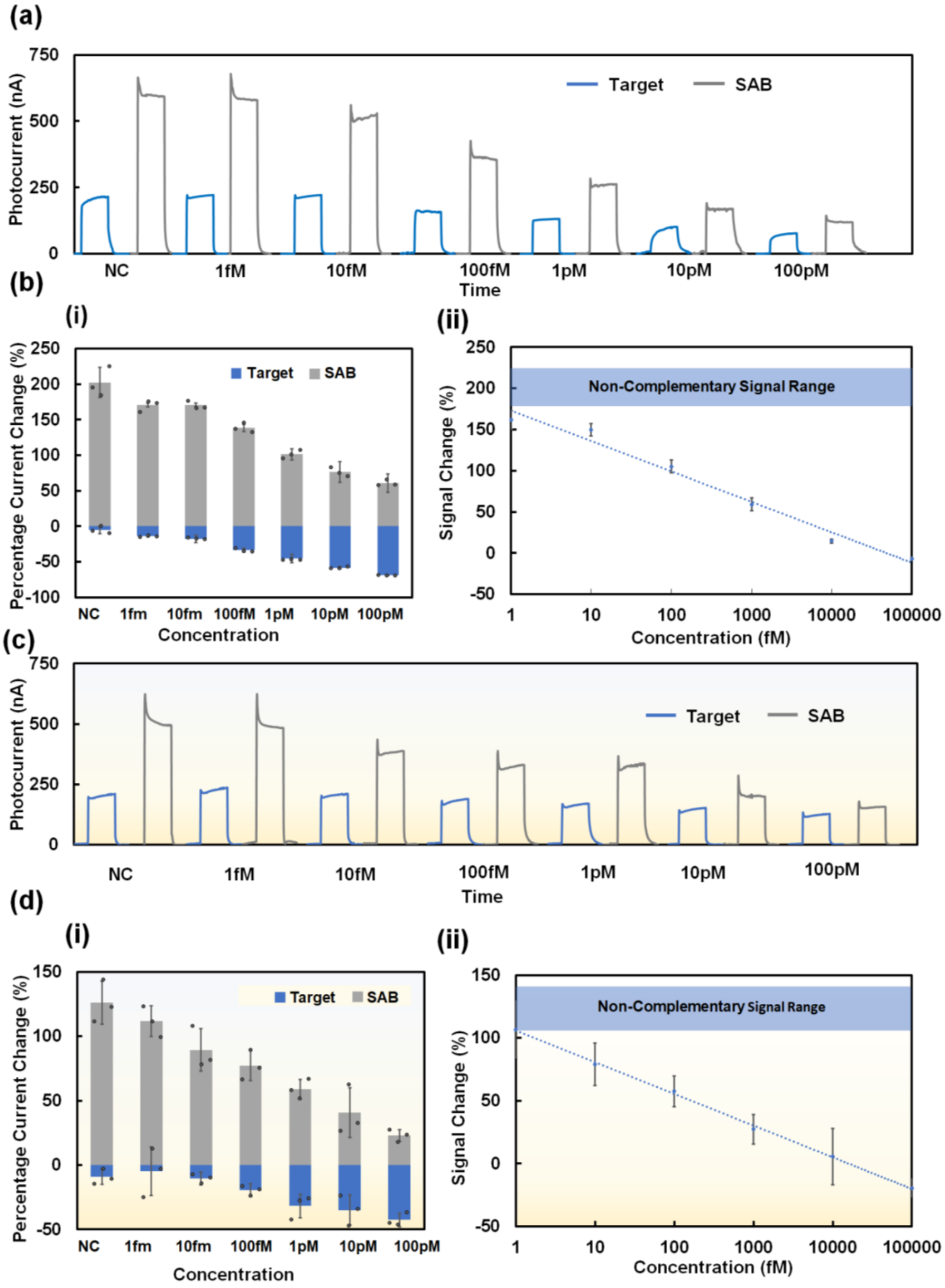

Figure 8-3: Limit-of-detection and sensitivity of the differential assay. All photocurrent measurements were performed at 0 V versus Ag/AgCl in 0.1 M ascorbic acid in 0.1 M PBS as electrolyte, illuminated using a

405 nm LED excitation source at 160 W/m^2 (a, c) PEC graphs demonstrate signal responses following target and SAB binding in PBS and urine respectively. (b, d) Jitter plots (i) demonstrating the signal changes obtained from target and SAB binding in buffer and urine respectively, obtained from (a) and (c). Representation of the differential signal (ii) obtained from the data presented in (i). The linear region of the calibration curve of the PBS graph was fitted using the equation $\Delta I\ \% = -49\ \log_{10}C + 173$ (correlation coefficient of 97.97%) while the equation $\Delta I\ \% = -25\ \log_{10}C + 106$ (correlation coefficient of 99.84%) was used to fit the urine data.

Following target binding, the current deceased by 48% ± 6%, 16% ± 4%,14% ± 9%, and 6% ± 3% for matched, 1-base mismatched, 2-base mismatched, and non-complementary (NC) sequences, respectively (Figure 8-4a). This trend is largely attributed to the varying hybridization efficiency in each scenario, with fewer base mismatches resulting in more efficient target binding.[315,529] The matched, 1-base mismatched, 2-base mismatched, and NC sequences exhibited a 109% ± 6%, 160% ± 9%, 179% ± 8%, and 202% ± 4% increase in signal magnitude respectively, following SAB binding (Figure 8-4a). In the case of the mismatched sequences, albeit inefficient, a fraction of the target sequences binds to available probe sites, still decreasing the available binding sites for SAB binding, which in turn reduces the SAB-induced signal enhancement. The differential signal enables highly distinguishable signal footprints to be realized for the different sequences with 60%, 123%, 163%, and 201% signal changes measured for matched, 1-base mismatched, 2-base mismatched, and NC sequences (Figure 8-4b). A statistical t-test was performed to assess the ability of the assays using one or two binding steps in distinguishing between different degrees of probe/target complementarity. Using differential signaling, we were able to distinguish between matched, 1-base mismatched, 2-base mismatched, and NC sequences (Figure 8-4b). On the contrary, the single target binding event can only distinguish matched from the 1-base mismatched sequence. The differential approach achieves a superior mismatch specificity with a high confidence level ($p<0.05$ for all scenarios) as compared to its *signal-off* analogue.

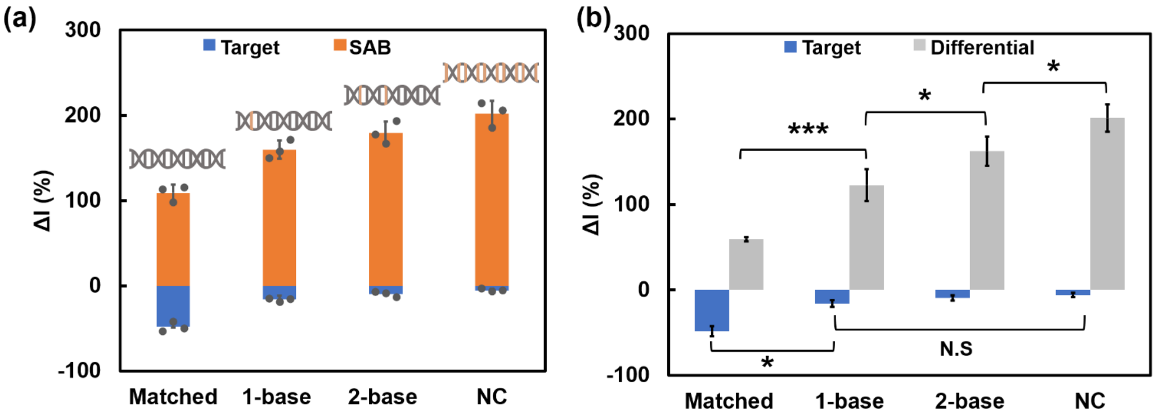

Figure 8-4: Specificity of the differential assay. (a) Change in PEC current following hybridization with 1 pM of matched, 1-base mismatched, 2-base mismatched, and NC targets and SAB binding measured in 0.1 M PBS with 0.1 M AA. b) Differential and signal-off responses for the target sequences in (a) with * and *** representing $p < 0.05$ and $p < 0.001$, respectively.

We further assessed the static and dynamic stability of the differential PEC biosensor. PEC measurements of the electrodes stored under static conditions over a 7-day period following probe deposition (Figure S8-7a) revealed a small decrease in biosensor photocurrent (8% decrease from day 1 to day 7). Furthermore, the stability of the photoelectrodes under dynamic conditions, multiple light excitation and potential application, was assessed for 15 measurement cycles in a period of 800 s (Figure S8-7b), indicate stable photocurrents with a relative standard deviation of 6.5%, thus highlighting the robustness of this biosensor.

8.5 Conclusion

In this work, we demonstrate a differential PEC assay using two subsequent and correlated hybridization events, first with an unlabeled target and then with a single amplification barcode tapping into the interaction of plasmatic and semiconductive nanoparticles, to detect unlabeled target DNA in both buffer and urine. The differential strategy exhibited a LOD of 3 fM in buffer and 5 fM in diluted urine, demonstrating significant improvement over a conventional signal-off strategy that used a single binding event (11 fM in buffer and 72 fM in urine) respectively. In addition to LOD, this assay enhanced the analytical sensitivity by a factor of three compared to an analogous assay that did not use differential signaling. The differential assay also demonstrated the ability to distinguish between sequences that were matched or contained 1- or 2-base mismatches with the detection probe, which was not possible using the non-differential approach. This work offers a new strategy for enhancing the limit-of-detection, sensitivity, and specificity of PEC biosensors, performance metrics that are key to the use of PEC biosensors in clinical decision making. The assay presented here, in terms of target length (25-mer) and concentration range (1 fM –100 pM), is ideally-suited for the analysis of short nucleic acid strands such as microRNA or DNA barcodes released from DNA machines such as DNAzymes,[530] CRISPR-Cas systems,[531]and strand displacement-based systems.[532]

8.6 Acknowledgement

This work was supported by NSERC, the Ontario Early Researcher Award granted to L.S., and a salary awarded to L.S. from the Canada Research Chairs Program. The electron microscopy was carried out at the Canadian Centre for Electron Microscopy (CCEM), a national facility supported by the NSERC and McMaster University. A.V and S.S. are recipients of the NSERC doctoral scholarships.

8.7 Supplementary Information

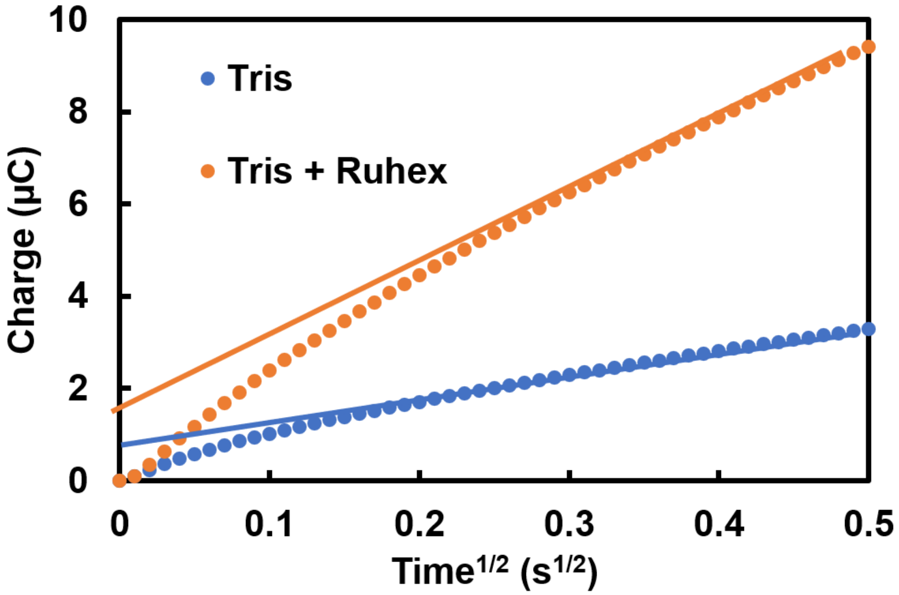

Figure S8-1: Chronocoulometric measurement of probe density. Blue dots represent the data obtained by running the scan with 10 mM Tris-buffer and orange dots represent the data obtained by running the scan with 100 µM Hexaammineruthenium (III) chloride in 10 mM Tris-buffer. Corresponding solid lines indicate the linear fit that was used to obtain the y-axis intercept.

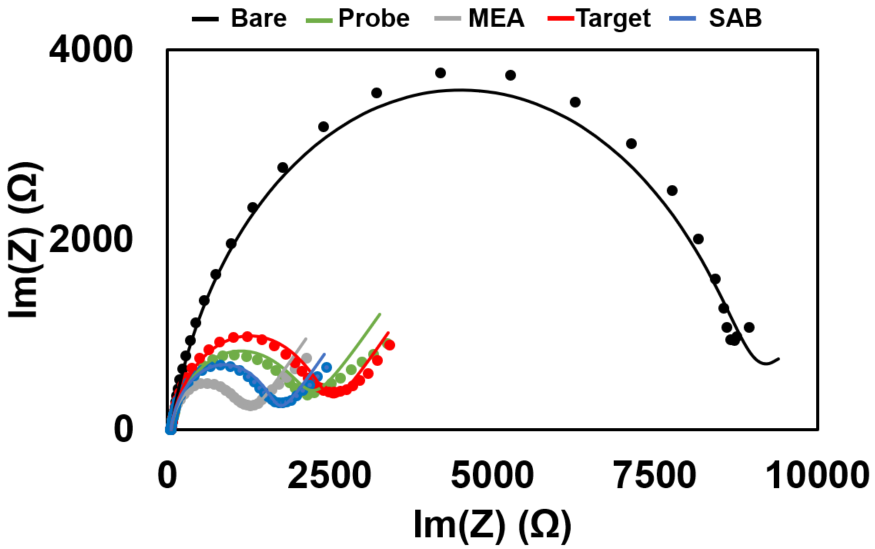

Figure S8-2: EIS measured at different fabrication steps of the differential PEC biosensor. The dots indicate the raw data points, whereas the solid line indicates the fit with the circuit model

Table S 8-1: Values of the charge transfer resistance (R_{ct}),constant phase element (CPE) and n, indicating the constant phase (-90*n) of the CPE for each step of the construction of the differential biosensor extracted from Figure S8-2.

	R_{ct} (kΩ)	CPE (μF)	n
Bare	8.8	8	0.9
Probe	1.96	4.6	0.85
MEA	1.12	5.43	0.91
Target	2.36	4.07	0.87
SAB	1.58	5.54	0.9

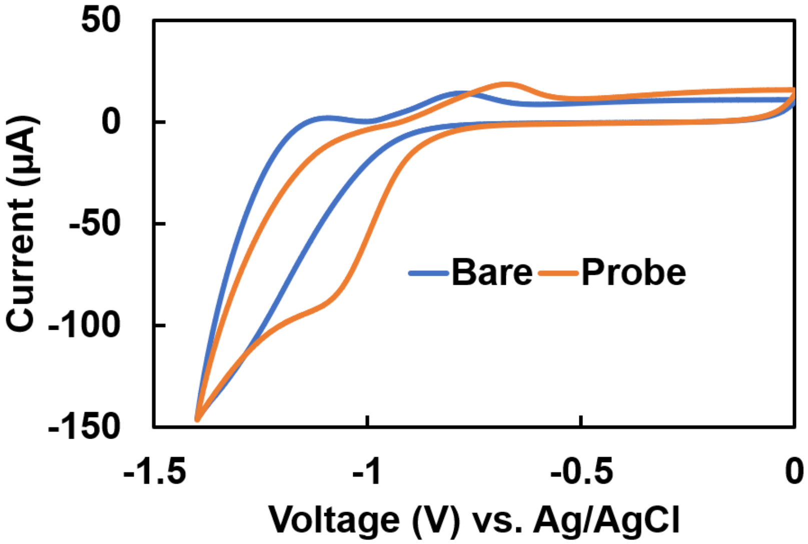

Figure S8-3: Cyclic voltammetry scan for TiO_2 electrodes before and after modification with ssDNA using 10 mM PBS as electrolyte and 50 mV/s scan rate.

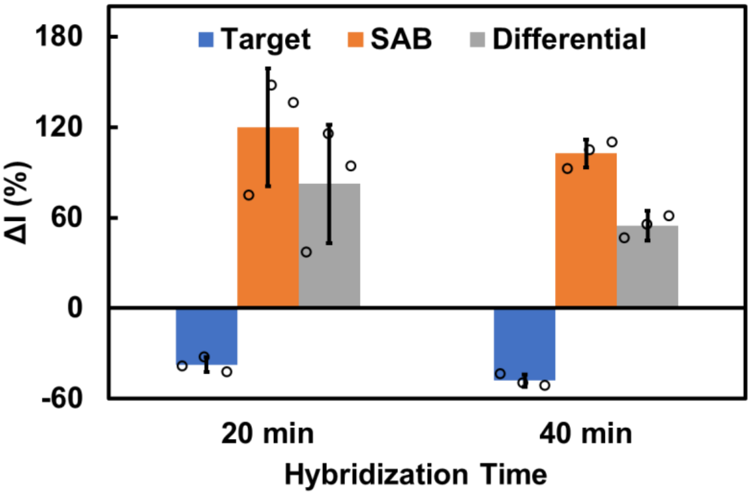

Figure S8-4: Comparison of photocurrent change in detecting 1 pM DNA targets spiked in buffer (PBS) at 20-minute and 40-minute hybridization times. The error bars indicate one standard deviation from the mean and calculated from at least three measurements performed at 0 V *versus* Ag/AgCl in 0.1 M ascorbic acid in 0.1 M PBS as electrolyte, illuminated using a 405 nm LED excitation source at 160 W/m^2.

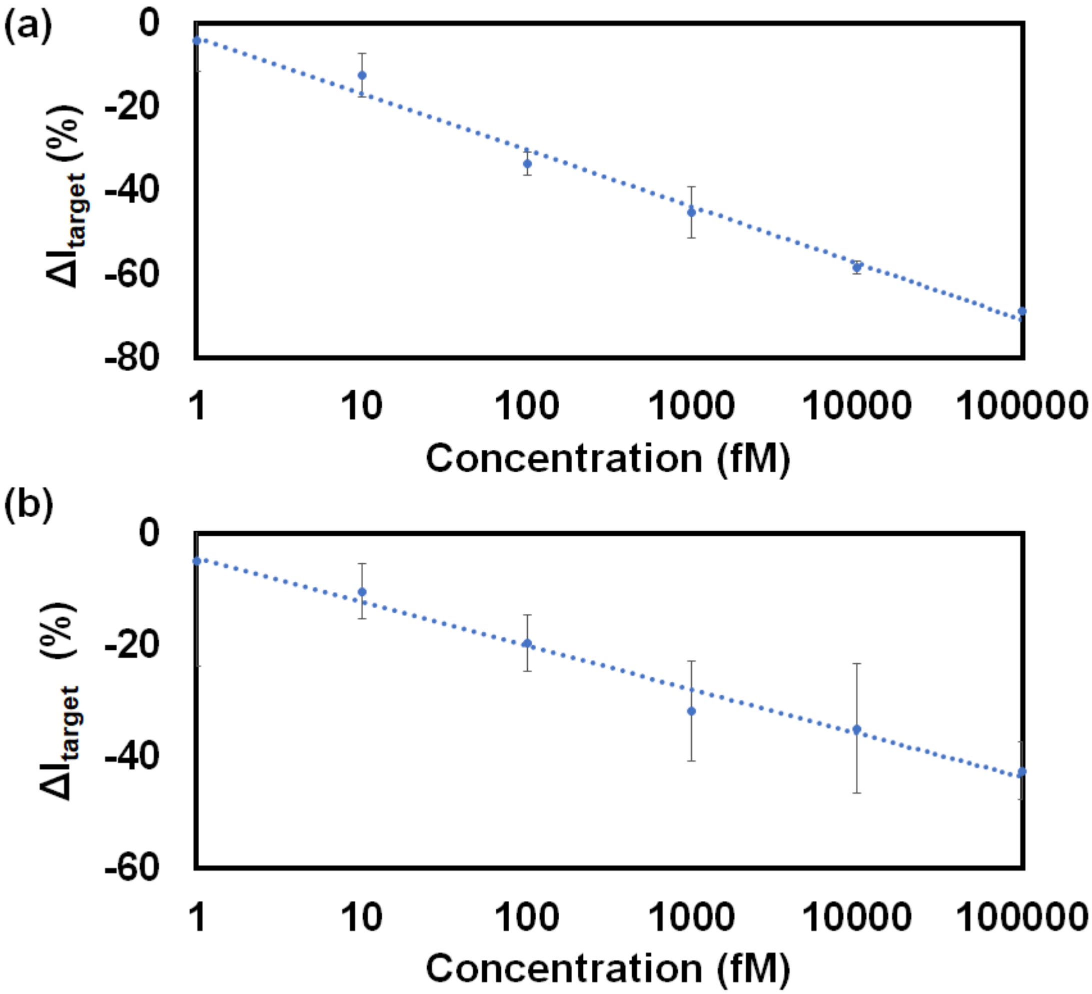

Figure S8-5: Limit of Detection in (a) PBS and (b) urine in the signal-off detection mode.

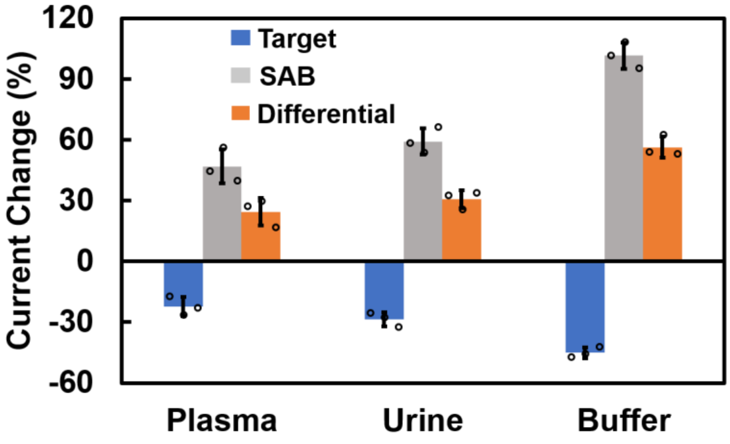

Figure S8-6: Signal changes measured with 1 pM DNA target spiked into human plasma, urine, and buffer. The error bars indicate one standard deviation from the mean, calculated from at least three measurements

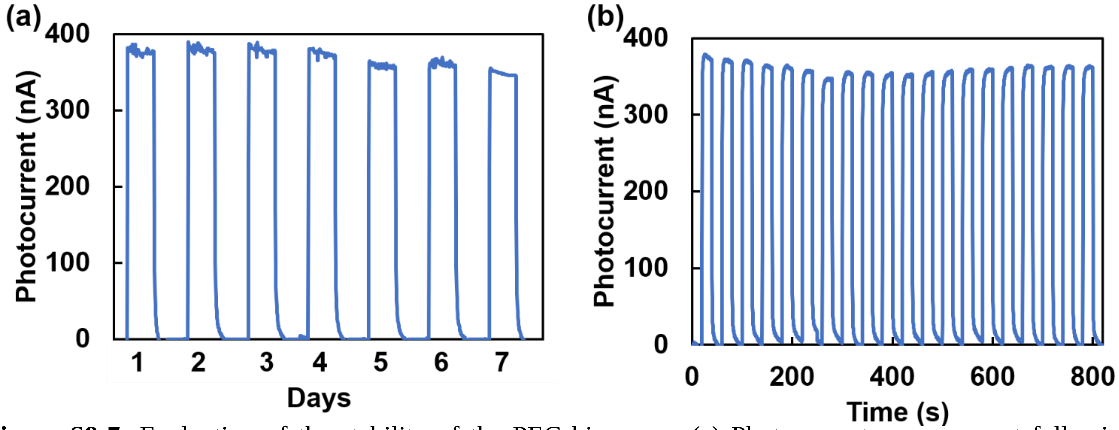

Figure S8-7: Evaluation of the stability of the PEC biosensor. (a) Photocurrent measurement following storage of probe modified electrodes for a period spanning 1-7 days. (b)Photocurrent measurement for 15 repeated cycles after probe modification. All photocurrent measurements were performed by applying 0 V vs. Ag/AgCl using 0.1 M ascorbic acid in 0.1 M PBS as electrolyte.

Chapter 9 Summary and Conclusions, Limitations and Future Work

This final chapter briefly summarizes the outcome of this thesis and the potential to use this knowledge for developing PEC biosensors. Additionally, the limitations of this work and proposed future directions are discussed.

9.1 Thesis Summary

The primary goal of this work was to investigate the interaction between the semiconductor NPs and plasmonic NPs for the PEC system and utilize these plasmonic NPs to develop strategies for designing practical PEC nucleic acid biosensors. We used CdTe QDs and TiO_2 NPs as semiconducting material to prepare photoelectrodes and Au NPs as a plasmonic label. Even though the interaction may vary when a different semiconductor or plasmonic NPs is used, this study provides a general idea regarding the interaction between a photoactive semiconductor and a plasmonic NP when connected via nucleic acid strands.

Solution-based electrode preparation was chosen due to its low-cost, industrial scalability, small footprint, and fast processing time. The surface morphology and surface coverage of the electrodes were characterized by scanning electron microscopy (SEM) and transmission electron microscopy (TEM). Electrochemical impedance spectroscopy (EIS) was used to measure the charge transfer resistance and capacitive properties at the electrochemical interface. PEC characterization was achieved through chopped light amperometry, and incident-light-to-photon-conversion-efficiency (IPCE) measurements. This work proves the response of two types of semiconductive NPs (e.g., CdTe QDs and

TiO_2 NPs), with both particles biofunctionalized to achieve a monolayer of the capture prove at its surface.

Photoelectrode fabricated from TiO_2 NPs were used to study Au NP interaction with the underlying substrate as it showed a higher photocurrent density (2.5-3 µA/cm^2 for TiO_2 and 1.5-1.8 µA/cm^2 for CdTe). Au NP concentration was varied on TiO_2 electrodes to investigate the concentration dependencies on the different excitation wavelengths. Higher anodic photocurrent can be obtained at UV light excitation than at visible light excitation when Au NP concentration is small. Therefore, UV light excitation was chosen for the nucleic acid sensing application in this work. Different mechanisms of the photocurrent modulation were investigated including direct charge transfer, and photocharging. Additionally, excitation energy dependent photoelectrochemical properties of Au NPs, when used without any semiconductor, were also investigated. It was shown that interband excitation of Au NPs are better suited for the PEC application which involves oxidation of the reactants. Based on the outcome of these studies, different methods of nucleic acid sensing were proposed. Finally, label-free detection with the femtomolar detection limit was demonstrated. The developed biosensing devices were further challenged with human urine samples.

9.2 Thesis Conclusions

i. The photoactive material deposition on the photoelectrodes was achieved by benchtop and solution-based methods. Solution-based processing is inexpensive, simple, homogeneous, and offers high throughput.[533] Only ITO deposition on glass or polystyrene electrodes was achieved by sputtering, which is also inexpensive relative to other physical vapor deposition techniques. The photoactive materials were chosen to have carboxyl (for CdTe) or aldehyde (for TiO_2) groups on their surface, to facilitate biofunctionalization of the photoelectrodes. The electrode fabrication procedure was optimized to achieve a high photocurrent.

ii. Photoelectrodes were prepared to achieve high electrochemically active surface area, along with high photoactivity by wrinkling the substrate and/or bestowing the photoelectrode with a mesoporous surface. Wrinkled structures helped to integrate a higher number of quantum dots on the electrode surface than planar electrodes. Mesoporous TiO_2 electrodes also help to achieve higher surface coverage as well as good transportation of optically excited charge carriers.

iii. The effect of Au NP concentration on the photoelectrochemical signal generated by the TiO_2 photoelectrodes was determined for different excitation wavelengths (*i.e.*, UV and visible). The visible excitation wavelength was chosen to excite the LSPR of Au NPs, where optically excited carrier generation in the TiO_2 NP is minimal. On the other hand, for UV excitation, interband hot carriers are generated in Au NPs along with electron-hole pairs in TiO_2. The effect of Au NP concentration differs for the two types of excitation modes used in this work. This study also helps to clarify the mechanism of the photocurrent enhancement when Au NPs are in contact with the modified TiO_2 NPs.

iv. The use of DNA as nanospacers between modified TiO_2 NPs and Au NPs was investigated. DNA is typically immobilized on the electrode by anchoring at one end. These DNA structures have dynamic motion when the biofunctionalized photoelectrodes are immersed in the electrolyte. Therefore, when considering the effect of the distance between two NPs connected by DNA complexes, it is critical to consider the statistical average distance between them. We further explained the distance dependencies of Au NPs and TiO_2 when separated by DNA strands.

v. Plasmon decay of Au NPs generates hot carriers, which either directly participate in redox reactions or helps to improve the efficiency of photocurrent generation in an adjacent semiconductor.[93,318,377,534] Interband excitation of Au NPs generates highly energetic hot holes in Au NPs, which can generate or enhance anodic photocurrent of the photoelectrodes if a suitable hole scavenger is present in the electrolyte. Due to the higher energy, interband hot holes are more efficient in oxidation reactions than intraband hot holes. Furthermore, hot hole mediated photocurrent generation directly in Au NP and in Au/TiO_2 structure, has been explicitly demonstrated.

vi. We have developed a label-free signal-off sensing system by utilizing wrinkled electrodes. Additionally, we proposed differential approaches to increase the sensitivity and specificity of the assay. A dual-electrode differential assay was developed here where Au NP-tagged target DNA introduces a *signal-off* response on one electrode and *signal-on* response on another. This is the first time a differential biosensing approach in PEC biosensing was developed. Finally, a label-free single electrode differential sensing strategy was developed where target DNA produced a *signal-off* response and subsequent hybridization with a signal-amplification-barcode produced a *signal-on* response.

vii. We showed nucleic acid detection in human urine samples both with electrochemical and photoelectrochemical transduction methods. Electrochemical devices were used in the microRNA 200b detection from 10 urine samples. A sensitivity/specificity ratio of 80%/80% was achieved from the clinical samples. The photoelectrochemical devices were further challenged to detect nucleic acid from human plasma samples.

9.3 Contribution to the Field

Use of wrinkled electrodes for enhancing photocurrent

This work showed the first-time fabrication and usage of the wrinkled photoelectrodes for biosensing applications. Pre-stressed PS was used as a substrate material to achieve the wrinkled surface morphology. Gabardo *et al.* demonstrated the application of the wrinkled electrodes in an electrochemical bioassay, where the wrinkling was achieved by depositing Au on the PS surface and heating it above the glass transition temperature (100 ˚C) of PS.[297]

However, ITO electrodes are usually preferred over Au electrode for PEC application. A major obstacle preventing the incorporation of ITO in wrinkled morphologies, is its high Young's modulus which introduces breakage and defects upon wrinkling.[306] To avoid the breaking of ITO, UV-ozone treated polystyrene was wrinkled before sputtering ITO on top of it. This approach paves the way to achieve a high-quality ITO surface on the wrinkled PS.

Hypothesis on statistical average distance between Au NP and TiO_2 NPs when separated by DNA

Double-stranded DNA has previously been used in literature as a nano-spacer between two NPs.[535,536] In most of these works, the single-stranded portion of the target and probe DNA have equal or nearly-equal lengths.[537,538] However, in order to promote good hybridization efficiency, extra bases are usually designed into the DNA sequence when utilizing NP-tagged single-stranded DNA (ssDNA) to hybridize with the immobilized single-stranded probe DNA.[539] If an electrode containing duplex DNA structures containing different lengths of the probe and capture DNAs - with NPs attached at both ends - are immersed in electrolytes, the distance between these two NPs can differ significantly because of the differences in the persistence length of ssDNA and dsDNA. We mathematically modeled the probability of collision of the NPs in such a scenario. Utilizing the model, we programmed the response of our signal transduction channels to work in either *signal-on* or *signal-off* modes by only varying the length of single-stranded probe DNA. The programming of PEC response by only varying the probe length has been reported first time for nucleic acid sensing.

Differential photoelectrochemical biosensing strategy

Although there are previous reports involving the combination of two signals to enhance sensitivity and reduce background noise in PEC biosensing using a ratiometric approach,[232,540] none of these employed *differential* methods. Taking the inspiration from the electronic amplifier circuits, a differential PEC biosensing strategy was developed for the first time to achieve a higher signal-to-noise ratio as well as suppress the background noise.[340,420,541] The differential sensor developed in this work displayed ultralow detection limit (femtomolar level) and higher sensitivity compared to their non-differential counterpart. Additionally, this novel differential strategy demonstrates the ability to distinguish single and double base-pair mismatch sequences from the target sequence, thus proving suitable suitable for the DNA mismatch studies.

Comparison of photocurrent at different excitation wavelengths directly from Au NP

We demonstrated direct redox reaction from interband hot holes in the Au NP electrode upon light excitation. The work performed in this thesis leads to the conclusion that the d-band holes are more effective in carrying out oxidation reactions than intraband hot holes. This is the first study to the best of the Author's knowledge where both interband and intraband hot carriers have been used to drive a single redox reaction using only Au NPs. Furthermore, the photocurrent generation efficiencies of these two types of hot carriers have been compared.

A novel bioassay design and implementation in the urine sample

A novel bioassay was developed for label-free detection of nucleic acids. A signal-amplification barcode (SAB) was introduced to the electrode after target hybridization, making the output signal inversely proportional to the concentration of the analyte. The inversely proportional signaling mechanism provides higher readout signal for lower concentration of the analytes, and thereby less likely to be affected by the environmental or instrumental noise than regular sandwich-based assays. Both electrochemical and photoelectrochemical transducers were used to verify the new assay design. The readout current obtained for the electrochemical assay is solely from the DNA-barcode and therefore, no background current exists in the system whereas for photoelectrochemical assay, both the photocurrents obtained after incubating with target and SAB were used for readout. By adopting a differential approach utilizing these two signals, DNA with complementary and mismatched sequences can be distinguished. This unique differential assay design using two-step readout has shown to improve limit-of-detection, specificity, and sensitivity.

9.4 Future Work

This section discusses some recommendations and ideas about solving the remaining challenges and directions based on the results obtained in this thesis. These suggestions encompass theoretical study, optimization of different parts of photoelectrochemical biosensor design, engineering, experimental plan, and materials research.

Automating the layer-by-layer deposition process

Chapter 3 describes the layer-by-layer deposition of CdTe QDs on a wrinkled substrate. The other works reported in this thesis also incorporate solution-based fabrication of photoelectrodes. Manual handling of these electrodes introduces the variability of the QD loading amount from one electrode to another. A relative change of photocurrent is used throughout this work to ensure that the change in electrode processing does not generate significant variation in output readout. This variation in the amount of photoactive material on the electrode also introduces variation in biofunctionalization and thereby the amount of captured target. Automation of the layer-by-layer processing, as well as other solution-based methods, will help to reduce the variability among the photoelectrodes because of the fabrication steps. Thus, automating the electrode fabrication steps might allow us to achieve less standard deviation in the signal and improved detection limit.

Developing mathematical model for wavelength and distance-dependent plasmonic effect

Extracting hot carriers from metal nanoparticles and utilizing them to drive redox reactions was investigated in this work. However, it is difficult to experimentally study the wavelength and distance dependence interaction of hot carriers with semiconductors in the presence of electron or hole scavenger in the electrolyte because of the short lifetime of the hot electrons and hot holes (100 fs – 1 ps).[542] Therefore, simulation-based studies can be used to gain further insights about carrier dynamics in the metal/semiconductor device.[385,394] There is no theoretical study reported on distance dependence and wavelength dependence effect on plasmonic carrier dynamics at metal/semiconductor interface with an applied potential bias. A finite-element-method or quantum electrodynamic analysis might provide a valuable tool for designing the PEC sensor to detect biomolecules.

Transient absorption spectroscopy study to examine the charge carrier dynamics when Au NP is connected to TiO_2 by DNA linker

Transient absorption spectroscopy (TAS) has been used in the literature to examine the electron temperature after photoexcitation, charge transfer direction and efficiency.[356,365] Ratchford *et al.* used TAS to quantify hot electron transfer in Au NP/TiO_2 structure where Au NP is embedded in the TiO_2 film.[328] Additionally, wavelength dependent hot carrier transfer was studied by TAS when Au NPs and TiO_2 are in contact or separated by the SiO_2 layer.[365] However, there is no TAS study probing Au NP and TiO_2 systems separated by a nucleic acid linker. Nucleic acids have been shown to conduct charge[543,544] and thereby can affect the hot carrier transfer. Experimental studies conducted via TAS might provide a better understanding of whether photocharging or hot electron transfer to TiO_2 is dominant when Au NP/TiO_2 systems are illuminated by UV light.

Investigating the effect of Au NP size and shape on biosensing

A major advantage of plasmonic NPs is their tunability of plasmonic properties by varying the size and shape of the particle.[95,545] In this work, we have used 12 nm spherical Au NP for biosensing application. The size of Au NP is large compared to the size of DNA used which may obstruct the access of available capture sites. Experimental observation of DNA hybridization efficiency for varying Au NP sizes may provide insights on the impact of Au NPs on the hybridization kinetics. Additionally, Govorov *et al.* demonstrated that higher electric field magnification and more hot spots can be obtained by using nanostar particles.[377] A study comprises different shape of Au NP (e.g., star, cube, triangle) for biosensing may help to achieve lower detection limit and higher sensitivity.

Investigating the effectivity of the bioassay used in this work for other types of biomolecule detection

In this thesis, we demonstrated the development of various photoelectrochemical bioassays for nucleic acid detection. A similar bioassay design as demonstrated in chapters 6, 7 and 8 can be used in other biomolecule sensing designs. Aptamer based bioassays can be used for protein or antibody detection, where target binding with aptamer can bring the plasmonic NP in proximity to the electrode or remove the plasmonic NPs from the electrode surface. Thereby introducing a signal change that can be directly correlated with the concentration of the analyte.

Performing clinical study using the micro-RNA sensor developed in this thesis

In chapter 7, we detected microRNA from human urine samples. The electrochemical sensor was challenged with 10 patient samples with a sensitivity of 80%. A larger sample population is required to study the transducer's effectivity in clinical diagnostics. A comparative study with PCR will help in understanding the relationship between disease progression and microRNA expression levels.

Multiplexed photoelectrochemical detection of biomarkers

Most of the POC devices reported in the literature are restricted to the detection of only one analyte of interest.[9,36,52] However, detection systems reliant on the sensing of a single biomarker for early disease detection is often criticized as it leads to false positives and negatives.[546] For example, a single microRNA detection usually is not sufficient to diagnose cancer.[547] Multi-analyte detection offers better disease diagnosis, monitoring and economical solution compared to single analyte detection device.[494,548,549] The nucleic acid sensors developed in this thesis are also designed to detect only one type of DNA/RNA at a time. However, photoelectrochemical methods have been used to detect more than one analyte using multiple bias potentials or using different wavelengths. In this work, a programmable photocurrent modulation was shown by utilizing different lengths of probe.

This can also be used to detect more than one analyte either by using different probe sequences or using different plasmonic nanoparticles such as Ag.

9.5 Final Remarks

We started this work with the aim to develop signal amplification strategies for PEC biosensors and improve the current understanding of the interaction mechanism between plasmonic NP and semiconductor.

Previously, only planar substrates were used to prepare electrodes for PEC biosensing. A higher electrochemical surface area was achieved using NPs or mesoporous structures. We utilized a wrinkled scaffold to deposit NPs and thereby enhance the electrochemical surface area, which in turn increased the photoelectrochemical signal. Additionally, prior to this work, plasmonic NPs were either used to enhance or reduce the photocurrent. However, we can now utilize plasmonic NPs to program the photocurrent modulation. Furthermore, this programmable feature can be used to obtain differential signaling that enhances the sensitivity and signal-to-noise ratio.

References

(1) Soleymani, L.; Li, F. Mechanistic Challenges and Advantages of Biosensor Miniaturization into the Nanoscale. *ACS Sensors* **2017**, *2* (4), 458–467. https://doi.org/10.1021/acssensors.7b00069.

(2) Bhalla, N.; Jolly, P.; Formisano, N.; Estrela, P. Introduction to Biosensors. *Essays Biochem.* **2016**, *60* (1), 1–8. https://doi.org/10.1042/EBC20150001.

(3) Thévenot, D. R.; Toth, K.; Durst, R. A.; Wilson, G. S. Electrochemical Biosensors: Recommended Definitions and Classification1International Union of Pure and Applied Chemistry: Physical Chemistry Division, Commission I.7 (Biophysical Chemistry); Analytical Chemistry Division, Commission V.5 (Electroanalytical Chemistry).1. *Biosens. Bioelectron.* **2001**, *16* (1), 121–131. https://doi.org/https://doi.org/10.1016/S0956-5663(01)00115-4.

(4) Nayak, S.; Blumenfeld, N. R.; Laksanasopin, T.; Sia, S. K. Point-of-Care Diagnostics: Recent Developments in a Connected Age. *Anal. Chem.* **2017**, *89* (1), 102–123. https://doi.org/10.1021/acs.analchem.6b04630.

(5) Kosack, C. S.; Page, A.; Klatser, P. R. A Guide to Aid the Selection of Diagnostic Tests. *Bull. World Health Organ.* **2017**, *95* (9), 639–645.

(6) Manocha, A.; Bhargava, S. Emerging Challenges in Point-of-Care Testing. *Curr. Med. Res. Pract.* **2019**, *9* (6), 227–230. https://doi.org/https://doi.org/10.1016/j.cmrp.2019.11.006.

(7) Kozel, T. R.; Burnham-Marusich, A. R. Point-of-Care Testing for Infectious Diseases: Past, Present, and Future. *J. Clin. Microbiol.* **2017**, *55* (8), 2313. https://doi.org/10.1128/JCM.00476-17.

(8) Kalorama Information. *Molecular Point-of-Care (POC) Markets*; 2019.

(9) Syedmoradi, L.; Daneshpour, M.; Alvandipour, M.; Gomez, F. A.; Hajghassem, H.; Omidfar, K. Point of Care Testing: The Impact of Nanotechnology. *Biosens. Bioelectron.* **2017**, *87*, 373–387. https://doi.org/https://doi.org/10.1016/j.bios.2016.08.084.

(10) Mabey, D.; Peeling, R. W.; Ustianowski, A.; Perkins, M. D. Diagnostics for the Developing World. *Nat. Rev. Microbiol.* **2004**, *2* (3), 231–240. https://doi.org/10.1038/nrmicro841.

(11) Kalorama Information. *The World Market for Molecular Diagnostics in the COVID-19 Era*; 2020.

(12) Point of Care/POC Diagnostics Market worth $46.7 billion by 2024 https://www.marketsandmarkets.com/PressReleases/point-of-care-diagnostic.asp (accessed Oct 19, 2020).

(13) Point of Care (POC) Diagnostics Industry Forecast to 2027 - Introduction of CLIA Waived Tests, Rise in Funding from Government & Private Institutions https://www.globenewswire.com/news-release/2020/04/08/2013356/0/en/Point-of-Care-POC-Diagnostics-Industry-Forecast-to-2027-Introduction-of-CLIA-Waived-Tests-Rise-in-Funding-from-Government-Private-Institutions.html (accessed Oct 19, 2020).

(14) Patrinos, G. P.; Danielson, P. B.; Ansorge, W. J. Chapter 1 - Molecular Diagnostics: Past, Present, and Future. In *Molecular Diagnostics (Third Edition)*; Patrinos, G. P., Ed.; Academic Press, 2017; pp 1–11. https://doi.org/https://doi.org/10.1016/B978-0-12-802971-8.00001-8.

(15) Hansen, S.; Abd El Wahed, A. Point-Of-Care or Point-Of-Need Diagnostic Tests: Time to Change Outbreak Investigation and Pathogen Detection. *Trop. Med. Infect. Dis.* **2020**, *5* (4), 151. https://doi.org/10.3390/tropicalmed5040151.

(16) Basile, K.; Kok, J.; Dwyer, D. E. Point-of-Care Diagnostics for Respiratory Viral Infections. *Expert Rev. Mol. Diagn.* **2018**, *18* (1), 75–83. https://doi.org/10.1080/14737159.2018.1419065.

(17) Sandbhor Gaikwad, P.; Banerjee, R. Advances in Point-of-Care Diagnostic Devices in Cancers. *Analyst* **2018**, *143* (6), 1326–1348. https://doi.org/10.1039/C7AN01771E.

(18) Gubala, V.; Harris, L. F.; Ricco, A. J.; Tan, M. X.; Williams, D. E. Point of Care Diagnostics: Status and Future. *Anal. Chem.* **2012**, *84* (2), 487–515. https://doi.org/10.1021/ac2030199.

(19) Reddy, B.; Hassan, U.; Seymour, C.; Angus, D. C.; Isbell, T. S.; White, K.; Weir, W.; Yeh, L.; Vincent, A.; Bashir, R. Point-of-Care Sensors for the Management of Sepsis. *Nat. Biomed. Eng.* **2018**, *2* (9), 640–648. https://doi.org/10.1038/s41551-018-0288-9.

(20) Willyard, C. Simpler Tests for Immune Cells Could Transform AIDS Care in Africa. *Nat. Med.* **2007**, *13* (10), 1131. https://doi.org/10.1038/nm1007-1131.

(21) Haney, K.; Tandon, P.; Divi, R.; Ossandon, M. R.; Baker, H.; Pearlman, P. C. The Role of

Affordable, Point-of-Care Technologies for Cancer Care in Low- and Middle-Income Countries: A Review and Commentary. *IEEE J. Transl. Eng. Heal. Med.* **2017**, *5*, 1–14. https://doi.org/10.1109/JTEHM.2017.2761764.

(22) Chikkaveeraiah, B. V.; Bhirde, A. A.; Morgan, N. Y.; Eden, H. S.; Chen, X. Electrochemical Immunosensors for Detection of Cancer Protein Biomarkers. *ACS Nano*. August 28, 2012, pp 6546–6561.

(23) Blandin Knight, S.; Crosbie, P. A.; Balata, H.; Chudziak, J.; Hussell, T.; Dive, C. Progress and Prospects of Early Detection in Lung Cancer. *Open Biol.* **2020**, *7* (9), 170070. https://doi.org/10.1098/rsob.170070.

(24) Ries, L. A. G.; Reichman, M. E.; Lewis, D. R.; Hankey, B. F.; Edwards, B. K. Cancer Survival and Incidence from the Surveillance, Epidemiology, and End Results (SEER) Program. *Oncol.* **2003**, *8* (6), 541–552.

(25) Ronkainen, N. J.; Halsall, H. B.; Heineman, W. R. Electrochemical Biosensors. *Chem. Soc. Rev.* **2010**, *39* (5), 1747–1763. https://doi.org/10.1039/B714449K.

(26) Rakotosamimanana, N.; Randrianirina, F.; Randremanana, R.; Raherison, M. S.; Rasolofo, V.; Solofomalala, G. D.; Spiegel, A.; Heraud, J. M. GeneXpert for the Diagnosis of COVID-19 in LMICs. *The Lancet Global Health*. Elsevier Ltd December 1, 2020, pp e1457–e1458. https://doi.org/10.1016/S2214-109X(20)30428-9.

(27) Srinivasan, B.; Tung, S. Development and Applications of Portable Biosensors. *J. Lab. Autom.* **2015**, *20* (4), 365–389. https://doi.org/10.1177/2211068215581349.

(28) Vashist, S. K. Point-of-Care Diagnostics: Recent Advances and Trends. *Biosensors* **2017**, *7* (4), 62-undefined. https://doi.org/10.3390/bios7040062.

(29) Nguyen, T.; Chidambara, V. A.; Andreasen, S. Z.; Golabi, M.; Huynh, V. N.; Linh, Q. T.; Bang, D. D.; Wolff, A. Point-of-Care Devices for Pathogen Detections: The Three Most Important Factors to Realise towards Commercialization. *TrAC Trends Anal. Chem.* **2020**, *131*, 116004. https://doi.org/https://doi.org/10.1016/j.trac.2020.116004.

(30) Yager, P.; Domingo, G. J.; Gerdes, J. Point-of-Care Diagnostics for Global Health. *Annu. Rev. Biomed. Eng.* **2008**, *10* (1), 107–144. https://doi.org/10.1146/annurev.bioeng.10.061807.160524.

(31) Wang, S.; Chinnasamy, T.; Lifson, M. A.; Inci, F.; Demirci, U. Flexible Substrate-Based Devices for Point-of-Care Diagnostics. *Trends Biotechnol.* **2016**, *34* (11), 909–921. https://doi.org/10.1016/j.tibtech.2016.05.009.

(32) Sher, M.; Zhuang, R.; Demirci, U.; Asghar, W. Paper-Based Analytical Devices for Clinical Diagnosis: Recent Advances in the Fabrication Techniques and Sensing Mechanisms. *Expert Rev. Mol. Diagn.* **2017**, *17* (4), 351–366. https://doi.org/10.1080/14737159.2017.1285228.

(33) Wang, S.; Lifson, M. A.; Liang, L.-G.; Sheng, Y.-F.; Demirci, U. Advances in Addressing Technical Challenges of Point-of-Care Diagnostics in Resource-Limited Settings. *Expert Rev. Mol. Diagn.* **2016**, *16* (4), 449–459. https://doi.org/10.1586/14737159.2016.1142877.

(34) Giljohann, D. A.; Mirkin, C. A. Drivers of Biodiagnostic Development. *Nature* **2009**, *462* (7272), 461–464. https://doi.org/10.1038/nature08605.

(35) da Silva, E. T. S. G.; Souto, D. E. P.; Barragan, J. T. C.; de F. Giarola, J.; de Moraes, A. C. M.; Kubota, L. T. Electrochemical Biosensors in Point-of-Care Devices: Recent Advances and Future Trends. *ChemElectroChem* **2017**, *4* (4), 778–794. https://doi.org/https://doi.org/10.1002/celc.201600758.

(36) Shrivastava, S.; Trung, T. Q.; Lee, N.-E. Recent Progress, Challenges, and Prospects of Fully Integrated Mobile and Wearable Point-of-Care Testing Systems for Self-Testing. *Chem. Soc. Rev.* **2020**, *49* (6), 1812–1866. https://doi.org/10.1039/C9CS00319C.

(37) Schoukroun-Barnes, L. R.; Macazo, F. C.; Gutierrez, B.; Lottermoser, J.; Liu, J.; White, R. J. Reagentless, Structure-Switching, Electrochemical Aptamer-Based Sensors. *Annu. Rev. Anal. Chem.* **2016**, *9* (1), 163–181. https://doi.org/10.1146/annurev-anchem-071015-041446.

(38) Choi, J. R.; Yong, K. W.; Tang, R.; Gong, Y.; Wen, T.; Li, F.; Pingguan-Murphy, B.; Bai, D.; Xu, F. Advances and Challenges of Fully Integrated Paper-Based Point-of-Care Nucleic Acid Testing. *TrAC Trends Anal. Chem.* **2017**, *93*, 37–50. https://doi.org/https://doi.org/10.1016/j.trac.2017.05.007.

(39) Alizadeh, N.; Salimi, A. Ultrasensitive Bioaffinity Electrochemical Sensors: Advances and New Perspectives. *Electroanalysis* **2018**, *30* (12), 2803–2840. https://doi.org/10.1002/elan.201800598.

(40) Shu, J.; Tang, D. Current Advances in Quantum-Dots-Based Photoelectrochemical Immunoassays. *Chem. – An Asian J.* **2017**, *12* (21), 2780–2789. https://doi.org/10.1002/asia.201701229.

(41) Zarei, M. Portable Biosensing Devices for Point-of-Care Diagnostics: Recent Developments and Applications. *TrAC Trends Anal. Chem.* **2017**, *91*, 26–41. https://doi.org/https://doi.org/10.1016/j.trac.2017.04.001.

(42) Kirste, R.; Rohrbaugh, N.; Bryan, I.; Bryan, Z.; Collazo, R.; Ivanisevic, A. Electronic Biosensors Based on III-Nitride Semiconductors. *Annu. Rev. Anal. Chem.* **2015**, *8* (1), 149–169. https://doi.org/10.1146/annurev-anchem-071114-040247.

(43) Fu, P.; Xing, S.; Xu, M.; Zhao, Y.; Zhao, C. Peptide Nucleic Acid-Based Electrochemical Biosensor for Simultaneous Detection of Multiple MicroRNAs from Cancer Cells with Catalytic Hairpin Assembly Amplification. *Sensors Actuators B Chem.* **2020**, *305*, 127545. https://doi.org/https://doi.org/10.1016/j.snb.2019.127545.

(44) Pang, J.; Chia, P. Y.; Lye, D. C.; Leo, Y. S. Progress and Challenges towards Pointof-Care Diagnostic Development for Dengue. *J. Clin. Microbiol.* **2017**, *55* (12), 3339–3349. https://doi.org/10.1128/JCM.00707-17.

(45) Chan, V.; Graves, D. J.; McKenzie, S. E. The Biophysics of DNA Hybridization with Immobilized Oligonucleotide Probes. *Biophys. J.* **1995**, *69* (6), 2243–2255. https://doi.org/10.1016/S0006-3495(95)80095-0.

(46) Squires, T. M.; Messinger, R. J.; Manalis, S. R. Making It Stick: Convection, Reaction and Diffusion in Surface-Based Biosensors. *Nat. Biotechnol.* **2008**, *26* (4), 417–426. https://doi.org/10.1038/nbt1388.

(47) Malhotra, B. D.; Ali, M. A. Nanomaterials in Biosensors: Fundamentals and Applications. *Nanomater. Biosens.* **2018**, 1–74. https://doi.org/10.1016/B978-0-323-44923-6.00001-7.

(48) Murugaiyan, S. B.; Ramasamy, R.; Gopal, N.; Kuzhandaivelu, V. Biosensors in Clinical Chemistry: An Overview. *Adv. Biomed. Res.* **2014**, *3*, 67. https://doi.org/10.4103/2277-9175.125848.

(49) Nguyen, V.-T.; Song, S.; Park, S.; Joo, C. Recent Advances in High-Sensitivity Detection Methods for Paper-Based Lateral-Flow Assay. *Biosens. Bioelectron.* **2020**, *152*, 112015. https://doi.org/https://doi.org/10.1016/j.bios.2020.112015.

(50) Fogel, R.; Limson, J. Developing Biosensors in Developing Countries: South Africa as a Case Study. *Biosensors* **2016**, *6* (1). https://doi.org/10.3390/bios6010005.

(51) Raiteri, R.; Grattarola, M.; Butt, H. J.; Skládal, P. Micromechanical Cantilever-Based Biosensors. *Sensors Actuators, B Chem.* **2001**, *79* (2–3), 115–126.

(52) Pashchenko, O.; Shelby, T.; Banerjee, T.; Santra, S. A Comparison of Optical, Electrochemical, Magnetic, and Colorimetric Point-of-Care Biosensors for Infectious Disease Diagnosis. *ACS Infect. Dis.* **2018**, *4* (8), 1162–1178. https://doi.org/10.1021/acsinfecdis.8b00023.

(53) Zhao, V. X. T.; Wong, T. I.; Zheng, X. T.; Tan, Y. N.; Zhou, X. Colorimetric Biosensors for Point-of-Care Virus Detections. *Mater. Sci. Energy Technol.* **2020**, *3*, 237–249. https://doi.org/https://doi.org/10.1016/j.mset.2019.10.002.

(54) Pohanka, M. Colorimetric Hand-Held Sensors and Biosensors with a Small Digital Camera as Signal Recorder, a Review. *Reviews in Analytical Chemistry*. De Gruyter January 1, 2020, pp 20–30. https://doi.org/10.1515/revac-2020-0111.

(55) Lee, J. H.; Wang, Z.; Liu, J.; Lu, Y. Highly Sensitive and Selective Colorimetric Sensors for Uranyl (UO_2^{2+}): Development and Comparison of Labeled and Label-Free DNAzyme-Gold Nanoparticle Systems. *J. Am. Chem. Soc.* **2008**, *130* (43), 14217–14226. https://doi.org/10.1021/ja803607z.

(56) Jalalian, S. H.; Karimabadi, N.; Ramezani, M.; Abnous, K.; Taghdisi, S. M. Electrochemical and Optical Aptamer-Based Sensors for Detection of Tetracyclines. *Trends Food Sci. Technol.* **2018**, *73*, 45–57. https://doi.org/https://doi.org/10.1016/j.tifs.2018.01.009.

(57) Narsaiah, K.; Jha, S. N.; Bhardwaj, R.; Sharma, R.; Kumar, R. Optical Biosensors for Food Quality and Safety Assurance—a Review. *J. Food Sci. Technol.* **2012**, *49* (4), 383–406.

https://doi.org/10.1007/s13197-011-0437-6.

(58) Jirimali, H. D. *Biomedical Engineering and Its Applications in Healthcare*; Paul, S., Ed.; Springer Singapore: Singapore, 2019. https://doi.org/10.1007/978-981-13-3705-5.

(59) Ramanathan, K.; Danielsson, B. Principles and Applications of Thermal Biosensors. *Biosens. Bioelectron.* **2001**, *16* (6), 417–423. https://doi.org/https://doi.org/10.1016/S0956-5663(01)00124-5.

(60) Mosbach, K. Thermal Biosensors. *Biosens. Bioelectron.* **1991**, *6* (3), 179–182. https://doi.org/https://doi.org/10.1016/0956-5663(91)80002-F.

(61) Xie, B.; Ramanathan, K.; Danielsson, B. Mini/Micro Thermal Biosensors and Other Related Devices for Biochemical/Clinical Analysis and Monitoring. *TrAC - Trends Anal. Chem.* **2000**, *19* (5), 340–349. https://doi.org/10.1016/S0165-9936(99)00211-3.

(62) Nabaei, V.; Chandrawati, R.; Heidari, H. Magnetic Biosensors: Modelling and Simulation. *Biosens. Bioelectron.* **2018**, *103*, 69–86. https://doi.org/https://doi.org/10.1016/j.bios.2017.12.023.

(63) Xianyu, Y.; Wang, Q.; Chen, Y. Magnetic Particles-Enabled Biosensors for Point-of-Care Testing. *TrAC Trends Anal. Chem.* **2018**, *106*, 213–224. https://doi.org/https://doi.org/10.1016/j.trac.2018.07.010.

(64) Pohanka, M. Overview of Piezoelectric Biosensors, Immunosensors and DNA Sensors and Their Applications. *Materials*. MDPI AG March 19, 2018, pp 448-undefined. https://doi.org/10.3390/ma11030448.

(65) Pohanka, M. The Piezoelectric Biosensors: Principles and Applications, a Review. *International Journal of Electrochemical Science*. Electrochemical Science Group 2017, pp 496–506. https://doi.org/10.20964/2017.01.44.

(66) Soper, S. A.; Brown, K.; Ellington, A.; Frazier, B.; Garcia-Manero, G.; Gau, V.; Gutman, S. I.; Hayes, D. F.; Korte, B.; Landers, J. L.; Larson, D.; Ligler, F.; Majumdar, A.; Mascini, M.; Nolte, D.; Rosenzweig, Z.; Wang, J.; Wilson, D. Point-of-Care Biosensor Systems for Cancer Diagnostics/Prognostics. *Biosens. Bioelectron.* **2006**, *21* (10), 1932–1942. https://doi.org/https://doi.org/10.1016/j.bios.2006.01.006.

(67) Yoo, E.-H.; Lee, S.-Y. Glucose Biosensors: An Overview of Use in Clinical Practice. *Sensors* **2010**, *10*, 4558–4576. https://doi.org/10.3390/s100504558.

(68) Goldstein, L. N.; Wells, M.; Vincent-Lambert, C. The Cost-Effectiveness of Upfront Point-of-Care Testing in the Emergency Department: A Secondary Analysis of a Randomised, Controlled Trial. *Scand. J. Trauma. Resusc. Emerg. Med.* **2019**, *27* (1). https://doi.org/10.1186/s13049-019-0687-2.

(69) Grieshaber, D.; MacKenzie, R.; Vörös, J.; Reimhult, E. Electrochemical Biosensors - Sensor Principles and Architectures. *Sensors* **2008**, *8*, 1400–1458. https://doi.org/10.3390/s8031400.

(70) Menon, S.; Mathew, M. R.; Sam, S.; Keerthi, K.; Kumar, K. G. Recent Advances and Challenges in Electrochemical Biosensors for Emerging and Re-Emerging Infectious Diseases. *J. Electroanal. Chem.* **2020**, *878*, 114596. https://doi.org/https://doi.org/10.1016/j.jelechem.2020.114596.

(71) Wu, D.; Rios-Aguirre, D.; Chounlakone, M.; Camacho-Leon, S.; Voldman, J. Sequentially Multiplexed Amperometry for Electrochemical Biosensors. *Biosens. Bioelectron.* **2018**, *117*, 522–529. https://doi.org/https://doi.org/10.1016/j.bios.2018.06.049.

(72) Zhao, W.-W.; Xu, J.-J.; Chen, H.-Y. Photoelectrochemical DNA Biosensors. *Chem. Rev.* **2014**, *114* (15), 7421–7441. https://doi.org/10.1021/cr500100j.

(73) Zhao, W.-W.; Xiong, M.; Li, X.-R.; Xu, J.-J.; Chen, H.-Y. Photoelectrochemical Bioanalysis: A Mini Review. *Electrochem. commun.* **2014**, *38*, 40–43. https://doi.org/https://doi.org/10.1016/j.elecom.2013.10.035.

(74) Voccia, D.; Palchetti, I. Photoelectrochemical Biosensors for Nucleic Acid Detection. *J. Nanosci. Nanotechnol.* **2015**, *15* (5), 3320–3332. https://doi.org/doi:10.1166/jnn.2015.10039.

(75) Tu, W.; Wang, Z.; Dai, Z. Selective Photoelectrochemical Architectures for Biosensing: Design, Mechanism and Responsibility. *TrAC Trends Anal. Chem.* **2018**, *105*, 470–483. https://doi.org/https://doi.org/10.1016/j.trac.2018.06.007.

(76) Zhao, W.-W.; Xu, J.-J.; Chen, H.-Y. Photoelectrochemical Aptasensing. *TrAC Trends Anal. Chem.* **2016**, *82*, 307–315. https://doi.org/https://doi.org/10.1016/j.trac.2016.06.020.

(77) Bard, A. J.; Faulkner, L. R.; York, N.; @bullet, C.; Brisbane, W.; Toronto, S. E.

ELECTROCHEMICAL METHODS Fundamentals and Applications. In *Electrochemistry. I. Faulkner, Larry R*; 1980. https://doi.org/10.1016/B978-0-12-381373-2.00056-9.

(78) Zhao, W.-W.; Xu, J.-J.; Chen, H.-Y. Photoelectrochemical Enzymatic Biosensors. *Biosens. Bioelectron.* **2017**, *92*, 294–304. https://doi.org/https://doi.org/10.1016/j.bios.2016.11.009.

(79) Bard, A. J. Photoelectrochemistry. *Science* **1980**, *207* (4427), 139–144.

(80) Zang, Y.; Lei, J.; Ju, H. Principles and Applications of Photoelectrochemical Sensing Strategies Based on Biofunctionalized Nanostructures. *Biosens. Bioelectron.* **2017**, *96*, 8–16. https://doi.org/https://doi.org/10.1016/j.bios.2017.04.030.

(81) Finklea, H. O. Photoelectrochemistry: Introductory Concepts. *J. Chem. Educ.* **1983**, *60* (4), 325. https://doi.org/10.1021/ed060p325.

(82) Zhao, W.-W.; Xu, J.-J.; Chen, H.-Y. Photoelectrochemical Bioanalysis: The State of the Art. *Chem. Soc. Rev.* **2015**, *44* (3), 729–741. https://doi.org/10.1039/C4CS00228H.

(83) Gratzel, M. Photoelectrochemical Cells. *Nature; London* **2001**. https://doi.org/10.1038/35104607.

(84) Nozik, A. J.; Memming, R. Physical Chemistry of Semiconductor-Liquid Interfaces. *J. Phys. Chem.* **1996**, *100* (31). https://doi.org/10.1021/jp953720e.

(85) Tryk, D.; Fujishima, A.; Honda, K. Recent Topics in Photoelectrochemistry: Achievements and Future Prospects. *Electrochim. Acta* **2000**, *45*, 236. https://doi.org/10.1016/S0013-4686(00)00337-6.

(86) Guijarro, N.; Prévot, M. S.; Sivula, K. Surface Modification of Semiconductor Photoelectrodes. *Phys. Chem. Chem. Phys.* **2015**, *17* (24), 15655–15674. https://doi.org/10.1039/C5CP01992C.

(87) Osterloh, F. E. Inorganic Nanostructures for Photoelectrochemical and Photocatalytic Water Splitting. *Chem. Soc. Rev.* **2013**, *42* (6), 2294–2320. https://doi.org/10.1039/C2CS35266D.

(88) Zeng, S.; Yong, K.-T.; Roy, I.; Dinh, X.-Q.; Yu, X.; Luan, F. A Review on Functionalized Gold Nanoparticles for Biosensing Applications. *Plasmonics* **2011**, *6* (3), 491. https://doi.org/10.1007/s11468-011-9228-1.

(89) Cao, X.; Ye, Y.; Liu, S. Gold Nanoparticle-Based Signal Amplification for Biosensing. *Anal. Biochem.* **2011**, *417* (1), 1–16. https://doi.org/https://doi.org/10.1016/j.ab.2011.05.027.

(90) Besteiro, L. V.; Kong, X. T.; Wang, Z.; Hartland, G.; Govorov, A. O. Understanding Hot-Electron Generation and Plasmon Relaxation in Metal Nanocrystals: Quantum and Classical Mechanisms. *ACS Photonics* **2017**, *4* (11), 2759–2781. https://doi.org/10.1021/acsphotonics.7b00751.

(91) Link, S.; El-Sayed, M. A. Size and Temperature Dependence of the Plasmon Absorption of Colloidal Gold Nanoparticles. *J. Phys. Chem. B* **1999**, *103* (21), 4212–4217. https://doi.org/10.1021/jp984796o.

(92) Sundararaman, R.; Narang, P.; Jermyn, A. S.; Goddard, W. A.; Atwater, H. A. Theoretical Predictions for Hot-Carrier Generation from Surface Plasmon Decay. *Nat. Commun.* **2014**, *5*, 5788. https://doi.org/10.1038/ncomms6788.

(93) Robatjazi, H.; Bahauddin, S. M.; Doiron, C.; Thomann, I. Direct Plasmon-Driven Photoelectrocatalysis. *Nano Lett.* **2015**, *15* (9), 6155–6161. https://doi.org/10.1021/acs.nanolett.5b02453.

(94) Guo, W.; Johnston-Peck, A. C.; Zhang, Y.; Hu, Y.; Huang, J.; Wei, W. D. Cooperation of Hot Holes and Surface Adsorbates in Plasmon-Driven Anisotropic Growth of Gold Nanostars. *J. Am. Chem. Soc.* **2020**, *142* (25), 10921–10925. https://doi.org/10.1021/jacs.0c03342.

(95) Lee, J. H.; Cho, H. Y.; Choi, H. K.; Lee, J. Y.; Choi, J. W. Application of Gold Nanoparticle to Plasmonic Biosensors. *Int. J. Mol. Sci.* **2018**, *19* (7), 2021. https://doi.org/10.3390/ijms19072021.

(96) Soleymani, L.; Li, F. Mechanistic Challenges and Advantages of Biosensor Miniaturization into the Nanoscale. *ACS Sensors* **2017**, *2* (4), 458–467. https://doi.org/10.1021/acssensors.7b00069.

(97) Zhao, W.-W.; Xu, J.-J.; Chen, H.-Y. Photoelectrochemical Immunoassays. *Anal. Chem.* **2018**, *90* (1), 615–627. https://doi.org/10.1021/acs.analchem.7b04672.

(98) Zhang, Y.; Luo, J.; Flewitt, A. J.; Cai, Z.; Zhao, X. Film Bulk Acoustic Resonators (FBARs) as Biosensors: A Review. *Biosens. Bioelectron.* **2018**, *116*, 1–15. https://doi.org/https://doi.org/10.1016/j.bios.2018.05.028.

(99) Špačková, B.; Wrobel, P.; Bocková, M.; Homola, J. Optical Biosensors Based on Plasmonic Nanostructures: A Review. *Proc. IEEE* **2016**, *104* (12), 2380–2408.

https://doi.org/10.1109/JPROC.2016.2624340.

(100) DeMiguel-Ramos, M.; Díaz-Durán, B.; Escolano, J.-M.; Barba, M.; Mirea, T.; Olivares, J.; Clement, M.; Iborra, E. Gravimetric Biosensor Based on a 1.3GHz AlN Shear-Mode Solidly Mounted Resonator. *Sensors Actuators B Chem.* **2017**, *239*, 1282–1288. https://doi.org/https://doi.org/10.1016/j.snb.2016.09.079.

(101) Yildiz, H. B.; Freeman, R.; Gill, R.; Willner, I. Electrochemical, Photoelectrochemical, and Piezoelectric Analysis of Tyrosinase Activity by Functionalized Nanoparticles. *Anal. Chem.* **2008**, *80* (8), 2811–2816. https://doi.org/10.1021/ac702401v.

(102) Golub, E.; Pelossof, G.; Freeman, R.; Zhang, H.; Willner, I. Electrochemical, Photoelectrochemical, and Surface Plasmon Resonance Detection of Cocaine Using Supramolecular Aptamer Complexes and Metallic or Semiconductor Nanoparticles. *Anal. Chem.* **2009**, *81* (22), 9291–9298. https://doi.org/10.1021/ac901551q.

(103) Bard, A. J.; Faulkner, L. R.; York, N.; @bullet, C.; Brisbane, W.; Toronto, S. E. *ELECTROCHEMICAL METHODS Fundamentals and Applications*; 1980. https://doi.org/10.1016/B978-0-12-381373-2.00056-9.

(104) Fan, G.-C.; Zhu, H.; Shen, Q.; Han, L.; Zhao, M.; Zhang, J.-R.; Zhu, J.-J. Enhanced Photoelectrochemical Aptasensing Platform Based on Exciton Energy Transfer between CdSeTe Alloyed Quantum Dots and SiO $_2$ @Au Nanocomposites. *Chem. Commun.* **2015**, *51* (32), 7023–7026. https://doi.org/10.1039/C5CC01935D.

(105) Han, Z.; Luo, M.; Chen, L.; Chen, J.; Li, C. A Photoelectrochemical Immunosensor for Detection of α-Fetoprotein Based on Au-ZnO Flower-Rod Heterostructures. *Appl. Surf. Sci.* **2017**, *402*, 429–435. https://doi.org/10.1016/j.apsusc.2017.01.137.

(106) Tu, W.; Wang, Z.; Dai, Z. Selective Photoelectrochemical Architectures for Biosensing: Design, Mechanism and Responsibility. *TrAC Trends Anal. Chem.* **2018**, *105*, 470–483. https://doi.org/https://doi.org/10.1016/j.trac.2018.06.007.

(107) Chen, Z.; Deutsch, T. G.; Dinh, H. N.; Domen, K.; Emery, K.; Forman, A. J.; Gaillard, N.; Garland, R.; Heske, C.; Jaramillo, T. F.; Kleiman-Shwarsctein, A.; Miller, E.; Takanabe, K.; Turner, J. Efficiency Definitions in the Field of PEC. In *SpringerBriefs in Energy*; 2013; pp 7–16. https://doi.org/10.1007/978-1-4614-8298-7_2.

(108) Kolesova, E. P.; Orlova, A. O.; Maslov, V. G.; Gun'ko, Y. K.; Cleary, O.; Baranov, A. V.; Fedorov, A. V. Photocatalytic Properties of Hybrid Nanostructures Based on Nanoparticles of TiO_2 and Semiconductor Quantum Dots. *Opt. Spectrosc.* **2018**, *125* (1), 99–103. https://doi.org/10.1134/S0030400X18070160.

(109) Fu, B.; Zhang, Z. Periodical 2D Photonic-Plasmonic Au/TiOx Nanocavity Resonators for Photoelectrochemical Applications. *Small* **2018**, *14* (20), 1703610. https://doi.org/10.1002/smll.201703610.

(110) Devadoss, A.; Sudhagar, P.; Terashima, C.; Nakata, K. Journal of Photochemistry and Photobiology C : Photochemistry Reviews Photoelectrochemical Biosensors : New Insights into Promising Photoelectrodes and Signal Ampli Fi Cation Strategies. **2015**, *24*, 43–63.

(111) Zhu, Y. C.; Zhang, N.; Ruan, Y. F.; Zhao, W. W.; Xu, J. J.; Chen, H. Y. Alkaline Phosphatase Tagged Antibodies on Gold Nanoparticles/TiO2Nanotubes Electrode: A Plasmonic Strategy for Label-Free and Amplified Photoelectrochemical Immunoassay. *Anal. Chem.* **2016**, *88* (11), 5626–5630. https://doi.org/10.1021/acs.analchem.6b01261.

(112) Zhao, W. W.; Xu, J. J.; Chen, H. Y. Photoelectrochemical DNA Biosensors. *Chem. Rev.* **2014**, *114* (15), 7421–7441. https://doi.org/10.1021/cr500100j.

(113) Tian, J.; Li, Y.; Dong, J.; Huang, M.; Lu, J. Photoelectrochemical TiO_2 Nanotube Arrays Biosensor for Asulam Determination Based on in-Situ Generation of Quantum Dots. *Biosens. Bioelectron.* **2018**, *110* (March), 1–7. https://doi.org/10.1016/j.bios.2018.03.038.

(114) Lin, Y.; Zhou, Q.; Tang, D.; Niessner, R.; Yang, H.; Knopp, D. Silver Nanolabels-Assisted Ion-Exchange Reaction with CdTe Quantum Dots Mediated Exciton Trapping for Signal-On Photoelectrochemical Immunoassay of Mycotoxins. *Anal. Chem.* **2016**, *88* (15), 7858–7866. https://doi.org/10.1021/acs.analchem.6b02124.

(115) Li, M.; Xiong, C.; Zheng, Y.; Liang, W.; Yuan, R.; Chai, Y. Ultrasensitive Photoelectrochemical

Biosensor Based on DNA Tetrahedron as Nanocarrier for Efficient Immobilization of CdTe QDs-Methylene Blue as Signal Probe with Near-Zero Background Noise. *Anal. Chem.* **2018**, *90* (13), 8211–8216. https://doi.org/10.1021/acs.analchem.8b01641.

(116) Hao, N.; Zhang, Y.; Zhong, H.; Zhou, Z.; Hua, R.; Qian, J.; Liu, Q.; Li, H.; Wang, K. Design of a Dual Channel Self-Reference Photoelectrochemical Biosensor. *Anal. Chem.* **2017**, *89* (19), 10133–10136. https://doi.org/10.1021/acs.analchem.7b03132.

(117) Lv, S.; Zhang, K.; Lin, Z.; Tang, D. Novel Photoelectrochemical Immunosensor for Disease-Related Protein Assisted by Hemin/G-Quadruplex-Based DNAzyme on Gold Nanoparticles to Enhance Cathodic Photocurrent on p-$CuBi_2O_4$ Semiconductor. *Biosens. Bioelectron.* **2017**, *96*, 317–323. https://doi.org/https://doi.org/10.1016/j.bios.2017.05.027.

(118) Gong, L.; Zhao, Z.; Lv, Y.-F.; Huan, S.-Y.; Fu, T.; Zhang, X.-B.; Shen, G.-L.; Yu, R.-Q. DNAzyme-Based Biosensors and Nanodevices. *Chem. Commun.* **2015**, *51* (6), 979–995. https://doi.org/10.1039/C4CC06855F.

(119) Ge, L.; Wang, W.; Hou, T.; Li, F. A Versatile Immobilization-Free Photoelectrochemical Biosensor for Ultrasensitive Detection of Cancer Biomarker Based on Enzyme-Free Cascaded Quadratic Amplification Strategy. *Biosens. Bioelectron.* **2016**, *77*, 220–226. https://doi.org/10.1016/J.BIOS.2015.09.041.

(120) Zang, Y.; Lei, J.; Hao, Q.; Ju, H. CdS/MoS2 Heterojunction-Based Photoelectrochemical DNA Biosensor via Enhanced Chemiluminescence Excitation. *Biosens. Bioelectron.* **2016**, *77*, 557–564. https://doi.org/10.1016/j.bios.2015.10.010.

(121) Wang, M.; Yin, H.; Zhou, Y.; Sui, C.; Wang, Y.; Meng, X.; Waterhouse, G. I. N.; Ai, S. Photoelectrochemical Biosensor for MicroRNA Detection Based on a MoS_2/g-C_3N_4/Black TiO_2 Heterojunction with Histostar@AuNPs for Signal Amplification. *Biosens. Bioelectron.* **2019**, *128*, 137–143. https://doi.org/https://doi.org/10.1016/j.bios.2018.12.048.

(122) Wang, Y.-F.; Wang, H.-Y.; Li, Z.-S.; Zhao, J.; Wang, L.; Chen, Q.-D.; Wang, W.-Q.; Sun, H.-B. Electron Extraction Dynamics in CdSe and CdSe/CdS/ZnS Quantum Dots Adsorbed with Methyl Viologen. *J. Phys. Chem. C* **2014**, *118* (31), 17240–17246. https://doi.org/10.1021/jp5024789.

(123) Matylitsky, V. V.; Dworak, L.; Breus, V. V.; Basché, T.; Wachtveitl, J. Ultrafast Charge Separation in Multiexcited CdSe Quantum Dots Mediated by Adsorbed Electron Acceptors. *J. Am. Chem. Soc.* **2009**, *131* (7), 2424–2425. https://doi.org/10.1021/ja808084y.

(124) Han, Z.; Luo, M.; Chen, L.; Pan, H.; Chen, J.; Li, C. A Photoelectrochemical Biosensor for Determination of DNA Based on Flower Rod-like Zinc Oxide Heterostructures. *Microchim. Acta* **2017**, *184* (8), 2541–2549. https://doi.org/10.1007/s00604-017-2257-5.

(125) Hong, Z.; Jing, L.; Shusheng, Z. Quantum Dot-Based Photoelectric Conversion for Biosensing Applications. Trends in Analytical Chemistry 67 (2015) 56–73. *Trends in Anal. Chem.* **2015**, *67*, 56–73.

(126) Yu, K. J.; Yan, Z.; Han, M.; Rogers, J. A. Inorganic Semiconducting Materials for Flexible and Stretchable Electronics. *npj Flex. Electron.* **2017**, *1* (1), 4. https://doi.org/10.1038/s41528-017-0003-z.

(127) Jiang, Y.; Tian, B. Inorganic Semiconductor Biointerfaces. *Nat. Rev. Mater.* **2018**, *3* (12), 473–490. https://doi.org/10.1038/s41578-018-0062-3.

(128) Nelson, J. Organic Photovoltaic Films. *Curr. Opin. Solid State Mater. Sci.* **2002**, *6* (1), 87–95. https://doi.org/https://doi.org/10.1016/S1359-0286(02)00006-2.

(129) Tomkiewicz, M.; Woodall, J. M. Photoelectrolysis of Water with Semiconductor Materials. *J. Electrochem. Soc* **1977**, *124* (9), 1436–1440. https://doi.org/10.1149/1.2133669.

(130) Wang, Y.; Tang, J.; Zhou, T.; Da, P.; Li, J.; Kong, B.; Yang, Z.; Zheng, G. Reversible Chemical Tuning of Charge Carriers for Enhanced Photoelectrochemical Conversion and Probing of Living Cells. *Small* **2014**, *10* (23), 4967–4974. https://doi.org/10.1002/smll.201401059.

(131) Liu, L.; Hensel, J.; Fitzmorris, R. C.; Li, Y.; Zhang, J. Z. Preparation and Photoelectrochemical Properties of CdSe/TiO<sup>2 Hybrid Mesoporous Structures. *J. Phys. Chem. Lett.* **2010**, *1* (1), 155–160. https://doi.org/10.1021/jz900122u.

(132) Chen, X.; Mao, S. S. Titanium Dioxide Nanomaterials : Synthesis , Properties , Modifications , and Applications. **2007**. https://doi.org/10.1021/cr0500535.

(133) Daghrir, R.; Drogui, P.; Robert, D. Modified TiO $_2$ For Environmental Photocatalytic Applications: A Review. *Ind. Eng. Chem. Res.* **2013**, *52* (10), 3581–3599. https://doi.org/10.1021/ie303468t.

(134) Du, J.; Yang, M.; Zhang, F.; Cheng, X.; Wu, H.; … H. Q.-C.; 2018, U. Enhanced Charge Separation of CuS and CdS Quantum-Dot-Cosensitized Porous TiO2-Based Photoanodes for Photoelectrochemical Water Splitting. *Elsevier* **2017**.

(135) Liu, P. P.; Liu, X.; Huo, X. H.; Tang, Y.; Xu, J.; Ju, H. TiO $_2$ –BiVO $_4$ Heterostructure to Enhance Photoelectrochemical Efficiency for Sensitive Aptasensing. *ACS Appl. Mater. Interfaces* **2017**, *9* (32), 27185–27192. https://doi.org/10.1021/acsami.7b07047.

(136) Komathi, S.; Muthuchamy, N.; Lee, K.-P.; Gopalan, A.-I. Fabrication of a Novel Dual Mode Cholesterol Biosensor Using Titanium Dioxide Nanowire Bridged 3D Graphene Nanostacks. *Biosens. Bioelectron.* **2016**, *84*, 64–71. https://doi.org/10.1016/J.BIOS.2015.11.042.

(137) Mitchell, K.; Fahrenbruch, A. L.; Bube, R. H. Photovoltaic Determination of Optical-absorption Coefficient in CdTe. *J. Appl. Phys.* **1977**, *48* (2), 829–830. https://doi.org/10.1063/1.323636.

(138) Sarkar, S.; Pal, S.; Sarkar, P. Electronic Structure and Band Gap Engineering of CdTe Semiconductor Nanowires. *J. Mater. Chem.* **2012**, *22* (21), 10716. https://doi.org/10.1039/c2jm16810c.

(139) Wang, G.; Yang, X.; Qian, F.; Zhang, J. Z.; Li, Y. Double-Sided CdS and CdSe Quantum Dot Co-Sensitized ZnO Nanowire Arrays for Photoelectrochemical Hydrogen Generation. *Nano Lett.* **2010**, *10* (3), 1088–1092. https://doi.org/10.1021/nl100250z.

(140) Zhou, H.; Liu, J.; Zhang, S. Quantum Dot-Based Photoelectric Conversion for Biosensing Applications. *TrAC Trends Anal. Chem.* **2015**, *67*, 56–73. https://doi.org/10.1016/J.TRAC.2014.12.007.

(141) Yue, Z.; Lisdat, F.; Parak, W. J.; Hickey, S. G.; Tu, L.; Sabir, N.; Dorfs, D.; Bigall, N. C. Quantum-Dot-Based Photoelectrochemical Sensors for Chemical and Biological Detection. *ACS Appl. Mater. Interfaces* **2013**, *5* (8), 2800–2814. https://doi.org/10.1021/am3028662.

(142) Özgür, Ü.; Alivov, Y. I.; Liu, C.; Teke, A.; Reshchikov, M. A.; Doğan, S.; Avrutin, V.; Cho, S.-J.; Morkoç, H. A Comprehensive Review of ZnO Materials and Devices. *J. Appl. Phys.* **2005**, *98* (4), 041301. https://doi.org/10.1063/1.1992666.

(143) Tu, W.; Lei, J.; Wang, P.; Ju, H. Photoelectrochemistry of Free-Base-Porphyrin-Functionalized Zinc Oxide Nanoparticles and Their Applications in Biosensing. *Chem. - A Eur. J.* **2011**, *17* (34), 9440–9447. https://doi.org/10.1002/chem.201100577.

(144) Kang, Z.; Yan, X.; Wang, Y.; Bai, Z.; Liu, Y.; Zhang, Z.; Lin, P.; Zhang, X.; Yuan, H.; Zhang, X.; Zhang, Y. Electronic Structure Engineering of Cu2O Film/ZnO Nanorods Array All-Oxide p-n Heterostructure for Enhanced Photoelectrochemical Property and Self-Powered Biosensing Application. *Sci. Rep.* **2015**, *5* (1), 7882. https://doi.org/10.1038/srep07882.

(145) Zhao, K.; Yan, X.; Gu, Y.; Kang, Z.; Bai, Z.; Cao, S.; Liu, Y.; Zhang, X.; Zhang, Y. Self-Powered Photoelectrochemical Biosensor Based on CdS/RGO/ZnO Nanowire Array Heterostructure. *Small* **2016**, *12* (2), 245–251. https://doi.org/10.1002/smll.201502042.

(146) Qiao, Y.; Li, J.; Li, H.; Fang, H.; Fan, D.; Wang, W. A Label-Free Photoelectrochemical Aptasensor for Bisphenol A Based on Surface Plasmon Resonance of Gold Nanoparticle-Sensitized ZnO Nanopencils. *Biosens. Bioelectron.* **2016**, *86*, 315–320. https://doi.org/10.1016/J.BIOS.2016.06.062.

(147) Liu, F.; Zhang, Y.; Yu, J.; Wang, S.; Ge, S.; Song, X. Application of ZnO/Graphene and S6 Aptamers for Sensitive Photoelectrochemical Detection of SK-BR-3 Breast Cancer Cells Based on a Disposable Indium Tin Oxide Device. *Biosens. Bioelectron.* **2014**, *51*, 413–420. https://doi.org/10.1016/J.BIOS.2013.07.066.

(148) Jiang, D.; Du, X.; Liu, Q.; Hao, N.; Wang, K. MoS 2 /Nitrogen Doped Graphene Hydrogels p-n Heterojunction: Efficient Charge Transfer Property for Highly Sensitive and Selective Photoelectrochemical Analysis of Chloramphenicol. *Biosens. Bioelectron.* **2019**, *126*, 463–469. https://doi.org/10.1016/j.bios.2018.11.018.

(149) Rim, Y. S.; Chen, H.; Zhu, B.; Bae, S.-H.; Zhu, S.; Li, P. J.; Wang, I. C.; Yang, Y. Interface Engineering of Metal Oxide Semiconductors for Biosensing Applications. *Adv. Mater. Interfaces* **2017**, *4* (10), 1700020. https://doi.org/10.1002/admi.201700020.

(150) Kadian, S.; Arya, B. D.; Kumar, S.; Sharma, S. N.; Chauhan, R. P.; Srivastava, A.; Chandra, P.; Singh, S. P. Synthesis and Application of PHT-TiO $_2$ Nanohybrid for Amperometric Glucose Detection in Human Saliva Sample. *Electroanalysis* **2018**, *30* (11), 2793–2802. https://doi.org/10.1002/elan.201800207.

(151) Cheng, Y.; Xiong, P.; Yun, C. S.; Strouse, G. F.; Zheng, J. P.; Yang, R. S.; Wang, Z. L. Mechanism and Optimization of PH Sensing Using SnO2 Nanobelt Field Effect Transistors. *Nano Lett.* **2008**, *8* (12), 4179–4184. https://doi.org/10.1021/nl801696b.

(152) Ikeda, A.; Nakasu, M.; Ogasawara, S.; Nakanishi, H.; Nakamura, M.; Kikuchi, J. I. Photoelectrochemical Sensor with Porphyrin-Deposited Electrodes for Determination of Nucleotides in Water. *Org. Lett.* **2009**, *11* (5), 1163–1166. https://doi.org/10.1021/ol900037q.

(153) Da, H.; Liu, H.; Zheng, Y.; Yuan, R.; Chai, Y. A Highly Sensitive VEGF165 Photoelectrochemical Biosensor Fabricated by Assembly of Aptamer Bridged DNA Networks. *Biosens. Bioelectron.* **2018**, *101*, 213–218. https://doi.org/https://doi.org/10.1016/j.bios.2017.10.032.

(154) Shi, X. M.; Mei, L. P.; Wang, Q.; Zhao, W. W.; Xu, J. J.; Chen, H. Y. Energy Transfer between Semiconducting Polymer Dots and Gold Nanoparticles in a Photoelectrochemical System: A Case Application for Cathodic Bioanalysis. *Anal. Chem.* **2018**, *90* (7), 4277–4281. https://doi.org/10.1021/acs.analchem.8b00839.

(155) Xu, J.; Wang, S.; Wang, G.-J. N.; Zhu, C.; Luo, S.; Jin, L.; Gu, X.; Chen, S.; Feig, V. R.; To, J. W. F.; Rondeau-Gagné, S.; Park, J.; Schroeder, B. C.; Lu, C.; Oh, J. Y.; Wang, Y.; Kim, Y.-H.; Yan, H.; Sinclair, R.; Zhou, D.; Xue, G.; Murmann, B.; Linder, C.; Cai, W.; Tok, J. B.-H.; Chung, J. W.; Bao, Z. Highly Stretchable Polymer Semiconductor Films through the Nanoconfinement Effect. *Science* **2017**, *355* (6320), 59–64. https://doi.org/10.1126/science.aah4496.

(156) Zhao, X.; Chaudhry, S. T.; Mei, J. Heterocyclic Building Blocks for Organic Semiconductors. **2017**. https://doi.org/10.1016/bs.aihch.2016.04.009.

(157) Malliaras, G. . Photovoltaic Devices from Organic Semiconductors. In *Encyclopedia of Materials: Science and Technology*; Elsevier, 2004; pp 6981–6986. https://doi.org/10.1016/b0-08-043152-6/01237-7.

(158) Wang, A.; Wong-Ng, W.; Lan, Y.; Wang, C.; Fu, L. Recent Advances of Graphitic Carbon Nitride-Based Structures and Applications in Catalyst, Sensing, Imaging, and LEDs. *Nano-Micro Lett.* **2017**, *9* (4). https://doi.org/10.1007/s40820-017-0148-2.

(159) Su, F.; Mathew, S. C.; Lipner, G.; Fu, X.; Antonietti, M.; Blechert, S.; Wang, X. Mpg-C 3 N 4 -Catalyzed Selective Oxidation of Alcohols Using O 2 and Visible Light. *J. Am. Chem. Soc.* **2010**, *132* (46), 16299–16301. https://doi.org/10.1021/ja102866p.

(160) Ong, W.-J.; Tan, L.-L.; Ng, Y. H.; Yong, S.-T.; Chai, S.-P. Graphitic Carbon Nitride (g-C3N4)-Based Photocatalysts for Artificial Photosynthesis and Environmental Remediation: Are We a Step Closer To Achieving Sustainability? *Chem. Rev.* **2016**, *116* (12), 7159–7329. https://doi.org/10.1021/acs.chemrev.6b00075.

(161) Zhu, J.; Xiao, P.; Li, H.; Carabineiro, S. A. C. Graphitic Carbon Nitride: Synthesis, Properties, and Applications in Catalysis. *ACS Appl. Mater. Interfaces* **2014**, *6* (19), 16449–16465. https://doi.org/10.1021/am502925j.

(162) Wu, G.; Hu, Y.; Liu, Y.; Zhao, J.; Chen, X.; Whoehling, V.; Plesse, C.; Nguyen, G. T. M.; Vidal, F.; Chen, W. Graphitic Carbon Nitride Nanosheet Electrode-Based High-Performance Ionic Actuator. *Nat. Commun.* **2015**, *6*. https://doi.org/10.1038/ncomms8258.

(163) Liu, X.; Dai, L. Carbon-Based Metal-Free Catalysts. *Nat. Rev. Mater.* **2016**, *1* (11). https://doi.org/10.1038/natrevmats.2016.64.

(164) Tong, Z.; Yang, D.; Li, Z.; Nan, Y.; Ding, F.; Shen, Y.; Jiang, Z. Thylakoid-Inspired Multishell g-C_3N_4Nanocapsules with Enhanced Visible-Light Harvesting and Electron Transfer Properties for High-Efficiency Photocatalysis. *ACS Nano* **2017**, *11* (1), 1103–1112. https://doi.org/10.1021/acsnano.6b08251.

(165) Panneri, S.; Thomas, M.; Ganguly, P.; Nair, B. N.; Mohamed, A. P.; Warrier, K. G. K.; Hareesh, U. S. C3N4 Anchored ZIF 8 Composites: Photo-Regenerable, High Capacity Sorbents as Adsorptive Photocatalysts for the Effective Removal of Tetracycline from Water. *Catal. Sci. Technol.* **2017**, *7* (10), 2118–2128. https://doi.org/10.1039/c7cy00348j.

(166) Shi, X. M.; Fan, G. C.; Tang, X.; Shen, Q.; Zhu, J. J. Ultrasensitive Photoelectrochemical Biosensor for the Detection of HTLV-I DNA: A Cascade Signal Amplification Strategy Integrating λ-Exonuclease Aided Target Recycling with Hybridization Chain Reaction and Enzyme Catalysis. *Biosens. Bioelectron.* **2018**, *109*, 190–196. https://doi.org/10.1016/j.bios.2018.03.023.

(167) Li, C.; Du, Y.; Wang, D.; Yin, S.; Tu, W.; Chen, Z.; Kraft, M.; Chen, G.; Xu, R. Unique P-Co-N Surface Bonding States Constructed on g-C_3N_4 Nanosheets for Drastically Enhanced Photocatalytic Activity of H2 Evolution. *Adv. Funct. Mater.* **2017**, *27* (4), 1–8. https://doi.org/10.1002/adfm.201604328.

(168) Maeda, K.; Wang, X.; Nishihara, Y.; Lu, D.; Antonietti, M.; Domen, K. Photocatalytic Activities of Graphitic Carbon Nitride Powder for Water Reduction and Oxidation under Visible Light. *J. Phys. Chem. C* **2009**, *113* (12), 4940–4947. https://doi.org/10.1021/jp809119m.

(169) Zhang, Y.; Schnepp, Z.; Cao, J.; Ouyang, S.; Li, Y.; Ye, J.; Liu, S. Biopolymer-Activated Graphitic Carbon Nitride towards a Sustainable Photocathode Material. **2013**. https://doi.org/10.1038/srep02163.

(170) Zheng, Y.; Liu, J.; Liang, J.; Jaroniec, M.; Qiao, S. Z. Graphitic Carbon Nitride Materials: Controllable Synthesis and Applications in Fuel Cells and Photocatalysis. *Energy Environ. Sci.* **2012**, *5* (5), 6717. https://doi.org/10.1039/c2ee03479d.

(171) Khan, M. S.; Wang, C.; Zhang, Y.; Zhang, X.; Wei, Q.; Bao, C.; Fan, D.; Liu, Q. A Novel Label-Free Photoelectrochemical Sensor Based on N,S-GQDs and CdS Co-Sensitized Hierarchical Zn_2SnO_4 Cube for Detection of Cardiac Troponin I. *Biosens. Bioelectron.* **2018**, *106* (January), 14–20. https://doi.org/10.1016/j.bios.2018.01.050.

(172) Wang, H.; Wang, Y.; Zhang, Y.; Wang, Q.; Ren, X.; Wu, D.; Wei, Q. Photoelectrochemical Immunosensor for Detection of Carcinoembryonic Antigen Based on 2D TiO_2 Nanosheets and Carboxylated Graphitic Carbon Nitride. *Sci. Rep.* **2016**, *6*, 27385.

(173) Liu, Y.; Yan, K.; Zhang, J. Graphitic Carbon Nitride Sensitized with CdS Quantum Dots for Visible-Light-Driven Photoelectrochemical Aptasensing of Tetracycline. *ACS Appl. Mater. Interfaces* **2015**, *2015*. https://doi.org/10.1021/acsami.5b08275.

(174) Kesters, J.; Verstappen, P.; Kelchtermans, M.; Lutsen, L.; Vanderzande, D.; Maes, W. Porphyrin-Based Bulk Heterojunction Organic Photovoltaics: The Rise of the Colors of Life. *Adv. Energy Mater.* **2015**, *5* (13), 1–20. https://doi.org/10.1002/aenm.201500218.

(175) Lash, T. D. Benziporphyrins, a Unique Platform for Exploring the Aromatic Characteristics of Porphyrinoid Systems. *Org. Biomol. Chem.* **2015**, *13* (29), 7846–7878. https://doi.org/10.1039/C5OB00892A.

(176) Zang, Y.; Lei, J.; Ling, P.; Ju, H. Catalytic Hairpin Assembly-Programmed Porphyrin-DNA Complex as Photoelectrochemical Initiator for DNA Biosensing. *Anal. Chem.* **2015**, *87* (10), 5430–5436. https://doi.org/10.1021/acs.analchem.5b00888.

(177) Shu, J.; Qiu, Z.; Zhuang, J.; Xu, M.; Tang, D. In Situ Generation of Electron Donor to Assist Signal Amplification on Porphyrin-Sensitized Titanium Dioxide Nanostructures for Ultrasensitive Photoelectrochemical Immunoassay. *ACS Appl. Mater. Interfaces* **2015**, *7* (42), 23812–23818. https://doi.org/10.1021/acsami.5b08742.

(178) Shi, X. M.; Fan, G. C.; Shen, Q.; Zhu, J. J. Photoelectrochemical DNA Biosensor Based on Dual-Signal Amplification Strategy Integrating Inorganic-Organic Nanocomposites Sensitization with λ-Exonuclease-Assisted Target Recycling. *ACS Appl. Mater. Interfaces* **2016**, *8* (51), 35091–35098. https://doi.org/10.1021/acsami.6b14466.

(179) Kwon, S. J.; de Boer, A. L.; Petri, R.; Schmidt-Dannert, C. High-Level Production of Porphyrins in Metabolically Engineered Escherichia Coli: Systematic Extension of a Pathway Assembled from Overexpressed Genes Involved in Heme Biosynthesis. *Appl. Environ. Microbiol.* **2003**, *69* (8), 4875–4883. https://doi.org/10.1128/aem.69.8.4875-4883.2003.

(180) MedKoo Biosciences. Fe-TMPyP https://www.medkoo.com/products/15484.

(181) Wang, L.; Fernández-Terán, R.; Zhang, L.; Fernandes, D. L. A.; Tian, L.; Chen, H.; Tian, H. Organic Polymer Dots as Photocatalysts for Visible Light-Driven Hydrogen Generation. *Angew. Chemie - Int. Ed.* **2016**, *55* (40), 12306–12310. https://doi.org/10.1002/anie.201607018.

(182) Li, Y.; Zhang, N.; Zhao, W. W.; Jiang, D. C.; Xu, J. J.; Chen, H. Y. Polymer Dots for

Photoelectrochemical Bioanalysis. *Anal. Chem.* **2017**, *89* (9), 4945–4950. https://doi.org/10.1021/acs.analchem.7b00162.
(183) Zhang, N.; Shi, X. M.; Guo, H. Q.; Zhao, X. Z.; Zhao, W. W.; Xu, J. J.; Chen, H. Y. Gold Nanoparticle Couples with Entropy-Driven Toehold-Mediated DNA Strand Displacement Reaction on Magnetic Beads: Toward Ultrasensitive Energy-Transfer-Based Photoelectrochemical Detection of MiRNA-141 in Real Blood Sample. *Anal. Chem.* **2018**, *90* (20), 11892–11898. https://doi.org/10.1021/acs.analchem.8b01966.
(184) Zhou, X.; Zhang, P.; Lv, F.; Liu, L.; Wang, S. Photoelectrochemical Strategy for Discrimination of Microbial Pathogens Using Conjugated Polymers. *Chem. - An Asian J.* **2018**, *13* (22), 3469–3473. https://doi.org/10.1002/asia.201800783.
(185) Feng, X.; Liu, L.; Wang, S.; Zhu, D. Water-Soluble Fluorescent Conjugated Polymers and Their Interactions with Biomacromolecules for Sensitive Biosensors. *Chem. Soc. Rev.* **2010**, *39* (7), 2411–2419. https://doi.org/10.1039/b909065g.
(186) Wu, C.; Chiu, D. T. Highly Fluorescent Semiconducting Polymer Dots for Biology and Medicine. *Angew. Chemie Int. Ed.* **2013**, *52* (11), 3086–3109. https://doi.org/10.1002/anie.201205133.
(187) Yu, J.; Rong, Y.; Kuo, C.-T.; Zhou, X.-H.; Chiu, D. T. Recent Advances in the Development of Highly Luminescent Semiconducting Polymer Dots and Nanoparticles for Biological Imaging and Medicine. *Anal. Chem.* **2017**, *89* (1), 42–56. https://doi.org/10.1021/acs.analchem.6b04672.
(188) Wang, Q.; Ruan, Y.-F.; Zhao, W.-W.; Lin, P.; Xu, J.-J.; Chen, H.-Y. Semiconducting Organic–Inorganic Nanodots Heterojunctions: Platforms for General Photoelectrochemical Bioanalysis Application. *Anal. Chem.* **2018**, *90* (6), 3759–3765. https://doi.org/10.1021/acs.analchem.7b03852.
(189) Dyer-Smith, C.; Nelson, J. Organic Solar Cells. In *Practical Handbook of Photovoltaics*; Elsevier, 2012; pp 543–569. https://doi.org/10.1016/B978-0-12-385934-1.00016-7.
(190) Kus, M.; Alic, T. Y.; Kirbiyik, C.; Baslak, C.; Kara, K.; Kara, D. A. Synthesis of Nanoparticles. In *Handbook of Nanomaterials for Industrial Applications*; Elsevier, 2018; pp 392–429. https://doi.org/10.1016/B978-0-12-813351-4.00025-0.
(191) Wen, G.; Ju, H. Enhanced Photoelectrochemical Proximity Assay for Highly Selective Protein Detection in Biological Matrixes. *Anal. Chem.* **2016**, *88* (16), 8339–8345. https://doi.org/10.1021/acs.analchem.6b02740.
(192) Liu, Q.; Huan, J.; Hao, N.; Qian, J.; Mao, H.; Wang, K. Engineering of Heterojunction-Mediated Biointerface for Photoelectrochemical Aptasensing: Case of Direct Z-Scheme CdTe-Bi_2S_3 Heterojunction with Improved Visible-Light-Driven Photoelectrical Conversion Efficiency. *ACS Appl. Mater. Interfaces* **2017**, *9* (21), 18369–18376. https://doi.org/10.1021/acsami.7b04310.
(193) Chen, E. Y.; Milleville, C.; Zide, J. M. O.; Doty, M. F.; Zhang, J. Upconversion of Low-Energy Photons in Semiconductor Nanostructures for Solar Energy Harvesting. *MRS Energy Sustain.* **2018**, *5*, E16. https://doi.org/DOI: 10.1557/mre.2018.15.
(194) Naik, G. V.; Welch, A. J.; Briggs, J. A.; Solomon, M. L.; Dionne, J. A. Hot-Carrier-Mediated Photon Upconversion in Metal-Decorated Quantum Wells. *Nano Lett.* **2017**, *17* (8), 4583–4587. https://doi.org/10.1021/acs.nanolett.7b00900.
(195) Qiu, Z.; Shu, J.; Tang, D. Near-Infrared-to-Ultraviolet Light-Mediated Photoelectrochemical Aptasensing Platform for Cancer Biomarker Based on Core-Shell $NaYF_4$:Yb,Tm@TiO_2 Upconversion Microrods. *Anal. Chem.* **2018**, *90* (1), 1021–1028. https://doi.org/10.1021/acs.analchem.7b04479.
(196) Coropceanu, V.; Cornil, J.; da Silva Filho, D. A.; Olivier, Y.; Silbey, R.; Brédas, J.-L. Charge Transport in Organic Semiconductors. *Chem. Rev.* **2007**, *107* (4), 926–952. https://doi.org/10.1021/cr050140x.
(197) Hao, N.; Zhang, X.; Zhou, Z.; Qian, J.; Liu, Q.; Chen, S.; Zhang, Y.; Wang, K. Three-Dimensional Nitrogen-Doped Graphene Porous Hydrogel Fabricated Biosensing Platform with Enhanced Photoelectrochemical Performance. *Sensors Actuators B Chem.* **2017**, *250*, 476–483. https://doi.org/https://doi.org/10.1016/j.snb.2017.05.003.
(198) Dai, H.; Chen, S.; Li, Y.; Zeng, B.; Zhang, S.; Hong, Z.; Lin, Y. Photoelectrochemical Biosensor Constructed Using TiO2 Mesocrystals Based Multipurpose Matrix for Trypsin Detection. *Biosens. Bioelectron.* **2017**, *92*, 687–694. https://doi.org/10.1016/J.BIOS.2016.10.028.

(199) Long, Y.-T.; Kong, C.; Li, D.-W.; Li, Y.; Chowdhury, S.; Tian, H. Ultrasensitive Determination of Cysteine Based on the Photocurrent of Nafion-Functionalized CdS-MV Quantum Dots on an ITO Electrode. *Small* **2011**, *7* (12), 1624–1628. https://doi.org/10.1002/smll.201100427.

(200) Lim, J.; Bokare, A. D.; Choi, W. Visible Light Sensitization of TiO2 Nanoparticles by a Dietary Pigment, Curcumin, for Environmental Photochemical Transformations. *RSC Adv.* **2017**, *7* (52), 32488–32495. https://doi.org/10.1039/c7ra05276f.

(201) Yan, X.; Li, J.; Yang, R.; Li, Y.; Zhang, X.; Chen, J. A New Photoelectrochemical Aptasensor for Prion Assay Based on Cyclodextrin and Rhodamine B. *Sensors Actuators, B Chem.* **2018**, *255*, 2187–2193. https://doi.org/10.1016/j.snb.2017.09.030.

(202) Ma, H.; Fan, Q.; Fan, B.; Zhang, Y.; Fan, D.; Wu, D.; Wei, Q. Formation of Homogeneous Epinephrine-Melanin Solutions to Fabricate Electrodes for Enhanced Photoelectrochemical Biosensing. *Langmuir* **2018**, *34* (26), 7744–7750. https://doi.org/10.1021/acs.langmuir.8b00264.

(203) Yotsumoto Neto, S.; Luz, R. de C. S.; Damos, F. S. Visible LED Light Photoelectrochemical Sensor for Detection of L-Dopa Based on Oxygen Reduction on TiO2 Sensitized with Iron Phthalocyanine. *Electrochem. commun.* **2016**, *62*, 1–4. https://doi.org/https://doi.org/10.1016/j.elecom.2015.10.018.

(204) Li, Z.; Su, C.; Wu, D.; Zhang, Z. Gold Nanoparticles Decorated Hematite Photoelectrode for Sensitive and Selective Photoelectrochemical Aptasensing of Lysozyme. *Anal. Chem.* **2018**, *90* (1), 961–967. https://doi.org/10.1021/acs.analchem.7b04015.

(205) Wang, Y.; Zhou, Y.; Xu, L.; Han, Z.; Yin, H.; Ai, S. Photoelectrochemical Apta-Biosensor for Zeatin Detection Based on Graphene Quantum Dots Improved Photoactivity of Graphite-like Carbon Nitride and Streptavidin Induced Signal Inhibition. *Sensors Actuators B Chem.* **2018**, *257*, 237–244. https://doi.org/https://doi.org/10.1016/j.snb.2017.10.157.

(206) Zang, Y.; Lei, J.; Ju, H. Principles and Applications of Photoelectrochemical Sensing Strategies Based on Biofunctionalized Nanostructures. *Biosens. Bioelectron.* **2017**, *96*, 8–16. https://doi.org/https://doi.org/10.1016/j.bios.2017.04.030.

(207) Liu, S.; He, P.; Hussain, S.; Lu, H.; Zhou, X.; Lv, F.; Liu, L.; Dai, Z.; Wang, S. Conjugated Polymer-Based Photoelectrochemical Cytosensor with Turn-On Enable Signal for Sensitive Cell Detection. *ACS Appl. Mater. Interfaces* **2018**, *10* (7), 6618–6623. https://doi.org/10.1021/acsami.7b18275.

(208) Dai, H.; Zhang, S.; Hong, Z.; Lin, Y. A Potentiometric Addressable Photoelectrochemical Biosensor for Sensitive Detection of Two Biomarkers. *Anal. Chem.* **2016**, *88* (19), 9532–9538. https://doi.org/10.1021/acs.analchem.6b02101.

(209) Zhao, W.-W.; Wang, J.; Zhu, Y.-C.; Xu, J.-J.; Chen, H.-Y. Quantum Dots: Electrochemiluminescent and Photoelectrochemical Bioanalysis. **2015**. https://doi.org/10.1021/acs.analchem.5b00497.

(210) Smith, A. M.; Nie, S. Semiconductor Nanocrystals: Structure, Properties, and Band Gap Engineering. *Acc. Chem. Res.* **2010**, *43* (2), 190–200. https://doi.org/10.1021/ar9001069.

(211) Hao, N.; Lu, J.; Chi, M.; Xiong, M.; Zhang, Y.; Hua, R.; Wang, K. A Universal Photoelectrochemical Biosensor for Dual MicroRNA Detection Based on Two CdTe Nanocomposites. *J. Mater. Chem. B* **2019**, *7* (7), 1133–1141. https://doi.org/10.1039/C8TB03195A.

(212) Malekzad, H.; Zangabad, P. S.; Mirshekari, H.; Karimi, M.; Hamblin, M. R. Noble Metal Nanoparticles in Biosensors: Recent Studies and Applications. *Nanotechnol. Rev.* **2017**, *6* (3), 301–329. https://doi.org/10.1515/ntrev-2016-0014.

(213) Willner, I.; Patolsky, F.; Wasserman, J. Photoelectrochemistry with Controlled DNA-Cross-Linked CdS Nanoparticle Arrays. *Angew. Chemie* **2001**, *113* (10), 1913–1916. https://doi.org/10.1002/1521-3757(20010518)113:10<1913::AID-ANGE1913>3.0.CO;2-P.

(214) Chu, Y.; Wu, R.; Fan, G.-C.; Deng, A.-P.; Zhu, J.-J. Enzyme-Free Photoelectrochemical Biosensor Based on the Co-Sensitization Effect Coupled with Dual Cascade Toehold-Mediated Strand Displacement Amplification for the Sensitive Detection of MicroRNA-21. *ACS Sustain. Chem. Eng.* **2018**, *6* (9), 11633–11641. https://doi.org/10.1021/acssuschemeng.8b01857.

(215) Meng, L.; Li, Y.; Yang, R.; Zhang, X.; Du, C.; Chen, J. A Sensitive Photoelectrochemical Assay of

MiRNA-155 Based on a CdSe QDs//NPC-ZnO Polyhedra Photocurrent-Direction Switching System and Target-Triggered Strand Displacement Amplification Strategy. *Chem. Commun.* **2019**, *55* (15), 2182–2185. https://doi.org/10.1039/C8CC09411J.

(216) Yu, S.-Y.; Mei, L.-P.; Xu, Y.-T.; Xue, T.-Y.; Fan, G.-C.; Han, D.-M.; Chen, G.; Zhao, W.-W. Liposome-Mediated in Situ Formation of AgI/Ag/BiOI Z-Scheme Heterojunction on Foamed Nickel Electrode: A Proof-of-Concept Study for Cathodic Liposomal Photoelectrochemical Bioanalysis. *Anal. Chem.* **2019**, *91* (6), 3800–3804. https://doi.org/10.1021/acs.analchem.9b00352.

(217) Ju, Y.; Hu, X.; Zang, Y.; Cao, R.; Xue, H. Amplified Photoelectrochemical DNA Biosensor Based on a CdS Quantum Dot/WS_2 Nanosheet Heterojunction and Hybridization Chain Reaction-Mediated Enzymatic Hydrolysis. *Anal. Methods* **2019**, *11* (16), 2163–2169. https://doi.org/10.1039/C9AY00166B.

(218) Zhang, N.; Ma, Z.-Y.; Ruan, Y.-F.; Zhao, W.-W.; Xu, J.-J.; Chen, H.-Y. Simultaneous Photoelectrochemical Immunoassay of Dual Cardiac Markers Using Specific Enzyme Tags: A Proof of Principle for Multiplexed Bioanalysis. *Anal. Chem.* **2016**, *88* (4), 1990–1994. https://doi.org/10.1021/acs.analchem.5b04579.

(219) Xu, R.; Jiang, Y.; Xia, L.; Zhang, T.; Xu, L.; Zhang, S.; Liu, D.; Song, H. A Sensitive Photoelectrochemical Biosensor for AFP Detection Based on ZnO Inverse Opal Electrodes with Signal Amplification of CdS-QDs. *Biosens. Bioelectron.* **2015**, *74*, 411–417. https://doi.org/https://doi.org/10.1016/j.bios.2015.06.037.

(220) Pang, X.; Bian, H.; Su, M.; Ren, Y.; Qi, J.; Ma, H.; Wu, D.; Hu, L.; Du, B.; Wei, Q. Photoelectrochemical Cytosensing of RAW264.7 Macrophage Cells Based on a TiO_2 Nanoneedls@MoO_3 Array. *Anal. Chem.* **2017**, *89* (15), 7950–7957. https://doi.org/10.1021/acs.analchem.7b01038.

(221) Fu, N.; Hu, Y.; Shi, S.; Ren, S.; Liu, W.; Su, S.; Zhao, B.; Weng, L.; Wang, L. Au Nanoparticles on Two-Dimensional MoS_2 Nanosheets as a Photoanode for Efficient Photoelectrochemical MiRNA Detection. *Analyst* **2018**, *143* (7), 1705–1712. https://doi.org/10.1039/c8an00105g.

(222) Saha, S.; Chan, Y.; Soleymani, L. Enhancing the Photoelectrochemical Response of DNA Biosensors Using Wrinkled Interfaces. *ACS Appl. Mater. Interfaces* **2018**, *10* (37), 31178–31185. https://doi.org/10.1021/acsami.8b12286.

(223) Tu, W.; Cao, H.; Zhang, L.; Bao, J.; Liu, X.; Dai, Z. Dual Signal Amplification Using Gold Nanoparticles-Enhanced Zinc Selenide Nanoflakes and P19 Protein for Ultrasensitive Photoelectrochemical Biosensing of MicroRNA in Cell. *Anal. Chem.* **2016**, *88* (21), 10459–10465. https://doi.org/10.1021/acs.analchem.6b02381.

(224) Hao, N.; Hua, R.; Chen, S.; Zhang, Y.; Zhou, Z.; Qian, J.; Liu, Q.; Wang, K. Multiple Signal-Amplification via Ag and TiO_2 Decorated 3D Nitrogen Doped Graphene Hydrogel for Fabricating Sensitive Label-Free Photoelectrochemical Thrombin Aptasensor. *Biosens. Bioelectron.* **2018**, *101*, 14–20. https://doi.org/https://doi.org/10.1016/j.bios.2017.10.014.

(225) Wu, R.; Fan, G. C.; Jiang, L. P.; Zhu, J. J. Peptide-Based Photoelectrochemical Cytosensor Using a Hollow-TiO2 /EG/ZnIn2S4 Cosensitized Structure for Ultrasensitive Detection of Early Apoptotic Cells and Drug Evaluation. *ACS Appl. Mater. Interfaces* **2018**, *10* (5), 4429–4438. https://doi.org/10.1021/acsami.7b16054.

(226) Ge, S.; Lan, F.; Liang, L.; Ren, N.; Li, L.; Liu, H.; Yan, M.; Yu, J. Ultrasensitive Photoelectrochemical Biosensing of Cell Surface N-Glycan Expression Based on the Enhancement of Nanogold-Assembled Mesoporous Silica Amplified by Graphene Quantum Dots and Hybridization Chain Reaction. *ACS Appl. Mater. Interfaces* **2017**, *9* (8), 6670–6678. https://doi.org/10.1021/acsami.6b11966.

(227) Li, J.; Lin, X.; Zhang, Z.; Tu, W.; Dai, Z. Biosensors and Bioelectronics Red Light-Driven Photoelectrochemical Biosensing for Ultrasensitive and Scatheless Assay of Tumor Cells Based on Hypotoxic $AgInS_2$ Nanoparticles. **2019**, *126* (October 2018), 332–338.

(228) Zhuang, J.; Lai, W.; Xu, M.; Zhou, Q.; Tang, D. Plasmonic AuNP/g-C_3N_4 Nanohybrid-Based Photoelectrochemical Sensing Platform for Ultrasensitive Monitoring of Polynucleotide Kinase Activity Accompanying DNAzyme-Catalyzed Precipitation Amplification. *ACS Appl. Mater. Interfaces* **2015**, *7* (15), 8330–8338. https://doi.org/10.1021/acsami.5b01923.

(229) Zhang, K.; Lv, S.; Lin, Z.; Li, M.; Tang, D. Bio-Bar-Code-Based Photoelectrochemical Immunoassay for Sensitive Detection of Prostate-Specific Antigen Using Rolling Circle Amplification and Enzymatic Biocatalytic Precipitation. *Biosens. Bioelectron.* **2018**, *101*, 159–166. https://doi.org/https://doi.org/10.1016/j.bios.2017.10.031.

(230) Zhang, Y.; Hao, N.; Zhou, Z.; Hua, R.; Qian, J.; Liu, Q.; Li, H.; Wang, K. A Potentiometric Resolved Ratiometric Photoelectrochemical Aptasensor. *Chem. Commun.* **2017**, *53* (43), 5810–5813. https://doi.org/10.1039/C7CC01582H.

(231) Hao, N.; Hua, R.; Zhang, K.; Lu, J.; Wang, K. A Sunlight Powered Portable Photoelectrochemical Biosensor Based on a Potentiometric Resolve Ratiometric Principle. *Anal. Chem.* **2018**, *90* (22), 13207–13211. https://doi.org/10.1021/acs.analchem.8b03218.

(232) Hua, R.; Hao, N.; Lu, J.; Qian, J.; Liu, Q.; Li, H.; Wang, K. A Sensitive Potentiometric Resolved Ratiometric Photoelectrochemical Aptasensor for Escherichia Coli Detection Fabricated with Non-Metallic Nanomaterials. *Biosens. Bioelectron.* **2018**, *106*, 57–63. https://doi.org/https://doi.org/10.1016/j.bios.2018.01.053.

(233) Zhu, Y.-C.; Zhang, N.; Ruan, Y.-F.; Zhao, W.-W.; Xu, J.-J.; Chen, H.-Y. Alkaline Phosphatase Tagged Antibodies on Gold Nanoparticles/TiO_2 Nanotubes Electrode: A Plasmonic Strategy for Label-Free and Amplified Photoelectrochemical Immunoassay. *Anal. Chem.* **2016**, *88* (11), 5626–5630. https://doi.org/10.1021/acs.analchem.6b01261.

(234) Ge, S.; Liang, L.; Lan, F.; Zhang, Y.; Wang, Y.; Yan, M.; Yu, J. Photoelectrochemical Immunoassay Based on Chemiluminescence as Internal Excited Light Source. *Sensors Actuators B Chem.* **2016**, *234*, 324–331. https://doi.org/https://doi.org/10.1016/j.snb.2016.04.166.

(235) Shu, J.; Qiu, Z.; Zhou, Q.; Lin, Y.; Lu, M.; Tang, D. Enzymatic Oxydate-Triggered Self-Illuminated Photoelectrochemical Sensing Platform for Portable Immunoassay Using Digital Multimeter. *Anal. Chem.* **2016**, *88* (5), 2958–2966. https://doi.org/10.1021/acs.analchem.6b00262.

(236) Wang, Y.; Xu, J.; Ma, C.; Li, S.; Yu, J.; Ge, S.; Yan, M. A Chemiluminescence Excited Photoelectrochemistry Aptamer-Device Equipped with a Tin Dioxide Quantum Dot/Reduced Graphene Oxide Nanocomposite Modified Porous Au-Paper Electrode. *J. Mater. Chem. B* **2014**, *2* (22), 3462–3468. https://doi.org/10.1039/C4TB00233D.

(237) He, Y.; He, X.; Liu, X.; Gao, L.; Cui, H. Dynamically Tunable Chemiluminescence of Luminol-Functionalized Silver Nanoparticles and Its Application to Protein Sensing Arrays. **2014**. https://doi.org/10.1021/ac503123q.

(238) Augusto, F. A.; de Souza, G. A.; de Souza Júnior, S. P.; Khalid, M.; Baader, W. J. Efficiency of Electron Transfer Initiated Chemiluminescence. *Photochem. Photobiol.* **2013**, *89* (6), 1299–1317. https://doi.org/10.1111/php.12102.

(239) Fereja, T. H.; Hymete, A.; Gunasekaran, T. A Recent Review on Chemiluminescence Reaction, Principle and Application on Pharmaceutical Analysis. *ISRN Spectrosc.* **2013**, *2013*, 1–12. https://doi.org/10.1155/2013/230858.

(240) Shu, J.; Tang, D. Current Advances in Quantum-Dots-Based Photoelectrochemical Immunoassays. *Chem. – An Asian J.* **2017**, *12* (21), 2780–2789. https://doi.org/10.1002/asia.201701229.

(241) Hartland, G. V. Optical Studies of Dynamics in Noble Metal Nanostructures. *Chem. Rev.* **2011**, *111* (6), 3858–3887. https://doi.org/10.1021/cr1002547.

(242) Zhao, W.-W.; Wang, J.; Xu, J.-J.; Chen, H.-Y. Energy Transfer between CdS Quantum Dots and Au Nanoparticles in Photoelectrochemical Detection. *Chem. Commun.* **2011**, *47* (39), 10990. https://doi.org/10.1039/c1cc13952e.

(243) Han, D.-M.; Jiang, L.-Y.; Tang, W.-Y.; Xu, J.-J.; Chen, H.-Y. Photoelectrochemical Determination of Inorganic Mercury Ions Based on Energy Transfer between CdS Quantum Dots and Au Nanoparticles. *Electrochem. commun.* **2015**, *51*, 72–75. https://doi.org/10.1016/j.elecom.2014.12.002.

(244) Yun, C. S.; Javier, A.; Jennings, T.; Fisher, M.; Hira, S.; Peterson, S.; Hopkins, B.; Reich, N. O.; Strouse, G. F. Nanometal Surface Energy Transfer in Optical Rulers, Breaking the FRET Barrier. *J. Am. Chem. Soc.* **2005**, *127* (9), 3115–3119. https://doi.org/10.1021/ja043940i.

(245) Li, J.; Tu, W.; Li, H.; Han, M.; Lan, Y.; Dai, Z.; Bao, J. In Situ-Generated Nano-Gold Plasmon-Enhanced Photoelectrochemical Aptasensing Based on Carboxylated Perylene-Functionalized

Graphene. *Anal. Chem.* **2014**, *86* (2), 1306–1312. https://doi.org/10.1021/ac404121c.

(246) Ma, Z.-Y.; Xu, F.; Qin, Y.; Zhao, W.-W.; Xu, J.-J.; Chen, H.-Y. Invoking Direct Exciton–Plasmon Interactions by Catalytic Ag Deposition on Au Nanoparticles: Photoelectrochemical Bioanalysis with High Efficiency. *Anal. Chem.* **2016**, *88* (8), 4183–4187. https://doi.org/10.1021/acs.analchem.6b00503.

(247) Zhang, L.; Sun, Y.; Liang, Y.-Y.; He, J.-P.; Zhao, W.-W.; Xu, J.-J.; Chen, H.-Y. Ag Nanoclusters Could Efficiently Quench the Photoresponse of CdS Quantum Dots for Novel Energy Transfer-Based Photoelectrochemical Bioanalysis. *Biosens. Bioelectron.* **2016**, *85*, 930–934. https://doi.org/https://doi.org/10.1016/j.bios.2016.06.018.

(248) Ma, Z.-Y.; Ruan, Y.-F.; Xu, F.; Zhao, W.-W.; Xu, J.-J.; Chen, H.-Y. Protein Binding Bends the Gold Nanoparticle Capped DNA Sequence: Toward Novel Energy-Transfer-Based Photoelectrochemical Protein Detection. *Anal. Chem.* **2016**, *88* (7), 3864–3871. https://doi.org/10.1021/acs.analchem.6b00012.

(249) Fan, G.-C.; Zhu, H.; Du, D.; Zhang, J.-R.; Zhu, J.-J.; Lin, Y. Enhanced Photoelectrochemical Immunosensing Platform Based on CdSeTe@CdS:Mn Core–Shell Quantum Dots-Sensitized TiO_2 Amplified by CuS Nanocrystals Conjugated Signal Antibodies. *Anal. Chem.* **2016**, *88* (6), 3392–3399. https://doi.org/10.1021/acs.analchem.6b00144.

(250) Liu, Q.; Huan, J.; Dong, X.; Qian, J.; Hao, N.; You, T.; Mao, H.; Wang, K. Resonance Energy Transfer from CdTe Quantum Dots to Gold Nanorods Using MWCNTs/RGO Nanoribbons as Efficient Signal Amplifier for Fabricating Visible-Light-Driven "on-off-on" Photoelectrochemical Acetamiprid Aptasensor. *Sensors Actuators B Chem.* **2016**, *235*, 647–654. https://doi.org/https://doi.org/10.1016/j.snb.2016.05.154.

(251) Shen, Q.; Han, L.; Fan, G.; Abdel-Halim, E. S.; Jiang, L.; Zhu, J.-J. Highly Sensitive Photoelectrochemical Assay for DNA Methyltransferase Activity and Inhibitor Screening by Exciton Energy Transfer Coupled with Enzyme Cleavage Biosensing Strategy. *Biosens. Bioelectron.* **2015**, *64*, 449–455. https://doi.org/https://doi.org/10.1016/j.bios.2014.09.044.

(252) Li, R.; Liu, Y.; Yan, T.; Li, Y.; Cao, W.; Wei, Q.; Du, B. A Competitive Photoelectrochemical Assay for Estradiol Based on in Situ Generated CdS-Enhanced TiO_2. *Biosens. Bioelectron.* **2015**, *66*, 596–602. https://doi.org/https://doi.org/10.1016/j.bios.2014.12.002.

(253) Hu, T.; Zheng, Y. N.; Li, M. J.; Liang, W. Bin; Chai, Y. Q.; Yuan, R. A Highly Sensitive Photoelectrochemical Assay with Donor-Acceptor-Type Material as Photoactive Material and Polyaniline as Signal Enhancer. *Anal. Chem.* **2018**, *90* (10), 6096–6101. https://doi.org/10.1021/acs.analchem.8b00093.

(254) Yan, Z.; Wang, Z.; Miao, Z.; Liu, Y. Dye-Sensitized and Localized Surface Plasmon Resonance Enhanced Visible-Light Photoelectrochemical Biosensors for Highly Sensitive Analysis of Protein Kinase Activity. *Anal. Chem.* **2016**, *88* (1), 922–929. https://doi.org/10.1021/acs.analchem.5b03661.

(255) Li, R.; Liu, Y.; Cheng, L.; Yang, C.; Zhang, J. Photoelectrochemical Aptasensing of Kanamycin Using Visible Light-Activated Carbon Nitride and Graphene Oxide Nanocomposites. *Anal. Chem.* **2014**, *86* (19), 9372–9375. https://doi.org/10.1021/ac502616n.

(256) Bettazzi, F.; Laschi, S.; Voccia, D.; Gellini, C.; Pietraperzia, G.; Falciola, L.; Pifferi, V.; Testolin, A.; Ingrosso, C.; Placido, T.; Comparelli, R.; Curri, M. L.; Palchetti, I. Ascorbic Acid-Sensitized Au Nanorods-Functionalized Nanostructured TiO_2 Transparent Electrodes for Photoelectrochemical Genosensing. *Electrochim. Acta* **2018**, *276*, 389–398. https://doi.org/10.1016/J.ELECTACTA.2018.04.146.

(257) Hou, T.; Xu, N.; Wang, W.; Ge, L.; Li, F. Truly Immobilization-Free Diffusivity-Mediated Photoelectrochemical Biosensing Strategy for Facile and Highly Sensitive MicroRNA Assay. *Anal. Chem.* **2018**, *90* (15), 9591–9597. https://doi.org/10.1021/acs.analchem.8b02523.

(258) Li, R.; Yan, R.; Bao, J.; Tu, W.; Dai, Z. A Localized Surface Plasmon Resonance-Enhanced Photoelectrochemical Biosensing Strategy for Highly Sensitive and Scatheless Cell Assay under Red Light Excitation. *Chem. Commun.* **2016**, *52* (79), 11799–11802. https://doi.org/10.1039/C6CC05964C.

(259) Zhang, N.; Ruan, Y.-F.; Zhang, L.-B.; Zhao, W.-W.; Xu, J.-J.; Chen, H.-Y. Nanochannels

Photoelectrochemical Biosensor. *Anal. Chem.* **2018**, *90* (3), 2341–2347. https://doi.org/10.1021/acs.analchem.7b04862.

(260) Fan, G.-C.; Shi, X.-M.; Zhang, J.-R.; Zhu, J.-J. Cathode Photoelectrochemical Immunosensing Platform Integrating Photocathode with Photoanode. *Anal. Chem.* **2016**, *88* (21), 10352–10356. https://doi.org/10.1021/acs.analchem.6b03473.

(261) Xu, F.; Zhu, Y.-C.; Ma, Z.-Y.; Zhao, W.-W.; Xu, J.-J.; Chen, H.-Y. An Ultrasensitive Energy-Transfer Based Photoelectrochemical Protein Biosensor. *Chem. Commun.* **2016**, *52* (14), 3034–3037. https://doi.org/10.1039/C5CC09963C.

(262) Shu, J.; Qiu, Z.; Lv, S.; Zhang, K.; Tang, D. Plasmonic Enhancement Coupling with Defect-Engineered TiO_{2-x}: A Mode for Sensitive Photoelectrochemical Biosensing. *Anal. Chem.* **2018**, *90* (4), 2425–2429. https://doi.org/10.1021/acs.analchem.7b05296.

(263) Mitzi, D. B. Solution-Processed Inorganic Semiconductors. *J. Mater. Chem.* **2004**, *14* (15), 2355. https://doi.org/10.1039/b403482a.

(264) Schweikart, A.; Horn, A.; Böker, A.; Fery, A. Controlled Wrinkling as a Novel Method for the Fabrication of Patterned Surfaces. *Adv. Polym. Sci.* **2010**, *227* (1), 75–99. https://doi.org/10.1007/12-2009-22.

(265) Tang, Y.; Chai, Y.; Liu, X.; Li, L.; Yang, L.; Liu, P.; Zhou, Y.; Ju, H.; Cheng, Y. A Photoelectrochemical Aptasensor Constructed with Core-Shell CuS-TiO_2 Heterostructure for Detection of Microcystin-LR. *Biosens. Bioelectron.* **2018**, *117*, 224–231. https://doi.org/https://doi.org/10.1016/j.bios.2018.06.007.

(266) Zhou, Q.; Lin, Y.; Zhang, K.; Li, M.; Tang, D. Reduced Graphene Oxide/BiFeO3 Nanohybrids-Based Signal-on Photoelectrochemical Sensing System for Prostate-Specific Antigen Detection Coupling with Magnetic Microfluidic Device. *Biosens. Bioelectron.* **2018**, *101*, 146–152. https://doi.org/https://doi.org/10.1016/j.bios.2017.10.027.

(267) Bierman, M. J.; Jin, S. Potential Applications of Hierarchical Branching Nanowires in Solar Energy Conversion. *Energy Environ. Sci.* **2009**, *2* (10), 1050–1059. https://doi.org/10.1039/B912095E.

(268) Kim, J. B.; Kim, P.; Pégard, N. C.; Oh, S. J.; Kagan, C. R.; Fleischer, J. W.; Stone, H. A.; Loo, Y.-L. Wrinkles and Deep Folds as Photonic Structures in Photovoltaics. *Nat. Photonics* **2012**, *6*, 327–332. https://doi.org/10.1038/nphoton.2012.70.

(269) Woo, S. M.; Gabardo, C. M.; Soleymani, L. Prototyping of Wrinkled Nano-/Microstructured Electrodes for Electrochemical DNA Detection. *Anal. Chem.* **2014**. https://doi.org/10.1021/ac5036296.

(270) Wang, C.; Zhang, H.; Yang, F.; Fan, Y.; Liu, Q. Enhanced Light Scattering Effect of Wrinkled Transparent Conductive ITO Thin Film. *RSC Adv.* **2017**, *7* (41), 25483–25487. https://doi.org/10.1039/C7RA02726E.

(271) Gabardo, C. M.; Yang, J.; Smith, N. J.; Adams-McGavin, R. C.; Soleymani, L. Programmable Wrinkling of Self-Assembled Nanoparticle Films on Shape Memory Polymers. *ACS Nano* **2016**, *10* (9), 8829–8836. https://doi.org/10.1021/acsnano.6b04584.

(272) Rodríguez-Hernández, J. Wrinkled Interfaces: Taking Advantage of Surface Instabilities to Pattern Polymer Surfaces. *Prog. Polym. Sci.* **2015**, *42*, 1–41. https://doi.org/10.1016/j.progpolymsci.2014.07.008.

(273) Gabardo, C. M.; Hosseini, A.; Soleymani, L. A New Wrinkle in Biosensors: Wrinkled Electrodes Could Be a Breakthrough for Lab-on-A-Chip Devices. *IEEE Nanotechnol. Mag.* **2016**, *10* (2), 6–18. https://doi.org/10.1109/MNANO.2016.2539999.

(274) Mcalpine, M. C.; Ahmad, H.; Wang, D.; Heath, J. R. Highly Ordered Nanowire Arrays on Plastic Substrates for Ultrasensitive Flexible Chemical Sensors. *Nat. Mater.* **2007**, *6*, 379–384. https://doi.org/10.1038/nmat1891.

(275) Hu, J.; Zhu, Y.; Huang, H.; Lu, J. Recent Advances in Shape-Memory Polymers: Structure, Mechanism, Functionality, Modeling and Applications. *Progress in Polymer Science*. December 2012, pp 1720–1763.

(276) Moon, J.; Kim, E.; Park, S. K.; Lee, K.; Shin, J.-W.; Cho, D.-H.; Lee, J.; Joo, C. W.; Cho, N. S.; Han, J.-H.; Yu, B.-G.; Yoo, S.; Lee, J.-I. Organic Wrinkles for Energy Efficient Organic Light Emitting Diodes. *Org. Electron.* **2015**, *26*, 273–278.

https://doi.org/https://doi.org/10.1016/j.orgel.2015.07.046.

(277) Zhang, B.; Meng, H.; Wang, X.; Li, J.; Chang, H.; Wei, W. Fe^{3+} Doped ZnO-Ag Photocatalyst for Photoelectrochemical Sensing Platform of Ultrasensitive Hg2+ Detection Using Exonuclease III-Assisted Target Recycling and DNAzyme-Catalyzed Amplification. *Sensors Actuators B Chem.* **2018**, *255*, 2531–2537. https://doi.org/10.1016/J.SNB.2017.09.058.

(278) Soleymani, L.; Fang, Z.; Sargent, E. H.; Kelley, S. O. Programming the Detection Limits of Biosensors through Controlled Nanostructuring. *Nat. Nanotechnol.* **2009**, *4* (12), 844–848.

(279) Bard, A. J. Photoelectrochemistry and Heterogeneous Photo-Catalysis at Semiconductors. *J. Photochem.* **1979**, *10*, 59–75.

(280) Lu, W.; Jin, Y.; Wang, G.; Chen, D.; Li, J. Enhanced Photoelectrochemical Method for Linear DNA Hybridization Detection Using Au-Nanopaticle Labeled DNA as Probe onto Titanium Dioxide Electrode. *Biosens. Bioelectron.* **2008**, *23* (10), 1534–1539. https://doi.org/https://doi.org/10.1016/j.bios.2008.01.011.

(281) Wen, G.; Ju, H. Enhanced Photoelectrochemical Proximity Assay for Highly Selective Protein Detection in Biological Matrixes. *Anal. Chem.* **2016**, *88* (16), 8339–8345. https://doi.org/10.1021/acs.analchem.6b02740.

(282) Devadoss, A.; Sudhagar, P.; Terashima, C.; Nakata, K.; Fujishima, A. Photoelectrochemical Biosensors: New Insights into Promising Photoelectrodes and Signal Amplification Strategies. *J. Photochem. Photobiol. C Photochem. Rev.* **2015**, *24*, 43–63. https://doi.org/10.1016/j.jphotochemrev.2015.06.002.

(283) Shu, J.; Qiu, Z.; Lv, S.; Zhang, K.; Tang, D. Plasmonic Enhancement Coupling with Defect-Engineered TiO_{2-x}: A Mode for Sensitive Photoelectrochemical Biosensing. *Anal. Chem.* **2018**, *90* (4), 2425–2429. https://doi.org/10.1021/acs.analchem.7b05296.

(284) Lv, S.; Zhang, K.; Zeng, Y.; Tang, D. Double Photosystems-Based ‘Z-Scheme’ Photoelectrochemical Sensing Mode for Ultrasensitive Detection of Disease Biomarker Accompanying Three-Dimensional DNA Walker. *Anal. Chem.* **2018**, *90* (11), 7086–7093. https://doi.org/10.1021/acs.analchem.8b01825.

(285) Zhang, N.; Zhang, L.; Ruan, Y.-F.; Zhao, W.-W.; Xu, J.-J.; Chen, H.-Y. Quantum-Dots-Based Photoelectrochemical Bioanalysis Highlighted with Recent Examples. *Biosens. Bioelectron.* **2017**, *94*, 207–218. https://doi.org/https://doi.org/10.1016/j.bios.2017.03.011.

(286) Matsui, T.; Tsukiji, M.; Saika, H.; Toyama, T.; Okamoto, H. Influence of Substrate Texture on Microstructure and Photovoltaic Performances of Thin Film Polycrystalline Silicon Solar Cells. *J. Non. Cryst. Solids* **2002**, *299–302*, 1152–1156. https://doi.org/https://doi.org/10.1016/S0022-3093(01)01083-3.

(287) González-Pedro, V.; Xu, X.; Mora-Seró, I.; Bisquert, J. Modeling High-Efficiency Quantum Dot Sensitized Solar Cells. *ACS Nano* **2010**, *4* (10), 5783–5790. https://doi.org/10.1021/nn101534y.

(288) Vlachopoulos, N.; Liska, P.; Augustynski, J.; Graetzel, M. Very Efficient Visible Light Energy Harvesting and Conversion by Spectral Sensitization of High Surface Area Polycrystalline Titanium Dioxide Films. *J. Am. Chem. Soc.* **1988**, *110* (4), 1216–1220. https://doi.org/10.1021/ja00212a033.

(289) Müller, J.; Rech, B.; Springer, J.; Vanecek, M. TCO and Light Trapping in Silicon Thin Film Solar Cells. *Sol. Energy* **2004**, *77* (6), 917–930. https://doi.org/https://doi.org/10.1016/j.solener.2004.03.015.

(290) Boto, A. N.; Kok, P.; Abrams, D. S.; Braunstein, S. L.; Williams, C. P.; Dowling, J. P. Quantum Interferometric Optical Lithography: Exploiting Entanglement to Beat the Diffraction Limit. *Phys. Rev. Lett.* **2000**, *85* (13), 2733–2736. https://doi.org/10.1103/PhysRevLett.85.2733.

(291) Hsu, H.-H.; Selvaganapathy, P. R.; Soleymani, L. Bottom-Up Top-Down Fabrication of Structurally and Functionally Tunable Hierarchical Palladium Materials. *J. Electrochem. Soc.* **2014**, *161* (7), 3078–3086. https://doi.org/10.1149/2.011407jes.

(292) Gabardo, C. M.; Soleymani, L. Deposition, Patterning, and Utility of Conductive Materials for the Rapid Prototyping of Chemical and Bioanalytical Devices. *Analyst* **2016**, *141*, 3511. https://doi.org/10.1039/c6an00210b.

(293) Krasheninnikov, A. V.; Banhart, F. Engineering of Nanostructured Carbon Materials with Electron

or Ion Beams. *Nat. Mater.* **2007**, *6* (10), 723–733. https://doi.org/10.1038/nmat1996.

(294) Jersch, J.; Dickmann, K. Nanostructure Fabrication Using Laser Field Enhancement in the near Field of a Scanning Tunneling Microscope Tip. *Appl. Phys. Lett.* **1996**, *68* (6), 868–870. https://doi.org/10.1063/1.116527.

(295) Valbusa, U.; Boragno, C.; De Mongeot, F. B. Nanostructuring Surfaces by Ion Sputtering. *J. Phys. Condens. Matter* **2002**, *14* (35), 8153–8175. https://doi.org/10.1088/0953-8984/14/35/301.

(296) Gabardo, C. M.; Zhu, Y.; Soleymani, L.; Moran-Mirabal, J. M. Bench-Top Fabrication of Hierarchically Structured High-Surface-Area Electrodes. *Adv. Funct. Mater.* **2013**, *23* (24), 3030–3039. https://doi.org/10.1002/adfm.201203220.

(297) Gabardo, C. M.; Adams-McGavin, R. C.; Fung, B. C.; Mahoney, E. J.; Fang, Q.; Soleymani, L. Rapid Prototyping of All-Solution-Processed Multi-Lengthscale Electrodes Using Polymer-Induced Thin Film Wrinkling. *Sci. Rep.* **2017**, *7*, 42543. https://doi.org/10.1038/srep42543.

(298) Lu, C.; Mohwald, H.; Fery, A. A Lithography-Free Method for Directed Colloidal Crystal Assembly Based on Wrinkling. *Soft Matter* **2007**, *3* (12), 1530–1536. https://doi.org/10.1039/B712706E.

(299) Lahav, M.; Heleg-Shabtai, V.; Wasserman, J.; Katz, E.; Willner, I.; Dürr, H.; Hu, Y.-Z.; Bossmann, S. H. Photoelectrochemistry with Integrated Photosensitizer−Electron Acceptor and Au-Nanoparticle Arrays. *J. Am. Chem. Soc.* **2000**, *122* (46), 11480–11487. https://doi.org/10.1021/ja002568d.

(300) Sun, W.-T.; Yu, Y.; Pan, H.-Y.; Gao, X.-F.; Chen, Q.; Peng, L.-M. CdS Quantum Dots Sensitized TiO_2 Nanotube-Array Photoelectrodes. *J. Am. Chem. Soc.* **2008**, *130* (4), 1124–1125. https://doi.org/10.1021/ja0777741.

(301) Wang, L.; Tang, F.; Ozawa, K.; Lu, G. Q. Layer-By-Layer Assembled Thin Films of Inorganic Nanomaterials: Fabrication and Photo-Electrochemical Properties. *Int. J. Surf. Sci. Eng.* **2009**, *3* (1–2), 44–63. https://doi.org/10.1504/IJSURFSE.2009.024361.

(302) Callen, B. W. Remote Plasma and Ultraviolet–Ozone Modification of Polystyrene. *J. Vac. Sci. Technol. A Vacuum, Surfaces, Film.* **1995**, *13* (4), 2023–2029. https://doi.org/10.1116/1.579647.

(303) Zhao, W.-W.; Wang, J.; Xu, J.-J.; Chen, H.-Y. Energy Transfer between CdS Quantum Dots and Au Nanoparticles in Photoelectrochemical Detection. *Chem. Commun.* **2011**, *47* (39), 10990. https://doi.org/10.1039/c1cc13952e.

(304) Shrivastava, A.; Gupta, V. Methods for the Determination of Limit of Detection and Limit of Quantitation of the Analytical Methods. *Chronicles Young Sci.* **2011**, *2* (1), 21–25. https://doi.org/10.4103/2229-5186.79345.

(305) Genzer, J.; Groenewold, J. Soft Matter with Hard Skin: From Skin Wrinkles to Templating and Material Characterization. *Soft Matter* **2006**, *2* (4), 310. https://doi.org/10.1039/b516741h.

(306) Chen, Z.; Cotterell, B.; Wang, W. The Fracture of Brittle Thin Films on Compliant Substrates in Flexible Displays. *Eng. Fract. Mech.* **2002**, *69* (5), 597–603. https://doi.org/https://doi.org/10.1016/S0013-7944(01)00104-7.

(307) Torres, J. M.; Stafford, C. M.; Vogt, B. D. Manipulation of the Elastic Modulus of Polymers at the Nanoscale: Influence of UV−Ozone Cross-Linking and Plasticizer. *ACS Nano* **2010**, *4* (9), 5357–5365. https://doi.org/10.1021/nn100720z.

(308) Zhang, X.; Xu, Y.; Yang, Y.; Jin, X.; Ye, S.; Zhang, S.; Jiang, L. A New Signal-on Photoelectrochemical Biosensor Based on a Graphene/Quantum-Dot Nanocomposite Amplified by the Dual-Quenched Effect of Bipyridinium Relay and AuNPs. *Chem. - A Eur. J.* **2012**, *18* (51), 16411–16418. https://doi.org/10.1002/chem.201202213.

(309) Fan, G.; Han, L.; Zhang, J.; Zhu, J. Enhanced Photoelectrochemical Strategy for Ultrasensitive DNA Detection Based on Two Different Sizes of CdTe Quantum Dots Cosensitized TiO_2 /CdS:Mn Hybrid Structure. *Anal. Chem.* **2014**, *86* (21), 10877–10884. https://doi.org/10.1021/ac503043w.

(310) Hodes, G.; Howell, I. D. J.; Peter, L. M. Nanocrystalline Photoelectrochemical Cells: A New Concept In Photovoltaic Cells. *J. Electrochem. Soc.* **1992**, *139* (11), 3136–3140. https://doi.org/10.1149/1.2069045.

(311) Li, J.; Wu, N. Semiconductor-Based Photocatalysts and Photoelectrochemical Cells for Solar Fuel Generation: A Review. *Catal. Sci. Technol.* **2015**, *5* (3), 1360–1384.

https://doi.org/10.1039/C4CY00974F.

(312) Liu, X.-P.; Chen, J.-S.; Mao, C.; Niu, H.-L.; Song, J.-M.; Jin, B.-K. Enhanced Photoelectrochemical DNA Sensor Based on TiO_2/Au Hybrid Structure. *Biosens. Bioelectron.* **2018**, *116*, 23–29. https://doi.org/https://doi.org/10.1016/j.bios.2018.05.036.

(313) Shi, X.-M.; Fan, G.-C.; Shen, Q.; Zhu, J.-J. Photoelectrochemical DNA Biosensor Based on Dual-Signal Amplification Strategy Integrating Inorganic–Organic Nanocomposites Sensitization with λ-Exonuclease-Assisted Target Recycling. *ACS Appl. Mater. Interfaces* **2016**, *8* (51), 35091–35098. https://doi.org/10.1021/acsami.6b14466.

(314) Wang, G.-L.; Liu, K.-L.; Shu, J.-X.; Gu, T.-T.; Wu, X.-M.; Dong, Y.-M.; Li, Z.-J. A Novel Photoelectrochemical Sensor Based on Photocathode of PbS Quantum Dots Utilizing Catalase Mimetics of Bio-Bar-Coded Platinum Nanoparticles/G-Quadruplex/Hemin for Signal Amplification. *Biosens. Bioelectron.* **2015**, *69*, 106–112. https://doi.org/https://doi.org/10.1016/j.bios.2015.02.027.

(315) Zhang, L.; Sun, Y.; Liang, Y.-Y.; He, J.-P.; Zhao, W.-W.; Xu, J.-J.; Chen, H.-Y. Ag Nanoclusters Could Efficiently Quench the Photoresponse of CdS Quantum Dots for Novel Energy Transfer-Based Photoelectrochemical Bioanalysis. *Biosens. Bioelectron.* **2016**, *85*, 930–934. https://doi.org/https://doi.org/10.1016/j.bios.2016.06.018.

(316) Lu, W.; Wang, G.; Jin, Y.; Yao, X.; Hu, J.; Li, J. Label-Free Photoelectrochemical Strategy for Hairpin DNA Hybridization Detection on Titanium Dioxide Electrode. *Appl. Phys. Lett.* **2006**, *89* (26), 263902. https://doi.org/10.1063/1.2420786.

(317) Qiu, Z.; Shu, J.; Tang, D. Near-Infrared-to-Ultraviolet Light-Mediated Photoelectrochemical Aptasensing Platform for Cancer Biomarker Based on Core–Shell $NaYF_4$:Yb,Tm@TiO_2 Upconversion Microrods. *Anal. Chem.* **2018**, *90* (1), 1021–1028. https://doi.org/10.1021/acs.analchem.7b04479.

(318) Hou, W.; Cronin, S. B. A Review of Surface Plasmon Resonance Enhanced Photocatalysis. *Adv. Funct. Mater.* **2013**, *23*, 1612–1619. https://doi.org/10.1002/adfm.201202148.

(319) Qiu, Z.; Shu, J.; Tang, D. Plasmonic Resonance Enhanced Photoelectrochemical Aptasensors Based on G-C_3N_4/Bi_2MoO_6. *Chem. Commun.* **2018**, *54* (52), 7199–7202. https://doi.org/10.1039/C8CC04211J.

(320) Li, Z.; Su, C.; Wu, D.; Zhang, Z. Gold Nanoparticles Decorated Hematite Photoelectrode for Sensitive and Selective Photoelectrochemical Aptasensing of Lysozyme. *Anal. Chem.* **2018**, *90* (1), 961–967. https://doi.org/10.1021/acs.analchem.7b04015.

(321) Choi, H.; Chen, W. T.; Kamat, P. V. Know Thy Nano Neighbor. Plasmonic versus Electron Charging Effects of Metal Nanoparticles in Dye-Sensitized Solar Cells. *ACS Nano* **2012**, *6* (5), 4418–4427. https://doi.org/10.1021/nn301137r.

(322) Ni, M.; Leung, M. K. H.; Leung, D. Y. C.; Sumathy, K. A Review and Recent Developments in Photocatalytic Water-Splitting Using TiO_2 for Hydrogen Production. *Renew. Sustain. Energy Rev.* **2007**, *11* (3), 401–425. https://doi.org/https://doi.org/10.1016/j.rser.2005.01.009.

(323) Tokudome, H.; Yamada, Y.; Sonezaki, S.; Ishikawa, H.; Bekki, M.; Kanehira, K.; Miyauchi, M. Photoelectrochemical Deoxyribonucleic Acid Sensing on a Nanostructured TiO_2 Electrode. *Appl. Phys. Lett.* **2005**, *87* (21), 213901. https://doi.org/10.1063/1.2135392.

(324) Ochiai, T.; Fujishima, A. Photoelectrochemical Properties of TiO_2 Photocatalyst and Its Applications for Environmental Purification. *J. Photochem. Photobiol. C Photochem. Rev.* **2012**, *13*, 247–262. https://doi.org/10.1016/j.jphotochemrev.2012.07.001.

(325) Xagas, A. .; Bernard, M. .; Hugot-Le Goff, A.; Spyrellis, N.; Loizos, Z.; Falaras, P. Surface Modification and Photosensitisation of TiO_2 Nanocrystalline Films with Ascorbic Acid. *J. Photochem. Photobiol. A Chem.* **2000**, *132* (1–2), 115–120. https://doi.org/10.1016/S1010-6030(00)00202-1.

(326) Fujishima, A.; Rao, T. N.; Tryk, D. A. Titanium Dioxide Photocatalysis. *J. Photochem. Photobiol. C Photochem. Rev.* **2000**, *1*, 1–21. https://doi.org/10.1016/S1389-5567(00)00002-2.

(327) Lan, Y.; Lu, Y.; Ren, Z. Mini Review on Photocatalysis of Titanium Dioxide Nanoparticles and Their Solar Applications. *Nano Energy* **2013**, *2* (5), 1031–1045. https://doi.org/https://doi.org/10.1016/j.nanoen.2013.04.002.

(328) Ratchford, D. C.; Dunkelberger, A. D.; Vurgaftman, I.; Owrutsky, J. C.; Pehrsson, P. E. Quantification of Efficient Plasmonic Hot-Electron Injection in Gold Nanoparticle–TiO_2 Films. *Nano Lett.* **2017**, *17* (10), 6047–6055. https://doi.org/10.1021/acs.nanolett.7b02366.

(329) Du, L.; Furube, A.; Hara, K.; Katoh, R.; Tachiya, M. Ultrafast Plasmon Induced Electron Injection Mechanism in Gold–TiO_2 Nanoparticle System. *J. Photochem. Photobiol. C Photochem. Rev.* **2013**, *15*, 21–30. https://doi.org/https://doi.org/10.1016/j.jphotochemrev.2012.11.001.

(330) Achermann, M. Exciton-Plasmon Interactions in Metal-Semiconductor Nanostructures. *J. Phys. Chem. Lett.* **2010**, *1* (19), 2837–2843. https://doi.org/10.1021/jz101102e.

(331) Clavero, C. Plasmon-Induced Hot-Electron Generation at Nanoparticle/Metal-Oxide Interfaces for Photovoltaic and Photocatalytic Devices. *Nat. Photonics* **2014**, *8*, 95.

(332) Yen, Y.-C.; Chen, J.-A.; Ou, S.; Chen, Y.-S.; Lin, K.-J. Plasmon-Enhanced Photocurrent Using Gold Nanoparticles on a Three-Dimensional TiO_2 Nanowire-Web Electrode. *Sci. Rep.* **2017**, *7* (1), 42524. https://doi.org/10.1038/srep42524.

(333) Pu, Y.-C.; Wang, G.; Chang, K.-D.; Ling, Y.; Lin, Y.-K.; Fitzmorris, B. C.; Liu, C.-M.; Lu, X.; Tong, Y.; Zhang, J. Z.; Hsu, Y.-J.; Li, Y. Au Nanostructure-Decorated TiO_2 Nanowires Exhibiting Photoactivity Across Entire UV-Visible Region for Photoelectrochemical Water Splitting. *Nano Lett.* **2013**, *13* (8), 3817–3823. https://doi.org/10.1021/nl4018385.

(334) Chandrasekharan, N.; Kamat, P. V. Improving the Photoelectrochemical Performance of Nanostructured TiO_2 Films by Adsorption of Gold Nanoparticles †. *J. Phys. Chem. B* **2002**, *104* (46), 10851–10857. https://doi.org/10.1021/jp0010029.

(335) Naseri, N.; Amiri, M.; Moshfegh, A. Z. Visible Photoenhanced Current-Voltage Characteristics of Au:TiO_2 Nanocomposite Thin Films as Photoanodes. *J. Phys. D. Appl. Phys.* **2010**, *43* (10), 105405. https://doi.org/10.1088/0022-3727/43/10/105405.

(336) Li, J.; Cushing, S. K.; Zheng, P.; Meng, F.; Chu, D.; Wu, N. Plasmon-Induced Photonic and Energy-Transfer Enhancement of Solar Water Splitting by a Hematite Nanorod Array. *Nat. Commun.* **2013**, *4*, 2651. https://doi.org/10.1038/ncomms3651.

(337) Rayalu, S. S.; Jose, D.; Joshi, M. V; Mangrulkar, P. A.; Shrestha, K.; Klabunde, K. Photocatalytic Water Splitting on Au/TiO_2 Nanocomposites Synthesized through Various Routes: Enhancement in Photocatalytic Activity Due to SPR Effect. *Appl. Catal. B Environ.* **2013**, *142–143*, 684–693. https://doi.org/https://doi.org/10.1016/j.apcatb.2013.05.057.

(338) Murdoch, M.; Waterhouse, G. I. N.; Nadeem, M. A.; Metson, J. B.; Keane, M. A.; Howe, R. F.; Llorca, J.; Idriss, H. The Effect of Gold Loading and Particle Size on Photocatalytic Hydrogen Production from Ethanol over Au/TiO_2 Nanoparticles. *Nat. Chem.* **2011**, *3*, 489.

(339) Subramanian, V.; Wolf, E.; Kamat, P. V. Semiconductor−Metal Composite Nanostructures. To What Extent Do Metal Nanoparticles Improve the Photocatalytic Activity of TiO_2 Films? *J. Phys. Chem. B* **2001**, *105* (46), 11439–11446. https://doi.org/10.1021/jp011118k.

(340) Saha, S.; Victorious, A.; Pandey, R.; Clifford, A.; Zhitomirsky, I.; Soleymani, L. Differential Photoelectrochemical Biosensing Using DNA Nanospacers to Modulate Electron Transfer between Metal and Semiconductor Nanoparticles. *ACS Appl. Mater. Interfaces* **2020**, *12* (33), 36895–36905. https://doi.org/10.1021/acsami.0c09443.

(341) Tran, H.; Pera, F.; McPherson, D. S.; Viorel, D.; Voinigescu, S. P. 6-k/Spl Omega/ 43-Gb/s Differential Transimpedance-Limiting Amplifier with Auto-Zero Feedback and High Dynamic Range. *IEEE J. Solid-State Circuits* **2004**, *39* (10), 1680–1689. https://doi.org/10.1109/JSSC.2004.833547.

(342) Hao, N.; Zhang, Y.; Zhong, H.; Zhou, Z.; Hua, R.; Qian, J.; Liu, Q.; Li, H.; Wang, K. Design of a Dual Channel Self-Reference Photoelectrochemical Biosensor. *Anal. Chem.* **2017**, *89* (19), 10133–10136. https://doi.org/10.1021/acs.analchem.7b03132.

(343) Victorious, A.; Clifford, A.; Saha, S.; Zhitomirsky, I.; Soleymani, L. Integrating TiO_2 Nanoparticles within a Catecholic Polymeric Network Enhances the Photoelectrochemical Response of Biosensors. *J. Phys. Chem. C* **2019**, *123* (26), 16186–16193. https://doi.org/10.1021/acs.jpcc.9b02740.

(344) Sakib, S.; Pandey, R.; Soleymani, L.; Zhitomirsky, I. Surface Modification of TiO_2 for Photoelectrochemical DNA Biosensors. *Med. DEVICES SENSORS* **2020**, *3* (2).

https://doi.org/10.1002/mds3.10066.

(345) Grabar, K. C.; Freeman, R. G.; Hommer, M. B.; Natan, M. J. Preparation and Characterization of Au Colloid Monolayers. *Anal. Chem.* **1995**, *67* (4), 735–743. https://doi.org/10.1021/ac00100a008.

(346) Chandrasekharan, N.; Kamat, P. V. Improving the Photoelectrochemical Performance of Nanostructured TiO_2 Films by Adsorption of Gold Nanoparticles. *J. Phys. Chem. B* **2000**, *104* (46), 10851–10857. https://doi.org/10.1021/jp0010029.

(347) Zhang, J.; Song, S.; Wang, L.; Pan, D.; Fan, C. A Gold Nanoparticle-Based Chronocoulometric DNA Sensor for Amplified Detection of DNA. *Nat. Protoc.* **2007**, *2* (11), 2888–2895.

(348) Moon, S. Y.; Song, H. C.; Gwag, E. H.; Nedrygailov, I. I.; Lee, C.; Kim, J. J.; Doh, W. H.; Park, J. Y. Plasmonic Hot Carrier-Driven Oxygen Evolution Reaction on Au Nanoparticles/TiO_2 Nanotube Arrays. *Nanoscale* **2018**, *10* (47), 22180–22188. https://doi.org/10.1039/C8NR05144E.

(349) Pinchuk, A.; Kreibig, U.; Hilger, A. Optical Properties of Metallic Nanoparticles: Influence of Interface Effects and Interband Transitions. *Surf. Sci.* **2004**, *557* (1), 269–280. https://doi.org/https://doi.org/10.1016/j.susc.2004.03.056.

(350) Pinchuk, A.; Plessen, G. von; Kreibig, U. Influence of Interband Electronic Transitions on the Optical Absorption in Metallic Nanoparticles. *J. Phys. D. Appl. Phys.* **2004**, *37* (22), 3133–3139. https://doi.org/10.1088/0022-3727/37/22/012.

(351) Tan, S.; Argondizzo, A.; Ren, J.; Liu, L.; Zhao, J.; Petek, H. Plasmonic Coupling at a Metal/Semiconductor Interface. *Nat. Photonics* **2017**, *11* (12), 806–812. https://doi.org/10.1038/s41566-017-0049-4.

(352) Li, J.; Cushing, S. K.; Chu, D.; Zheng, P.; Bright, J.; Castle, C.; Manivannan, A.; Wu, N. Distinguishing Surface Effects of Gold Nanoparticles from Plasmonic Effect on Photoelectrochemical Water Splitting by Hematite. *J. Mater. Res.* **2016**, *31* (11), 1608–1615. https://doi.org/DOI: 10.1557/jmr.2016.102.

(353) Meng, F.; Cushing, S. K.; Li, J.; Hao, S.; Wu, N. Enhancement of Solar Hydrogen Generation by Synergistic Interaction of $La_2Ti_2O_7$ Photocatalyst with Plasmonic Gold Nanoparticles and Reduced Graphene Oxide Nanosheets. *ACS Catal.* **2015**, *5* (3), 1949–1955. https://doi.org/10.1021/cs5016194.

(354) Naphade, R. A.; Tathavadekar, M.; Jog, J. P.; Agarkar, S.; Ogale, S. Plasmonic Light Harvesting of Dye Sensitized Solar Cells by Au-Nanoparticle Loaded TiO_2 Nanofibers. *J. Mater. Chem. A* **2014**, *2* (4), 975–984. https://doi.org/10.1039/C3TA13246C.

(355) An, X.; Hu, C.; Liu, H.; Qu, J. Hierarchical Nanotubular Anatase/Rutile/TiO_2(B) Heterophase Junction with Oxygen Vacancies for Enhanced Photocatalytic H_2 Production. *Langmuir* **2018**, *34* (5), 1883–1889. https://doi.org/10.1021/acs.langmuir.7b03745.

(356) Minutella, E.; Schulz, F.; Lange, H. Excitation-Dependence of Plasmon-Induced Hot Electrons in Gold Nanoparticles. *J. Phys. Chem. Lett.* **2017**, *8* (19), 4925–4929. https://doi.org/10.1021/acs.jpclett.7b02043.

(357) Gelderman, K.; Lee, L.; Donne, S. W. Flat-Band Potential of a Semiconductor: Using the Mott–Schottky Equation. *J. Chem. Educ.* **2007**, *84* (4), 685. https://doi.org/10.1021/ed084p685.

(358) Schlather, A. E.; Manjavacas, A.; Lauchner, A.; Marangoni, V. S.; DeSantis, C. J.; Nordlander, P.; Halas, N. J. Hot Hole Photoelectrochemistry on Au@SiO_2@Au Nanoparticles. *J. Phys. Chem. Lett.* **2017**, *8* (9), 2060–2067. https://doi.org/10.1021/acs.jpclett.7b00563.

(359) Gomes Silva, C.; Juárez, R.; Marino, T.; Molinari, R.; García, H. Influence of Excitation Wavelength (UV or Visible Light) on the Photocatalytic Activity of Titania Containing Gold Nanoparticles for the Generation of Hydrogen or Oxygen from Water. *J. Am. Chem. Soc.* **2011**, *133* (3), 595–602. https://doi.org/10.1021/ja1086358.

(360) Nbelayim, P.; Kawamura, G.; Kian Tan, W.; Muto, H.; Matsuda, A. Systematic Characterization of the Effect of Ag@TiO_2 Nanoparticles on the Performance of Plasmonic Dye-Sensitized Solar Cells. *Sci. Rep.* **2017**, *7* (1), 15690. https://doi.org/10.1038/s41598-017-15541-z.

(361) Lim, S. P.; Pandikumar, A.; Lim, H. N.; Ramaraj, R.; Huang, N. M. Boosting Photovoltaic Performance of Dye-Sensitized Solar Cells Using Silver Nanoparticle-Decorated N,S-Co-Doped-TiO2 Photoanode. *Sci. Rep.* **2015**, *5*, 11922.

(362) Wen, C.; Ishikawa, K.; Kishima, M.; Yamada, K. Effects of Silver Particles on the Photovoltaic

Properties of Dye-Sensitized TiO_2 Thin Films. *Sol. Energy Mater. Sol. Cells* **2000**, *61* (4), 339–351. https://doi.org/https://doi.org/10.1016/S0927-0248(99)00117-8.
(363) Zhao, J.; Nguyen, S. C.; Ye, R.; Ye, B.; Weller, H.; Somorjai, G. A.; Alivisatos, A. P.; Toste, F. D. A Comparison of Photocatalytic Activities of Gold Nanoparticles Following Plasmonic and Interband Excitation and a Strategy for Harnessing Interband Hot Carriers for Solution Phase Photocatalysis. *ACS Cent. Sci.* **2017**, *3* (5), 482–488. https://doi.org/10.1021/acscentsci.7b00122.
(364) Li, H.; Li, Z.; Yu, Y.; Ma, Y.; Yang, W.; Wang, F.; Yin, X.; Wang, X. Surface-Plasmon-Resonance-Enhanced Photoelectrochemical Water Splitting from Au-Nanoparticle-Decorated 3D TiO_2 Nanorod Architectures. *J. Phys. Chem. C* **2017**, *121* (22), 12071–12079. https://doi.org/10.1021/acs.jpcc.7b03566.
(365) Cushing, S. K.; Li, J.; Bright, J.; Yost, B. T.; Zheng, P.; Bristow, A. D.; Wu, N. Controlling Plasmon-Induced Resonance Energy Transfer and Hot Electron Injection Processes in Metal@TiO_2 Core–Shell Nanoparticles. *J. Phys. Chem. C* **2015**, *119* (28), 16239–16244. https://doi.org/10.1021/acs.jpcc.5b03955.
(366) Cushing, S. K.; Wu, N. Photocatalyst-SPR Enhanced Solar Energy Harvesting-Interface. *Electrochem. Soc. Interface* **2013**, *22* (2), 63–67.
(367) Wu, N. Plasmonic Metal–Semiconductor Photocatalysts and Photoelectrochemical Cells: A Review. *Nanoscale* **2018**, *10* (6), 2679–2696.
(368) Xu, Z.; Lin, Y.; Yin, M.; Zhang, H.; Cheng, C.; Lu, L.; Xue, X.; Fan, H. J.; Chen, X.; Li, D. Understanding the Enhancement Mechanisms of Surface Plasmon-Mediated Photoelectrochemical Electrodes: A Case Study on Au Nanoparticle Decorated TiO_2 Nanotubes. *Adv. Mater. Interfaces* **2015**, *2* (13), 1500169. https://doi.org/10.1002/admi.201500169.
(369) Bettazzi, F.; Laschi, S.; Voccia, D.; Gellini, C.; Pietraperzia, G.; Falciola, L.; Pifferi, V.; Testolin, A.; Ingrosso, C.; Placido, T.; Comparelli, R.; Curri, M. L.; Palchetti, I. Ascorbic Acid-Sensitized Au Nanorods-Functionalized Nanostructured TiO_2 Transparent Electrodes for Photoelectrochemical Genosensing. *Electrochim. Acta* **2018**, *276*, 389–398. https://doi.org/https://doi.org/10.1016/j.electacta.2018.04.146.
(370) Nootchanat, S.; Ninsonti, H.; Baba, A.; Ekgasit, S.; Thammacharoen, C.; Shinbo, K.; Kato, K.; Kaneko, F. Investigation of Localized Surface Plasmon/Grating-Coupled Surface Plasmon Enhanced Photocurrent in TiO_2 Thin Films. *Phys. Chem. Chem. Phys.* **2014**, *16* (44), 24484–24492. https://doi.org/10.1039/C4CP03885A.
(371) Hao, Q.; Shan, X.; Lei, J.; Zang, Y.; Yang, Q.; Ju, H. A Wavelength-Resolved Ratiometric Photoelectrochemical Technique: Design and Sensing Applications. *Chem. Sci.* **2016**, *7* (1), 774–780. https://doi.org/10.1039/C5SC03336E.
(372) Qiu, Z.; Shu, J.; Liu, J.; Tang, D. Dual-Channel Photoelectrochemical Ratiometric Aptasensor with up-Converting Nanocrystals Using Spatial-Resolved Technique on Homemade 3D Printed Device. *Anal. Chem.* **2019**, *91* (2), 1260–1268. https://doi.org/10.1021/acs.analchem.8b05455.
(373) Moskovits, M. The Case for Plasmon-Derived Hot Carrier Devices. *Nat. Nanotechnol.* **2015**, *10*, 6.
(374) Wang, C.; Nie, X.-G.; Shi, Y.; Zhou, Y.; Xu, J.-J.; Xia, X.-H.; Chen, H.-Y. Direct Plasmon-Accelerated Electrochemical Reaction on Gold Nanoparticles. *ACS Nano* **2017**, *11* (6), 5897–5905. https://doi.org/10.1021/acsnano.7b01637.
(375) Hartland, G. V; Besteiro, L. V; Johns, P.; Govorov, A. O. What's so Hot about Electrons in Metal Nanoparticles? *ACS Energy Lett.* **2017**, *2* (7), 1641–1653. https://doi.org/10.1021/acsenergylett.7b00333.
(376) Govorov, A. O.; Zhang, W.; Skeini, T.; Richardson, H.; Lee, J.; Kotov, N. A. Gold Nanoparticle Ensembles as Heaters and Actuators: Melting and Collective Plasmon Resonances. *Nanoscale Res. Lett.* **2006**, *1* (1), 84. https://doi.org/10.1007/s11671-006-9015-7.
(377) Zhang, H.; Govorov, A. O. Optical Generation of Hot Plasmonic Carriers in Metal Nanocrystals: The Effects of Shape and Field Enhancement. *J. Phys. Chem. C* **2014**, *118* (14), 7606–7614. https://doi.org/10.1021/jp500009k.
(378) Ma, X. C.; Dai, Y.; Yu, L.; Huang, B. B. Energy Transfer in Plasmonic Photocatalytic Composites. *Light Sci. Appl.* **2016**, *5* (2), e16017–e16017. https://doi.org/10.1038/lsa.2016.17.
(379) Linic, S.; Christopher, P.; Xin, H.; Marimuthu, A. Catalytic and Photocatalytic Transformations on

Metal Nanoparticles with Targeted Geometric and Plasmonic Properties. *Acc. Chem. Res.* **2013**, *46* (8), 1890–1899. https://doi.org/10.1021/ar3002393.

(380) Dal Forno, S.; Ranno, L.; Lischner, J. Material, Size, and Environment Dependence of Plasmon-Induced Hot Carriers in Metallic Nanoparticles. *J. Phys. Chem. C* **2018**, *122* (15), 8517–8527. https://doi.org/10.1021/acs.jpcc.8b00651.

(381) Bian, H.; Shu, X.; Zhang, J.; Yuan, B.; Wang, Y.; Liu, L.; Xu, G.; Chen, Z.; Wu, Y. Uniformly Dispersed and Controllable Ligand-Free Silver-Nanoparticle-Decorated TiO_2 Nanotube Arrays with Enhanced Photoelectrochemical Behaviors. *Chem Asian J* **2013**, *8*, 2746–2754. https://doi.org/10.1002/asia.201300438.

(382) Balamurugan, B.; Maruyama, T. Evidence of an Enhanced Interband Absorption in Au Nanoparticles: Size-Dependent Electronic Structure and Optical Properties. *Appl. Phys. Lett.* **2005**, *87* (14), 1–3. https://doi.org/10.1063/1.2077834.

(383) Hartland, G. V. Optical Studies of Dynamics in Noble Metal Nanostructures. *Chem. Rev.* **2011**, *111* (6), 3858–3887. https://doi.org/10.1021/cr1002547.

(384) Yu, Y.; Sundaresan, V.; Willets, K. A. Hot Carriers versus Thermal Effects: Resolving the Enhancement Mechanisms for Plasmon-Mediated Photoelectrochemical Reactions. *J. Phys. Chem. C* **2018**, *122* (9), 5040–5048. https://doi.org/10.1021/acs.jpcc.7b12080.

(385) Cortés, E.; Xie, W.; Cambiasso, J.; Jermyn, A. S.; Sundararaman, R.; Narang, P.; Schlücker, S.; Maier, S. A. Plasmonic Hot Electron Transport Drives Nano-Localized Chemistry. *Nat. Commun.* **2017**, *8*, 14880.

(386) Brown, A. M.; Sundararaman, R.; Narang, P.; Goddard, W. A.; Atwater, H. A. Nonradiative Plasmon Decay and Hot Carrier Dynamics: Effects of Phonons, Surfaces, and Geometry. *ACS Nano* **2016**, *10* (1), 957–966. https://doi.org/10.1021/acsnano.5b06199.

(387) Atwater, H. A.; Polman, A. Plasmonics for Improved Photovoltaic Devices. *Nat. Mater.* **2010**, *9*, 205.

(388) Takai, A.; Kamat, P. V. Capture, Store, and Discharge. Shuttling Photogenerated Electrons across TiO_2–Silver Interface. *ACS Nano* **2011**, *5* (9), 7369–7376. https://doi.org/10.1021/nn202294b.

(389) Cushing, S. K.; Li, J.; Meng, F.; Senty, T. R.; Suri, S.; Zhi, M.; Li, M.; Bristow, A. D.; Wu, N. Photocatalytic Activity Enhanced by Plasmonic Resonant Energy Transfer from Metal to Semiconductor. *J. Am. Chem. Soc.* **2012**, *134* (36), 15033–15041. https://doi.org/10.1021/ja305603t.

(390) Brongersma, M. L.; Halas, N. J.; Nordlander, P. Plasmon-Induced Hot Carrier Science and Technology. *Nat. Nanotechnol.* **2015**, *10*, 25.

(391) Furube, A.; Hashimoto, S. Insight into Plasmonic Hot-Electron Transfer and Plasmon Molecular Drive: New Dimensions in Energy Conversion and Nanofabrication. *NPG Asia Mater.* **2017**, *9* (12), e454. https://doi.org/10.1038/am.2017.191.

(392) Stewart, M. E.; Anderton, C. R.; Thompson, L. B.; Maria, J.; Gray, S. K.; Rogers, J. A.; Nuzzo, R. G. Nanostructured Plasmonic Sensors. *Chem. Rev.* **2008**, *108* (2), 494–521. https://doi.org/10.1021/cr068126n.

(393) Mukherjee, S.; Libisch, F.; Large, N.; Neumann, O.; Brown, L. V; Cheng, J.; Lassiter, J. B.; Carter, E. A.; Nordlander, P.; Halas, N. J. Hot Electrons Do the Impossible: Plasmon-Induced Dissociation of H_2 on Au. *Nano Lett.* **2013**, *13* (1), 240–247. https://doi.org/10.1021/nl303940z.

(394) Govorov, A. O.; Zhang, H.; Gun'ko, Y. K. Theory of Photoinjection of Hot Plasmonic Carriers from Metal Nanostructures into Semiconductors and Surface Molecules. *J. Phys. Chem. C* **2013**, *117* (32), 16616–16631. https://doi.org/10.1021/jp405430m.

(395) Barman, T.; Hussain, A. A.; Sharma, B.; Pal, A. R. Plasmonic Hot Hole Generation by Interband Transition in Gold-Polyaniline. *Sci. Rep.* **2015**, *5*, 18276. https://doi.org/10.1038/srep18276.

(396) Berdakin, M.; Douglas-Gallardo, O. A.; Sánchez, C. G. Interplay between Intra- and Interband Transitions Associated with the Plasmon-Induced Hot Carrier Generation Process in Silver and Gold Nanoclusters. *J. Phys. Chem. C* **2020**, *124* (2), 1631–1639. https://doi.org/10.1021/acs.jpcc.9b10871.

(397) Haiss, W.; Thanh, N. T. K.; Aveyard, J.; Fernig, D. G. Determination of Size and Concentration of Gold Nanoparticles from UV-Vis Spectra. *Anal. Chem.* **2007**, *79* (11), 4215–4221.

(398) Charlé, K.-P.; Schulze, W.; Winter, B. The Size Dependent Shift of the Surface Plasmon Absorption Band of Small Spherical Metal Particles. *Zeitschrift für Phys. D Atoms, Mol. Clust.* **1989**, *12* (1), 471–475. https://doi.org/10.1007/BF01427000.

(399) Georgiev, P.; Simeonova, S.; Tsekov, R.; Balashev, K. Dependence of Plasmon Spectra of Small Gold Nanoparticles from Their Size: An Atomic Force Microscopy Experimental Approach. *Plasmonics* **2020**, *15* (2), 371–377. https://doi.org/10.1007/s11468-019-01034-4.

(400) Persson, B. N. J. Polarizability of Small Spherical Metal Particles: Influence of the Matrix Environment. *Surf. Sci.* **1993**, *281* (1), 153–162. https://doi.org/https://doi.org/10.1016/0039-6028(93)90865-H.

(401) Lee, C.; Park, Y.; Park, J. Y. Hot Electrons Generated by Intraband and Interband Transition Detected Using a Plasmonic Cu/TiO_2 Nanodiode. *RSC Adv.* **2019**, *9* (32), 18371–18376. https://doi.org/10.1039/C9RA02601K.

(402) Imani, R.; Pazoki, M.; Tiwari, A.; Boschloo, G.; Turner, A. P. F.; Kralj-Iglič, V.; Iglič, A. Band Edge Engineering of TiO_2@DNA Nanohybrids and Implications for Capacitive Energy Storage Devices. *Nanoscale* **2015**, *7* (23), 10438–10448. https://doi.org/10.1039/C5NR02533H.

(403) Hsu, C.-P.; Lee, K.-M.; Huang, J. T.-W.; Lin, C.-Y.; Lee, C.-H.; Wang, L.-P.; Tsai, S.-Y.; Ho, K.-C. EIS Analysis on Low Temperature Fabrication of TiO_2 Porous Films for Dye-Sensitized Solar Cells. *Electrochim. Acta* **2008**, *53* (25), 7514–7522. https://doi.org/10.1016/J.ELECTACTA.2008.01.104.

(404) Longo, C.; Nogueira, A. F.; De Paoli, M.-A.; Cachet, H. Solid-State and Flexible Dye-Sensitized TiO_2 Solar Cells: A Study by Electrochemical Impedance Spectroscopy. *J. Phys. Chem. B* **2002**, *106* (23), 5925–5930. https://doi.org/10.1021/jp014456u.

(405) Narang, P.; Ravishankar, S.; Atwater, H. A. Plasmonic Hot Carrier Dynamics in Solid-State and Chemical Systems for Energy Conversion. *Nanophotonics* **2016**, *5* (1), 96–111. https://doi.org/10.1515/nanoph-2016-0007.

(406) Besteiro, L. V; Yu, P.; Wang, Z.; Holleitner, A. W.; Hartland, G. V; Wiederrecht, G. P.; Govorov, A. O. The Fast and the Furious: Ultrafast Hot Electrons in Plasmonic Metastructures. Size and Structure Matter. *Nano Today* **2019**, *27*, 120–145. https://doi.org/https://doi.org/10.1016/j.nantod.2019.05.006.

(407) Saavedra, J. R. M.; Asenjo-Garcia, A.; García de Abajo, F. J. Hot-Electron Dynamics and Thermalization in Small Metallic Nanoparticles. *ACS Photonics* **2016**, *3* (9), 1637–1646. https://doi.org/10.1021/acsphotonics.6b00217.

(408) Ha, H.; An, H.; Yoo, M.; Lee, J.; Kim, H. Y. Catalytic CO Oxidation by CO-Saturated Au Nanoparticles Supported on CeO_2: Effect of CO Coverage. *J. Phys. Chem. C* **2017**, *121* (48), 26895–26902. https://doi.org/10.1021/acs.jpcc.7b09780.

(409) Lopez, N.; Janssens, T. V. W.; Clausen, B. S.; Xu, Y.; Mavrikakis, M.; Bligaard, T.; Nørskov, J. K. On the Origin of the Catalytic Activity of Gold Nanoparticles for Low-Temperature CO Oxidation. *J. Catal.* **2004**, *223* (1), 232–235. https://doi.org/https://doi.org/10.1016/j.jcat.2004.01.001.

(410) Liu, Y.; Chen, F.; Wang, Q.; Wang, J.; Wang, J.; Gebremariam, T. T. Surface Plasmon-Enhanced Activity and Stability for Methanol Oxidation on Gold Caviar-like Assembly under Solar Light. *J. Mater. Chem. A* **2018**, *6* (22), 10515–10524. https://doi.org/10.1039/c8ta02222d.

(411) Shiao, M.-H.; Lin, C.-T.; Huang, H. J.; Chen, P.-H.; Liao, B.-H.; Tseng, F.-G.; Lin, Y.-S. Novel Gold Dendritic Nanoflowers Deposited on Titanium Nitride for Photoelectrochemical Cells. *J. Solid State Electrochem.* **2018**, *22* (10), 3077–3084. https://doi.org/10.1007/s10008-018-4004-1.

(412) Yu, Y.; Wijesekara, K. D.; Xi, X.; Willets, K. A. Quantifying Wavelength-Dependent Plasmonic Hot Carrier Energy Distributions at Metal/Semiconductor Interfaces. *ACS Nano* **2019**, *13* (3), 3629–3637. https://doi.org/10.1021/acsnano.9b00219.

(413) Mubeen, S.; Hernandez-Sosa, G.; Moses, D.; Lee, J.; Moskovits, M. Plasmonic Photosensitization of a Wide Band Gap Semiconductor: Converting Plasmons to Charge Carriers. *Nano Lett.* **2011**, *11* (12), 5548–5552. https://doi.org/10.1021/nl203457v.

(414) Dagher, M.; Kleinman, M.; Ng, A.; Juncker, D. Ensemble Multicolour FRET Model Enables Barcoding at Extreme FRET Levels. *Nat. Nanotechnol.* **2018**, *13* (10), 925–932. https://doi.org/10.1038/s41565-018-0205-0.

(415) Pons, T.; Medintz, I. L.; Sapsford, K. E.; Higashiya, S.; Grimes, A. F.; English, D. S.; Mattoussi, H. On the Quenching of Semiconductor Quantum Dot Photoluminescence by Proximal Gold Nanoparticles. *Nano Lett.* **2007**, *7* (10), 3157–3164.

(416) Zeng, X.; Ma, S.; Bao, J.; Tu, W.; Dai, Z. Using Graphene-Based Plasmonic Nanocomposites to Quench Energy from Quantum Dots for Signal-on Photoelectrochemical Aptasensing. *Anal. Chem.* **2013**, *85* (24), 11720–11724. https://doi.org/10.1021/ac403408y.

(417) Xing, H.; Zhang, C. L.; Ruan, G.; Zhang, J.; Hwang, K.; Lu, Y. Multimodal Detection of a Small Molecule Target Using Stimuli-Responsive Liposome Triggered by Aptamer–Enzyme Conjugate. *Anal. Chem.* **2016**, *88* (3), 1506–1510. https://doi.org/10.1021/acs.analchem.5b04031.

(418) Sergelen, K.; Liedberg, B.; Knoll, W.; Dostálek, J. A Surface Plasmon Field-Enhanced Fluorescence Reversible Split Aptamer Biosensor. *Analyst* **2017**, *142* (16), 2995–3001. https://doi.org/10.1039/c7an00970d.

(419) Victorious, A.; Saha, S.; Pandey, R.; Didar, T. F.; Soleymani, L. Affinity-Based Detection of Biomolecules Using Photo-Electrochemical Readout. *Front. Chem.* **2019**, *7*, 617. https://doi.org/10.3389/fchem.2019.00617.

(420) Lai, R. Y.; Lee, S.; Soh, H. T.; Plaxco, K. W.; Heeger, A. J. Differential Labeling of Closely Spaced Biosensor Electrodes via Electrochemical Lithography. *Langmuir* **2006**, *22* (4), 1932–1936. https://doi.org/10.1021/la052132h.

(421) Zheng, Y.-N.; Liang, W.-B.; Xiong, C.-Y.; Zhuo, Y.; Chai, Y.-Q.; Yuan, R. Universal Ratiometric Photoelectrochemical Bioassay with Target-Nucleotide Transduction-Amplification and Electron-Transfer Tunneling Distance Regulation Strategies for Ultrasensitive Determination of MicroRNA in Cells. *Anal. Chem.* **2017**, *89* (17), 9445–9451. https://doi.org/10.1021/acs.analchem.7b02270.

(422) Wang, Y.; Li, M.; Zhu, Y.; Ge, S.; Yu, J.; Yan, M.; Song, X. A Visible Light Photoelectrochemical Sensor for Tumor Marker Detection Using Tin Dioxide Quantum Dot-Graphene as Labels. *Analyst* **2013**, *138* (23), 7112–7118. https://doi.org/10.1039/c3an01410j.

(423) Dai, H.; Zhang, S.; Hong, Z.; Lin, Y. A Potentiometric Addressable Photoelectrochemical Biosensor for Sensitive Detection of Two Biomarkers. *Anal. Chem.* **2016**, *88* (19), 9532–9538. https://doi.org/10.1021/acs.analchem.6b02101.

(424) Hao, N.; Hua, R.; Zhang, K.; Lu, J.; Wang, K. A Sunlight Powered Portable Photoelectrochemical Biosensor Based on a Potentiometric Resolve Ratiometric Principle. *Anal. Chem.* **2018**, *90* (22), 13207–13211. https://doi.org/10.1021/acs.analchem.8b03218.

(425) Huang, Y.-L.; Chang, W. S.; Van, C. N.; Liu, H.-J.; Tsai, K.-A.; Chen, J.-W.; Kuo, H.-H.; Tzeng, W.-Y.; Chen, Y.-C.; Wu, C.-L.; Luo, C.-W.; Hsu, Y.-J.; Chu, Y.-H. Tunable Photoelectrochemical Performance of Au/$BiFeO_3$ Heterostructure. *Nanoscale* **2016**, *8* (34), 15795–15801. https://doi.org/10.1039/C6NR04997D.

(426) Li, J.-M.; Cheng, H.-Y.; Chiu, Y.-H.; Hsu, Y.-J. ZnO–Au–SnO_2 Z-Scheme Photoanodes for Remarkable Photoelectrochemical Water Splitting. *Nanoscale* **2016**, *8* (34), 15720–15729. https://doi.org/10.1039/C6NR05605A.

(427) Li, J.-M.; Tsao, C.-W.; Fang, M.-J.; Chen, C.-C.; Liu, C.-W.; Hsu, Y.-J. TiO_2-Au-Cu_2O Photocathodes: Au-Mediated Z-Scheme Charge Transfer for Efficient Solar-Driven Photoelectrochemical Reduction. *ACS Appl. Nano Mater.* **2018**, *1* (12), 6843–6853. https://doi.org/10.1021/acsanm.8b01678.

(428) Chen, K.-H.; Pu, Y.-C.; Chang, K.-D.; Liang, Y.-F.; Liu, C.-M.; Yeh, J.-W.; Shih, H.-C.; Hsu, Y.-J. Ag-Nanoparticle-Decorated SiO_2 Nanospheres Exhibiting Remarkable Plasmon-Mediated Photocatalytic Properties. *J. Phys. Chem. C* **2012**, *116* (35), 19039–19045. https://doi.org/10.1021/jp306555j.

(429) Chiu, Y.-H.; Naghadeh, S. B.; Lindley, S. A.; Lai, T.-H.; Kuo, M.-Y.; Chang, K.-D.; Zhang, J. Z.; Hsu, Y.-J. Yolk-Shell Nanostructures as an Emerging Photocatalyst Paradigm for Solar Hydrogen Generation. *Nano Energy* **2019**, *62*, 289–298. https://doi.org/https://doi.org/10.1016/j.nanoen.2019.05.008.

(430) Cao, C.; Zhang, F.; Goldys, E. M.; Gao, F.; Liu, G. Advances in Structure-Switching Aptasensing towards Real Time Detection of Cytokines. *TrAC Trends Anal. Chem.* **2018**, *102*, 379–396. https://doi.org/https://doi.org/10.1016/j.trac.2018.03.002.

(431) Anne, A.; Demaille, C. Electron Transport by Molecular Motion of Redox-DNA Strands: Unexpectedly Slow Rotational Dynamics of 20-Mer Ds-DNA Chains End-Grafted onto Surfaces via C6 Linkers. *J. Am. Chem. Soc.* **2008**, *130* (30), 9812–9823. https://doi.org/10.1021/ja801074m.

(432) Ferapontova, E. E. DNA Electrochemistry and Electrochemical Sensors for Nucleic Acids. *Annu. Rev. Anal. Chem.* **2018**, *11* (1), 197–218. https://doi.org/10.1146/annurev-anchem-061417-125811.

(433) Sakib, S.; Pandey, R.; Soleymani, L.; Zhitomirsky, I. Surface Modification of TiO_2 for Photoelectrochemical DNA Biosensors. *Med. DEVICES SENSORS* **2020**, *3* (2), e10066. https://doi.org/10.1002/mds3.10066.

(434) Saha, S.; Chan, Y.; Soleymani, L. Enhancing the Photoelectrochemical Response of DNA Biosensors Using Wrinkled Interfaces. *ACS Appl. Mater. Interfaces* **2018**, *10* (37), 31178–31185. https://doi.org/10.1021/acsami.8b12286.

(435) Rivetti, C.; Walker, C.; Bustamante, C. Polymer Chain Statistics and Conformational Analysis of DNA Molecules with Bends or Sections of Different Flexibility. *J. Mol. Biol.* **1998**, *280* (1), 41–59. https://doi.org/10.1006/JMBI.1998.1830.

(436) White, T. P.; Catchpole, K. R. Plasmon-Enhanced Internal Photoemission for Photovoltaics: Theoretical Efficiency Limits. *Appl. Phys. Lett.* **2012**, *101* (7), 073905. https://doi.org/10.1063/1.4746425.

(437) Liu, Z.; Hou, W.; Pavaskar, P.; Aykol, M.; Cronin, S. B. Plasmon Resonant Enhancement of Photocatalytic Water Splitting under Visible Illumination. *Nano Lett.* **2011**, *11* (3), 1111–1116. https://doi.org/10.1021/nl104005n.

(438) Cushing, S. K.; Wu, N. Progress and Perspectives of Plasmon-Enhanced Solar Energy Conversion. *J. Phys. Chem. Lett.* **2016**, *7* (4), 666–675. https://doi.org/10.1021/acs.jpclett.5b02393.

(439) Li, J.; Cushing, S. K.; Zheng, P.; Senty, T.; Meng, F.; Bristow, A. D.; Manivannan, A.; Wu, N. Solar Hydrogen Generation by a CdS-Au-TiO_2 Sandwich Nanorod Array Enhanced with Au Nanoparticle as Electron Relay and Plasmonic Photosensitizer. *J. Am. Chem. Soc.* **2014**, *136* (23), 8438–8449. https://doi.org/10.1021/ja503508g.

(440) Zhang, J.; Li, Z.; Zhang, J.; Guo, S.; Li, G.; Fang, Q. Efficient Base-Free Direct Oxidation of Glucose to Gluconic Acid over TiO_2 -Supported Gold Clusters. *Nanoscale* **2018**, *11*, 1326–1334. https://doi.org/10.1039/c8nr08143c.

(441) Asapu, R.; Ciocarlan, R.-G.; Claes, N.; Blommaerts, N.; Minjauw, M.; Ahmad, T.; Dendooven, J.; Cool, P.; Bals, S.; Denys, S.; Detavernier, C.; Lenaerts, S.; Verbruggen, S. W. Plasmonic Near-Field Localization of Silver Core–Shell Nanoparticle Assemblies via Wet Chemistry Nanogap Engineering. *ACS Appl. Mater. Interfaces* **2017**, *9* (47), 41577–41585. https://doi.org/10.1021/acsami.7b13965.

(442) Tian, Y.; Tatsuma, T. Mechanisms and Applications of Plasmon-Induced Charge Separation at TiO_2 Films Loaded with Gold Nanoparticles. *J. Am. Chem. Soc.* **2005**, *127* (20), 7632–7637. https://doi.org/10.1021/ja042192u.

(443) Cushing, S. K.; Wu, N. Plasmon-Enhanced Solar Energy Harvesting. *Electrochem. Soc. Interface* **2013**, *22* (2), 63–67.

(444) Hühn, J.; Carrillo-Carrion, C.; Soliman, M. G.; Pfeiffer, C.; Valdeperez, D.; Masood, A.; Chakraborty, I.; Zhu, L.; Gallego, M.; Yue, Z.; Carril, M.; Feliu, N.; Escudero, A.; Alkilany, A. M.; Pelaz, B.; del Pino, P.; Parak, W. J. Selected Standard Protocols for the Synthesis, Phase Transfer, and Characterization of Inorganic Colloidal Nanoparticles. *Chem. Mater.* **2017**, *29* (1), 399–461. https://doi.org/10.1021/acs.chemmater.6b04738.

(445) Lin, P.; Liu, D.; Wei, W.; Guo, J.; Ke, S.; Zeng, X.; Chen, S. A Novel Protein Binding Strategy for Energy-Transfer-Based Photoelectrochemical Detection of Enzymatic Activity of Botulinum Neurotoxin A. *Electrochem. commun.* **2018**, *97*, 114–118. https://doi.org/https://doi.org/10.1016/j.elecom.2018.11.004.

(446) Zhong, X.; Lv, J.; Xue, S.; Yuan, R.; Chai, Y. An Electrochemical Assay Based on Acid-Induced Dissolution of Nanoparticles to Trigger Enzyme-Free Cleavage for Target Detection. *J. Electrochem. Soc.* **2018**, *165* (5), B223–B226. https://doi.org/10.1149/2.1151805jes.

(447) Wei, H.; Wang, Y.; Zhang, H.; Zhao, H.; Jiang, W. Au Nanoparticles Fluorescence Switch-Mediated Target Recycling Amplification Strategy for Sensitive Nucleic Acid Detection. *RSC Adv.*

2016, *6* (13), 10650–10654. https://doi.org/10.1039/C5RA23761K.

(448) Wen, G.; Dong, W.; Liu, B.; Li, Z.; Fan, L. A Novel Nonenzymatic Cascade Amplification for Ultrasensitive Photoelectrochemical DNA Sensing Based on Target Driven to Initiate Cyclic Assembly of Hairpins. *Biosens. Bioelectron.* **2018**, *117*, 91–96. https://doi.org/https://doi.org/10.1016/j.bios.2018.05.054.

(449) Sundah, N. R.; Ho, N. R. Y.; Lim, G. S.; Natalia, A.; Ding, X.; Liu, Y.; Seet, J. E.; Chan, C. W.; Loh, T. P.; Shao, H. Barcoded DNA Nanostructures for the Multiplexed Profiling of Subcellular Protein Distribution. *Nat. Biomed. Eng.* **2019**, *3* (9), 684–694. https://doi.org/10.1038/s41551-019-0417-0.

(450) Filik, H.; Avan, A. A. Nanostructures for Nonlabeled and Labeled Electrochemical Immunosensors: Simultaneous Electrochemical Detection of Cancer Markers: A Review. *Talanta* **2019**, *205*, 120153. https://doi.org/https://doi.org/10.1016/j.talanta.2019.120153.

(451) Keshavarz, M.; Behpour, M.; Rafiee-pour, H.-A. Recent Trends in Electrochemical MicroRNA Biosensors for Early Detection of Cancer. *RSC Adv.* **2015**, *5* (45), 35651–35660. https://doi.org/10.1039/C5RA01726B.

(452) Pereira da Silva Neves, M. M.; González-García, M. B.; Hernández-Santos, D.; Fanjul-Bolado, P. Future Trends in the Market for Electrochemical Biosensing. *Curr. Opin. Electrochem.* **2018**, *10*, 107–111. https://doi.org/https://doi.org/10.1016/j.coelec.2018.05.002.

(453) Shabaninejad, Z.; Yousefi, F.; Movahedpour, A.; Ghasemi, Y.; Dokanehiifard, S.; Rezaei, S.; Aryan, R.; Savardashtaki, A.; Mirzaei, H. Electrochemical-Based Biosensors for MicroRNA Detection: Nanotechnology Comes into View. *Anal. Biochem.* **2019**, *581*, 113349. https://doi.org/https://doi.org/10.1016/j.ab.2019.113349.

(454) Dai, Y.; Liu, C. C. Recent Advances on Electrochemical Biosensing Strategies toward Universal Point-of-Care Systems. *Angew. Chemie Int. Ed.* **2019**, *58* (36), 12355–12368. https://doi.org/10.1002/anie.201901879.

(455) Li, X.; Dou, B.; Yuan, R.; Xiang, Y. Mismatched Catalytic Hairpin Assembly and Ratiometric Strategy for Highly Sensitive Electrochemical Detection of MicroRNA from Tumor Cells. *Sensors Actuators B Chem.* **2019**, *286*, 191–197. https://doi.org/https://doi.org/10.1016/j.snb.2019.01.152.

(456) Wang, Z.; Yu, R.; Zeng, H.; Wang, X.; Luo, S.; Li, W.; Luo, X.; Yang, T. Nucleic Acid-Based Ratiometric Electrochemiluminescent, Electrochemical and Photoelectrochemical Biosensors: A Review. *Microchim. Acta* **2019**, *186* (7), 405. https://doi.org/10.1007/s00604-019-3514-6.

(457) Zhang, Z.; Lanz, R. B.; Xiao, L.; Wang, L.; Hartig, S. M.; Ittmann, M. M.; Feng, Q.; He, B. The Tumor Suppressive MiR-200b Subfamily Is an ERG Target Gene in Human Prostate Tumors. *Oncotarget* **2016**, *7* (25), 37993–38003. https://doi.org/10.18632/oncotarget.9366.

(458) Souza, M. F. de; Kuasne, H.; Barros-Filho, M. de C.; Cilião, H. L.; Marchi, F. A.; Fuganti, P. E.; Paschoal, A. R.; Rogatto, S. R.; Cólus, I. M. de S. Circulating MRNAs and MiRNAs as Candidate Markers for the Diagnosis and Prognosis of Prostate Cancer. *PLoS One* **2017**, *12* (9), e0184094-.

(459) Song, C.-J.; Chen, H.; Chen, L.-Z.; Ru, G.-M.; Guo, J.-J.; Ding, Q.-N. The Potential of MicroRNAs as Human Prostate Cancer Biomarkers: A Meta-Analysis of Related Studies. *J. Cell. Biochem.* **2018**, *119* (3), 2763–2786. https://doi.org/10.1002/jcb.26445.

(460) Kingham, T. P.; Alatise, O. I.; Vanderpuye, V.; Casper, C.; Abantanga, F. A.; Kamara, T. B.; Olopade, O. I.; Habeebu, M.; Abdulkareem, F. B.; Denny, L. Treatment of Cancer in Sub-Saharan Africa. *Lancet Oncol.* **2013**, *14* (4), e158–e167. https://doi.org/https://doi.org/10.1016/S1470-2045(12)70472-2.

(461) Bruix, J.; Sherman, M.; Diseases, A. A. for the S. of L. Management of Hepatocellular Carcinoma: An Update. *Hepatology* **2011**, *53* (3), 1020–1022. https://doi.org/10.1002/hep.24199.

(462) Jaffee, E. M.; Dang, C. Van; Agus, D. B.; Alexander, B. M.; Anderson, K. C.; Ashworth, A.; Barker, A. D.; Bastani, R.; Bhatia, S.; Bluestone, J. A.; Brawley, O.; Butte, A. J.; Coit, D. G.; Davidson, N. E.; Davis, M.; DePinho, R. A.; Diasio, R. B.; Draetta, G.; Frazier, A. L.; Futreal, A.; Gambhir, S. S.; Ganz, P. A.; Garraway, L.; Gerson, S.; Gupta, S.; Heath, J.; Hoffman, R. I.; Hudis, C.; Hughes-Halbert, C.; Ibrahim, R.; Jadvar, H.; Kavanagh, B.; Kittles, R.; Le, Q.-T.; Lippman, S. M.; Mankoff, D.; Mardis, E. R.; Mayer, D. K.; McMasters, K.; Meropol, N. J.; Mitchell, B.; Naredi, P.; Ornish, D.; Pawlik, T. M.; Peppercorn, J.; Pomper, M. G.; Raghavan, D.; Ritchie, C.;

Schwarz, S. W.; Sullivan, R.; Wahl, R.; Wolchok, J. D.; Wong, S. L.; Yung, A. Future Cancer Research Priorities in the USA: A Lancet Oncology Commission. *Lancet Oncol.* **2017**, *18* (11), e653–e706. https://doi.org/https://doi.org/10.1016/S1470-2045(17)30698-8.

(463) Crowley, E.; Di Nicolantonio, F.; Loupakis, F.; Bardelli, A. Liquid Biopsy: Monitoring Cancer-Genetics in the Blood. *Nat. Rev. Clin. Oncol.* **2013**, *10* (8), 472–484. https://doi.org/10.1038/nrclinonc.2013.110.

(464) Pös, O.; Biró, O.; Szemes, T.; Nagy, B. Circulating Cell-Free Nucleic Acids: Characteristics and Applications. *Eur. J. Hum. Genet.* **2018**, *26* (7), 937–945. https://doi.org/10.1038/s41431-018-0132-4.

(465) Underhill, H. R.; Kitzman, J. O.; Hellwig, S.; Welker, N. C.; Daza, R.; Baker, D. N.; Gligorich, K. M.; Rostomily, R. C.; Bronner, M. P.; Shendure, J. Fragment Length of Circulating Tumor DNA. *PLOS Genet.* **2016**, *12* (7), e1006162-.

(466) Kilgour, E.; Rothwell, D. G.; Brady, G.; Dive, C. Liquid Biopsy-Based Biomarkers of Treatment Response and Resistance. *Cancer Cell* **2020**, *37* (4), 485–495. https://doi.org/https://doi.org/10.1016/j.ccell.2020.03.012.

(467) Valadi, H.; Ekström, K.; Bossios, A.; Sjöstrand, M.; Lee, J. J.; Lötvall, J. O. Exosome-Mediated Transfer of MRNAs and MicroRNAs Is a Novel Mechanism of Genetic Exchange between Cells. *Nat. Cell Biol.* **2007**, *9* (6), 654–659. https://doi.org/10.1038/ncb1596.

(468) Mateescu, B.; Kowal, E. J. K.; van Balkom, B. W. M.; Bartel, S.; Bhattacharyya, S. N.; Buzás, E. I.; Buck, A. H.; de Candia, P.; Chow, F. W. N.; Das, S.; Driedonks, T. A. P.; Fernández-Messina, L.; Haderk, F.; Hill, A. F.; Jones, J. C.; Van Keuren-Jensen, K. R.; Lai, C. P.; Lässer, C.; di Liegro, I.; Lunavat, T. R.; Lorenowicz, M. J.; Maas, S. L. N.; Mäger, I.; Mittelbrunn, M.; Momma, S.; Mukherjee, K.; Nawaz, M.; Pegtel, D. M.; Pfaffl, M. W.; Schiffelers, R. M.; Tahara, H.; Théry, C.; Tosar, J. P.; Wauben, M. H. M.; Witwer, K. W.; Nolte-‘t Hoen, E. N. M. Obstacles and Opportunities in the Functional Analysis of Extracellular Vesicle RNA – an ISEV Position Paper. *J. Extracell. Vesicles* **2017**, *6* (1), 1286095. https://doi.org/10.1080/20013078.2017.1286095.

(469) Li, J.; Tan, S.; Kooger, R.; Zhang, C.; Zhang, Y. MicroRNAs as Novel Biological Targets for Detection and Regulation. *Chem. Soc. Rev.* **2014**, *43* (2), 506–517. https://doi.org/10.1039/C3CS60312A.

(470) Suryawanshi, S.; Vlad, A. M.; Lin, H.-M.; Mantia-Smaldone, G.; Laskey, R.; Lee, M.; Lin, Y.; Donnellan, N.; Klein-Patel, M.; Lee, T.; Mansuria, S.; Elishaev, E.; Budiu, R.; Edwards, R. P.; Huang, X. Plasma MicroRNAs as Novel Biomarkers for Endometriosis and Endometriosis-Associated Ovarian Cancer. *Clin. Cancer Res.* **2013**, *19* (5), 1213. https://doi.org/10.1158/1078-0432.CCR-12-2726.

(471) Tribolet, L.; Kerr, E.; Cowled, C.; Bean, A. G. D.; Stewart, C. R.; Dearnley, M.; Farr, R. J. MicroRNA Biomarkers for Infectious Diseases: From Basic Research to Biosensing. *Frontiers in Microbiology*. Frontiers Media S.A. June 3, 2020, p 1197. https://doi.org/10.3389/fmicb.2020.01197.

(472) Gillespie, P.; Ladame, S.; O’Hare, D. Molecular Methods in Electrochemical MicroRNA Detection. *Analyst* **2019**, *144* (1), 114–129. https://doi.org/10.1039/C8AN01572D.

(473) Parikh, A.; Lee, C.; Joseph, P.; Marchini, S.; Baccarini, A.; Kolev, V.; Romualdi, C.; Fruscio, R.; Shah, H.; Wang, F.; Mullokandov, G.; Fishman, D.; D’Incalci, M.; Rahaman, J.; Kalir, T.; Redline, R. W.; Brown, B. D.; Narla, G.; DiFeo, A. MicroRNA-181a Has a Critical Role in Ovarian Cancer Progression through the Regulation of the Epithelial–Mesenchymal Transition. *Nat. Commun.* **2014**, *5* (1), 2977. https://doi.org/10.1038/ncomms3977.

(474) Schwarzenbach, H.; Nishida, N.; Calin, G. A.; Pantel, K. Clinical Relevance of Circulating Cell-Free MicroRNAs in Cancer. *Nat. Rev. Clin. Oncol.* **2014**, *11*, 145–156.

(475) Tkach, M.; Théry, C. Communication by Extracellular Vesicles: Where We Are and Where We Need to Go. *Cell* **2016**, *164* (6), 1226–1232. https://doi.org/https://doi.org/10.1016/j.cell.2016.01.043.

(476) Matsumura, T.; Sugimachi, K.; Iinuma, H.; Takahashi, Y.; Kurashige, J.; Sawada, G.; Ueda, M.; Uchi, R.; Ueo, H.; Takano, Y.; Shinden, Y.; Eguchi, H.; Yamamoto, H.; Doki, Y.; Mori, M.; Ochiya, T.; Mimori, K. Exosomal MicroRNA in Serum Is a Novel Biomarker of Recurrence in

Human Colorectal Cancer. *Br. J. Cancer* **2015**, *113* (2), 275–281. https://doi.org/10.1038/bjc.2015.201.

(477) Braicu, C.; Tomuleasa, C.; Monroig, P.; Cucuianu, A.; Berindan-Neagoe, I.; Calin, G. A. Exosomes as Divine Messengers: Are They the Hermes of Modern Molecular Oncology? *Cell Death Differ.* **2015**, *22* (1), 34–45. https://doi.org/10.1038/cdd.2014.130.

(478) Endzeliņš, E.; Berger, A.; Melne, V.; Bajo-Santos, C.; Soboļevska, K.; Ābols, A.; Rodriguez, M.; Šantare, D.; Rudņickiha, A.; Lietuvietis, V.; Llorente, A.; Linē, A. Detection of Circulating MiRNAs: Comparative Analysis of Extracellular Vesicle-Incorporated MiRNAs and Cell-Free MiRNAs in Whole Plasma of Prostate Cancer Patients. *BMC Cancer* **2017**, *17* (1), 730. https://doi.org/10.1186/s12885-017-3737-z.

(479) Salido-Guadarrama, A. I.; Morales-Montor, J. G.; Rangel-Escareño, C.; Langley, E.; Peralta-Zaragoza, O.; Colin, J. L. C.; Rodriguez-Dorantes, M. Urinary MicroRNA-Based Signature Improves Accuracy of Detection of Clinically Relevant Prostate Cancer within the Prostate-Specific Antigen Grey Zone. *Mol. Med. Rep.* **2016**, *13* (6), 4549–4560. https://doi.org/10.3892/mmr.2016.5095.

(480) Shu, J.; Qiu, Z.; Zhou, Q.; Lin, Y.; Lu, M.; Tang, D. Enzymatic Oxydate-Triggered Self-Illuminated Photoelectrochemical Sensing Platform for Portable Immunoassay Using Digital Multimeter. *Anal. Chem.* **2016**, *88* (5), 2958–2966. https://doi.org/10.1021/acs.analchem.6b00262.

(481) Tavallaie, R.; McCarroll, J.; Le Grand, M.; Ariotti, N.; Schuhmann, W.; Bakker, E.; Tilley, R. D.; Hibbert, D. B.; Kavallaris, M.; Gooding, J. J. Nucleic Acid Hybridization on an Electrically Reconfigurable Network of Gold-Coated Magnetic Nanoparticles Enables MicroRNA Detection in Blood. *Nat. Nanotechnol.* **2018**, *13* (11), 1066–1071. https://doi.org/10.1038/s41565-018-0232-x.

(482) Yuan, Y.-H.; Wu, Y.-D.; Chi, B.-Z.; Wen, S.-H.; Liang, R.-P.; Qiu, J.-D. Simultaneously Electrochemical Detection of MicroRNAs Based on Multifunctional Magnetic Nanoparticles Probe Coupling with Hybridization Chain Reaction. *Biosens. Bioelectron.* **2017**, *97*, 325–331. https://doi.org/https://doi.org/10.1016/j.bios.2017.06.022.

(483) Zhang, Y.; Liu, L.; Xi, F.; Wu, T.; Lin, X. A Simple Layer-by-Layer Assembly Strategy for a Reagentless Biosensor Based on a Nanocomposite of Methylene Blue-Multiwalled Carbon Nanotubes. *Electroanalysis* **2010**, *22* (3), 277–285. https://doi.org/https://doi.org/10.1002/elan.200900307.

(484) Turchinovich, A.; Weiz, L.; Langheinz, A.; Burwinkel, B. Characterization of Extracellular Circulating MicroRNA. *Nucleic Acids Res.* **2011**, *39* (16), 7223–7233. https://doi.org/10.1093/nar/gkr254.

(485) Chowdhury, S. K. R.; Gemin, A.; Singh, G. High Activity of Mitochondrial Glycerophosphate Dehydrogenase and Glycerophosphate-Dependent ROS Production in Prostate Cancer Cell Lines. *Biochem. Biophys. Res. Commun.* **2005**, *333* (4), 1139–1145. https://doi.org/https://doi.org/10.1016/j.bbrc.2005.06.017.

(486) Sardana, G.; Jung, K.; Stephan, C.; Diamandis, E. P. Proteomic Analysis of Conditioned Media from the PC3, LNCaP, and 22Rv1 Prostate Cancer Cell Lines: Discovery and Validation of Candidate Prostate Cancer Biomarkers. *J. Proteome Res.* **2008**, *7* (8), 3329–3338. https://doi.org/10.1021/pr8003216.

(487) Koo, K. M.; Carrascosa, L. G.; Shiddiky, M. J. A.; Trau, M. Poly(A) Extensions of MiRNAs for Amplification-Free Electrochemical Detection on Screen-Printed Gold Electrodes. *Anal. Chem.* **2016**, *88* (4), 2000–2005. https://doi.org/10.1021/acs.analchem.5b04795.

(488) Vanacore, D.; Boccellino, M.; Rossetti, S.; Cavaliere, C.; D'Aniello, C.; Di Franco, R.; Romano, F. J.; Montanari, M.; La Mantia, E.; Piscitelli, R.; Nocerino, F.; Cappuccio, F.; Grimaldi, G.; Izzo, A.; Castaldo, L.; Pepe, M. F.; Malzone, M. G.; Iovane, G.; Ametrano, G.; Stiuso, P.; Quagliuolo, L.; Barberio, D.; Perdonà, S.; Muto, P.; Montella, M.; Maiolino, P.; Veneziani, B. M.; Botti, G.; Caraglia, M.; Facchini, G. Micrornas in Prostate Cancer: An Overview. *Oncotarget* **2017**, *8* (30), 50240–50251. https://doi.org/10.18632/oncotarget.16933.

(489) Lötvall, J.; Hill, A. F.; Hochberg, F.; Buzás, E. I.; Di Vizio, D.; Gardiner, C.; Gho, Y. S.; Kurochkin, I. V; Mathivanan, S.; Quesenberry, P.; Sahoo, S.; Tahara, H.; Wauben, M. H.; Witwer, K. W.; Théry, C. Minimal Experimental Requirements for Definition of Extracellular Vesicles and

Their Functions: A Position Statement from the International Society for Extracellular Vesicles. *J. Extracell. Vesicles* **2014**, *3* (1), 26913. https://doi.org/10.3402/jev.v3.26913.

(490) Soekmadji, C.; Riches, J. D.; Russell, P. J.; Ruelcke, J. E.; McPherson, S.; Wang, C.; Hovens, C. M.; Corcoran, N. M.; BioResource, A. P. C. C.; Hill, M. M.; Nelson, C. C. Modulation of Paracrine Signaling by CD9 Positive Small Extracellular Vesicles Mediates Cellular Growth of Androgen Deprived Prostate Cancer. *Oncotarget* **2016**, *8* (32), 52237–52255. https://doi.org/10.18632/oncotarget.11111.

(491) Svenningsen, P.; Sabaratnam, R.; Jensen, B. L. Urinary Extracellular Vesicles: Origin, Role as Intercellular Messengers and Biomarkers; Efficient Sorting and Potential Treatment Options. *Acta Physiol.* **2020**, *228* (1), e13346. https://doi.org/https://doi.org/10.1111/apha.13346.

(492) He, M.; Liu, Y.; Deng, X.; Qi, S.; Sun, X.; Liu, G.; Liu, Y.; Liu, Y.; Zhao, M. Down-Regulation of MiR-200b-3p by Low P73 Contributes to the Androgen-Independence of Prostate Cancer Cells. *Prostate* **2013**, *73* (10), 1048–1056. https://doi.org/10.1002/pros.22652.

(493) Catto, J. W. F.; Alcaraz, A.; Bjartell, A. S.; De Vere White, R.; Evans, C. P.; Fussel, S.; Hamdy, F. C.; Kallioniemi, O.; Mengual, L.; Schlomm, T.; Visakorpi, T. MicroRNA in Prostate, Bladder, and Kidney Cancer: A Systematic Review. *Eur. Urol.* **2011**, *59* (5), 671–681. https://doi.org/https://doi.org/10.1016/j.eururo.2011.01.044.

(494) Stuopelytė, K.; Daniūnaitė, K.; Jankevičius, F.; Jarmalaitė, S. Detection of MiRNAs in Urine of Prostate Cancer Patients. *Medicina (B. Aires).* **2016**, *52* (2), 116–124. https://doi.org/10.1016/j.medici.2016.02.007.

(495) Li, S.; Liang, Z.; Xu, L.; Zou, F. MicroRNA-21: A Ubiquitously Expressed pro-Survival Factor in Cancer and Other Diseases. *Mol. Cell. Biochem.* **2012**, *360* (1), 147–158. https://doi.org/10.1007/s11010-011-1052-6.

(496) Soekmadji, C.; Russell, P.; Nelson, C. Exosomes in Prostate Cancer: Putting Together the Pieces of a Puzzle. *Cancers (Basel).* **2013**, *5* (4), 1522–1544. https://doi.org/10.3390/cancers5041522.

(497) Silver, D. A.; Pellicer, I.; Fair, W. R.; Heston, W. D.; Cordon-Cardo, C. Prostate-Specific Membrane Antigen Expression in Normal and Malignant Human Tissues. *Clin. Cancer Res.* **1997**, *3* (1), 81.

(498) O'Keefe, D. S.; Bacich, D. J.; Heston, W. D. W. Prostate Specific Membrane Antigen. In *Prostate Cancer: Biology, Genetics, and the New Therapeutics*; Chung, L. W. K., Isaacs, W. B., Simons, J. W., Eds.; Humana Press: Totowa, NJ, 2001; pp 307–326. https://doi.org/10.1007/978-1-59259-009-4_18.

(499) Chang, T. J.; Juan, C. C.; Yin, P. H.; Chi, C. W.; Tsay, H. J. Up-Regulation of Beta-Actin, Cyclophilin and GAPDH in N1S1 Rat Hepatoma. *Oncol. Rep.* **1998**, *5* (2), 469–540. https://doi.org/10.3892/or.5.2.469.

(500) Ruan, W.; Lai, M. Actin, a Reliable Marker of Internal Control? *Clinica Chimica Acta*. Elsevier October 1, 2007, pp 1–5. https://doi.org/10.1016/j.cca.2007.07.003.

(501) Waikar, S. S.; Sabbisetti, V. S.; Bonventre, J. V. Normalization of Urinary Biomarkers to Creatinine during Changes in Glomerular Filtration Rate. *Kidney Int.* **2010**, *78* (5), 486–494. https://doi.org/https://doi.org/10.1038/ki.2010.165.

(502) Park, Y. H.; Shin, H. W.; Jung, A. R.; Kwon, O. S.; Choi, Y.-J.; Park, J.; Lee, J. Y. Prostate-Specific Extracellular Vesicles as a Novel Biomarker in Human Prostate Cancer. *Sci. Rep.* **2016**, *6* (1), 30386. https://doi.org/10.1038/srep30386.

(503) Etheridge, A.; Lee, I.; Hood, L.; Galas, D.; Wang, K. Extracellular MicroRNA: A New Source of Biomarkers. *Mutat. Res. Mol. Mech. Mutagen.* **2011**, *717* (1), 85–90. https://doi.org/https://doi.org/10.1016/j.mrfmmm.2011.03.004.

(504) Williams, L. V; Veliceasa, D.; Vinokour, E.; Volpert, O. V. MiR-200b Inhibits Prostate Cancer EMT, Growth and Metastasis. *PLoS One* **2014**, *8* (12), e83991-.

(505) Adams-McGavin, R. C.; Chan, Y.; Gabardo, C. M.; Yang, J.; Skreta, M.; Fung, B. C.; Soleymani, L. Nanoporous and Wrinkled Electrodes Enhance the Sensitivity of Glucose Biosensors. *Electrochim. Acta* **2017**, *242*, 1–9. https://doi.org/https://doi.org/10.1016/j.electacta.2017.04.108.

(506) Shi, G.; Ye, D.; Yao, X.; Zhang, S.; Dai, B.; Zhang, H.; Shen, Y.; Zhu, Y.; Zhu, Y.; Xiao, W.; Ma, C. Involvement of MicroRNA-21 in Mediating Chemo-Resistance to Docetaxel in Androgen-

Independent Prostate Cancer PC3 Cells. *Acta Pharmacol. Sin.* **2010**, *31* (7), 867–873. https://doi.org/10.1038/aps.2010.48.

(507) Wang, B.; Cao, J.-T.; Liu, Y.-M. Recent Progress of Heterostructure-Based Photoelectrodes in Photoelectrochemical Biosensing: A Mini Review. *Analyst* **2020**, *145* (4), 1121–1128. https://doi.org/10.1039/C9AN02448D.

(508) Qiu, Z.; Tang, D. Nanostructure-Based Photoelectrochemical Sensing Platforms for Biomedical Applications. *J. Mater. Chem. B* **2020**, *8* (13), 2541–2561. https://doi.org/10.1039/C9TB02844G.

(509) Shen, X.; Liu, D.; Zhu, C.; Li, Y.; Liu, Y.; You, T. Photoelectrochemical and Electrochemical Ratiometric Aptasensing: A Case Study of Streptomycin. *Electrochem. commun.* **2020**, *110*, 106637. https://doi.org/https://doi.org/10.1016/j.elecom.2019.106637.

(510) Wang, M.; Yin, H.; Zhou, Y.; Sui, C.; Wang, Y.; Meng, X.; Waterhouse, G. I. N.; Ai, S. Photoelectrochemical Biosensor for MicroRNA Detection Based on a MoS_2/g-C_3N_4/Black TiO_2 Heterojunction with Histostar@AuNPs for Signal Amplification. *Biosens. Bioelectron.* **2019**, *128*, 137–143. https://doi.org/https://doi.org/10.1016/j.bios.2018.12.048.

(511) Da, P.; Li, W.; Lin, X.; Wang, Y.; Tang, J.; Zheng, G. Surface Plasmon Resonance Enhanced Real-Time Photoelectrochemical Protein Sensing by Gold Nanoparticle-Decorated TiO_2 Nanowires. *Anal. Chem.* **2014**, *86* (13), 6633–6639. https://doi.org/10.1021/ac501406x.

(512) Guo, L.; Li, Z.; Marcus, K.; Navarro, S.; Liang, K.; Zhou, L.; Mani, P. D.; Florczyk, S. J.; Coffey, K. R.; Orlovskaya, N.; Sohn, Y.-H.; Yang, Y. Periodically Patterned Au-TiO_2 Heterostructures for Photoelectrochemical Sensor. *ACS Sensors* **2017**, *2* (5), 621–625. https://doi.org/10.1021/acssensors.7b00251.

(513) Shu, J.; Tang, D. Recent Advances in Photoelectrochemical Sensing: From Engineered Photoactive Materials to Sensing Devices and Detection Modes. *Anal. Chem.* **2020**, *92* (1), 363–377. https://doi.org/10.1021/acs.analchem.9b04199.

(514) Zhao, M.; Fan, G. C.; Chen, J. J.; Shi, J. J.; Zhu, J. J. Highly Sensitive and Selective Photoelectrochemical Biosensor for Hg^{2+} Detection Based on Dual Signal Amplification by Exciton Energy Transfer Coupled with Sensitization Effect. *Anal. Chem.* **2015**, *87* (24), 12340–12347. https://doi.org/10.1021/acs.analchem.5b03721.

(515) Yan, Z.; Wang, Z.; Miao, Z.; Liu, Y. Dye-Sensitized and Localized Surface Plasmon Resonance Enhanced Visible-Light Photoelectrochemical Biosensors for Highly Sensitive Analysis of Protein Kinase Activity. *Anal. Chem.* **2016**, *88* (1), 922–929. https://doi.org/10.1021/acs.analchem.5b03661.

(516) Huang, Y.-L.; Chang, W. S.; Van, C. N.; Liu, H.-J.; Tsai, K.-A.; Chen, J.-W.; Kuo, H.-H.; Tzeng, W.-Y.; Chen, Y.-C.; Wu, C.-L.; Luo, C.-W.; Hsu, Y.-J.; Chu, Y.-H. Tunable Photoelectrochemical Performance of Au/$BiFeO_3$ Heterostructure. *Nanoscale* **2016**, *8* (34), 15795–15801. https://doi.org/10.1039/C6NR04997D.

(517) Steel, A. B.; Herne, T. M.; Tarlov, M. J. Electrochemical Quantitation of DNA Immobilized on Gold. *Anal. Chem.* **1998**, *70* (22), 4670–4677. https://doi.org/10.1021/ac980037q.

(518) Reynaldo, L. P.; Vologodskii, A. V; Neri, B. P.; Lyamichev, V. I. The Kinetics of Oligonucleotide Replacements. *J. Mol. Biol.* **2000**, *297* (2), 511–520. https://doi.org/https://doi.org/10.1006/jmbi.2000.3573.

(519) Baker, B. A.; Milam, V. T. Hybridization Kinetics between Immobilized Double-Stranded DNA Probes and Targets Containing Embedded Recognition Segments. *Nucleic Acids Res.* **2011**, *39* (15), e99–e99. https://doi.org/10.1093/nar/gkr293.

(520) Traeger, J. C.; Schwartz, D. K. Surface-Mediated DNA Hybridization: Effects of DNA Conformation, Surface Chemistry, and Electrostatics. *Langmuir* **2017**, *33* (44), 12651–12659. https://doi.org/10.1021/acs.langmuir.7b02675.

(521) Schwarzenbach, H.; Hoon, D. S. B.; Pantel, K. Cell-Free Nucleic Acids as Biomarkers in Cancer Patients. *Nat. Rev. Cancer* **2011**, *11* (6), 426–437. https://doi.org/10.1038/nrc3066.

(522) Hayes, J.; Peruzzi, P. P.; Lawler, S. MicroRNAs in Cancer: Biomarkers, Functions and Therapy. *Trends Mol. Med.* **2014**, *20* (8), 460–469. https://doi.org/10.1016/j.molmed.2014.06.005.

(523) Zhou, S.; Jin, J.; Wang, J.; Zhang, Z.; Freedman, J. H.; Zheng, Y.; Cai, L. MiRNAS in Cardiovascular Diseases: Potential Biomarkers, Therapeutic Targets and Challenges. *Acta*

Pharmacol. Sin. **2018**, *39* (7), 1073–1084. https://doi.org/10.1038/aps.2018.30.

(524) Manzanares-Palenzuela, C. L.; Fernandes, E. G. R.; Lobo-Castañón, M. J.; López-Ruiz, B.; Zucolotto, V. Impedance Sensing of DNA Hybridization onto Nanostructured Phthalocyanine-Modified Electrodes. *Electrochim. Acta* **2016**, *221*, 86–95. https://doi.org/https://doi.org/10.1016/j.electacta.2016.10.140.

(525) Tu, W.; Cao, H.; Zhang, L.; Bao, J.; Liu, X.; Dai, Z. Dual Signal Amplification Using Gold Nanoparticles-Enhanced Zinc Selenide Nanoflakes and P19 Protein for Ultrasensitive Photoelectrochemical Biosensing of MicroRNA in Cell. *Anal. Chem.* **2016**, *88* (21), 10459–10465. https://doi.org/10.1021/acs.analchem.6b02381.

(526) Ateş Sönmezoğlu, Ö.; Akın, S.; Terzi, B.; Mutlu, S.; Sönmezoğlu, S. An Effective Approach for High-Efficiency Photoelectrochemical Solar Cells by Using Bifunctional DNA Molecules Modified Photoanode. *Adv. Funct. Mater.* **2016**, *26* (47), 8776–8783. https://doi.org/10.1002/adfm.201603454.

(527) Lim, S. P.; Pandikumar, A.; Huang, N. M.; Lim, H. N. Facile Synthesis of Au@TiO_2 Nanocomposite and Its Application as a Photoanode in Dye-Sensitized Solar Cells. *RSC Adv.* **2015**, *5* (55), 44398–44407. https://doi.org/10.1039/C5RA06220A.

(528) Johansson, M. A.; Hellenäs, K.-E. Matrix Effects in Immunobiosensor Determination of Clenbuterol in Urine and Serum. *Analyst* **2004**, *129* (5), 438–442. https://doi.org/10.1039/B316723B.

(529) Jin, Y.; Yao, X.; Liu, Q.; Li, J. Hairpin DNA Probe Based Electrochemical Biosensor Using Methylene Blue as Hybridization Indicator. *Biosens. Bioelectron.* **2007**, *22* (6), 1126–1130. https://doi.org/10.1016/j.bios.2006.04.011.

(530) Zhao, Y.; Zhou, L.; Tang, Z. Cleavage-Based Signal Amplification of RNA. *Nat. Commun.* **2013**, *4* (1), 1493. https://doi.org/10.1038/ncomms2492.

(531) Bruch, R.; Baaske, J.; Chatelle, C.; Meirich, M.; Madlener, S.; Weber, W.; Dincer, C.; Urban, G. A. Biosensors: CRISPR/Cas13a-Powered Electrochemical Microfluidic Biosensor for Nucleic Acid Amplification-Free MiRNA Diagnostics (Adv. Mater. 51/2019). *Adv. Mater.* **2019**, *31* (51), 1970365. https://doi.org/https://doi.org/10.1002/adma.201970365.

(532) Miao, P.; Zhang, T.; Xu, J.; Tang, Y. Electrochemical Detection of MiRNA Combining T7 Exonuclease-Assisted Cascade Signal Amplification and DNA-Templated Copper Nanoparticles. *Anal. Chem.* **2018**, *90* (18), 11154–11160. https://doi.org/10.1021/acs.analchem.8b03425.

(533) Kim, S. J.; Yoon, S.; Kim, H. J. Review of Solution-Processed Oxide Thin-Film Transistors. *Jpn. J. Appl. Phys.* **2014**, *53* (2S), 02BA02. https://doi.org/10.7567/jjap.53.02ba02.

(534) Dunklin, J. R.; Rose, A. H.; Zhang, H.; Miller, E. M.; van de Lagemaat, J. Plasmonic Hot Hole Transfer in Gold Nanoparticle-Decorated Transition Metal Dichalcogenide Nanosheets. *ACS Photonics* **2020**, *7* (1), 197–202. https://doi.org/10.1021/acsphotonics.9b01393.

(535) Li, M.; Cushing, S. K.; Wang, Q.; Shi, X.; Hornak, L. A.; Hong, Z.; Wu, N. Size-Dependent Energy Transfer between CdSe/ZnS Quantum Dots and Gold Nanoparticles. *J. Phys. Chem. Lett.* **2011**, *2* (17), 2125–2129. https://doi.org/10.1021/jz201002g.

(536) Yun, C. S.; Javier, A.; Jennings, T.; Fisher, M.; Hira, S.; Peterson, S.; Hopkins, B.; Reich, N. O.; Strouse, G. F. Nanometal Surface Energy Transfer in Optical Rulers, Breaking the FRET Barrier. *J. Am. Chem. Soc.* **2005**, *127* (9), 3115–3119. https://doi.org/10.1021/ja043940i.

(537) Zhao, W. W.; Yu, P. P.; Shan, Y.; Wang, J.; Xu, J. J.; Chen, H. Y. Exciton-Plasmon Interactions between CdS Quantum Dots and Ag Nanoparticles in Photoelectrochemical System and Its Biosensing Application. *Anal. Chem.* **2012**, *84* (14), 5892–5897. https://doi.org/10.1021/ac300127s.

(538) Su, S.; Sun, H.; Cao, W.; Chao, J.; Peng, H.; Zuo, X.; Yuwen, L.; Fan, C.; Wang, L. Dual-Target Electrochemical Biosensing Based on DNA Structural Switching on Gold Nanoparticle-Decorated MoS_2 Nanosheets. *ACS Appl. Mater. Interfaces* **2016**, *8* (11), 6826–6833. https://doi.org/10.1021/acsami.5b12833.

(539) Cederquist, K. B.; Keating, C. D. Hybridization Efficiency of Molecular Beacons Bound to Gold Nanowires: Effect of Surface Coverage and Target Length. *Langmuir* **2010**, *26* (23), 18273–18280. https://doi.org/10.1021/la1031703.

(540) Wu, Q.; Zhang, F.; Li, H.; Li, Z.; Kang, Q.; Shen, D. A Ratiometric Photoelectrochemical Immunosensor Based on G-C3N4@TiO$_2$ NTs Amplified by Signal Antibodies–Co 3 O 4 Nanoparticle Conjugates. *Analyst* **2018**, *143* (20), 5030–5037. https://doi.org/10.1039/C8AN01345D.

(541) Toumazou, C.; Lidgey, F. J.; Cheung, P. Y. K. Current-Mode Analogue Signal Processing Circuits-a Review of Recent Developments. In *IEEE International Symposium on Circuits and Systems*,; 1989; pp 1572–1575 vol.3. https://doi.org/10.1109/ISCAS.1989.100660.

(542) Tang, H.; Chen, C.-J.; Huang, Z.; Bright, J.; Meng, G.; Liu, R.-S.; Wu, N. Plasmonic Hot Electrons for Sensing, Photodetection, and Solar Energy Applications: A Perspective. *J. Chem. Phys.* **2020**, *152* (22), 220901. https://doi.org/10.1063/5.0005334.

(543) Grozema, F. C.; Berlin, Y. A.; Siebbeles, L. D. A. Sequence-Dependent Charge Transfer in Donor–DNA–Acceptor Systems: A Theoretical Study. *Int. J. Quantum Chem.* **1999**, *75* (6), 1009–1016. https://doi.org/10.1002/(SICI)1097-461X(1999)75:6<1009::AID-QUA5>3.0.CO;2-A.

(544) Arnold, A. R.; Grodick, M. A.; Barton, J. K. DNA Charge Transport: From Chemical Principles to the Cell. *Cell Chem. Biol.* **2016**, *23* (1), 183–197. https://doi.org/10.1016/j.chembiol.2015.11.010.

(545) Zhang, J. Z.; Noguez, C. Plasmonic Optical Properties and Applications of Metal Nanostructures. *Plasmonics* **2008**, *3* (4), 127–150. https://doi.org/10.1007/s11468-008-9066-y.

(546) Feng, T.; Qiao, X.; Wang, H.; Sun, Z.; Qi, Y.; Hong, C. An Electrochemical Immunosensor for Simultaneous Point-of-Care Cancer Markers Based on the Host–Guest Inclusion of β-Cyclodextrin–Graphene Oxide. *J. Mater. Chem. B* **2016**, *4* (5), 990–996. https://doi.org/10.1039/C5TB02480C.

(547) Jadon, N.; Jain, R.; Sharma, S.; Singh, K. Recent Trends in Electrochemical Sensors for Multianalyte Detection – A Review. *Talanta* **2016**, *161*, 894–916. https://doi.org/https://doi.org/10.1016/j.talanta.2016.08.084.

(548) Pakchin, P. S.; Nakhjavani, S. A.; Saber, R.; Ghanbari, H.; Omidi, Y. Recent Advances in Simultaneous Electrochemical Multi-Analyte Sensing Platforms. *TrAC Trends Anal. Chem.* **2017**, *92*, 32–41. https://doi.org/https://doi.org/10.1016/j.trac.2017.04.010.

(549) Xu, T.; Liu, N.; Yuan, J.; Ma, Z. Triple Tumor Markers Assay Based on Carbon-Gold Nanocomposite. *Biosens. Bioelectron.* **2015**, *70*, 161–166. https://doi.org/10.1016/j.bios.2015.03.036.